# Integrating EPR and computational modeling to measure protein structure and dynamics

by

**Xiaowei Bogetti**

B.S. Chemistry, Nankai University, 2015
B. Econ. Finance, Nankai University, 2015

Submitted to the Graduate Faculty of the

Dietrich School of Arts and Sciences in partial fulfillment

of the requirements for the degree of

Doctor of Philosophy

University of Pittsburgh

2023

UNIVERSITY OF PITTSBURGH

DIETRICH SCHOOL OF ARTS AND SCIENCES

This dissertation was presented

by

**Xiaowei Bogetti**

It was defended on

September 15, 2023

and approved by

Jennifer Laaser, Ph. D., Assistance Professor of Chemistry

Seth Horne, Ph. D., Professor of Chemistry

Junmei Wang, Ph. D., Associate Professor of Pharmaceutical Sciences

Dissertation Director: Sunil Saxena, Ph. D., Professor of Chemistry

## Integrating EPR and computational modeling to measure protein structure and dynamics

Xiaowei Bogetti, PhD

University of Pittsburgh, 2023

Electron paramagnetic resonance (EPR) spectroscopy coupled with site-directed spin labeling has become a powerful method for probing conformational diversity and dynamics of macromolecules. The sparse distance and dynamics information obtained from EPR measurements greatly benefit from computational modeling. In Chapter 1 of this dissertation, I provide a comprehensive overview of different modeling techniques that can be coupled with EPR. These computational approaches can be used to sample protein and label conformations, simulate EPR spectra, predict or refine protein structures and capture large-amplitude conformational transitions. In Chapter 2, I describe the development of new force field parameters for double histidine-copper(II) (dHis)-Cu(II)-based EPR labels. Molecular dynamics (MD) simulations based on these new force fields generate distance distributions between the labels in remarkable agreement with experiments. These MD-trajectories help us understand the orientational selectivity in double electron-electron resonance (DEER) using Cu(II)-based labels. In Chapter 3, I showcase a new strategy that enables sampling conformational changes at atomic resolution by combining dHis-Cu(II) EPR and weighted ensemble MD simulations. This strategy has been applied to sample a seconds-timescale conformational change in the homodimeric detoxification enzyme. These simulations reveal the negative cooperativity within the enzyme controlled by key residue-residue interactions, which may be essential for the enzyme to protect cells from a broad range of toxins. In Chapter 4, I discuss the development and application of an *in silico* approach to optimize DEER data acquisition in collaboration with my coworker. This optimal DEER acquisition scheme improves the efficiency of obtaining Cu(II)-based EPR distance distributions, and reduces the data collection time by as much as six fold. Overall, this body of work presents the potential of integrating EPR measurements and computational modeling to tackle various biophysical questions over a wide range of timescales.

## Table of Contents

**Preface ... xv**

**1.0 Introduction ... 1**

**1.1 Site-directed spin labeling ... 7**

**1.2 Small-amplitude fluctuations revealed by MD simulations detail the EPR spectra 9**

**1.3 Structure refinement and prediction using modeling coupled with PDS-EPR ... 15**

**1.4 Sampling of large-amplitude conformational changes using modeling with EPR distance restraints ... 18**

**1.5 An *in silico* method based on insights from MD for cost-efficient PDS-EPR measurements using dHis-Cu(II) labels at Q-band ... 22**

**1.6 Summary and outlook ... 23**

**1.7 Acknowledgements ... 24**

**2.0 Molecular Dynamics Simulations Based on Newly Developed Force Field Parameters for Cu$^{2+}$ Spin Labels Provide Insights into Double-Histidine-Based Double Electron–Electron Resonance ... 25**

**2.1 Introduction ... 25**

**2.2 Methods ... 28**

**2.2.1 Protein System Setup ... 28**

**2.2.2 Molecular Mechanics Force Field (MMFF) Parameterization ... 29**

**2.2.3 MD Simulations ... 32**

**2.2.4 DEER Experiment ... 33**

**2.3 Results and Discussion ... 34**

2.4 Conclusions ........................................................................................................ 48

2.5 Acknowledgements ................................................................................................ 49

3.0 Direct observation of negative cooperativity in a detoxification enzyme at the atomic level by EPR and simulation ........................................................................ 50

3.1 Introduction ........................................................................................................ 50

3.2 Materials and methods ........................................................................................ 53

3.2.1 Protein purification and sample preparation ..................................................53

3.2.2 CW-EPR and ESEEM measurements ............................................................55

3.2.3 EPR distance measurements .........................................................................55

3.2.4 Conventional molecular dynamics simulations ...............................................60

3.2.5 Weighted ensemble simulations .....................................................................62

3.3 Results and discussion ........................................................................................ 63

3.3.1 EPR distance distributions reveal an alternate ligand-free state ..................66

3.3.2 Conventional molecular dynamics simulations ...............................................73

3.3.3 Weighted ensemble MD generates direct views of negative cooperativity in the ligand-free ensemble ........................................................................................78

3.4 Conclusion ........................................................................................................... 93

3.5 Acknowledgement ................................................................................................. 94

4.0 An optimal acquisition scheme for Q-band EPR distance measurements using $Cu^{2+}$-based protein labels ........................................................................................ 95

4.1 Introduction ........................................................................................................ 95

4.2 Experimental ........................................................................................................ 98

4.2.1 Protein expression, purification, sample preparation, and EPR experiments ....98
4.2.2 MD simulation of dHis-$Cu^{2+}$-NTA labeled protein ....100
4.2.3 Monte-Carlo simulation ....101
4.2.4 Excitation profile of $\theta$ ....105
4.2.5 EPR distance measurements ....106
4.3 Results and discussion ....107
4.3.1 MD simulation provides initial angle and distance distributions ....107
4.3.2 The optimal DEER collection scheme ....110
4.3.3 Assumptions and generality of the acquisition scheme ....120
4.3.4 DEER on liganded hGSTA1-1 ....122
4.3.5 X-band DEER and MD results further proves the validity of the summed Q-band DEER ....127
4.4 Conclusions ....128
4.5 Acknowledgements ....129
5.0 Conclusions and future directions ....130
Bibliography ....134

# List of Tables

**Table 2-1. Structure Comparison.** ........................................................................................ **35**

**Table 3-1. Labeling efficiency of the dHis-Cu(II)-NTA labeled hGSTA1-1.** ........................ **58**

**Table 3-2. DEER acquisition parameters, modulation depths and SNR, for dHis-Cu(II)-NTA labeled K211H/E215H hGSTA1-1 with different GSHex concentrations (For all samples listed, hGSTA1-1 concentraion is 100 $\mu$M).** .................................................. **58**

**Table 3-3. DEER acquisition parameters, modulation depths and SNR for biological and technical repeats of dHis-Cu(II)-NTA labeled K211H/E215H hGSTA1-1 in the ligand-free state.** ........................................................................................................ **60**

# List of Figures

**Figure 1-1. Protein conformations and dynamics can be probed by EPR and simulations. . 2**

**Figure 1-2. Spin labels. .......................................................................................... 5**

**Figure 1-3. Different types of biophysical information that can be inquired by EPR techniques and can be supplemented with molecular modeling tools. ........................ 6**

**Figure 1-4. An example illustrating force field development for a spin label. ..................... 10**

**Figure 1-5. Predicting a conformational change using MMM. ............................................ 19**

**Figure 1-6. An integrated approach using PDS-EPR and weighted ensemble MD simulations to capture an seconds-timescale conformational change. .......................................... 21**

**Figure 2-1. DFT optimized structures of $Cu^{2+}$-based protein labels. .................................... 31**

**Figure 2-2. Comparison of distance distributions for $Cu^{2+}$–NTA-labeled GB1 mutants..... 38**

**Figure 2-3. $Cu^{2+}$- $Cu^{2+}$ distance distributions from each 200 ns MD run. ............................ 38**

**Figure 2-4. DEER distance distritions of dHis-$Cu^{2+}$ labeled GB1. ........................................ 39**

**Figure 2-5. Cα–Cα distance distributions of the spin-labeled sites. ...................................... 41**

**Figure 2-6. Distributions of $C\alpha$-$C\alpha$ distance. $C\alpha$-$C\alpha$ distance distributions. ........................ 42**

**Figure 2-7. Predicted $Cu^{2+}$ spatial distributions. ................................................................. 43**

**Figure 2-8. Molecular basis of orientational selectivity. ........................................................ 46**

**Figure 2-9. The angles $\gamma$ and $\eta$ as a function of simulation time of the $Cu^{2+}$-NTA labeled 6H/8H/28H/32H GB1. ........................................................................................ 47**

**Figure 2-10. Simulated DEER signals. ........................................................................ 48**

**Figure 3-1. The entire structure of the ligand-free hGSTA1-1 is missing. ........................... 51**

**Figure 3-2. Biological and technical repeats for DEER measurements on ligand-free dHis-Cu(II)-NTA labeled hGSTA1-1. .......... 57**

**Figure 3-3. Determination of relaxation times. .......... 58**

**Figure 3-4. 80 K CW-EPR spectra at X-band for dHis-Cu(II)-NTA bound hGSTA1-1 with different concentrations of GSHex ligand present. .......... 65**

**Figure 3-5. X-band ESEEM spectra for dHis-Cu(II)-NTA bound hGSTA1-1 with different concentrations of GSHex ligand present. The concentration of hGSTA1-1 for all samples is 100 μM. .......... 66**

**Figure 3-6. Q-band DEER results for dHis-Cu(II)-NTA bound hGSTA1-1 with different concentrations of GSHex ligand. .......... 67**

**Figure 3-7. 80 K CW-EPR and ESEEM spectra at X-band for dHis-Cu(II)-NTA bound hGSTA1-1 with binding sites saturated with 1 mM of different ligands, namely ethacrynic acid glutathione conjugate (EASG) and S-(2,4-dinitrophenyl)glutathione (GS-DNB). .......... 70**

**Figure 3-8. Comparison of Q-band DEER time-domain signals for dHis-Cu(II)-NTA bound hGSTA1-1 without and with different ligand present. .......... 70**

**Figure 3-9. Comparison of Q-band DEER results for dHis-Cu(II)-NTA bound hGSTA1-1 without and with different ligands. .......... 71**

**Figure 3-10. Detecting native binding sites of Cu(II)-NTA. .......... 72**

**Figure 3-11. Root-Mean-Square Fluctuation (RMSF) of each residue in each of the two monomers of the dimeric hGSTA1-1 enzyme. .......... 74**

**Figure 3-12. cMD sampled Cu(II)-Cu(II) distances with both ligands removed. .......... 75**

**Figure 3-13. cMD sampled Cu(II)-Cu(II) distances with one ligand removed. .......... 75**

**Figure 3-14. cMD sampled Cu(II)-Cu(II) distances with both ligand removed.................. 76**

**Figure 3-15. A single 1 $\mu$s cMD simulation for dHis-Cu(II)-NTA labeled hGSTA1-1 with the ligand from monomer B removed. ..................................................................... 76**

**Figure 3-16. cMD sampled Cu(II)-Cu(II) distance distributions. ........................................ 77**

**Figure 3-17. Combined EPR-weighted ensemble (WE) workflow was able to successfully generate atomically-detailed conformations of hGSTA1-1 in the ligand-free state. 79**

**Figure 3-18. Replicates of WE simulations. ................................................................ 81**

**Figure 3-19. Conventional MD (cMD) simulations started from hGSTA1-1 conformations extracted from our WE simulations, confirm that we are sampling conformations within the ligand-free state. ......................................................................... 84**

**Figure 3-20. Salt-bridge interactions between Arg221 of the $\alpha$9 helix and Asp42, and hydrophobic interactions between Phe220 and Phe10. ............................................ 85**

**Figure 3-21. Salt-bridge interactions between Arg221 of the $\alpha$9 helix and Glu39, and hydrophobic interactions between Phe220 and Tyr9. ............................................... 86**

**Figure 3-22. Additional conventional MD (cMD) simulations, started from hGSTA1-1 conformations extracted from our WE simulations in which both $\alpha$9 helices were delocalized, further reveal the stable states of the ligand-free ensemble................. 88**

**Figure 3-23. Traced trajectories for all five parallel cMD simulations starting from structures sampled from WE-MD simulation where both $\alpha$9 helices are delocalized. ........................................................................................................................ 89**

**Figure 3-24. The WE-MD sampled ligand-free hGSTA1-1 conformations that best describe the EPR distance distribution. ....................................................................... 91**

**Figure 4-1. CW-EPR and ESEEM experiments on dHis-Cu$^{2+}$-NTA labeled hGSTA1-1. ... 99**

**Figure 4-2. Distance distribution and relative angles between the two labels sampled from MD. ........ 102**

**Figure 4-3. Fitting of experimental FS-ESE spectrum of dHis-Cu$^{2+}$ labeled hGSTA1-1... 103**

**Figure 4-4. Determination of the broadening and the threshold parameters. .................... 104**

**Figure 4-5. Directions of $g \parallel$ and $g \perp$ within the dHis-Cu$^{2+}$-NTA complex. ...................... 108**

**Figure 4-6. Cu$^{2+}$ spatial distribution. ........................................................................ 109**

**Figure 4-7. In silico sample consisting of randomly oriented vectors with two spins......... 111**

**Figure 4-8. The Φ curve indicates the field for exciting the most spins.............................. 112**

**Figure 4-9. Identifying the minimum number of fields needed for Q-band DEER experiments. ........ 114**

**Figure 4-10. Spherical resprentations of unexcited spins after each iteration. .................. 116**

**Figure 4-11. Simulated DEER time traces based on the MD results. ................................. 117**

**Figure 4-12. Simulated DEER at four fields based on the MD results on hGSTA1-1........ 117**

**Figure 4-13. Simulated DEER time traces considering arbitrary cases. ............................ 119**

**Figure 4-14. Simulated DEER at four fields. ........................................................................ 120**

**Figure 4-15. DEER measurements at two fields are possible. ............................................ 121**

**Figure 4-16. DEER measurement at one field is possible by using ultra-wide band excitation. ........ 122**

**Figure 4-17. Experimental validation of the acquisition scheme. ....................................... 123**

**Figure 4-18. Determination of relaxation times. ................................................................ 123**

**Figure 4-19. The primary DEER time domain data. Determination of relaxation times. . 125**

**Figure 4-20. Comparison of DEER distance distribution using different analysis tools.... 125**

**Figure 4-21. Comparison of Q-band DEER collected at 3, 4 and 10 magnetic fields......... 126**

**Figure 4-22. Summed Q-band DEER signals compared to X-band DEER......................... 128**

# Preface

I would like to thank my advisor, Prof. Sunil Saxena, for giving me this great opportunity to learn and grow as a scientist in his lab for the past six years. The guidance, mentorship and support that Dr. Saxena has provided me have led to my confidence in myself as a scientist.

I would also like to thank my committee members, Prof. Seth Horne, Prof. Jennifer Laaser, and Prof. Junmei Wang for their time and feedbacks on my projects throughout my PhD career.

Next, I want to thank the Saxena lab members and alumni, to Dr. Matthew Lawless, Dr. Austin Gamble Jarvi, Dr. Shreya Ghosh, and Dr. Kevin Singewald for their patience, early input, collaborations, and guidance. To Zikri Hasanbasri, Joshua Casto, and Alysia Mandato, for going through all difficulties and working together as a team and friends. To Hannah Hunter, Shramana Palit, and Niko Moriglioni for being the "rising stars" of the lab to take over various responsibilities.

Last, I want to thank my friends and family. Thank you, Anthony, my parents, my grandparents, mom, dad, Eli, Ethan, Mommom, and Dandy for always supporting me and backing me up.

# 1.0 Introduction

*This work, written in collaboration with Sunil Saxena, has been submitted for publication.*

Electron paramagnetic resonance (EPR) has become a powerful spectroscopic method to measure the structural constraints and conformational dynamics of biomolecules. To perform EPR measurements on biomolecules, "EPR reporters" containing unpaired electron spin(s) are often incorporated through site-directed spin labeling (SDSL) techniques.[1] The application of SDSL-EPR is unconstrained by the size and complexity of systems including globular proteins, nucleic acids, and membrane proteins within native-like lipid bilayers or detergent.[1–11] Furthermore, EPR can also be used to examine protein structure and dynamics in-cell.[12–25]

Figure 1-1 outlines the use of EPR experiments to access a variety of biomolecular motions. In Figure 1-1A, we consider a case where the protein has two structural states that involves a large-amplitude conformational transition between state 1 and state 2. Within the two distinct states, residue-specific, small-scale fluctuations also occur. Large-scale conformational transitions are often triggered by ligand (shown in this example) or protein binding, temperature or pH change, or a change in ion concentration. Such conformational transition usually results in a gain of function. Oftentimes, however, the atomic structure of this functional state of the protein can be hard to resolve by experiment.

Several EPR methods exist to measure both large and small-scale protein dynamics. Continuous wave (CW)-EPR spectral lineshapes can reflect site-specific reorientational dynamics on the sub-ns to $\mu$s timescale.[26,27] As illustrated in Figure 1-1B, the dynamics of a double histidine (dHis)-Cu(II)-based label are simulated in three scenarios. The CW-EPR spectrum shown in blue was simulated at the rigid limit with slow dynamics, which exhibits a highly resolved g and hyperfine splitting. When the dHis-Cu(II) labels experience faster motions, the CW-EPR spectra exhibit partially- to fully-averaged g and hyperfine splitting, with simulated spectra at the intermediate (purple spectrum) and isotropic regime (red spectrum) plotted in Figure 1-1B, respectively.[28–31] In addition to CW-EPR, 2D-pulsed EPR methods primarily using nitroxide probes can be used to access dynamics on the 100s of nanoseconds to milliseconds timescales.[32–37]

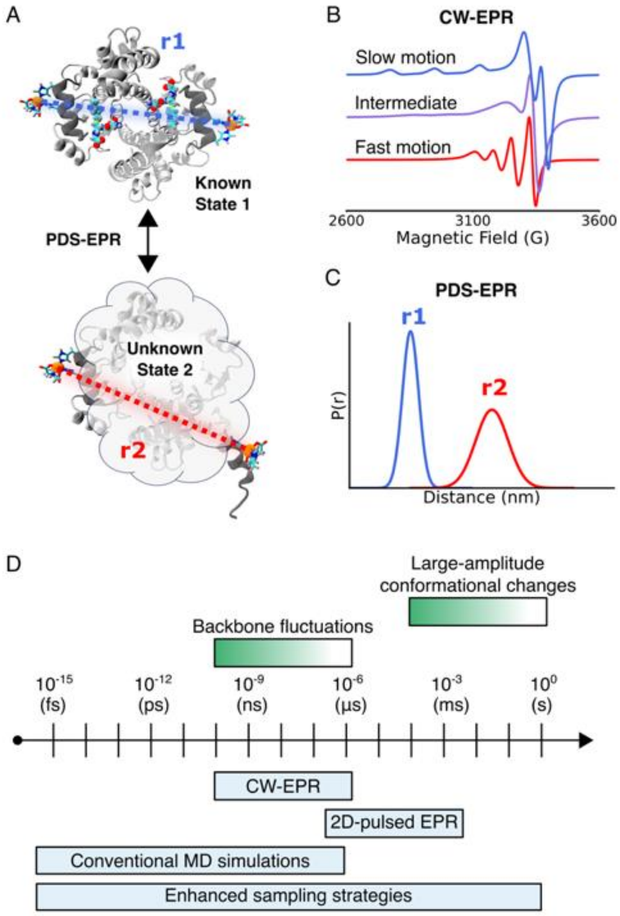

**Figure 1-1.** Protein conformations and dynamics can be probed by EPR and simulations. An example of a detoxification enzyme, hGSTA1-1, that can adopt two different conformational states. The conformational transition between the two states in this example is triggered by the presence and absence of ligands. Only the ligand-bound form (state 1) of hGSTA1-1 has been fully resolved (PDB: 1K3L). (B) CW-EPR can be used to access small-amplitude residue-specific dynamics. If the label experience slower dynamics, a broad CW-EPR spectrum depicted in blue is

observed. If a Cu(II)-based label experiences faster dynamics, a narrower CW-EPR is observed. (C) PDS-EPR can be used to probe conformational changes shown in (A). A change in protein conformation results in a change of EPR distance distributions (i.e., r1 to r2). (D) Timescales of molecular motions that are relevant to different EPR techniques. Conventional MD and enhanced sampling strategy can further supplement sparse EPR restraints.

On the other hand, pulsed-dipolar spectroscopy (PDS) can measure sparse distance constraints in the range of 2 to 8 nm,[38–40] and even up to 16 nm[41] for fully deuterated systems. Distance distributions such as those shown in Figure 1-1C reflect both the most populated conformation by the mode of the distribution, as well as the flexibility of the state by the distribution width. A large-amplitude conformational change, as shown in Figure 1-1A, is reported as a change in distance distribution shown in Figure 1-1C. Because PDS-EPR is typically performed on frozen samples, these measurements do not normally contain the timescale information of conformational transitions. However, a freeze-quench technique has been developed to obtain the time-resolved PDS-EPR, such that the process of conformational changes on a timescale longer than 80 $\mu$s can be monitored.[42–46] For slower biomolecular processes (i.e. seconds timescale and longer), PDS performed on manually frozen samples can provide the equilibrium constant of protein dimerization,[47] and diffusion equilibrium.[48] Beyond characterizing protein conformations at different states,[5,46,49–55] PDS-EPR has also been used to determine the relative orientations of interacting proteins,[56–61] locate metal and ligand binding sites, [62–69] and characterize protein-DNA interactions.[70–81]

Despite this progress, the use of EPR in biophysics faces two bottlenecks. The first challenge is the use of the common nitroxide-based spin labels.[1,2,49] The chemical structure of the common nitroxide labels is shown in Figure 1-2A. These spin labels are highly flexible, having five rotatable bonds connecting the nitroxide moiety to the protein backbone. Due to the flexibility of the nitroxide labels, the distance distributions based on nitroxide labels are often broad and dominated by sidechain flexibility, making it difficult to interpret protein backbone flexibility from the distance distributions..[72,82] This challenge is further discussed in section 1.1. The second challenge is that both CW- and PDS-EPR measurements provide dynamics information and distance restraints only on a few “grid points” of a biomolecule. If the protein structure is unknown as illustrated in Figure 1-1A, translating the sparse distance restraints into a protein structure is difficult.

To address the flexibility issue of the nitroxide labels, the dHis-Cu(II)-based labels were developed (Figure 1-2).[83–85] Due to the double chelation of two histidine residues to the Cu(II), such labels are rigid, with localized Cu(II) spatial distributions at the labeled sites. Distance distributions based on the dHis-Cu(II) labels have been shown to be up to five times narrower than nitroxide-based distance distributions.[83] These narrower distributions indicate a higher sensitivity of dHis-Cu(II) to backbone fluctuations than nitroxides. The use of dHis-Cu(II) labels has led to many biophysical applications in the past few years, including efficient localization of a metal binding site,[64] determination of the relative packing between interacting protein subunits,[86] and characterization of multiple active state conformations of a metal regulatory protein.[73] My area of focus in this work is to sample large-amplitude conformational change. As mentioned earlier, the large-amplitude conformational changes can be detected by a change in the PDS-EPR distance distributions. However, since PDS-EPR can only provide sparse distance information, the entire conformational ensemble of the unknown protein state can be ambiguous without modeling tools.

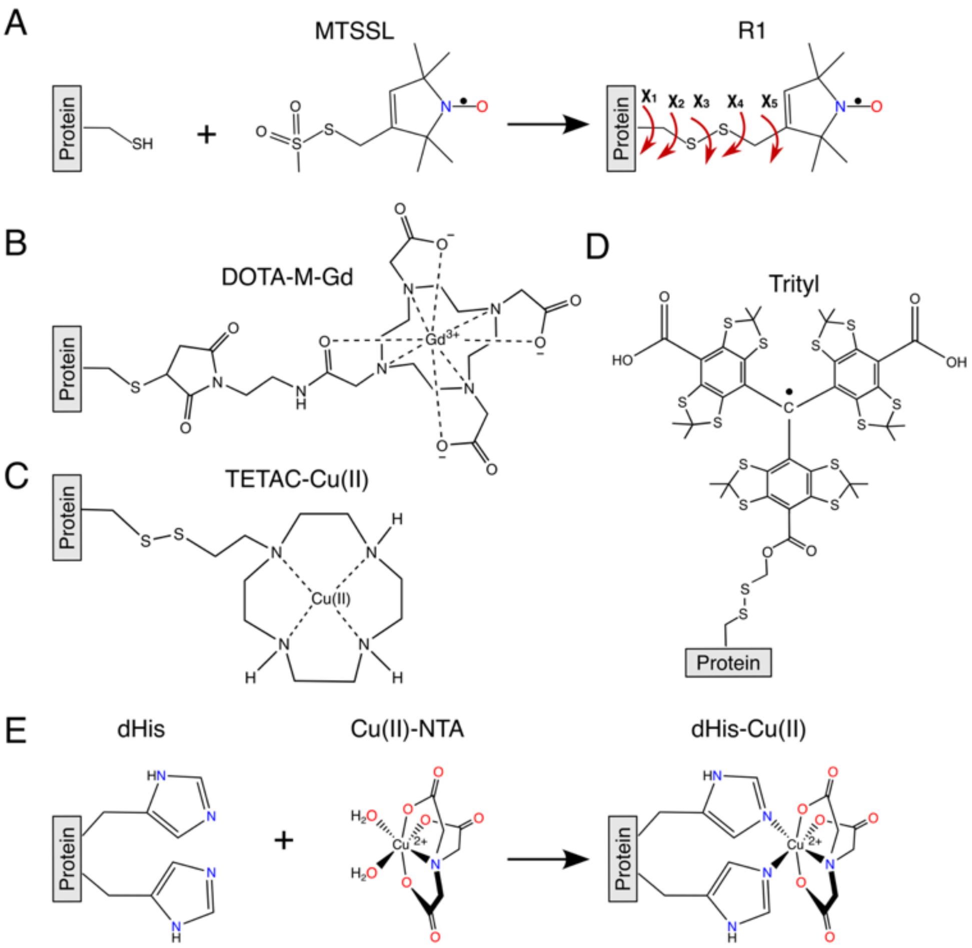

**Figure 1-2.** Spin labels. The thiol group of a cysteine residue reacts with the thiolsulfonate of (A) MTSSL to create an R1 sidechain. (B) Gd(III), (C) Cu(II) and (D) trityl label can also be attached to cysteine residues of a host protein. (E) The dHis motif chelates to a Cu(II)-complex to form a rigid dHis-Cu(II) based spin label.

Therefore, complementing EPR with modeling tools can provide further insights to interpret the EPR measurements. In this chapter, we first survey the different spin labels that have been used in EPR research. The introduction to SDSL in this chapter is meant to provide a background for the later discussion of modelling, but we note that detailed reviews of the technique are available elsewhere.[1,2,4,87–89] Next, we discuss available force field parameters for spin labels. The force fields allow atomistic molecular dynamics (MD) simulations of biomolecules with explicit spin labels. These simulations can access molecular timescales up to the microseconds range (Figure 1-1D). Then modeling techniques amenable to timescales of molecular motions beyond microseconds are discussed. Lastly, we discuss a new simulation approach that can potentially sample microseconds to seconds timescale molecular motions by detailing intermediates states during protein structural transition.[90] In addition, Figure 1-3 provides an overview of different modeling tools to supplement EPR measurements for a variety of biophysical information. The corresponding section numbers for each category of biophysical questions are detailed in this figure. Overall, we seek to provide a comprehensive picture of how modelling techniques help complement EPR measurements.

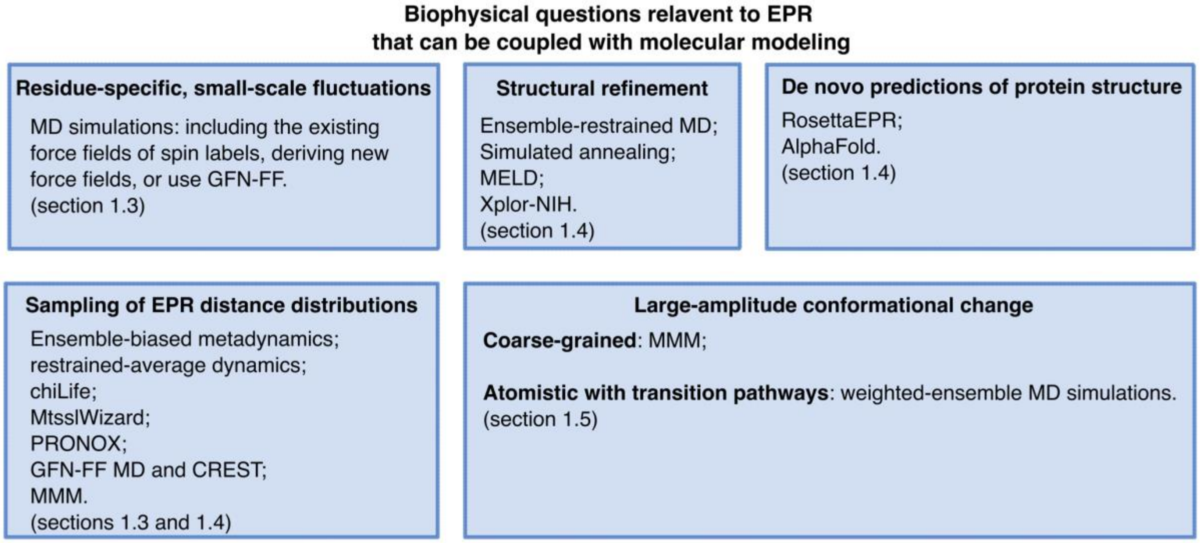

**Biophysical questions relavent to EPR that can be coupled with molecular modeling**

**Residue-specific, small-scale fluctuations**

MD simulations: including the existing force fields of spin labels, deriving new force fields, or use GFN-FF.
(section 1.3)

**Structural refinement**

Ensemble-restrained MD;
Simulated annealing;
MELD;
Xplor-NIH.
(section 1.4)

**De novo predictions of protein structure**

RosettaEPR;
AlphaFold.
(section 1.4)

**Sampling of EPR distance distributions**

Ensemble-biased metadynamics;
restrained-average dynamics;
chiLife;
MtsslWizard;
PRONOX;
GFN-FF MD and CREST;
MMM.
(sections 1.3 and 1.4)

**Large-amplitude conformational change**

**Coarse-grained**: MMM;

**Atomistic with transition pathways**: weighted-ensemble MD simulations.
(section 1.5)

**Figure 1-3.** Different types of biophysical information that can be inquired by EPR techniques and can be supplemented with molecular modeling tools. The relevant modeling techniques are detailed in the following sections that are indicated in this figure.

## 1.1 Site-directed spin labeling

To perform EPR measurements on biomolecules, spin labels are often strategically introduced through SDSL. For proteins, SDSL often involves selectively attaching spin labels to native or mutated cysteine residues through a reactive linker, such as thiolsulfonate or maleimide, as shown in Figure 1-2A. As a result, either a covalent disulfide or thioether bond (Figures 1-2A to 1-2C) is formed between the thiol sidechain of cysteine and the spin probe. Figure 1-2A shows that one of the most-used nitroxide labels, (1-Oxyl-2,2,5,5-tetramethyl-3-pyrroline-3-methyl) methanethiosulfonate spin label (MTSSL), reacts with a thiol group of cysteine and generates an R1 sidechain. Similar schemes can be used to incorporate gadolinium,[91,92] copper,[93] and trityl-based [7,24,94–96] spin labels, shown in Figures 1-2B to 1-2D. Variations in the linkers or functional groups of the above spin labels have enabled different applications.[1,49,87,97,98] For example, reduction-resistant labels, such as sterically-shielded nitroxide,[22,99] trityl,[7,24,94–96] and gadolinium labels,[100] have been employed to conduct in-cell measurements. The in-cell measurements have also been enabled by endogenous labeling strategies, which incorporate genetically-encoded, unnatural amino acids for SDSL to either bear a paramagnetic center, such as nitroxide, or a reactive moiety for post-translational conjugation.[23,101]

Continuous wave-EPR experiments using MTSSL labels can elucidate backbone dynamics of solvent-exposed $\alpha$-helices.[102,103] Interpreting backbone fluctuations at $\beta$-sheet sites based on CW-EPR spectral lineshapes is challenging due to potential steric interactions between the R1 sidechain and neighboring residues.[104] Despite the wide applicability of MTSSL labels, there are two main limitations. First, the cysteine dependence of the labeling reaction can be limiting for some proteins. In order to selectively label cysteine residues of interests, the fully-functional, cysteine-free mutant is required. As a result, proteins with even a few naturally occurring, functional cysteines can make site-specific labeling challenging. The second limitation of MTSSL labeling involves the flexibility of the label itself. Even if labelling is successful, the sidechains of cysteine-based labels, such as R1 and trityl, are highly flexible due to multiple rotatable bonds connecting the EPR active center to the protein backbone (Figure 1-2A), obscuring protein backbone flexibility. To circumvent the intrinsic flexibility of MTSSL labels, bifunctional nitroxide labels with reduced flexibility have been developed.[105,106]

An alternative to cysteine-based labeling that addresses both of the challenges described above involves a strategically-placed double histidine (dHis) motif has been developed to chelate a copper complex.[83–85] The coordinated nitrogen atoms to Cu(II) shown in Figure 1-2E are the deprotonated epsilon nitrogen. The proposed coordination environment of Cu(II) is based on crystal structures of Cu(II)-bound amine oxidases, human tyrosinases and tyrosinase-related protein 1.[107–111] This dHis labeling technique illustrated in Figure 1-2E, requires only the stoichiometric loading of Cu(II)-nitrilotriacetic acid (NTA) complex to every dHis. Thus, post-labeling purification is not needed.[85] With newly-developed labeling protocols, over 90% labeling efficiency of Cu(II) to dHis sites has been achieved.[31,112] Furthermore, the dHis-Cu(II)-NTA labels can be used in a variety of buffers, a range of pH and the presence of other metal ions without losing chelation.[112,113]

In addition to protein labels, SDSL has been utilized to introduce a multitude of spin labels in DNAs and RNAs to probe conformational dynamics, and there are several comprehensive reviews.[98,114–117] Only a broad summary of nucleic acid labels is provided here. The DNA and RNA labels are often incorporated as nitroxide-modified nucleic acids through covalent bonds to the backbone or through hydrogen bonding to an adjacent strand.[114] In addition to nitroxide-based DNA labels, other nucleic acid labels carrying gadolinium,[118,119] copper,[120–122] or trityl[95,123] moieties have also been developed. By creating a DNA G-quadruplex, Cu(II) can be chelated to four pyridines to generate a rigid DNA tetrad label.[120–122] Additionally, a Cu(II)-based DNA label involves the incorporation of a modified nucleotide containing a 2,2′-dipicolylamine (DPA) during the DNA synthesis to chelate to a Cu(II) ion.[124–126] The Cu(II)-DPA label is nucleotide-independent and thus applicable to any DNA sequence of interest. A similar strategy to label peptide nucleic acids (PNAs) utilizes two 8-hydroxyquinoline groups replacing complementary bases in a PNA helix to coordinate a Cu(II) ion.[127]

## 1.2 Small-amplitude fluctuations revealed by MD simulations detail the EPR spectra

Atomically-detailed molecular dynamics (MD) simulations have emerged as a powerful tool to sample molecular motions up to $\mu$s timescales (cf. Figure 1-1). As such, MD-trajectories have been used in many ways to connect EPR phenomenon to atomically detailed biomolecular motions. In this section, we discuss the use of MD to complement EPR data.

**Force field development for protein labels:** A requisite for MD is the availability of an appropriate force field. In Chapter 2, we present a detailed discussion of the force field derivation of the dHis-Cu(II)-based spin labels. We also discuss that MD simulations based on these new force fields help explain EPR distance distributions as well as orientational selectivity. In brief, a force field is an additive, classically-described energy equation that provides the energy of a molecule in different physical configurations, an example of which is shown in Figure 1-4. While there are many different forms of force fields (i.e., Amber,[128,129] CHARMM,[130,131] GROMOS[132,133] etc.), they usually contain two main contributions to the energy: bonded and nonbonded. The bonded terms of a force field often include two-atom bond vibrations, three-atom angle bending in the form of Hooke’s law and four-atom dihedral rotation in the form of a periodic potential. Nonbonded terms of a force field often include charge-charge interactions in the form of Coulomb’s law and van Der Waals interactions in the form of a Lennard Jones potential. The derivation of force field parameters, a necessary step before one can model spin labels, can be accomplished in many ways, but usually begins with the derivation of fixed charges for all atoms in the molecule (Figure 1-4B). Once charges are derived, a diverse set of conformations are generated that allow for the derivation of the bonded parameters. The following examples present the use of force fields with MD simulations.

Force field parameters are available for commonly used nitroxide-based spin labels, such as R1,[134] and have enabled many applications in EPR-assisted MD simulations. Due to the intrinsic flexibility of R1, and relatively long-timescale for rotation around the S-S bond (i.e. $\chi_3$ shown in Figure 1-2A) of these labels, multiple $\mu$s-long MD-trajectories are often needed to sufficiently sample R1 rotamers.[72,135–137] For faster sampling of the R1 sidechain rotamers within a model, a simplified dummy nitroxide label[138] has been created and parameterized.[137]

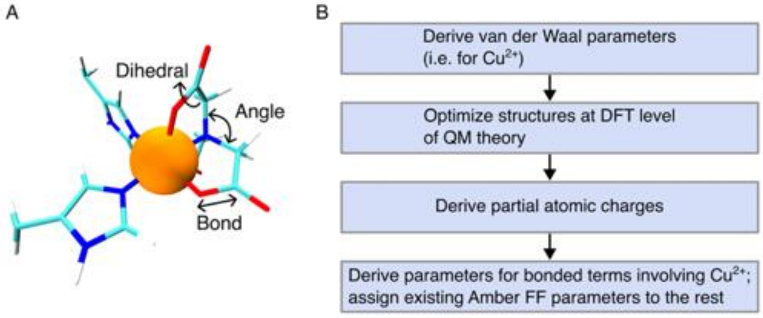

**Figure 1-4.** An example illustrating force field development for a spin label. Geometry optimized structure of a dHis-Cu(II)-NTA label. The bonded terms in the force field include bond vibrations, angles, and dihedrals. (B) The steps that are required for generating all related Amber parameters for dHis-Cu(II)-NTA labels.

Besides cysteine-dependent nitroxide labels, force field parameters for rigid dHis-Cu(II)-based protein labels[83–85] have been developed.[139] Previous double electron-electron resonance (DEER) experiments and MD simulations with the newly developed force fields for the dHis-Cu(II) labels have shown remarkable agreements between MD-sampled distance distributions and EPR distance distributions.[139]

To our knowledge, force field parameters for other types of EPR labels such as labels containing various organic radicals (i.e. trityl-based) and metal complexes (i.e. gadolinium-based) have not been developed.

**Force field development for nucleic acids labels:** While this chapter is primarily focused on simulations on spin-labeled proteins, for a complete overview of the available force field parameters for spin labels, we also include a brief discussion of nucleic acids labels. Similar to nitroxide-based protein labels, force field parameters have been derived for many nitroxide-based nucleic acid labels.[140–143] Similar to the applications of protein label force fields discussed above, MD simulations including nitroxide force fields led to direct observation of label conformers within DNA and RNA and description of nucleic acid conformations. These simulations also provided a molecular basis for orientational effects in DEER measurements.[141]

In addition to modeling nitroxide-based DNA labels, MD simulations with and without the Cu(II)-DPA labels reveal that the interspin distance distribution directly corresponds to that of the backbone atoms of the labeled sites.[125,126] Additionally, quantum mechanical calculations based on the MD trajectories of Cu(II)-labeled DNA and PNAs can help to explain the lack of orientational selectivity using such labels in DEER measurements at Q-band resonance frequencies.

**A general force field approach with an automated rotamer searching tool:** Derivation of force field parameters can be laborious for different spin labels, as any new label needs specialized new force fields. Therefore, there has been development on general force fields that are applicable to any system by applying a common set of parameters (bonded, angle, dihedral, etc.) to molecular functional groups. For example, any -CH3 group is assigned the same set of C-H bonded parameters, no matter if the system of interests is a protein, DNA, or organic molecule. In contrast, specialized force fields, such as protein force field ff19SB,[144] depend on which amino acid contains the -CH3 group, and specific bonded parameters are assigned to an alanine -CH3 group versus a valine -CH3 group. Recently, a general force field (GFN-FF) has been developed for the simulation of any (bio)chemical systems of interests, including spin-labeled proteins.[145] The generality of the GFN-FF is due to the wide coverage of chemical structures in the training set, ranging from small oxides to large metal-organic frameworks. The ability to treat inorganic molecules differentiates GFN-FF from other general force fields, such as SAGE,[146] GAFF[147] and OPLS.[148] The GFN-FF method is fast, taking only minutes to hours even when applied to complex structures composed of >1000 atoms. The GFN-FF approach only requires starting coordinates and a complete chemical composition of the system for atoms with atomic number smaller than 87. The topology and all potential-energy terms are then automatically generated.

**MD facilitates the interpretation of CW-EPR spectra and PDS-EPR distance distributions:** In the early stage of SDSL-EPR, the relationship between CW-EPR lineshapes and structural dynamics were understood based only on observations of the change in spectral lineshapes across different sites on a model protein.[102,103] However, this understanding was incomplete because the role of each dihedral angle (i.e. $\chi_1$ to $\chi_5$ in Figure 1-2A) in the spectral lineshape was not clear and it was based on limited crystal data.[149–152] Molecular dynamics were able to confirm that the steric refinement of the label are primarily contributors to the CW-EPR lineshapes.[153–158] The rotameric jumps in the dihedral angles appeared to occur in an anticorrelated manner such that the movements of the nitroxide moiety were not as large.[158] Simulations continue to validate the ability of new spin labels to directly report on protein backbone motions. Through CW-EPR and MD simulations, dHis-Cu(II) labels report backbone dynamics of both $\alpha$-helices and even on $\beta$-sheet sites.[28–30] These results also demonstrated the sensitivity of Cu(II)-based labels in probing subtle difference in dynamics over nitroxide.

Furthermore, MD trajectories can help assign conformations to different features of the CW-EPR lineshape.[159] Through examining site-specific dynamics using R1-based EPR together with MD simulations, two possible conformations of the GM2 activator protein were determined to explain the two-component CW-EPR spectra.[160] In addition, two dynamically different conformations of a detoxification enzyme have been identified through dHis-Cu(II)-based CW-EPR[28] and further confirmed through MD simulations. Molecular dynamics-trajectories can also be employed to simulate CW-EPR spectra.[134,155,156,158,161–167] The MD-based spectral simulations can be used to disentangle backbone motions from nitroxide sidechain motions, for example, on challenging systems such as membrane proteins.[136]

Beyond applications of atomistic simulations to CW-EPR, MD simulations have also been applied to sample PDS-EPR distance distributions. In Chapter 2, we present work that showcases sampling of the interspin distances of the dHis-Cu(II) labeled proteins using MD simulations. From MD-trajectories, sidechain conformations of spin labels can also be extracted[72,82,97,136,168,169] These rotamers were implemented in software packages to predict distance distributions. For example, multiscale modeling of macromolecules (MMM;[170] and the successor version MMMx[171]) software package predicts inter-spin distance distributions based on a solved protein structure and rotamer libraries. Similar rotamer libraries have been generated for nitroxide,[49,88,149,172–176] trityl,[7,24,94–96] dHis-Cu(II),[83–85] and Gd(III)-based[91,92,100] labels. Alternatively, instead of predicting EPR distance distributions based on a static protein structure, the DEER-PREdict[177] software predicts the Boltzmann-weighted inter-spin distance distribution based on conventional or biased MD trajectories. Other than MD-based approaches, rotamer libraries can be calculated by examining the accessible volume of a label[178,179] (i.e., MtsslWizard) or user-defined range of dihedral angles[180,181] (i.e., PRONOX). To implement the existing rotamer libraries from methods discussed above (i.e., MD, MMM, MtsslWizard, PRONOX) or generate custom rotamer libraries, a modeling package, chiLife,[182] has been recently developed and the label rotamers can be used for the prediction of EPR distance distributions.

To efficiently describe the conformers of spin labels in the MD simulations, a recent application of the GFN-FF methodology was alongside an efficient rotamer searching tool, CREST.[183] With a certain starting structure, the CREST method calculates the most probable conformers of the label with Boltzmann weights. The MD simulations of proteins with different conformers will then lead to a weighted distance distribution between the labels, which can then be directly compared to a DEER distance distribution. The combined CREST/MD and GFN-FF approach accelerates the prediction of protein conformational space together with the rotamer contribution to interpret the DEER distance distributions.

To identify macromolecular conformations that best explain PDS-EPR distance distributions, MD trajectories have also been utilized.[72,75,184] Previous work using PDS-EPR measurements of HIV-1 protease has captured different conformations and conformational flexibility of the flap region in the inhibitor-bound and unbound form.[185] A subsequent MD study on HIV-1 protease linked the flap conformations in different states to different EPR distance distributions.[186] Recently, the conformational ensembles of calcium-bound calmodulin were investigated by replica exchange MD simulations and PDS-EPR.[187] MD-sampled conformational clusters were directly fit to reproduce the EPR distance distributions and the relative population of each cluster was obtained. Another work used ensemble-biased metadynamics to efficiently sample multiple DEER distance distributions on a T4-lysozyme.[188] This method adds biasing potential to the simulation for enhancement of conformational sampling.

## 1.3 Structure refinement and prediction using modeling coupled with PDS-EPR

Regardless of the timescales of molecular motions, protein structures can be predicted or refined using a variety of modeling techniques. In this section, we first discuss the use of enhanced sampling techniques to refine protein conformations or predict PDS-EPR distance distributions. We next introduce the de novo predictions of protein structures that either incorporates or are validated by PDS-EPR distance distributions. Lastly, software packages, i.e., Xplor-NIH and modeling employing limited data (MELD), are discussed as additional methods to refine the structure of a protein or protein complex.

**Enhanced sampling strategies for structural refinement and sampling EPR distance distributions:** The enhanced sampling strategies employing EPR data are a straightforward extension to standard MD simulations and involve the addition of a biasing potential to confine protein motions. One such method, ensemble-restrained MD, directly incorporates PDS-EPR distance restraints into MD simulations and has been successful in the structural refinement of T4 lysozyme from distorted initial structures.[189] Ensemble-restrained MD has also been able to predict conformations of a membrane protein in vacuum, solution, micelle and lipids bilayers.[190]

Atomistic MD simulations containing biasing potentials can also assist in analyzing EPR distance distributions. For instance, an ensemble-biased metadynamics method has shown to facilitate confidence analysis of DEER data compared to the traditional Tikhonov regularization.[188,191] A follow-up study introduced a minimally biased simulation technique, called restrained-average dynamics that efficiently reproduces DEER time trace as well as distance distribution between labels.[192]

Another method that is an extension of conventional MD involves high temperature instead of biasing forces to overcome transition barriers. Simulated annealing approaches[193] have been used in a variety of contexts, and involve heating up the system before cooling it down to find stable conformations. Measurements from EPR experiments, including inter-spin distances from DEER measurements as well as the immersion depth from CW-EPR, have both been incorporated into simulated annealing MD to refine the structure of membrane-bound $\alpha$-synuclein.[194]

**De novo folding strategies coupled with PDS-EPR to predict protein conformations:** De novo strategies seek to determine a global minimum in energy for a protein that corresponds to its most stable conformation, often starting from only an amino acid sequence. These methods, in contrast to structural refinement methods, rely on a global energy function or pre-trained machine learning models rather than physics-based simulations (such as MD). Rosetta,[195] a de novo folding software to predict a protein structure, uses only an amino-acid sequence to search for the lowest-energy protein conformation based on a global energy function.[195]

Sparse EPR distance restraints can be readily incorporated into Rosetta global energy function, as done in the RosettaEPR method.[196] RosettaEPR has been able to predict the structure of T4-lysozyme with improved accuracy than Rosetta,[196,197] and an alternate conformation of a multidrug transporter.[198] In addition, for fast and accurate protein folding that uses unprocessed

EPR data containing noise, RosettaDEER developed[199] and applied to construct a missing loop of a type III secreted phospholipase effector in both the apo and holo states.[200] So far, RosettaEPR and RosettaDEER can only implement R1-based distance restraints into the energy term for prediction of protein conformations.

Instead of depending on a global energy function, AlphaFold relies on deep-learned neural networks to predict a protein structure primarily based on an input amino acid sequence.[201,202] By training these machine learning models based on a massive database of protein structures and sequences, AlphaFold is able to identify sequence-structure relationships in new sequences and determine a single stable structure with reasonable accuracy. The recent advent of AlphaFold has generated a completely new way of analyzing induced conformational changes.[203] By using a modified AlphaFold approach, diverse conformational states of transporter proteins were first generated,[203] which were further validated through systematic PDS-EPR measurements.[204]

**Xplor-NIH and MELD with PDS-EPR:** Other emerging simulation tools have incorporated EPR distance restraints to better sample protein conformations, including Xplor-NIH[205] and modeling employing limited data (MELD).[206] Xplor-NIH was initially designed to automatically interpret raw NMR signals into molecular structures.[207] In recent years, incorporation of EPR distance restraints obtained between interacting proteins in Xplor-NIH has enabled the prediction of the relative orientations of a multi-protein complex, such as the histone chaperone Vps75.[205] Alternatively, a free-energy-based computational method, MELD, determined protein structures using a Bayesian approach combined with limited experimental data.[207] The MELD approach utilizes free energy as criteria to choose conformational states that possibly correspond to the sparse experimental data. The sparse experimental data can be from NMR, EPR or cryo-EM, and the protein structure prediction from MELD performs well compared to RosettaEPR. The MELD approach can also be used with any spin labels that have available force fields.

## 1.4 Sampling of large-amplitude conformational changes using modeling with EPR distance restraints

The timescales of large-amplitude protein conformational switches are often above milliseconds, which is beyond the reach of conventional MD simulations. Supplementing PDS distance restraints in simulations can facilitate the sampling of protein conformations of interests. In this section, we discuss strategies that incorporate EPR distance restraints to obtain the "unknown" or "lesser-known" conformations of proteins.

**Prediction of conformational change by multiscale modeling of macromolecules:** The multiscale modeling of macromolecules (MMM) software package is one of the fastest computational techniques to sample large-amplitude protein conformational changes on milliseconds to seconds timescales demonstrated in Figure 1-1.[170] As illustrated in Figure 1-5, MMM generates a coarse-grained model based on an initial, resolved structure of the or a homology model of a protein. Next, MMM reads in nitroxide or dHis-Cu(II)-based EPR distance restraints obtained from the alternate state. In conjunction with elastic network modeling (ENM),[208] the distance restraints are translated into a network of forces that "stretch" or "compress" the protein model, and protein conformations in alternate functional states are thus generated.[73,209]

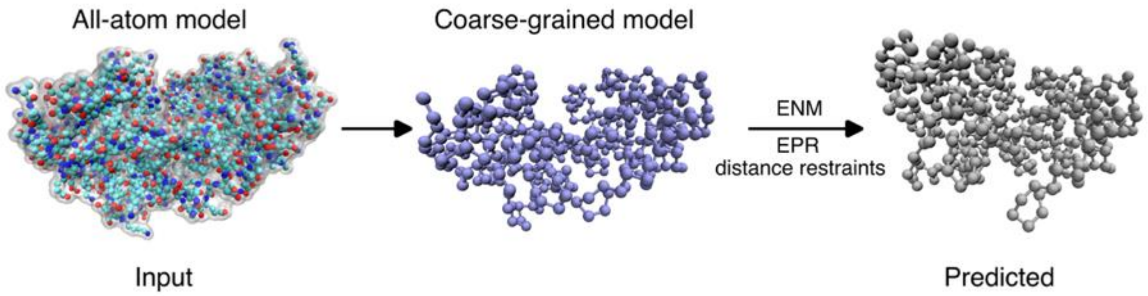

**Figure 1-5.** Predicting a conformational change using MMM. With an all-atom structure as an input, MMM software generates a coarse-grained model. Using elastic network modeling, MMM reads in the EPR distance restraints (or in combination with NMR restraints) to model large-scale conformational change, which generates the predicted model that best fits to the restraints.

This type of coarse-grained modeling is very efficient, taking only minutes on a desktop or laptop computer to capture large- scale conformational changes that occur on the seconds timescale. The ENM model is generated from an initial, resolved structure of the or a homology model. The coarse-grained ENM strategy built in MMM has been applied to large membrane-bound ion channels,[209] and protein-DNA[73] complex without the need of solvation or using specialized force fields for each compartment.[50,210,211] However, coarse-grained methods can be error prone due to the limited, sparse distance input. Nevertheless, MMM is still an important tool to quickly predict conformations, and can also be coupled with other experimental restraints, such as NMR and cryo-EM. In contrast to this coarse-grained method, Rosetta has recently been adapted to include multiple sources of experimental restraints to predict a conformational change.[212]

**Atomistic sampling of conformational change with continuous pathways:** A step beyond generating an unknown conformation is to detail the transition pathway that leads to the unknown conformation. Path sampling strategies are one class of methods that can not only generate unknown protein structures, but also unbiased transition pathways including both the stable and intermediate states. In Chapter 3, we discuss the first application of path sampling MD coupled with PDS-EPR that can potentially generate atomistic pathways for a large-amplitude conformational change in complex proteins.[90]

Figure 1-6 illustrates the sampling of conformational changes of a detoxification enzyme at atomic resolution. This detoxification enzyme, human glutathione S-transferase A1-1 (hGSTA1-1), is a homodimer and the ligand-bound structure of which was experimentally resolved (PDB: 1K3L),[213] shown in Figure 1-6A. The function of the C-terminal helices, $\alpha9$ (highlighted in dark gray), is to recruit toxins. In the absence of the $\alpha9$ helices, the enzyme is non-functional. However, in the ligand-free form, the structure of $\alpha9$ helices were unresolved, which led to the debate whether the key $\alpha9$ helices are disordered[213,214] or delocalized.[215,216] Therefore, the mechanism of activation remained unclear. In this recent work, a series of PDS-EPR experiments were performed on dHis-Cu(II)-NTA labeled hGSTA1-1 in different states. In the ligand-free state, shown in Figure 1-6B, a broad distance distribution was observed and the distances shift up to 4 Å and the distribution narrows as a function of ligand concentration, indicating structural rearrangements at the $\alpha9$ helices. Based on previous studies,[215,216] the $\alpha9$ helices potentially undergo seconds-timescale, large-amplitude conformational change in the ligand-free state to search for toxins. Thus, large root-mean-square-deviation (RMSD) values of the $\alpha9$ helices were sampled in the simulations.[90]

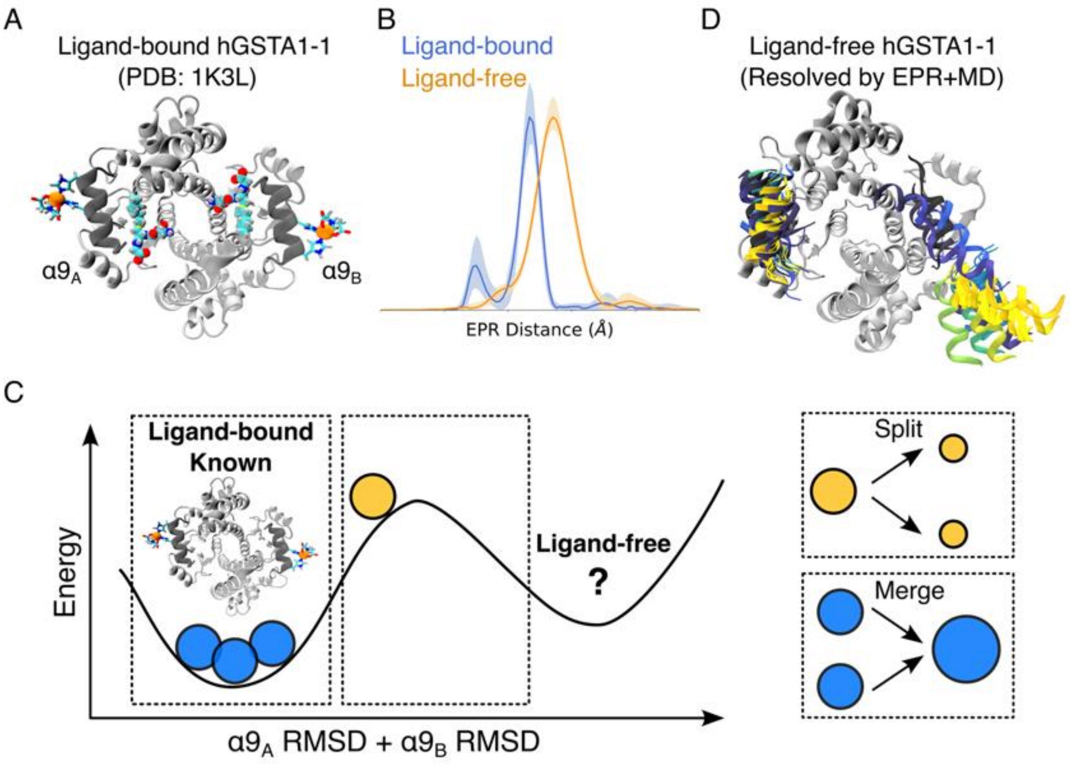

**Figure 1-6.** An integrated approach using PDS-EPR and weighted ensemble MD simulations to capture an seconds-timescale conformational change. (A) The ligand-bound structure of dimeric hGSTA1-1 (PDB: 1K3L). The ligand is shown in both monomers in cyan. The key C-terminal helices, α9, are shown as dark-gray cartoon, and the rest of the protein is shown in silver. (B) PDS-EPR distance distribution between the dHis-Cu(II) labels introduced to the α9 helices in the ligand-bound and ligand-free states. (C) Multiple parallel simulations were initiated by weighted ensemble strategy in the ligand-bound conformation of hGSTA1-1 (represented by orange spheres). If a simulation sampled larger RMSD values of α9 helices, this simulation (blue sphere) was split into two. Simulations that were stuck at the ligand-bound state (blue spheres) were chosen at random for termination. Continuous pathways were sampled from the ligand-bound conformation shown in (A) leading to the ligand-free conformation in (D), with a movie provided at: https://youtube.com/shorts/V6sBl0zN5kA.

Multiple parallel simulations were initiated by weighted ensemble (WE) strategy in the ligand-bound conformation of hGSTA1-1, represented as blue spheres in Figure 1-6C. When a simulation sampled larger RMSD values of $\alpha 9$ helices, this simulation (orange sphere) was split.

Thus, this promising simulation was given more chance of success. Simulations that sampled the ligand-bound state (purple spheres) were chosen at random for termination to save computation time.

Using WE coupled with EPR, seconds-long conformational transitions with continuous pathways were sampled in this work.[90] Shown in Figure 1-6D, the WE simulations reveal a mechanism for the conformational change: only one $\alpha9$ helix delocalizes at a time to recruit substrates. These simulations also confirmed that the $\alpha9$ helices are folded during the delocalization. Further, a mutually exclusive atomistic interaction formed between the $\alpha9$ and one monomer was identified, which is crucial for the negative cooperativity. This work highlights the important of atomically detailed sampling of such conformational transition. The potential negative cooperativity controlled by salt bridges and aromatic interactions can be likely diluted using coarse-grained or other biased strategies.

## 1.5 An *in silico* method based on insights from MD for cost-efficient PDS-EPR measurements using dHis-Cu(II) labels at Q-band

In Chapter 2, we discuss how MD simulations help understand the orientational effects using Cu(II)-based spin labels at both X-band and Q-band frequencies. Due to the large spectral linewidth of dHis-Cu(II) spectra (~ 5 GHz) at Q-band, the finite pulses typically used in EPR (100 MHz to 300 MHz) can only excite a small portion of the dHis-Cu(II) spectra, thus only some molecular orientations can be probed in a single DEER experiment. Due to the orientational selectivity of the Cu(II) labels at Q-band, many DEER measurements across different magnetic fields are required to sufficiently sample all molecular orientations and obtain an unbiased EPR distance distribution. In Chapter 4, I present an *in silico* procedure to optimally acquire DEER data on Cu(II)-labeled proteins at Q-band. The development and application of this method, in collaboration with Zikri Hasanbasri, uses key insights from MD-sampled conformations of the ligand bound, dHis-Cu(II)-NTA labeled hGSTA1-1. This optimal DEER acquisition approach allows us to reduce data acquisition time by six-fold compared to previous measurements. I also showcase how this modeling approach can be used in any systems, even proteins without any prior structural information. Additionally, our *in silico* procedure can be adapted to other Cu(II)-based systems, alternative paramagnetic ions, and other pulsed-EPR techniques.

## 1.6 Summary and outlook

Computational approaches enrich the interpretation of sparse EPR measurements, helping to answer biophysical questions over a wide range of timescales. To incorporate spin labels into MD simulations up to μs timescales, specialized force field for spin labels have been derived for nitroxide and Cu(II)-based spin labels. These simulations establish the missing bridge between residue-specific dynamics and conformational flexible to CW-EPR lineshapes and PDS-EPR distance distributions. Generic force fields (i.e. GFN-FF) can also be used to describe these and other moieties. To characterize protein conformational change on the milliseconds to seconds timescales, PDS-EPR restraints can be incorporated into the MMM or various de novo folding techniques to generate possible conformations or refine protein structure.

In many cases, however, it can be challenging to sample unknown conformations previously detected by EPR using all-atom MD simulations without an initial protein conformation or clear target state definition. One fascinating new direction towards this goal is to use the fast and efficient de novo folding methods to generate possible alternate states that correspond to EPR distance restraints. After these conformations have been generated, MD simulations can be performed to characterize each stable, alternate states. WE-MD simulations can also be used to obtain transition pathways between stable states and kinetics of the transitions.

## 1.7 Acknowledgements

This work was supported by the National Science Foundation (NSF MCB-2112871 and NSF BSF MCB-2006154). We would like to thank Dr. Kevin Singewald and Dr. Anthony Bogetti for valuable discussion.

# 2.0 Molecular Dynamics Simulations Based on Newly Developed Force Field Parameters for $Cu^{2+}$ Spin Labels Provide Insights into Double-Histidine-Based Double Electron–Electron Resonance

*This work, in collaboration with Shreya Ghosh, Austin Gamble Jarvi, Junmei Wang, and Sunil Saxena, was published in the Journal of Physical Chemistry B, 2020, volume 124, issue 14, pages 2788-2797. The thesis author collected all experimental data, performed all simulations and molecular modeling, analyzed all data and prepared the manuscript. This work was featured on a supplementary cover for the journal.*

## 2.1 Introduction

Pulsed electron paramagnetic resonance (EPR) techniques[38,217–224] that probe nanometer-range distance constraints have become powerful methods to determine macromolecular structure and conformational changes even in large-membrane proteins and in protein–protein and nucleic acid complexes.[58,59,105,209,225–236] Such techniques involve the measurement of the dipolar interaction between unpaired electron spins of EPR reporters that are often site specifically incorporated in macromolecules. The standard reporter for proteins involves the site-directed spin labeling of cysteine residues with a nitroxide label, most commonly 1-oxyl-2,2,5,5-tetramethylpyrroline-3-methylmethanethiosulfonate (MTSL).[49] The unpaired electron in MTSL is delocalized in the N–O bond of the pyrrole moiety, which is separated from the Cα of the protein residue by five freely rotatable bonds. As a result, distance measurements using MTSL lead to broad distance distributions due to the intrinsic flexibility of the linker. As such, translating the nitroxide distance distributions to protein backbone fluctuations is still ambiguous.[72,82] Alternative nitroxide labels that are more rigid, such as the bifunctional label, have also been developed.[8,105,237] But such rigid labels come at a cost of complex schemes required to introduce the labels in the proteins. In addition, the reliance on cysteine limits application to many proteins, such as kinases, which typically have functional, nonmodifiable cysteines. Besides developing better nitroxide labels, significant efforts have also been made to relate nitroxide conformational dynamics to protein backbone fluctuations using computational techniques.[169,179,180] Despite such efforts, the accurate prediction of protein backbone fluctuations from distance measurements still remains a challenge. Therefore, efforts toward the development of small and rigid spin labels for precise distance measurements have been a key priority.

Metal-based spin labels have become a promising alternative.[93,238,239] Along with nitroxides, they can also serve the purpose of orthogonal labeling. One such metal-based labeling technique that has shown great promise is the double-histidine (dHis) $Cu^{2+}$-binding motif.[240] The dHis motif involves the strategic placement of two histidine residues in the i and i + 4 positions for an α-helix and i and i + 2 positions for a β-sheet site for chelation to the $Cu^{2+}$-ion. The labeling technique, thus, does not rely on chemical conjugation with a cysteine residue, which provides another handle for labeling proteins. To ensure specific binding of $Cu^{2+}$ solely to the dHis motif, $Cu^{2+}$ is introduced as a complex with chelating ligands such as iminodiacetic acid (IDA)[84,240] or nitrilotriacetic acid (NTA).[85] These copper complexes show high binding affinity to the dHis motif, with an apparent dissociation constant as low as sub-micromolar.[241]

Being simultaneously bound to the $Cu^{2+}$ complex, the two histidine side chains have very limited mobility, thereby making dHis–$Cu^{2+}$–IDA/NTA much more rigid than the standard nitroxide labels. As a result, distance measurements performed using the dHis–Cu$^{2+}$ labeling scheme have provided significantly narrower distance distributions compared to its nitroxide counterparts.[240,242] The rigid dHis–Cu$^{2+}$ label has shown significantly improved resolution, capable of readily measuring structural constraints in two or more distinct functional states of a protein present simultaneously in solution.[242,243] In addition, the technique has opened up new avenues such as determination of the precise and facile location of a native paramagnetic metal ion within a protein[64] and measurement of the relative orientations of two spin-labeled protein sites.[86] These results provide impetus for further development of the dHis–Cu$^{2+}$ labeling technique, especially from a computational aspect to exploit the full potential of the label.

Several methods such as ab initio calculations, molecular dynamics (MD), Monte Carlo simulations, and rotamer libraries are available for capturing the behavior of the nitroxide spin labels when incorporated inside a protein or nucleic acids. For dHis–Cu$^{2+}$–IDA/NTA, one such effort has been made by incorporating a library of rotamers based on the conformational space of the label in the multiscale modeling of the macromolecular systems (MMM) software.[244] EPR distance constraints obtained using the dHis–Cu$^{2+}$ motif in conjunction with the elastic network modeling in MMM have been able to generate models of protein conformations in different functional states.[242] Such coarse-grained modeling helps to visualize large-scale conformational exchange or structural fluctuations that occur on a slower time scale (e.g., milliseconds).

However, if one needs to view backbone fluctuations, side-chain vibrations, or rotamer exchange, which occur in the pico- to nanosecond range, then more detailed modeling is required. The most common way of capturing such atomic details of the macromolecules is by performing molecular dynamics (MD) simulations. MD simulations in combination with EPR distance constraints have been able to elucidate conformational distributions of biomacromolecules, ascertain the validity of structural models as well as refine protein structures, obtain conformations in different functional states, and probe the types of interactions between atoms.[135,137,186,194,196,245–250] However, the availability of high-quality molecular mechanics models for $Cu^{2+}$–IDA or $Cu^{2+}$–NTA is a prerequisite for MD simulations.

In this work, we have developed force field parameters for $Cu^{2+}$–IDA and $Cu^{2+}$–NTA complexes to be used for MD simulations on dHis-labeled protein systems. High-level density functional theory (DFT) calculations were first performed to build the optimized geometry of the spin labels. Consequently, appropriate bond lengths, bond angles, dihedral angles, partial charges, and force constants were developed for the $Cu^{2+}$–IDA and $Cu^{2+}$–NTA labels. Finally, we incorporated the spin labels on a protein with two dHis motifs. From the trajectories of the MD simulations, we obtained the $Cu^{2+}$–$Cu^{2+}$ distance distribution, which we then compared to the experimental results. Overall, in combination with EPR and MD, we show that the dHis–$Cu^{2+}$ motif can indeed provide precise information about protein conformation and flexibility.

## 2.2 Methods

### 2.2.1 Protein System Setup

The protein of interest was the B1 immunoglobulin-binding domain of protein G (GB1). We used the crystal structure (PDB: 4WH4)[240] where the sites 6 and 8 on a β-sheet and sites 28 and 32 on an α-helix were histidine residues. Crystallographic water molecules were removed. For the 15H/17H/28H/32H GB1 mutant, we generated the initial structure from PDB: 4WH4 through computational mutagenesis. Since the histidine mutations on the β-sheet are now on sites 15 and

17, we mutated residues Glu15 and Thr17 into histidine. Simultaneously, the histidine residues at sites 6 and 8 in the crystal structure was replaced with residues isoleucine and asparagine, respectively, based on the wild-type GB1 sequence. The tleap program in Amber was used to generate the histidine side chains at sites 15 and 17 and add the missing H atoms to each residue.[128]

For both protein mutants, proper rotamers of dHis were chosen from PYMOL for the incorporation of $Cu^{2+}$–IDA or $Cu^{2+}$–NTA.[251] dHis–$Cu^{2+}$–IDA or dHis–$Cu^{2+}$–NTA was aligned to the dHis sites of the proteins.

### 2.2.2 Molecular Mechanics Force Field (MMFF) Parameterization

Transferability, compatibility, and high accuracy are the main features of a high-quality MMFF. We derived the force field parameters for the $Cu^{2+}$ coordination complexes to be compatible with AMBER additive force fields including ff14SB[252] and a general AMBER force field (GAFF).[147] Two model compounds, bis(imidazole)–$Cu^{2+}$–NTA and bis(imidazole)–$Cu^{2+}$–IDA, as shown in Figure 2-1, were applied to derive force field parameters.

We derived the van der Waals parameter of $Cu^{2+}$ in coordinated complexes using ionization potential (I = 0.283939 eV) and atomic polarizability ($\alpha = 6.2$ Å$^3$) of $Cu^{2+}$. First, r parameter was estimated using Equation 2-1, and then adjusted using Equation 2-2.

$$r \approx \sqrt[3]{\frac{3\alpha}{4\pi}}$$ **Equation 2-1**

$$r_{vdw} = 1.333267r + 0.689127$$ **Equation 2-2**

A good correlation was found between $r$ and $r_{vdw}$ obtained by crystallographic measurements. The correlation coefficient square of the fitting, $R^2$ is 0.95. Therefore, the $r_{vdw}$ parameter can be reliably predicted. The dispersion energy $E_{AB}^{disp}$ is a function of ionization potential and atomic polarizability, as such, the depth of potential well, $\varepsilon$, could be estimated using Equations 2-3 and 2-4.

$$E_{AB}^{disp} \approx -\frac{3I_A I_B}{2(I_A + I_B)} \frac{\alpha_A \alpha_B}{R^6} = -\frac{B}{R^6}$$ **Equation 2-3**

$$\varepsilon = \frac{B}{2(2r)^6}$$ **Equation 2-4**

The bonded force field parameters[253–255] were derived following the AMBER force field development strategy.

The atomic charges were derived using the RESP program[256] to fit the HF/6-31G* electrostatic potentials after the geometries were optimized at B3LYP/6-311++G(d,p) level, with the solvent effect being taken into account using the polarizable continuum model implemented in the GAUSSIAN 16 software package.[257] We chose B3LYP to be more consistent with the established protocols in AMBER force field development. Another consideration is that the range-separated methods (such as CAM and wB97X) are better choice when one wants to study weak interaction, charge transfer, and so on. For the purpose of FF parameterization, the difference between B3LYP and range-separated methods are not significant. We did optimization for the two model compounds using CAM-B3LYP/6-311++G(d,p) and the optimized geometries are essentially same to those by B3LYP/6-311++G(d,p). The root-mean-square deviations are 0.064 and 0.044 Å, for IDA and NTA, respectively. For bond lengths involved by $Cu^{2+}$, the average difference is 0.025 Å (1.2%) and 0.030 Å (1.3%) for IDA and NTA, respectively. As to bond angles with $Cu^{2+}$ in the middle, i.e. X-$Cu^{2+}$-Y (X and Y are atom types other than $Cu^{2+}$), the average difference is 0.56° (0.53%) and 0.33° (0.32%), for IDA and NTA, correspondingly. The differences are much smaller for those bonds with $Cu^{2+}$ not in the middle.

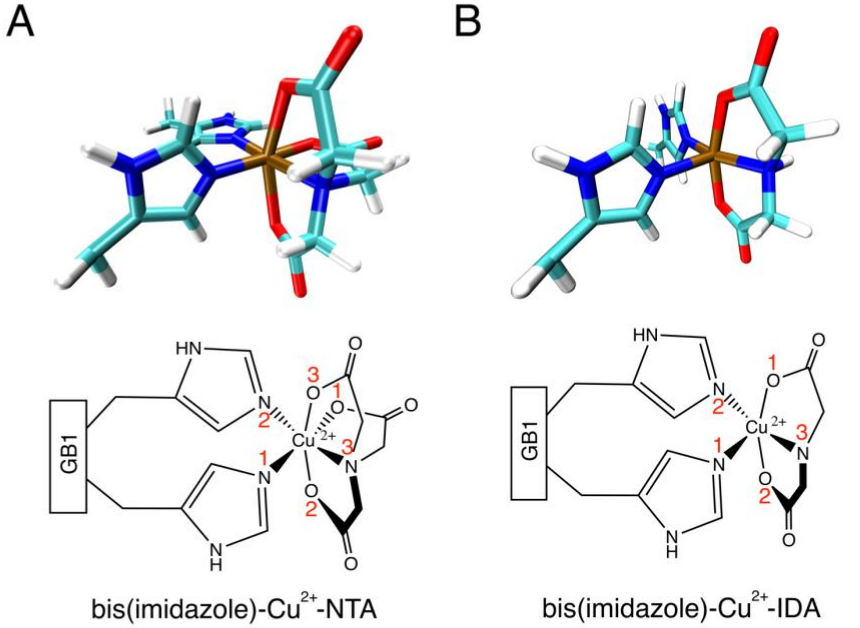

**Figure 2-1.** DFT optimized structures of $Cu^{2+}$-based protein labels. Top panel shows the DFT-optimized structures of (A) bis(imidazole)–$Cu^{2+}$–NTA (B) and bis(imidazole)–$Cu^{2+}$–IDA. $Cu^{2+}$ center is shown in brown. Bottom panel shows the two-dimensional (2D) representation of bis(imidazole)–$Cu^{2+}$–NTA and bis(imidazole)–$Cu^{2+}$–IDA, respectively.

Three residue topologies, representing bis(imidazole)– $Cu^{2+}$–NTA, bis(imidazole)– $Cu^{2+}$–IDA, and the main-chain part of the HIE residue (i.e., histidine with hydrogen on the epsilon nitrogen), were prepared using the residuegen program in the Antechamber package.[258] The last residue is needed as the partial charges of the HIE side chain were recalculated using the model compounds while those of the main-chain atoms remain unchanged. The two model compounds of $Cu^{2+}$ complexes were assigned ff14SB atom types and the substitutes of the missing the force field parameters came from GAFF. However, as expected, there was no substitute available for force parameters involving $Cu^{2+}$. The following describes the strategies of deriving the missing force field parameters. The equilibrium bond length and bond angle values were obtained by doing statistical analyses on the B3LYP/6-311++G(d,p)-optimized geometries. The force constants of bond stretching and bond angle bending were calculated using an empirical formula described elsewhere.[147] The two parameters for $Cu^{2+}$ to be used in the force constant calculations were derived by minimizing the differences between the vibrational frequencies calculated by ab initio and normal mode analyses on the developed molecular mechanics models. We applied a weight to each vibration mode depending on the contribution of $Cu^{2+}$ in this mode—the larger the contribution of $Cu^{2+}$, the larger the weight for this mode. The torsional angle parameters with $Cu^{2+}$ being at the second or third position were set to 0.0, as usually done for metallic atom types in MMFF.[259]

### 2.2.3 MD Simulations

All proteins were simulated with the ff14SB AMBER force field.[128] Solvent waters were treated with the TIP3P water model.[260] The spin-labeled protein was solvated in a cubic water box. The box size was roughly 60 $Å^3$ for spin-labeled GB1. Chloride and sodium ions were added to neutralize the systems with a final concentration of 150 mM. All simulations were performed using the pmemd program in the AMBER18 software package. The solvated systems were energy-minimized with a harmonic restraint force constant applied to the main-chain protein. The restraint was gradually released from 20, 10, 5, and 1 to 0 kcal/(mol $Å^2$) over a total of 12 000 steps. The minimized structures were then equilibrated with a Berendsen barostat at 298.15 K for 3.2 ns with progressively decreasing harmonic restraint force constants of 20, 10, 5, and 1 kcal/(mol $Å^2$).[261]

Each system was then gradually heated from 0 to 298.15 K. The time step for integration of motions was 2 fs for the heating, equilibrium, and the following production phases. The temperature was maintained at 298.15 K for the production simulation. Periodic boundary conditions along with particle mesh Ewald (PME) were applied to accurately account for the long-range electrostatic interactions. The temperature was controlled with the Langevin thermostat using a collision frequency of 5.0 $ps^{-1}$. The pressure was maintained at 1 atm with a relaxation time of 1.0 ps. SHAKE was used to restrain all bonds involving hydrogen. A nonbonded cutoff of 10 Å was applied. All systems reached equilibrium after 2 ns, and the total simulation time was 200 ns. To eliminate the possible influence of the starting conformation, five independent MD runs were performed for the $Cu^{2+}$–NTA-labeled 6H/8H/28H/32H and 15H/17H/28H/32H GB1 mutants using the equilibrated structures. Each of the independent simulations was assigned initial velocities randomly, using a random number generator seed.

### 2.2.4 DEER Experiment

To acquire distance information between labeled sites of $Cu^{2+}$–IDA-labeled 15H/17H/28H/32H GB1 mutants, the DEER experiment was performed. The DEER experiment was performed with a Bruker E580 spectrometer and a 1 kW amplifier at an X-band frequency at 20 K. The resonator was over-coupled to a bandwidth of 200 MHz. A four-pulse DEER with 16-step phase cycling was carried out with the sequence $(\pi/2)\ \upsilon_A - \tau - (\pi)\ \upsilon_A - \tau + T - (\pi)\ \upsilon_B - \tau_2 - T - (\pi)\ \upsilon_A - \tau_2 -$ echo. A square pulse of 24 ns at pump frequency ($\upsilon_B$) was used. Observer pulses were square-shaped with a π pulse length of 30 ns. The step size was 10 ns and incremented over 139 points. DeerAnalysis2018 was used to analyze the data.[262]

## 2.3 Results and Discussion

So far, the MMM software has been able to generate the rotamer libraries for $Cu^{2+}$–NTA and $Cu^{2+}$–IDA spin labels.[244] In this software, rotamers of $Cu^{2+}$–NTA/IDA are computed and incorporated into the crystal structures of the protein. Furthermore, the program uses elastic network modeling and EPR distances in different functional states to calculate structural models of the protein in each state. Such analysis can provide perspective on the large-amplitude changes in protein conformation that typically occur in the microsecond–millisecond range. However, to view protein backbone fluctuations occurring in the pico- to nanosecond range, molecular dynamics simulations are useful.

To accurately model our $Cu^{2+}$ labels, we developed MMFF parameters for bis(imidazole)–$Cu^{2+}$–NTA and bis(imidazole)– $Cu^{2+}$–IDA to replicate the dHis– $Cu^{2+}$–NTA/IDA label. We first used the B3LYP/6-311++G(d,p) basis set to optimize the geometry of the $Cu^{2+}$ label structures, as described in the Methods section. The optimized structures of bis(imidazole)–$Cu^{2+}$–NTA and bis(imidazole)–$Cu^{2+}$–IDA are shown in Figure 2-1, and the ab initio-optimized bond angles and bond lengths are summarized in Table 2-1. For bis(imidazole)–$Cu^{2+}$–IDA, the $Cu^{2+}$ is coordinated to the two nitrogen atoms of the imidazole moieties and one nitrogen and two oxygen atoms of the IDA. These results are consistent with prior EPR results[84,85] and with the crystallographic results of a $Cu^{2+}$ complexed with IDA and two imidazole ligands.[263] The results are also similar to the previously DFT-optimized models of $Cu^{2+}$–IDA that were incorporated in the MMM software.[244] Notably, our optimized structure has only five coordinating atoms to the $Cu^{2+}$. Typically, most common Type 2 $Cu^{2+}$ complexes exist with a six-coordinate octahedral geometry.[264] We attempted to add one water molecule so that the coordination number becomes six for bis(imidazole)–$Cu^{2+}$–

IDA. However, this water molecule could not be kept in a proper position and the distance between $Cu^{2+}$ and oxygen of the water was larger than 4.0 Å after the optimization.

**Table 2-1.** Structure Comparison. Structure Comparison of Bis(imidazole)–$Cu^{2+}$–NTA[265] and Bis(imidazole)–$Cu^{2+}$–IDA[263] of Crystal Structures, DFT-Optimized Structure Published by Ghosh et al., [244] and the Optimized Structure in This Work. Structures and labels of atoms of bis(imidazole)– $Cu^{2+}$–NTA/IDA are shown in Figure 2. Distances between atoms and the bond angle of bis(imidazole)–$Cu^{2+}$–NTA are shown in the left four columns, referred to as A; distances between atoms and the bond angle of bis(imidazole)– $Cu^{2+}$–IDA are shown in the right four columns, referred to as B. Crystal A/B represents the crystal structures of bis(imidazole)– $Cu^{2+}$–NTA/IDA. MMM A/B represents the optimized structures by Ghosh et al. QM A/B represents the optimized structures from this work.

| Bond (Å) or angle (deg) | Crystal A | MMM A | QM A | Bond (Å) or angle (deg) | Crystal B | MMM B | QM B |
|---|---|---|---|---|---|---|---|
| N1–$Cu^{2+}$ | 1.998 | 2.033 | 2.042 | N1–$Cu^{2+}$ | 1.987 | 2.216 | 2.309 |
| N2–$Cu^{2+}$ | 2.006 | 2.034 | 2.063 | N2–$Cu^{2+}$ | 2.001 | 2.012 | 2.004 |
| N3–$Cu^{2+}$ | 2.257 | 2.360 | 2.156 | N3–$Cu^{2+}$ | 2.085 | 2.057 | 2.029 |
| O1–$Cu^{2+}$ | 1.943 | 1.986 | 1.982 | O1–$Cu^{2+}$ | 1.956 | 2.011 | 2.011 |
| O2–$Cu^{2+}$ | | | 2.408 | O2–$Cu^{2+}$ | 2.225 | 2.014 | 2.008 |
| O3–$Cu^{2+}$ | 1.986 | 2.027 | 2.423 | O3–$Cu^{2+}$ | | | |
| N1–$Cu^{2+}$–N2 | 89.2 | 93.2 | 92.7 | N1–$Cu^{2+}$–N2 | 92.1 | 101.4 | 101.1 |

The bis(imidazole)–$Cu^{2+}$–NTA-optimized structure shows a six-coordination environment of $Cu^{2+}$, involving two nitrogens from the imidazoles and one nitrogen and three oxygen atoms from the NTA ligand. The results are consistent with EPR (39) and the results from the crystal structure of $Cu^{2+}$ complexed with NTA and two imidazole molecules.[265] However, the optimized structure does not agree with that used in MMM. The MMM model is a penta-coordinated $Cu^{2+}$ containing keto-linked imidazole molecules. Such keto-bridging between imidazole moieties was meant to facilitate formation of a six-coordinate $Cu^{2+}$ complex and likely does not completely represent the native double-histidine nature of $Cu^{2+}$–NTA.

The molecular mechanics models for bis(imidazole)–$Cu^{2+}$–NTA and bis(imidazole)–$Cu^{2+}$–IDA were developed following the philosophy of AMBER additive force field development. The average unsigned errors of the vibration frequencies are 36.41 and 33.78 $cm^{-1}$ for the NTA and IDA model compounds, respectively. The corresponding root-mean-square errors of 65.2 and 61.4 $cm^{-1}$ are also much smaller than the average error of GAFF-predicted vibrational frequencies. We evaluated the two model compounds by running 2000 step minimization and 1 nanosecond MD simulations using a generalized Born model (igb = 1) to account for the solvent effect.[266] The root-mean-square deviations (RMSDs) between the minimized and ab initio geometries are 0.43 and 0.58 Å for the NTA and IDA model compounds, respectively. Both MD simulations are very stable, and 500 snapshots were collected for plotting RMSD ~ simulation time curves. The heavy-atom RMSDs of 500 snapshots are 1.11 ± 0.20 and 1.42 ± 0.27 Å for the NTA and IDA model compounds, respectively. These results are very reasonable for large model compounds like bis(imidazole)–$Cu^{2+}$–NTA and bis(imidazole)–$Cu^{2+}$–IDA.

After optimizing the geometries and developing force fields for the dHis–$Cu^{2+}$ complexes, we must put them in the context of a protein to perform relevant MD simulations. For MD analysis, we considered two spin-labeled mutants of GB1. GB1 is a stable, globular protein[267,268] with both α-helix and β-sheet secondary structures. GB1 has been well characterized by EPR, NMR, and X-ray crystallography.[269–277] This thorough understanding makes GB1 an appropriate model system for testing the feasibility of performing MD simulations on spin-labeled proteins with spin labels located at different secondary structures. In this work, we used the 6H/8H/28H/32H and 15H/17H/28H/32H mutants of GB1. The β-sheet dHis sites were 6H/8H and 15H/17H, while the α-helix dHis site was 28H/32H. All structures were built starting from the initial GB1 crystal structure (PDB: 4WH4). The B3LYP-optimized structures of $Cu^{2+}$–IDA or $Cu^{2+}$–NTA were then attached to the dHis sites.

Five independent MD runs of 200 ns were performed to reduce the influence of the starting conformation. The distance between the two $Cu^{2+}$ centers was calculated for all MD frames saved every 10 ps of the MD trajectory. Figure 2-2 shows the distance distributions obtained from one of the MD runs compared to the experimental distributions, as well as the distributions estimated using the MMM software. The four other independent MD runs gave very similar results (Figure 2-3). The experimental EPR distance measurements on $Cu^{2+}$–NTA-labeled 6H/8H/28H/32H and 15H/17H/28H/32H GB1, $Cu^{2+}$–IDA-labeled 6H/8H/28H/32H GB1 were previously published.[84,85] The validations to these distance distributions have been provided in Figure 2-4. The distance measurement for $Cu^{2+}$–IDA-labeled 15H/17H/28H/32H GB1 was obtained and validated for this work (data shown in Figure 2-4).

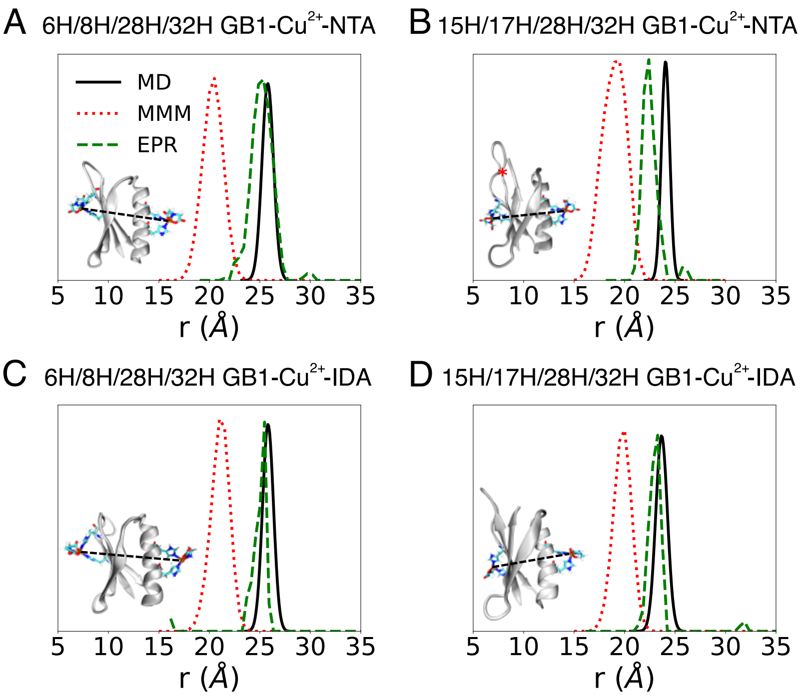

**Figure 2-2.** Comparison of distance distributions for Cu$^{2+}$–NTA-labeled GB1 mutants. (A) 6H/8H/28H/32H GB1, (B) 15H/17H/28H/32H GB1, (C) Cu$^{2+}$–IDA-labeled 6H/8H/28H/32H GB1 and (D) 15H/17H/28H/32H GB1 with the solution structure shown as cartoons in the bottom left of each panel. The distributions of the Cu$^{2+}$–Cu$^{2+}$ distances obtained from EPR measurements, MMM simulations, and 200 ns MD simulations are shown by these green dashed lines, red dotted lines, and black solid lines, respectively.

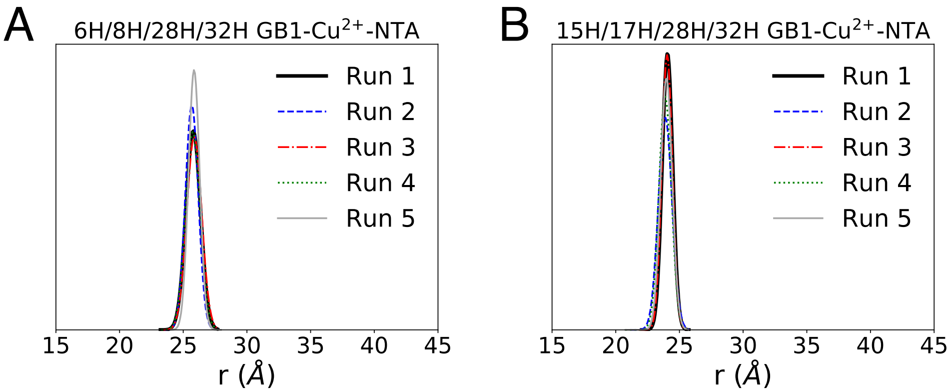

**Figure 2-3.** Cu$^{2+}$- Cu$^{2+}$ distance distributions from each 200 ns MD run. (A) Cu$^{2+}$-NTA labeled 6H/8H/28H/32H GB1 and (B) Cu$^{2+}$-NTA labeled 15H/17H/28H/32H GB1. For these two systems, the most probable distances from each run agrees within 0.2 Å, with the difference in standard deviation within 0.1 Å.

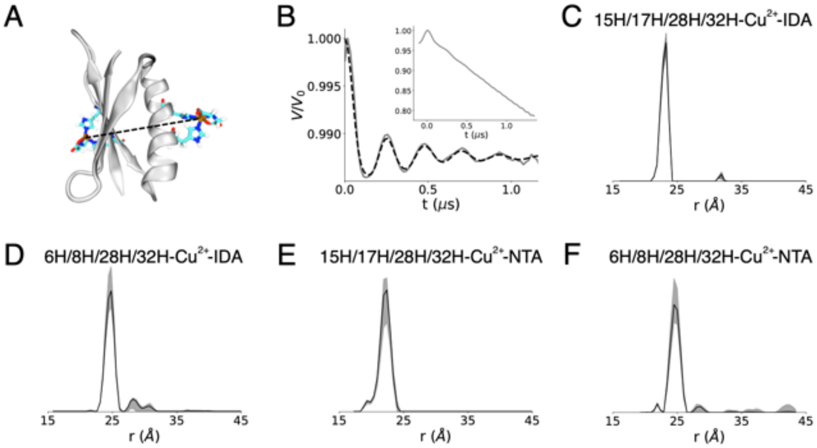

**Figure 2-4.** DEER distance distritions of dHis-Cu$^{2+}$ labeled GB1. (A) Cu$^{2+}$-IDA labeled 15H/17H/28H/32H GB1. (B) Background subtracted time-domain DEER data (grey solid line) and the corresponding fit (black dashed) using Tikhonov regularization. The inset shows the raw time-domain DEER data (grey solid) with background exponential decay shown in black dashed line. (C) Distance distribution between the Cu$^{2+}$ centers obtained from DeerAnalysis20181 with the uncertainty in grey using validation tool. (D), (E) and (F) show the validations in grey shades for the previously published distance distributions of Cu$^{2+}$-IDA labeled 6H/8H/28H/32H GB1, Cu$^{2+}$-NTA labeled 6H/8H/28H/32H and 15H/17H/28H/32H GB1.

For Cu$^{2+}$–NTA-labeled 6H/8H/28H/32H and 15H/17H/28H/32H GB1 mutants, the most probable distances from MD simulations agreed well with the EPR experiments. The difference between MD simulations and DEER experiments was within the experimental error and the resolution of the crystal structure (2.2 Å for 4WH4). Overall, the MD simulations showed significantly improved agreement with the experimental EPR data than MMM. The most probable distances from MD agree within 1–2 Å, whereas the MMM distributions are within 4–5 Å. Additionally, the distribution width of the MD simulations is in better agreement with the experimental data within 1 Å, whereas the MMM distribution width is larger than the EPR experimental distribution width by 2–4 Å. Distance distributions generated using the $Cu^{2+}$–IDA label showed similar distance distributions as the $Cu^{2+}$–NTA-labeled systems (Figure 2-2C,D).

As expected, the solution structures of the proteins with $Cu^{2+}$–NTA labels compared to those with $Cu^{2+}$–IDA labels do not show significant difference during simulation. The improved predictions of distances from the MD simulations compared to the previously reported MMM results are likely due to (1) the inclusion of protein dynamics; (2) the use of the detailed atomistic force field ff14SB with the explicit solvent to calculate forces and propagate dynamics for the spin-labeled protein; and (3) the optimized structure of bis(imidazole)–$Cu^{2+}$–NTA with more realistic coordination environment to $Cu^{2+}$.

Based on these factors, it is unsurprising that MD provides a closer agreement with the experimental EPR results than MMM. However, both techniques are still valuable and are complementary when used together. The true strength of MMM lies in that one can use sparse distance constraints to obtain model structures of proteins in different functional states. These conformational changes from one functional state to another involve large-amplitude slow motions, which, for large proteins, are often not accessible to NMR, crystallography, or conventional MD simulations. Another advantage of the MMM software is that it only takes minutes to a few hours to generate protein conformations in different functional states. On the other hand, a 200 ns standard MD simulation on a moderate-sized protein will normally take a few days to a few weeks depending on the type of supercomputing resources available. The results in Figure 2-2 suggest that MMM can be used to obtain initial models of such functional states that can be subsequently refined by atomistic MD simulations.

To further verify the robustness of the force fields, we performed 200 ns MD simulations on 6H/8H/28H/32H GB1 15H/17H/28H/32H GB1 without the $Cu^{2+}$ labels. Figures 2-5 and 2-6 show the Cα–Cα distance distributions of the labeled sites sampled from the MD simulations with the labels (blue solid line) and without the labels (black dotted line). The Cα–Cα distances from the crystal structure[240] or the initial structure are shown as red dashed vertical lines. The most probable Cα–Cα distances from the MD simulations of labeled proteins are in reasonable agreement with those obtained for the unlabeled protein with a difference less than 1 Å, suggesting that the *in silico* formation of the coordination compound with the $Cu^{2+}$ labels does not induce large changes in protein dynamics and structure. Site 8-related distances show slightly broader distributions, possibly due to the fact that it is located at the edge of the β-sheet and is more flexible, whose location is indicated in the inset of Figure 2B as a red asterisk, whereas sites 6, 15, and 17 are located in the middle of the β-sheet. The data also validate the use of EPR distance measurements and the MD simulations to infer site-specific information on protein flexibility.

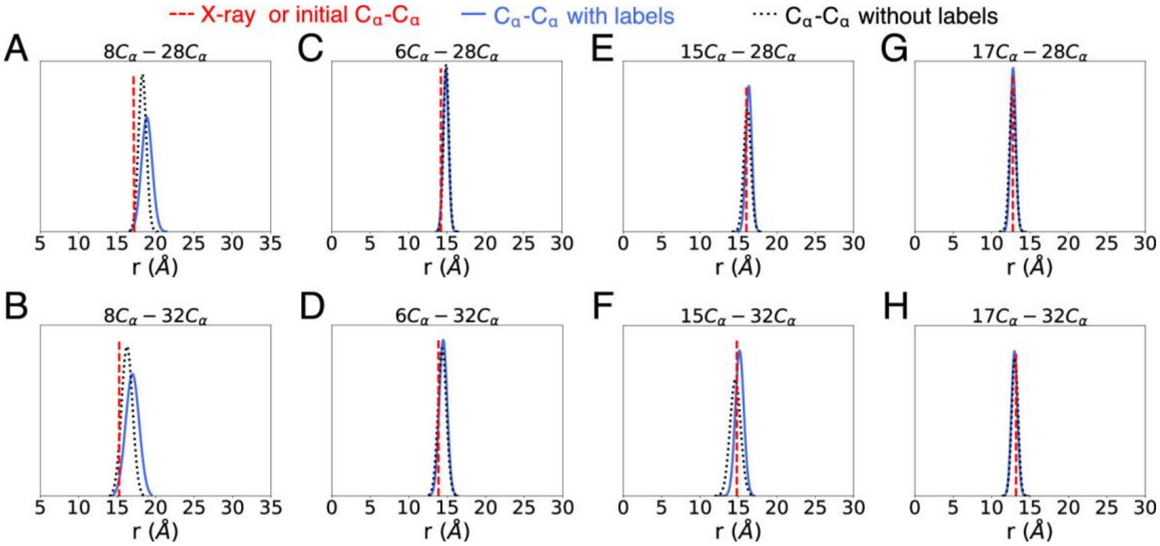

**Figure 2-5.** Cα–Cα distance distributions of the spin-labeled sites. Distributions of Cα–Cα distance of the spin-labeled sites for 6H/8H/28H/32H and 15H/17H/28H/32H GB1 with $Cu^{2+}$–NTA labels (blue solid); the corresponding Cα–Cα distance distributions without spin labels (black dotted). The Cα–Cα distances from the crystal structure or the initial structure for simulation are shown as red dashed vertical lines. Cα–Cα distances for 6H/8H/28H/32H between (A) sites 8 and 28, (B) sites 8 and 32, (C) sites 6 and 28, and (D) sites 6 and 32. Cα–Cα distances for 15H/17H/28H/32H between (E) sites 15 and 28, (F) sites 15 and 32, (G) sites 17 and 28, and (H) sites 17 and 32.

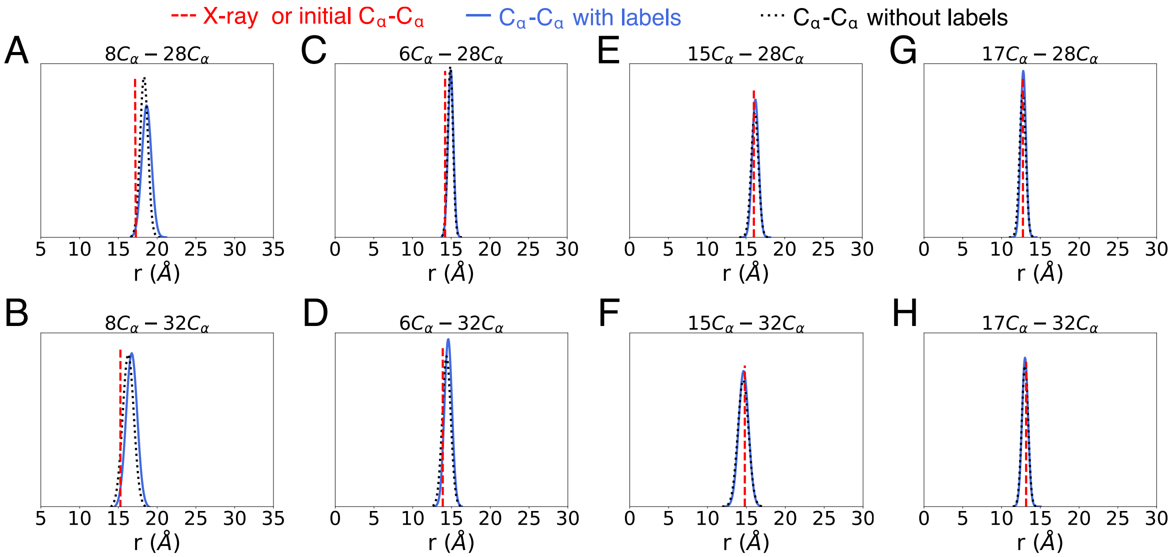

**Figure 2-6.** Distributions of $\mathbf{C_\alpha}$-$\mathbf{C_\alpha}$ distance. $\mathbf{C_\alpha}$-$\mathbf{C_\alpha}$ distance distributions. Distributions of $\mathbf{C_\alpha}$-$\mathbf{C_\alpha}$ distance. $\mathbf{C_\alpha}$-$\mathbf{C_\alpha}$ distance distributions of the spin-labeled sites for 6H/8H/28H/32H and 15H/17H/28H/32H GB1 with $Cu^{2+}$-IDA labels (blue solid), the corresponding $\mathbf{C_\alpha}$-$\mathbf{C_\alpha}$ distance distributions without spin labels (black dotted). The $\mathbf{C_\alpha}$-$\mathbf{C_\alpha}$ distances from crystal structure[278] or the initial structure for simulation are shown as red dashed vertical lines. $\mathbf{C_\alpha}$-$\mathbf{C_\alpha}$ distances for 6H/8H/28H/32H between (A) Sites 8 and 28, (B) Sites 8 and 32, (C) Sites 6 and 28; (D) Sites 6 and 32. $\mathbf{C_\alpha}$-$\mathbf{C_\alpha}$ distances for 15H/17H/28H/32H between (E) Sites 15 and 28, (F) Sites 15 and 32, (G) Sites 17 and 28; (H) Sites 17 and 32.

To visualize the atomic properties of the dHis–$Cu^{2+}$ DEER experiments, Figure 2-7A plots the predicted $Cu^{2+}$ positions of $Cu^{2+}$–NTA-labeled 6H/8H/28H/32H GB1 from MD simulations, compared to those obtained from MMM using a space-filling model in Figure 2-7B. Similar to MMM predictions, MD simulations of $Cu^{2+}$–NTA-labeled 6H/8H/28H/32H GB1 show very localized $Cu^{2+}$ positions, indicating a narrow distance distribution between the labeled sites. Figure 2-7C shows the predicted conformers of the common nitroxide label, R1, by MMM. The comparison of copper positions (Figure 2-7A,B) versus R1 positions (Figure 2-7C) dramatically illustrates the rigidity of the $Cu^{2+}$ and the power and potential of $Cu^{2+}$-based distance measurements to accurately resolve a myriad of protein structural and conformational aspects, such as conformational changes, quaternary structural arrangements, protein–protein interactions, and more.

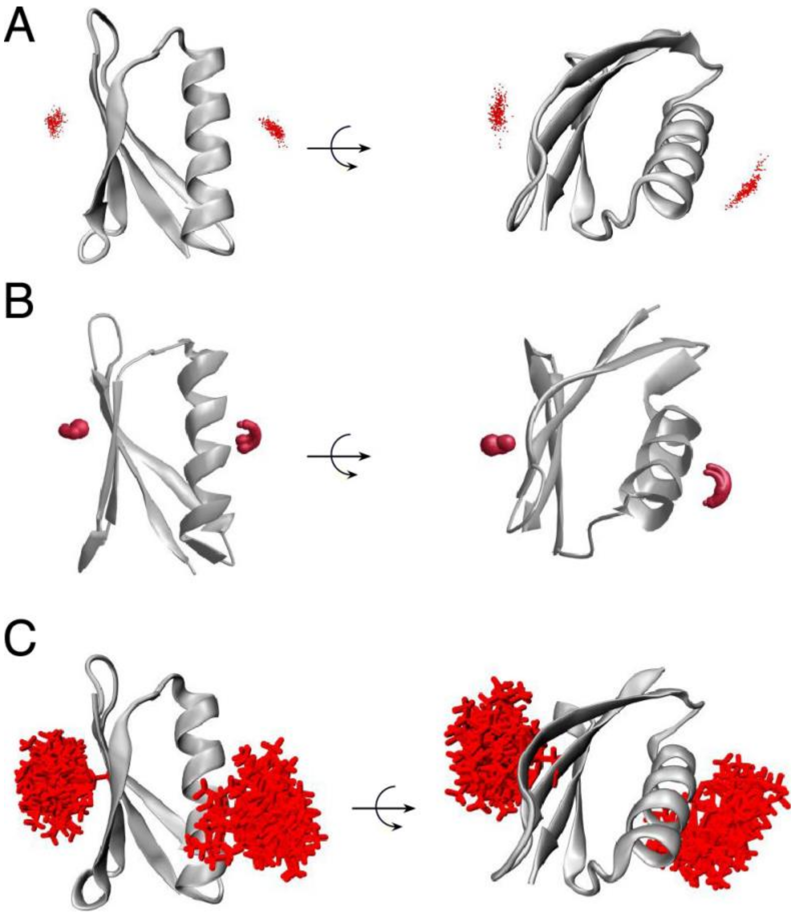

**Figure 2-7.** Predicted $Cu^{2+}$ spatial distributions. Distributions of $Cu^{2+}$–NTA-labeled 6H/8H/28H/32H GB1 were generated by MD simulations (A), MMM (B) and nitroxide label R1 distribution in MMM (C).

In addition to the distance information, the MD simulations also help explain orientational effects in $Cu^{2+}$–dHis-based DEER. In DEER, orientational effects are due to the excitation of only a fraction of the total EPR spectrum, which can sometimes result in the selection of a small subset of all possible molecular orientations.[86,120,279–285] Such orientational effects cause DEER experiments performed at different magnetic fields to show distinctly different signals. For nitroxides, orientational selectivity is usually not observed at the X-band (∼9.5 GHz) due to the flexibility of the linker and the interplay of hyperfine anisotropies and g-splittings. Both factors effectively mix orientations across the spectrum such that even the limited excitation of DEER effectively samples multiple molecular orientations.[238,286] Ultra-wide-band excitation can also overcome this limitation by effectively exciting the entire EPR spectrum.[287] On the other hand, highly rigid labels can exhibit orientational selectivity and can be used to measure orientational information.[280,284,288–291]

For dHis-based $Cu^{2+}$-labels, orientational effects are also uncommon at X-band frequencies, despite the rigidity of the label.[84–86,240] We have previously postulated that the g-tensor of the $Cu^{2+}$ has a distribution of orientations, which may act to randomize the selected molecular orientations.[281]

The MD results provide evidence for this postulate and allow us to examine the role of molecular and residual fluctuations in the orientational selectivity of rigid $Cu^{2+}$-based systems. First, the $Cu^{2+}$ coordination fluctuates during the course of the MD simulations; for example, the distance between $Cu^{2+}$ and the imidazole nitrogen changes by ∼30% with a range of 1.74–2.39 Å and an average distance of 2.07 Å. The high plasticity of the $Cu^{2+}$ coordination leads to a range of g-tensor values, which we calculated for a range of conformations in the MD simulations using the CAM-B3LYP QM method and 6-311++G(d,p) basis set. The g-tensor values changed by up to 10% due to changes in the ligand to $Cu^{2+}$ distances and the torsion angles. More importantly, changes in torsion angles and coordination lead to a large change in the orientations of $g_{\parallel}$. Second, rotameric fluctuations of the side chain lead to changes in g-tensor directions. Together these effects reduce orientational selectivity.

Here we analyzed just the effects of rotameric fluctuations. Figure 2-8A shows the coordination environment of $Cu^{2+}$, with $g_{\|}$ perpendicular to the equatorially coordinated ligands. Figure 2-8B shows the molecular reference frame of the dHis–$Cu^{2+}$-labeled GB1 and the three angles that define the relative orientations of the two $Cu^{2+}$. We calculated each angle across every frame of our MD results for the $Cu^{2+}$–NTA-labeled 6H/8H/28H/32H GB1. Figures 2-8C and 2-9 show $\chi$, $\gamma$, and $\eta$ as a function of time. Note that $\chi$ was shown to have the highest influence on the resultant DEER signals at the X-band.[281] Interestingly, all angles sample a broad range of values, with the standard deviations in angles being greater than 10°, as shown in Figure 5D. More precisely, the observed mean angles and standard distributions in MD are 97.5°; 10.6° (mean; standard deviation) for $\gamma$; 100.0°; 11.3° for $\chi$, and 101.6°; 12.9° for $\eta$. Previous experimental Q-band DEER data was consistent with 75°; 10° for $\gamma$, 80°; 10° for $\chi$, and 22.5°; 10° for $\eta$.[86] Notably, we have reasonable agreement between the MD and previously reported values for $\chi$ and $\gamma$, although there is a discrepancy in the values of $\eta$.

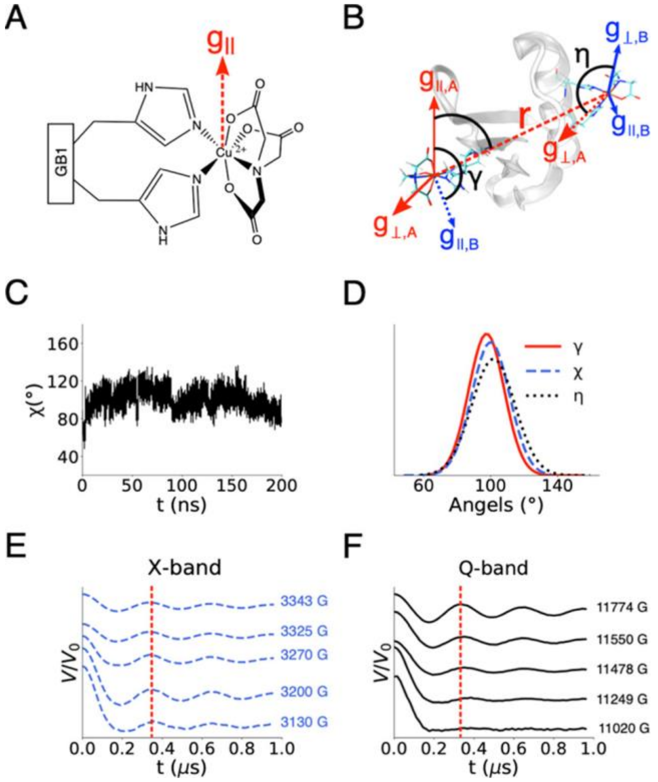

**Figure 2-8.** Molecular basis of orientational selectivity. Coordination environment of $Cu^{2+}$ binding to NTA and dHis. The imidazole nitrogens bind to $Cu^{2+}$ equatorially, leading to the definition of $g_{\parallel}$ being perpendicular to the equatorial plane. (B) The principal axes for spin A (red) and spin B (blue) are defined, with relative orientations between the two spins indicated by three angles, γ, χ, and η. (C) The angle χ as a function of simulation time. (D) The distributions of angle γ, χ, and η. (E) and (F) Simulated DEER signal at the selected fields at X-band frequency and Q-band frequency, respectively. The red dashed line indicates the first period of the modulations at all fields of the X-band or at 11774 G ($g_{\parallel}$) of the Q-band. The orientational selectivity is mostly washed out due to the σ being above 10.0° at the X-band frequency, whereas it is overt at the Q-band frequency.

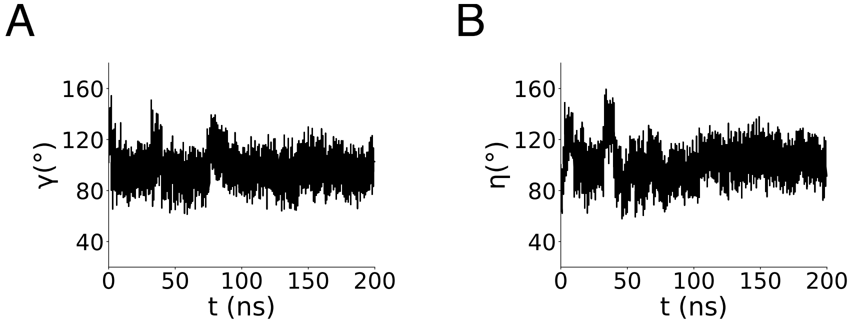

**Figure 2-9.** The angles $\boldsymbol{\gamma}$ and $\boldsymbol{\eta}$ as a function of simulation time of the $Cu^{2+}$-NTA labeled 6H/8H/28H/32H GB1. The angles are defined in Figure 2-8B.

More importantly, the MD results clearly show that minor fluctuations in the dihedral angles of the side chains and $Cu^{2+}$ coordination lead to an appreciable orientational distribution between the two $Cu^{2+}$ ions, even though the metal ions are relatively fixed. To emphasize this point, we simulated DEER signals at both the X-band and Q-band using the set of angles obtained from MD, as shown in Figure 2-8E,F, respectively. Using our angles and, more importantly, our standard deviations as determined from MD, it is clear that orientational effects are washed out at the X-band, but not at the Q-band. It is also notable that the X-band simulations agree well with the previous results, but the modulation frequencies of the Q-band simulations do not, as shown in Figure 2-10. This is likely due to the discrepancy in the $\eta$ angle, which shows that while $\chi$ may be the most influential at the X-band the influence of all three angles contributes to the Q-band signal. These results as a whole not only present MD simulations as another complementary tool in the orientational analysis of dHis–$Cu^{2+}$ systems but also provide clear evidence that the absence of orientational selectivity in $Cu^{2+}$ at the X-band is due to molecular fluctuations, imparting a distribution in g-tensor orientations. More practically, these results suggest that X-band DEER can be used to readily measure distance distributions using the dHis label. On the other hand, the Q-band DEER may provide information on the relative orientations of different secondary structure elements.[86]

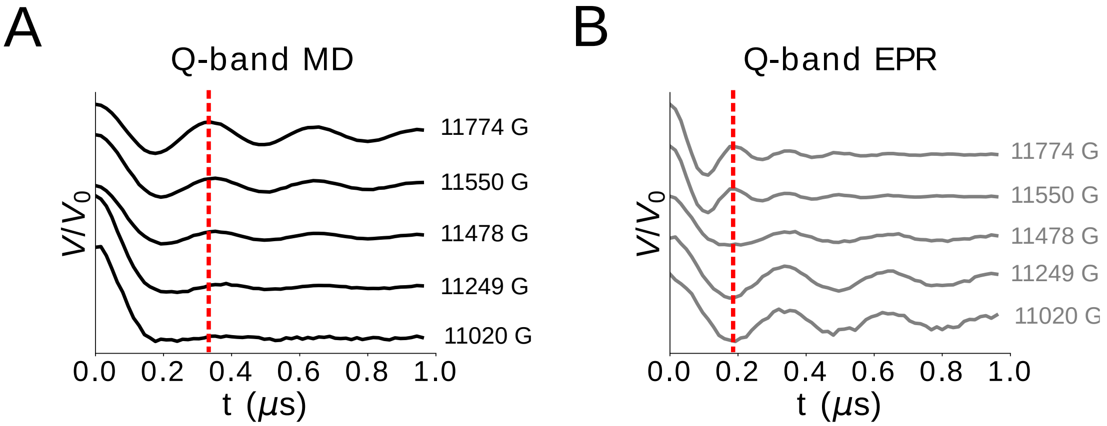

**Figure 2-10.** Simulated DEER signals. Simulated DEER signal based on MD simulations compared with (B) simulated DEER data based on experiment at selected fields at Q-band frequency. The red dashed line indicates the first period of the modulations at 11774 G ($g_{||}$). There is disagreement in the modulation periods between the MD simulations and DEER results. However, both simulations do show orientational selectivity.

## 2.4 Conclusions

In conclusion, we have developed force field parameters for the spin labels dHis–$Cu^{2+}$–NTA and dHis–$Cu^{2+}$–IDA. Molecular mechanics modeling based on the newly developed force field parameters also shows remarkable agreement with the EPR measurements. The MD simulations indicate that protein backbone flexibility is similar both with and without the label, which suggests that the force fields are robust and, importantly, that the spin label does not perturb protein dynamics. In addition, the MD simulations provide insight into the localized spatial distribution of the $Cu^{2+}$ labels, which leads to precise structural constraints for biophysical measurements. This work also confirms the hypothesis that the label exhibits sufficient orientational distribution such that orientational selectivity is not observed at the X-band but achievable at the Q-band frequency. Therefore, distance measurements using such dHis labels can be readily performed at the X-band, while Q-band DEER may provide angular information. Finally, the distance measurements using the dHis label can be combined with MD simulations to refine protein structure, gain insights into protein dynamics, and to characterize protein functions.

## 2.5 Acknowledgements

This research was supported by the National Science Foundation (NSF MCB-1613007). Simulations were performed with support from the Center for Research Computing at the University of Pittsburgh. The EPR spectrometer was supported by the National Science Foundation (NSF MRI-1725678). This chapter adapted with permission from reference 139. Copyright 2020 American Chemical Society.

# 3.0 Direct observation of negative cooperativity in a detoxification enzyme at the atomic level by EPR and simulation

*This work, in collaboration with Anthony T. Bogetti, Joshua Casto, Gordon Rule, Lillian Chong and Sunil Saxena has been accepted at Protein Science, 2023. The thesis author and Anthony T. Bogetti contributed equally to this work. The thesis author collected the majority of the EPR data, analyzed all the EPR results, and performed molecular dynamics simulations. Anthony Bogetti performed and analyzed all the weighted ensemble molecular dynamics simulations. The thesis author and Anthony Bogetti prepared the manuscript.*

## 3.1 Introduction

Glutathione S-transferases (GSTs) are a family of detoxification enzymes found in many organisms. Human GST A1-1 (hGSTA1-1) is a homodimer, with each monomer containing an active site that deactivates cellular toxins in cells by conjugating the toxins to glutathione.[292,293] There is much evidence that hGSTA1-1 exists in a large ensemble of states.[215,294] The structure of the S-hexylglutathione (GSHex)-bound hGSTA1-1 has previously been solved by X-ray crystallography and is shown in Figure 3-1A.[213] In this ligand-bound structure, the C-terminal $\alpha 9$ helix of each monomer (highlighted in blue in Figure 3-1A and labeled as $\alpha 9_A$ and $\alpha 9_B$ respectively, for monomers A and B) functions as a "lid" over the corresponding active/binding site. This helix plays an essential role in the catalytic function of the dimer. Mutations of highly conserved sites at the $\alpha 9$ helix significantly decrease the catalytic efficiency of hGSTA1-1.[295,296]

In addition, the protein is non-functional in the absence of this helix.[297] There are two main types of interactions that are present at the interface of the hGSTA1-1 dimer and the $\alpha 9$ helix. The highly conserved Tyr9, Phe10 (interface) and Phe220 (at $\alpha 9$ helix) residues form an aromatic cluster in the ligand-bound structure.[214,298] Hydrophobic interactions between Tyr9/Phe10 and Phe220 are believed to lock $\alpha 9$ over the active site.[295] In addition, the salt bridge between the conserved Asp42 ($\alpha 2$ helix, which is adjacent to $\alpha 9$) and Arg221 (right after the $\alpha 9$ helix) residues is believed to affix the $\alpha 9$ helix as a lid over the active sites and may be important for inactivating cellular toxins.[299]

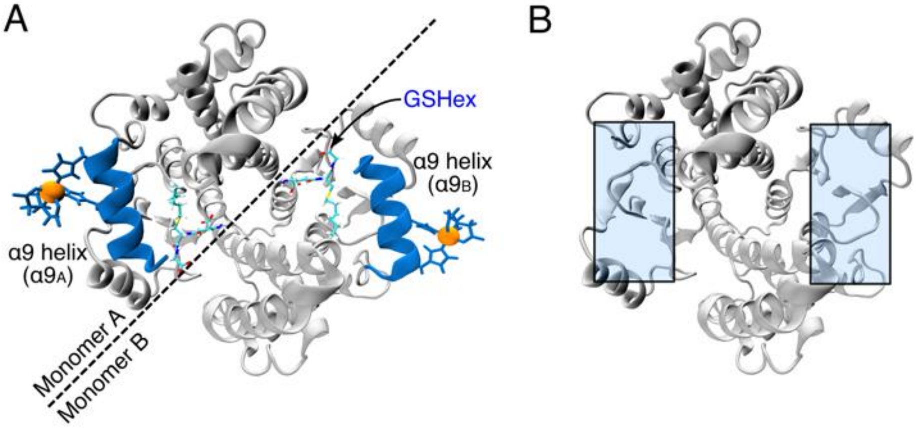

**Figure 3-1.** The entire structure of the ligand-free hGSTA1-1 is missing. (A) Crystal structure of GSHex-bound hGSTA1-1 (PDB: 1K3L). The ligand GSHex is highlighted in cyan. The $\boldsymbol{\alpha}$9 helices at the C-termini are highlighted in blue. The dHis-Cu(II)-NTA EPR labels (blue sticks with the Cu(II) atoms represented as orange spheres) are introduced to the $\boldsymbol{\alpha}$9 helix to capture the change in the distance distribution between the labels upon introducing different concentrations of GSHex. (B) In the absence of a ligand, the structure of the $\boldsymbol{\alpha}$9 helices is unresolved. The blue boxes highlight where the $\boldsymbol{\alpha}$9 helices are in the GSHex-bound structure.

However, the entire structure of ligand-free hGSTA1-1 has yet to be resolved. In the available structure of the ligand-free hGSTA1-1 dimer, shown in Figure 3-1B, the $\alpha 9$ helix of each monomer is largely missing,[300] which has left unanswered questions about the relation of the structure and dynamics to function for this critical helix. There are conflicting hypotheses about the structure of the $\alpha 9$ region in the ligand-free state. Some reports suggest that the $\alpha 9$ region is disordered,[5,9] while others suggest that the region is helical,[295,300,301] but delocalized (i.e., undocked) with respect to the binding sites.[215,216] In addition, knowledge of the full $\alpha 9$ conformational ensemble in the ligand-free state, as well as information on how the two monomers interact, is essential to fully understand the atomic-level structural details and function for this enzyme.

Here, we characterize the ligand-free conformational ensemble of the hGSTA1-1 enzyme in atomistic detail using a combination of pulsed EPR distance measurements and weighted ensemble molecular dynamics (MD) simulations. Pulsed EPR distance measurements,[38,39,218,219,221–223] generally enabled by site-directed spin labeling, are powerful probes for protein-protein[56–58] and protein-nucleic acid[70,71] interactions, metal and ligand binding sites,[62–64] and macromolecular conformational changes.[5,46,187,302–308] Such measurements can also be performed *in cells*.[12–17] In this work we employ a Cu(II)-based protein labeling scheme which involves the strategic placement of two histidine residues (dHis) to allow rigid chelation to a Cu(II) complex. In addition, the introduction of the Cu(II) in complex with the chelating agent, such as iminodiacetic acid[84] or nitrilotriacetic acid (NTA)[85], increases the specificity of Cu(II) binding to dHis sites and avoids nonspecific binding of Cu(II) to elsewhere in the protein. The dHis-Cu(II) protein labels are incisive probes of protein conformational change, since the dHis-Cu(II) based distance measurements can yield distance distributions that are up to five times narrower compared to commonly used nitroxide labels.[83] We performed such distance measurements on several ligands, which all suggested a restriction of the conformational space occupied by the $\alpha 9$ helices of hGSTA1-1 in the presence of ligand. In addition, the data showed a change in the positioning of the two helices. Based on this insight we exploited MD simulations to gain knowledge on slow conformational dynamics. To enable simulation of the seconds-timescale transition between alternate states of hGSTA1-1, we applied the weighted ensemble (WE) path sampling strategy.[309,310] The WE strategy has been demonstrated to be orders of magnitude more efficient in generating pathways and rate constants for rare events such as protein-protein binding on the multi-microsecond timescale[311] and the large-scale opening of the coronavirus spike protein on the seconds timescale.[312] Computational strategies have been able to use EPR data to predict distance distributions (MMM,[170] DEER-PREdict,[177] ensemble-biased metadynamics[188]) and predict or refine protein structures (MELD,[206] restrained ensemble MD,[137] RosettaEPR[196]). In this work, we demonstrate how the WE strategy can use EPR data as a guide to focus simulation on transitions, providing continuous pathways without applying any biasing forces.

## 3.2 Materials and methods

### 3.2.1 Protein purification and sample preparation

For the EPR experiments, we mutated Lys211 and Glu215 in the $\alpha 9$ helix of each monomer to histidines. The Cu(II)-NTA complex was then attached to this dHis site. As shown in previous work,[243] the Lys211His and Glu215His mutations do not perturb the enzyme activity. The Lys211His/Glu215His mutant was expressed in Luria broth and purified based on the previously described protocol.[28] The ligand S-hexylglutathione (GSHex) was purchased from Sigma Aldrich. The synthesis of ethacrynic acid glutathione conjugate (EASG) and S-(2,4-dinitrophenyl)glutathione (GS-DNB) were based on the previously published protocols.[313,314]

Since hGSTA1-1 is a homodimer, a dHis mutant provides two Cu(II)-NTA labeling sites. The purified protein was concentrated, aliquoted to ~220 $\mu$M in sodium phosphate buffer (pH=6.5, 50 mM sodium phosphate and 150 mM NaCl) and stored at -80 ℃.

All samples for EPR measurements were prepared based on the protocol described in previous work.[31,85,112] Briefly a 10 mM stock solution of Cu(II)-NTA and a 3-N-morpholinopropanesulfonic acid (MOPS) buffer (pH=7.4, 50 mM MOPS, 100 mM NaCl in $D_2O$) were prepared.[112] The Cu(II)-labelling can be performed in a variety of buffer,[112] and over a range of pH,[113] to provide sensitive[315] measurements of a wide range of biophysical information.[28,64,73,86,316]

The hGSTA1-1 samples contained 100 $\mu$M hGSTA1-1 dimer, 200 $\mu$M Cu(II)-NTA, and a GSHex concentration of 0 $\mu$M, 50 $\mu$M, 100 $\mu$M, 150 $\mu$M, 200 $\mu$M and 400 $\mu$M. Samples containing the EASG and GS-DNB ligands were prepared with a ligand concentration of 1 mM to ensure all active sites are saturated with ligands. The apparent dissociation constant ($K_D$) of hGSTA1-1 to GSHex has been determined in previous work to be 70 nM.[317] Although the binding affinities of the EASG and GS-DNB ligand have not been determined, we expect sub-micromolar affinity of these ligands due to their hydrophobic nature. Thus, given the concentration of the hGSTA1-1 protein relative to the $K_D$ values, stoichiometric binding of the ligand to the binding sites is expected until all hGSTA1-1 is fully loaded with ligands. The sample used for a biological repeat was prepared with 400 $\mu$M hGSTA1-1 dimer and 800 $\mu$M Cu(II)-NTA. All EPR samples were incubated at 4 ℃ for 35 min to achieve maximum binding efficiency of Cu(II)-NTA before 40% (v/v) $D_6$- glycerol was added as a cryoprotectant. All samples were placed in quartz tubes with I.D. = 2 mm and O.D. = 3 mm and were flash frozen using liquid MAP-Pro Propylene/propane gas. A detailed protocol for dHis-Cu(II) sample preparation has been published elsewhere.[31]

### 3.2.2 CW-EPR and ESEEM measurements

To determine the coordination environment of Cu(II)-NTA labeled hGSTA1-1, continuous wave (CW)-EPR and electron spin echo envelope modulation (ESEEM)[318,319] experiments were performed at 80 K on each sample with a Bruker ElexSys E680 X-band FT/CW spectrometer equipped with a Bruker EN4118X-MD5 resonator. The CW-EPR spectra contain 1024 points over a magnetic field range of 2000 G centered at 3100 G. The spectra were collected at ~9.71 GHz, with a modulation frequency of 100 kHz, a conversion time of 20.48 ms, a modulation amplitude of 4 G, attenuation of 30 dB and 100 scans. The CW-EPR spectra for each sample were simulated with EasySpin.[320]

The pulse sequence of the ESEEM experiments was $(\pi/2) - \tau - (\pi/2) - t - (\pi/2) - \tau -$echo.[318,319] The pulse delay time, $\tau$, between the first two pulses was 140 ns. The second pulse delay time, t, was stepped out by 16 ns for a total of 1024 points from an initial value of 288 ns. The ESEEM experiments were performed at the magnetic field with the most intense echo. Four-step phase cycling was applied to eliminate the undesired echo.[321,322] The ESEEM measurements for each sample were acquired for ~12 hours. A stretched exponential decay was used to fit the background and subtracted from the time-domain signal. Hamming was used to filter the noise from the signal followed by zero filling of 2048 points. Fast Fourier transform was then applied, and the absolute values were taken to form the ESEEM spectra.

### 3.2.3 EPR distance measurements

To determine the distance distribution between EPR labels within hGSTA1-1, four-pulse double electron-electron resonance (DEER) experiments[39] were performed at 18 K and at Q-band frequency. The measurements were performed with a Bruker ElexSys E580 spectrometer with a Bruker ER5106-QT2 resonator and a 300 W amplifier. The dHis-Cu(II)-based DEER time-domain signal for each sample were averaged over three measurements with pump pulses at strategically selected magnetic fields. Specifically, the pump pulses were placed at 100 G, 580 G and 827 G lower than the maximum of the field swept-electron spin echo spectrum. The three magnetic fields were chosen based on a recent work which showed that this acquisition scheme properly samples all molecular orientations[323] The pulse sequence used was $(\pi/2)\upsilon_A - \tau – (\pi)\ \upsilon_A - \tau + t - (\pi)\ \upsilon_B - T - t - (\pi)\upsilon_A - T -$ echo. A 16-step phase cycling was used. The observer pulses, $(\pi/2)\upsilon_A$ and $(\pi)\upsilon_A$, were rectangular pulses with pulse lengths of 12 ns and 24 ns (or 10 ns and 20 ns), respectively. An 82 ns chirp pulse was used for the pump pulse, $(\pi)\ \upsilon_B$ to properly account for any short distances. The pump pulse was set with a frequency from -300 MHz to -100 MHz relative to the observer pulses. The interval, t, was incremented by a step size of 20 ns (or 30 ns for one of the biological repeats shown in Figure 3-2) over 365 points (or 237 points if the step size was 30 ns). A long dipolar evolution time of ~7 $\mu$s was achieved using deuterated solvent to enhance the phase memory relaxation time to over 9 $\mu$s (Figure 3-3).[40] DEERAnalysis21 was used to analyze the DEER results.[262] Further experimental details,[324] including labeling efficiency, DEER parameters, modulation depth, and signal-to-noise ratio (SNR) are provided in Tables 3-1 to 3-3. Labeling efficiency of Cu(II)-NTA to dHis sites in our work is determined through CW-EPR experiments, which can also be optimized through pulsed dipolar EPR based on previous work.[325]

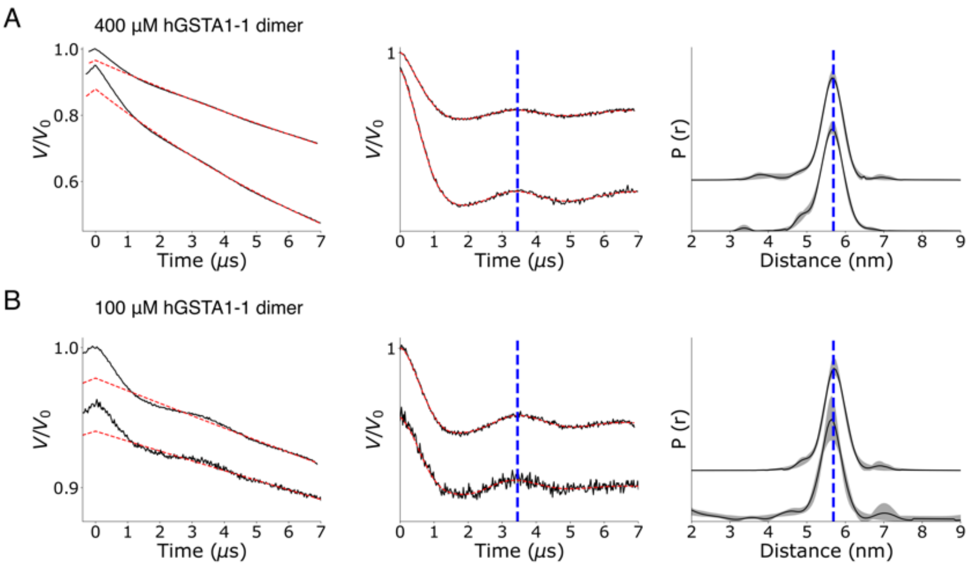

**Figure 3-2.** Biological and technical repeats for DEER measurements on ligand-free dHis-Cu(II)-NTA labeled hGSTA1-1. DEER samples are prepared with two different hGSTA1-1 dimer concentrations, (A) 400 mM hGSTA1-1 dimer concentration and (B) 100 mM hGSTA1-1 dimer concentration, respectively. For each of the sample, two technical repeats were performed. The left panel shows the primary DEER time-domain signals in black solid curves with background signals in red dashed curves. The middle panel shows the background subtracted DEER time-domain signal with Tikhonov fit shown in red dashed curves. The vertical blue dashed line shows the same modulation period between the two measurements. The right panel shows the corresponding distance distributions from the middle panel with uncertainty shown in grey shade. The distance distributions are analyzed by DEERAnalysis21. The most probable distance as well as the distribution width all agree within the uncertainty for all repeats. For the sample containing 400 mM hGSTA1-1 dimer, the top DEER trace in the left panel used a 200 MHz 82 ns chirp pulse at the pump frequency, and the bottom trace used a 200 MHz 250 ns chirp pulse at the pump frequency resulting a larger modulation depth. For the sample containing 100 mM hGSTA1-1 dimer, the two DEER experiments were set up with two different tunning performed by different students.

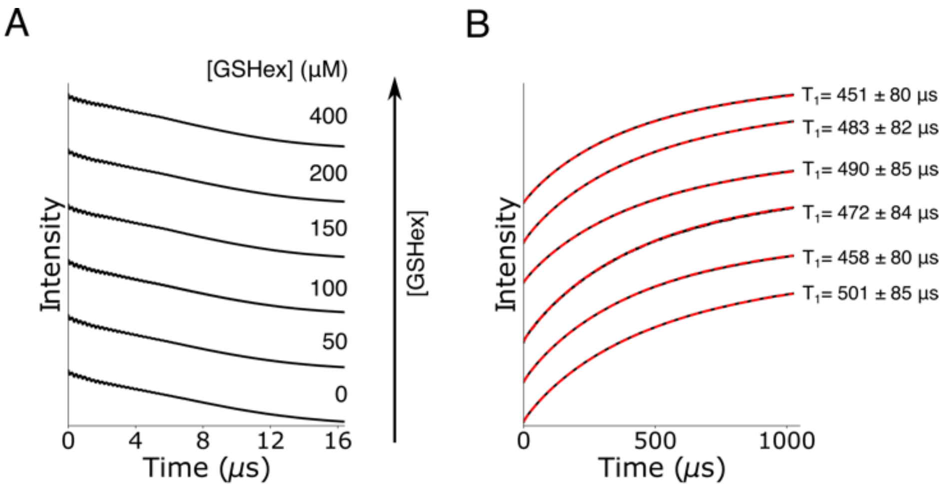

**Figure 3-3.** Determination of relaxation times. (A) Primary Hahn echo decay data for samples with different GSHex concentration labeled in each plot. The hGSTA1-1 dimer concentration of each sample was 100 mM. Due to the TWT gate time limit, the full two-pulse decay could not be collected. The best fit using the stretched exponential decay shows a phase memory time, $T_m$, of over 9 $\mu s$ for each sample. (B) Primary inversion recovery data and fit of the stretched exponential decay with the form $I(t) = c * [1 - 2 * e^{-(\frac{t}{T_1})^y}]$ for each $Cu^{2+}$-NTA labeled hGSTA1-1 with different ligand concentration. The best fit, shown as the dashed red lines, suggests that $T_1$ for each sample are all between 450 $\mu s$ to 500 $\mu s$.

**Table 3-1.** Labeling efficiency of the dHis-Cu(II)-NTA labeled hGSTA1-1.

| Construct | Protein conc. [$\mu$M] | Label conc. [$\mu$M] | Labeling efficiency % |
|---|---|---|---|
| K211H/E215H | 100 | 196 | 98 |

**Table 3-2.** DEER acquisition parameters, modulation depths and SNR, for dHis-Cu(II)-NTA labeled K211H/E215H hGSTA1-1 with different GSHex concentrations (For all samples listed, hGSTA1-1 concentraion is 100 $\mu$M). [a] For dHis-Cu(II)-NTA labeled hGSTA1-1, we performed Q-band DEER experiments at three optimally-positioned magnetic fields that were identified in previous work. Thus, we provide the number of averages at each of the three

fields, from lower to higher field. [b] SNR was calculated with respect to the modulation depth and automatically determined by ComparativeDeerAnalyzer.

| | dHis-Cu(II)-NTA labeled K211H/E215H | | | | | |
|---|---|---|---|---|---|---|
| GSHex [$\mu$M] | 0 | 50 | 100 | 150 | 200 | 400 |
| $(\pi/2)\upsilon_A$ (ns) | 10 | 12 | 12 | 12 | 10 | 10 |
| $(\pi)\upsilon_A$ (ns) | 20 | 24 | 24 | 24 | 20 | 20 |
| $(\pi)\ \upsilon_B$ | 82 ns 200 MHz chirp | 82 ns 200 MHz chirp | 82 ns 200 MHz chirp | 82 ns 200 MHz chirp | 82 ns 200 MHz chirp | 82 ns 200 MHz chirp |
| $\tau$ | 600 | 600 | 600 | 600 | 600 | 600 |
| T | 7400 | 7400 | 7400 | 7400 | 7400 | 7400 |
| $\Delta t$ | 20 | 20 | 20 | 20 | 20 | 20 |
| SRT (ms) | 1.5 | 1.5 | 1.5 | 1.5 | 1.5 | 1.5 |
| Shots per point | 20 | 20 | 20 | 20 | 20 | 20 |
| No. of averages [a] | 44; 64; 36 | 36; 35; 36 | 43; 37; 33 | 57; 41; 36 | 40; 70; 31 | 33; 42; 36 |
| Modulation depth % | 2.3 | 2.7 | 2.9 | 2.3 | 2.4 | 2.5 |
| SNR [b] | 51 | 61 | 56 | 53 | 58 | 60 |

**Table 3-3.** DEER acquisition parameters, modulation depths and SNR for biological and technical repeats of dHis-Cu(II)-NTA labeled K211H/E215H hGSTA1-1 in the ligand-free state. [a] For dHis-Cu(II)-NTA labeled hGSTA1-1, we performed Q-band DEER experiments at three optimally-positioned magnetic fields that were identified in previous work. Thus, we provide the number of averages at each of the three fields, from lower to higher field. [b] SNR was calculated with respect to the modulation depth and automatically determined by ComparativeDeerAnalyzer.

| | dHis-Cu(II)-NTA labeled K211H/E215H | | |
|---|---|---|---|
| [hGSTA1-1] [$\mu$M] | 100 | 400 | 400 |
| $(\pi/2)\upsilon_A$ (ns) | 10 | 14 | 14 |
| $(\pi)\upsilon_A$ (ns) | 20 | 28 | 28 |
| $(\pi)\ \upsilon_B$ | 100 ns 200 MHz chirp | 250 ns 200 MHz chirp | 82 ns 100MHz chirp |
| $\tau$ | 600 | 600 | 400 |
| T | 7800 | 7400 | 7200 |
| $\Delta t$ | 20 | 30 | 20 |
| SRT (ms) | 1.5 | 1.5 | 1.5 |
| Shots per point | 20 | 20 | 20 |
| No. of averages [a] | 11; 29; 15 | 55; 16; 9 | 29; 14; 10 |
| Modulation depth % | 2.2 | 7.6 | 3.7 |
| SNR [b] | 20 | 77 | 60 |

### 3.2.4 Conventional molecular dynamics simulations

As initial explorations of hGSTA1-1 dynamics, both in its ligand-free state and bound states with one or two GSHex ligands present, we performed five 1 μs conventional molecular dynamics (cMD) simulations of each system. Heavy-atom (all atoms except hydrogen) coordinates for the protein were extracted from the GSHex-bound hGSTA1-1 crystal structure (PDB:1K3L)[213]. The Reduce algorithm, as implemented in MolProbity,[326] was used to correct Asn/Gln/His flips in the X-ray protein structure and the LeAP module of the AMBER software was used to protonate each titratable residue for neutral pH. Residues Lys211 and Glu215 were mutated to histidine residues, followed by aligning the dHis-Cu(II)-NTA complex to the dHis sites. Proper bonds were then added between the aligned dHis-Cu(II)-NTA and protein backbone to form the dHis-Cu(II)-NTA labeled hGSTA1-1. GAFF2 force field parameters[147] were used for the dHis-Cu(II)-NTA spin label, as previously developed,[139] and for the GSHex ligand.

Each dHis-Cu(II)-NTA labeled hGSTA1-1 system was solvated in a truncated octahedral water box with crystal waters retained. The AMBER ff19SB force field[144] was used along with the OPC water model.[327] The cMD simulations were performed using the pmemd module of the AMBER20 software package. Sodium chloride was added to neutralize the charge.

Each system was first energy-minimized without any restraints over 2000 steps to relieve the unfavorable interactions. The energy minimized structures were gradually heated to 298 K in the NVT ensemble for 20 ps with restraints applied to all heavy atoms of the protein and ligands. The structures were subsequently equilibrated in the NPT ensemble for 1 ns using the Langevin thermostat with the same restraints on the solute. A 1-ns unrestrained equilibration in the NPT ensemble was then performed using the Monte-Carlo barostat (100 steps between volume change attempts) and a weak Langevin thermostat (collision frequency of 1 $ps^{-1}$) followed by the production simulations. To enable a 2 fs time step, all bonds to hydrogen were constrained to their equilibrium values using the SHAKE algorithm.[328] Short-range nonbonded interactions were truncated at 10 Å and long-range electrostatics interactions were treated using the particle mesh Ewald methods with periodic boundary conditions.

### 3.2.5 Weighted ensemble simulations

To enhance the conformational sampling of ligand-free GST, we performed weighted ensemble (WE) simulations starting from the crystal structure of hGSTA1-1 (PDB:1K3L)[213] with the ligand in each monomer removed. The resulting structure was then solvated and equilibrated per the procedure in the preceding section before beginning WE. Unlike the cMD simulations, WE simulations focus computing power on simulating transitions between stable states rather than the stable states themselves.[309] All WE simulations were performed with the open-source WESTPA 2.0 software package.[329] WE sampling typically involves partitioning a progress coordinate into bins, followed by running multiple, short trajectories in parallel. At fixed time intervals, a resampling procedure is applied which either replicates or terminates trajectories to give a target number of trajectories per bin. During this resampling procedure, trajectory weights, which are assigned at the start of the WE simulation, are rigorously tracked such that all the weights sum to one at any given time during the simulation. For simulations starting from both $\alpha 9$ helices localized over the binding site, we employed a one-dimensional progress coordinate consisting of the sum of the heavy-atom (all atoms except hydrogen) RMSD of both $\alpha 9$ helices (one from each monomer) after alignment on the rest of the protein dimer. To construct this coordinate, the main body of protein dimer (i.e., the grey parts of the protein in Figure 3-1A) was aligned, and the RMSD of the $\alpha 9$ helices were calculated. The more the deviation of the helix from its initial position the greater is the RMSD. This RMSD metric will be referred to as $\alpha 9_X$ RMSD, where X is either A or B for the two monomers. Thus, the one-dimensional coordinate used in this case was

$\alpha 9_A$ RMSD + $\alpha 9_B$ RMSD. For the WE simulations starting from one helix delocalized, our one-dimensional progress coordinate consisted of the $\alpha 9_X$ RMSD of *only* the helix still localized over the binding site. The minimal adaptive binning (MAB) scheme[330] was used with five evenly spaced bins between the trailing and leading trajectories; as typically done with this scheme, trailing and leading trajectories as well as a bottleneck trajectory[330] in the direction of increasing RMSD were each assigned to their own bins. A resampling time interval of 50 ps was used to maintain a target number of 5 trajectories per bin. A total of three independent WE simulations were run.

To monitor any change in structure of the individual $\alpha 9$ helices, we calculated the heavy-atom RMSD of each α9 helix after alignment on its starting structure. Thus, any change in helical structure would result in an increase in RMSD. We refer to this RMSD metric as the helicity metric in the remainder of this manuscript.

## 3.3 Results and discussion

In this work, we used a combination of DEER experiments and weighted ensemble MD simulations to resolve the conformational ensemble of the ligand-free hGSTA1-1 enzyme at the atomic level. The EPR experiments focused on a Lys211His/Glu215His mutant of the enzyme, and this double histidine (dHis) site was labeled with the Cu(II)-nitrilotriacetic acid (NTA) complex. The Lys211His and Glu215His mutations are in the α9 helix and do not perturb enzyme activity as shown in previous work.[243] Given that hGSTA1-1 is a homodimer, there are two spin labeling sites, one in each monomer. The weighted ensemble MD simulations focused on the wild-type enzyme.

To verify that the Cu(II)-NTA label binds specifically to the dHis sites of hGSTA1-1, we first performed continuous wave (CW)-EPR and ESEEM experiments. CW-EPR is sensitive to the directly coordinated atoms, especially the equatorially coordinated nitrogen and oxygen atoms of histidine residues shown in Figure 3-4. Figure 3-4B shows that in the presence of different GSHex concentration, the CW-EPR lineshape and intensity stay the same. The $g_{\parallel}$ and $A_{\parallel}$ values are consistent with equatorial coordination from multiple N atoms,[331] which supports the conclusion of Cu(II) binding to dHis and NTA nitrogen atoms. Next ESEEM experiments were conducted to probe the coordination of the complex to the dHis site. ESEEM experiments are sensitive to nuclear coordination at 3-8 Å away from the unpaired electron of the spin label. In our case, the ESEEM experiments measure the hyperfine interactions between the electron spin and the imidazole nitrogen atoms that are not directly coordinated to the Cu(II), as highlighted in Figure 3-5. The time-domain ESEEM signals for all samples are shown in Figure 3-5A, with the same modulations appearing in each sample at different GSHex concentrations. The corresponding ESEEM spectra show characteristic peaks located around 0.5 MHz, 1.0 MHz, 1.5 MHz and 4 MHz that are due to the imidazole nitrogens highlighted in the inset.[107,332–335] Based on the CW-EPR and ESEEM experiments, we confirmed the specific binding of Cu(II)-NTA to only the dHis sites of hGSTA1-1, rather than any other histidine residues or protein backbone.

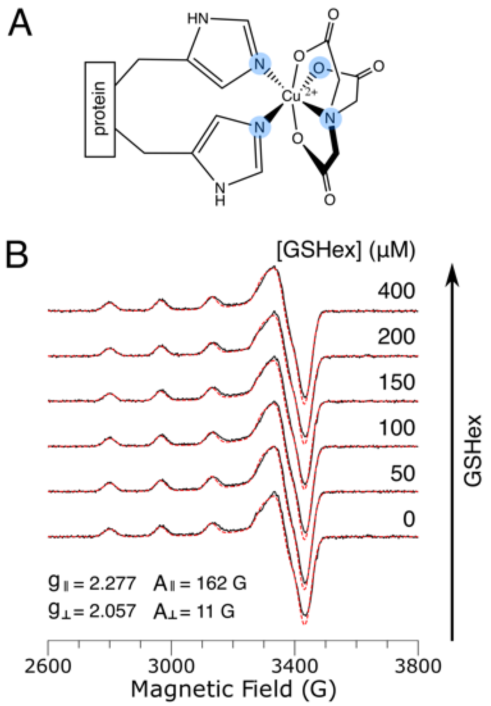

**Figure 3-4.** 80 K CW-EPR spectra at X-band for dHis-Cu(II)-NTA bound hGSTA1-1 with different concentrations of GSHex ligand present. The concentration of hGSTA1-1 for all samples is 100 μM. (A) CW-EPR is sensitive to the direct coordination environment of Cu(II), especially the atoms coordinated equatorially (highlighted in blue) to the Cu(II) center, which includes histidine and NTA nitrogen atoms and NTA oxygen atom. (B) With different amount of GSHex present, the CW-EPR spectra is unchanged (solid, black line). The CW-EPR spectra show a single component fit, with with $\boldsymbol{g}_{\parallel} = \mathbf{2.277}$, $\boldsymbol{A}_{\parallel} = \mathbf{162}\ \boldsymbol{G}$, $\boldsymbol{g}_{\perp} = \mathbf{2.057}$, and $\boldsymbol{A}_{\perp} = \mathbf{11}\ \boldsymbol{G}$ overlaid (red dashed line). The $\boldsymbol{g}_{\parallel}$ and $\boldsymbol{A}_{\parallel}$ values are consistent with multiple nitrogen atoms coordinating to Cu(II) shown in (A).

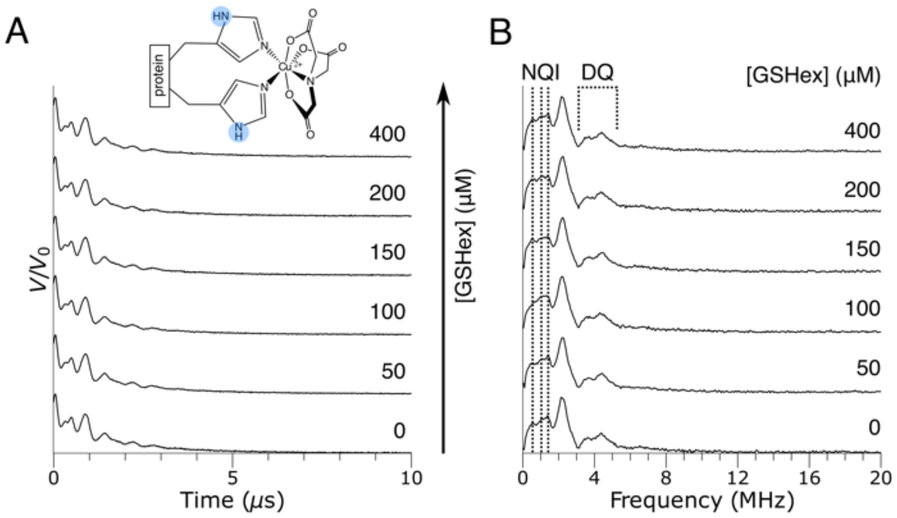

**Figure 3-5.** X-band ESEEM spectra for dHis-Cu(II)-NTA bound hGSTA1-1 with different concentrations of GSHex ligand present. The concentration of hGSTA1-1 for all samples is 100 μM. (A) Time-domain ESEEM signals for each sample with corresponding ligand concentrations. ESEEM is sensitive to the nuclear spin of atoms within 3-8 Å (highlighted in blue in the inset) of the EPR-active species, Cu(II) in our case. The ESEEM experiments are performed in the H blind spot, thus signals from H are minimized. (B) Fourier-transformed ESEEM spectra for each ratio of GSHex to hGSTA1-1 monomer. Characteristic peaks shown in each sample located around 0.5, 1.0, 1.5, indicated by three dotted vertical lines labeled as NQI (nuclear quadrupole interaction), and 4 MHz, labeled as DQ (double quantum), suggest proper coordination of imidazole nitrogen to Cu(II). The peak around 2 MHz appears due to the presence of deuterium in the solvent.

### 3.3.1 EPR distance distributions reveal an alternate ligand-free state

To characterize the conformational ensemble of the ligand-free hGSTA1-1 protein and any metastable states that result upon binding the GSHex substrate ligand, we performed a series of DEER experiments on the labeled hGSTA1-1 samples. Each sample was titrated with different hGSTA1-1:GSHex concentration ratios. For these experiments, the samples contained 100 $\mu$M hGSTA1-1 and a GSHex concentration of 0 $\mu$M, 50 $\mu$M, 100 $\mu$M, 150 $\mu$M, 200 $\mu$M and 400 $\mu$M.

Note that a GSHex concentration of 200 $\mu$M nominally corresponds to a fully loaded protein with two GSHex available for the two binding sites, one in each monomer. For each sample, the specific binding of Cu(II)-NTA to dHis sites was verified by continuous wave (CW)-EPR and electron spin echo envelope modulation (ESEEM)[318,319] experiments. These results are shown in Figures 3-4 and 3-5.

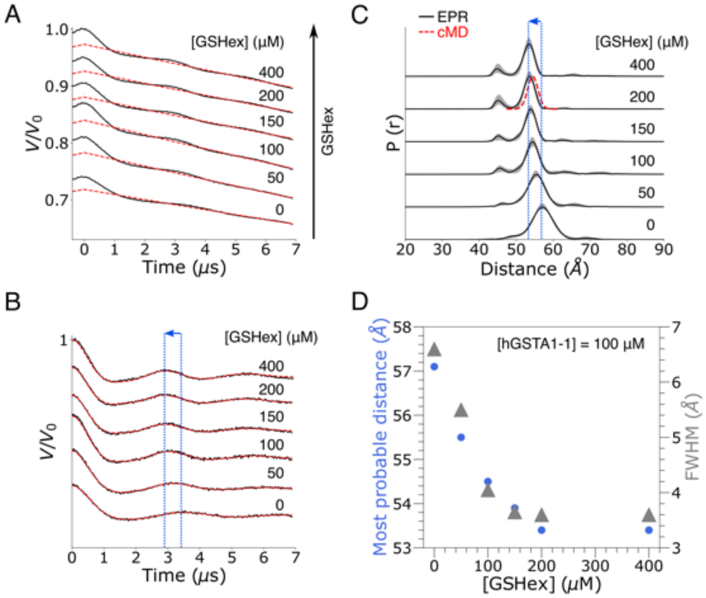

**Figure 3-6.** Q-band DEER results for dHis-Cu(II)-NTA bound hGSTA1-1 with different concentrations of GSHex ligand. hGSTA1-1 concentration is 100 µM. (A) The solid, black curves show the primary DEER time-domain signals with increasing amount of GSHex ligand. The background signal is shown as dashed, red curves. The DEER signals were collected and averaged over three optimally positioned magnetic fields to account for all possible orientations of the hGSTA1-1 dimer. (B) The black curves show the background-subtracted DEER time trace corresponding to (A), with the Tikhonov fit shown using red dashed lines. The modulation periods shorten with GSHex concentration, as indicated by the arrow between the two vertical lines, and plateaus once one equivalent of GSHex is added. (C) Resulting distance distribution at each GSHex concentrations. The uncertainty is shaded in grey. With more ligand present, the most probable distance shifts from ~57.1 Å to ~53.4 Å, and the full width at half maximum (FWHM) decreases from ~6.7 Å to ~3.6 Å. Based on the GSHex-bound crystal structure (PDB:1K3L), the expected Cu(II)-Cu(II) distance is 53.6 Å. For direct comparison, the cMD sampled Cu(II)-Cu(II) distance distribution in the GSHex-

bound form is plotted as red dashed line. (D) The trend in the most probable distance, shown as blue dots, and FWMH values, shown as grey triangles, at each GSHex concentration.

Next, DEER experiments were performed to measure the Cu(II)-Cu(II) distance distribution. The primary DEER time-domain signals are presented as black solid lines in Figure 3-6. The primary DEER signal for each sample was performed at Q-band frequency (~34 GHz) and averaged over measurements at three optimal magnetic fields. The averaged DEER time-domain signal properly accounts for all molecular orientations and thus mitigates negative effects of orientational selectivity normally observed for measurements at Q-band.[323] The background subtracted DEER signals are shown in Figure 3-6B. The signals, even in the complete absence of ligand, show clear modulations. Thus, we can conclude that $\alpha$9 helix in the ligand-free hGSTA1-1 is likely folded. With increasing GSHex concentration from 0 to 200 $\mu$M, the modulation period shifted from 3.4 $\mu s$ to 2.9 $\mu s$, which indicates that the most probable Cu(II)-Cu(II) distance decreased as more GSHex was added. The modulation of the DEER signals also became more resolved with the addition of GSHex ligand, indicating a narrowing of the distance distribution.

To extract the distance distributions, we applied the comparative DEER analyzer (CDA)[336,337] to the time traces. The resulting distributions are shown in Figure 3-6C. In the ligand-free state, a broad EPR distance distribution that ranges from ca. 45 Å – 65 Å is observed, which suggests that the $\alpha$9 helix samples a wide range of conformations. With increasing GSHex ligand concentration, the distribution narrows, and the most probable distance shifts to lower distances. The most probable distance shows a maximum decrease of around 4 Å, as function of added GSHex ligand. This result indicates there is a subtle, yet noticeable difference in the most probable arrangement of the $\alpha$9 helix in the ligand-free state versus the ligand-bound states.

We observed a gradual (non-discrete) shift and narrowing of the distance distribution with increasing GSHex ligand concentration (Figures 3-6C-D). In particular, the most probable distance and full width at half maximum (FWHM) decreased significantly with increasing ligand concentration up to 100 $\mu$M at which point only half of the possible binding sites are occupied. Beyond this concentration and up to 200 $\mu$M, the most probable distance and FWHM continued to decrease, but more slowly. Although the shift and narrowing of the distance distribution was observed with increasing ligand concentration, the modulation depth across all samples remained mostly the same ($2.5\pm0.4$ %).

To further explore the conformational changes of the hGSTA1-1 enzyme in the presence of different product ligands, we prepared hGSTA1-1 with ethacrynic acid glutathione conjugate (EASG) and S-(2,4-dinitrophenyl)glutathione (GS-DNB). Such experiments are important given the high substrate promiscuity of hGSTA1-1. The Cu(II)-NTA loading for these samples were verified through CW-EPR and ESEEM experiments detailed in the Figure 3-7. The primary DEER signals are shown in Figure 3-8. Interestingly, we observed similar distance distributions between Cu(II)-NTA labels in the GS-DNB- and GSHex-bound samples; in the EASG-bound sample, the distribution was broader with a longer, most probable distance (Figure 3-9). The EASG is a larger ligand compared to GS-DNB and GSHex, which brings the two $\alpha$9 helices to a more open state as suggested in previous work.[214,295,338] The variation in the EPR distance distributions among these ligands provides us with further evidence that the $\alpha$9 helices in hGSTA1-1 populate a broad range of conformations, and the relative positions of the two $\alpha$9 helices are different in the ligand bound versus the ligand-free states. Furthermore, they suggest that conformational sampling is relatively independent of the nature of the glutathione adduct for this enzyme.

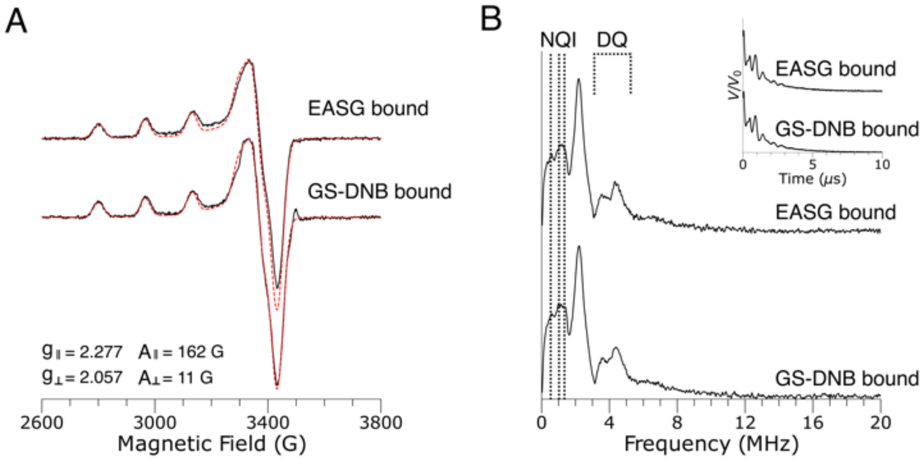

**Figure 3-7.** 80 K CW-EPR and ESEEM spectra at X-band for dHis-Cu(II)-NTA bound hGSTA1-1 with binding sites saturated with 1 mM of different ligands, namely ethacrynic acid glutathione conjugate (EASG) and S-(2,4-dinitrophenyl)glutathione (GS-DNB). (A) The CW-EPR spectra for each ligand bound sample show a single component fit, with $\boldsymbol{g_{\parallel} = 2.277}$, $\boldsymbol{A_{\parallel} = 162\ G}$, $\boldsymbol{g_{\perp} = 2.057}$, and $\boldsymbol{A_{\perp} = 11\ G}$ overlaid (red dashed line). The $\boldsymbol{g_{\parallel}}$ and $\boldsymbol{A_{\parallel}}$ values are consistent with multiple nitrogen atoms coordinating to Cu(II). (B) Fourier-transformed ESEEM spectra for EASG bound and GS-DNB bound hGSTA1-1. Characteristic peaks shown in each sample located below 2MHz, indicated by three dotted vertical lines and labeled as NQI (nuclear quadrupole interaction) and ~4 MHz, labeled as DQ (double quantum), suggest proper coordination of imidazole nitrogen to Cu(II). The peak around 2 MHz appears due to the presence of deuterium in the solvent. The inset shows the time-domain ESEEM signals for both samples.

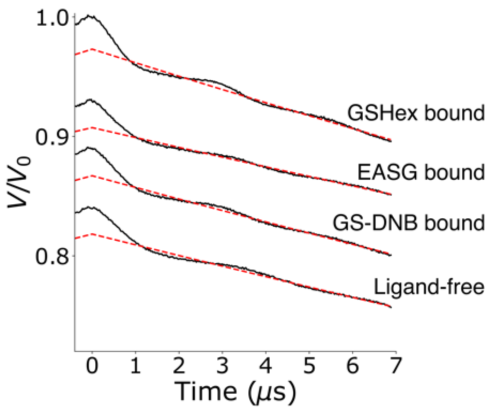

**Figure 3-8.** Comparison of Q-band DEER time-domain signals for dHis-Cu(II)-NTA bound hGSTA1-1 without and with different ligand present. The solid, black curves show the primary DEER time-domain signals with different

ligand present and without ligand. The background signal is shown as dashed, red curves. The DEER signals were collected and averaged over three optimally positioned magnetic fields to account for all possible orientations of the hGSTA1-1 dimer.[323]

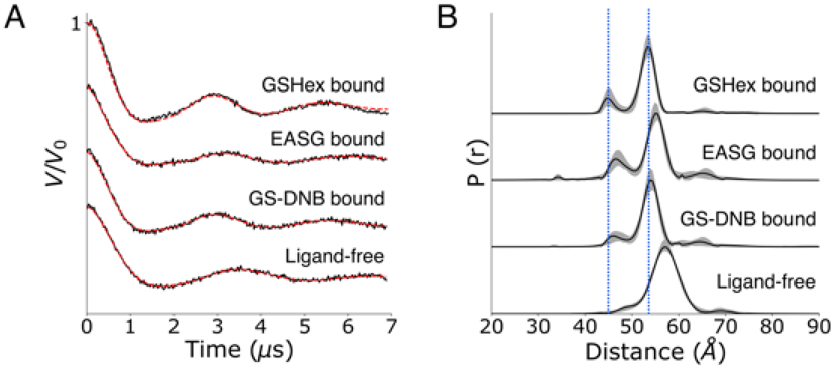

**Figure 3-9.** Comparison of Q-band DEER results for dHis-Cu(II)-NTA bound hGSTA1-1 without and with different ligands. The black curves show the background-subtracted DEER time traces. The Tikhonov fit is shown by red lines. The EASG and GS-DNB bound samples contained five equivalents of ligand per hGSTA1-1 monomer to ensure ligand saturation of the binding sites. (B) The resulting distance distributions analyzed by DEERAnalysis21. The most probable distances of the major and minor distance populations for GSHex bound sample are labeled with vertical lines to aid comparison.

A minor peak in the distance distributions between 45 Å and 50 Å appeared across all ligand-bound samples. For the GSHex bound sample this peak occurs at ~45 Å and is labeled with a blue vertical line in Figure 3-9B. The peak differs in the most probable distance for the EASG and GS-DNB bound samples. This peak is not due to orientational artifact, as we performed DEER experiments at three carefully chosen magnetic fields that properly samples all molecular orientations. Previous work on this protein has shown averaging DEER measurements over up to 10 magnetic fields did not show difference in the time-domain signal and the resulting distance distribution.[323] In addition, this minor peak is not likely to result from Cu(II)-NTA binding elsewhere in the protein. First, we observed a single component in the CW-EPR spectra. Further, the ESEEM data on Lys211His/Glu215His show only His-coordination. Second, although there are three native histidine residues, they are buried. Further, CW-EPR and ESEEM experiments on WT protein suggest that Cu(II)-NTA does not bind to any native histidine residues of wild-type (WT) hGSTA1-1. These data are shown in Figure 3-10. Thus, the distance around 45 Å is likely due to a different conformational state of ligand-bound hGSTA1-1. Similar populations between the two major distances were also observed for different ligand-bound hGSTA1-1, shown in Figure 3-9.

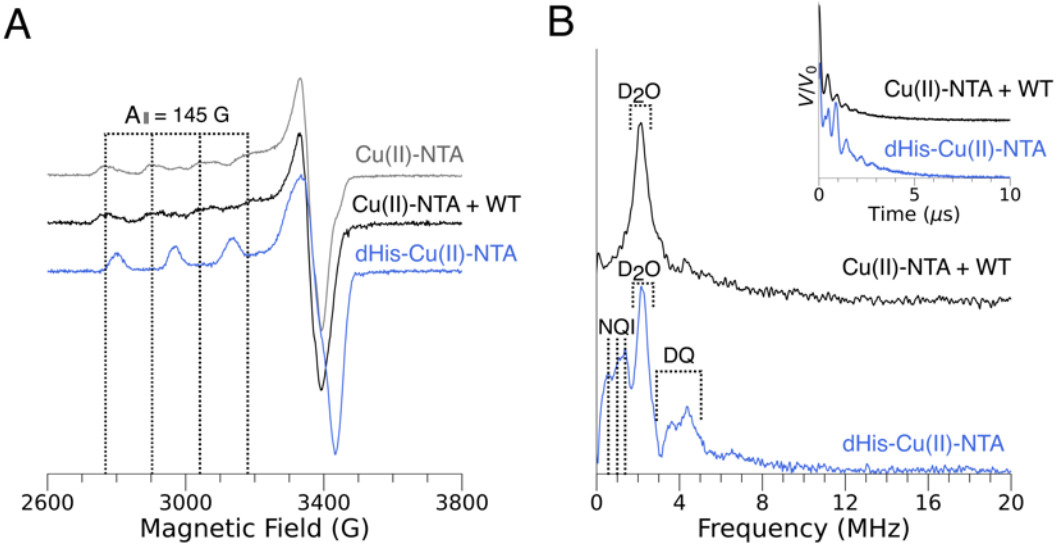

**Figure 3-10.** Detecting native binding sites of Cu(II)-NTA. (A) Top grey trace shows 80 K CW-EPR spectrum at X-band for free 100 $\mu$M dHis-Cu(II)-NTA in 3-N-morpholinopropanesulfonic acid (MOPS) buffer (pH=7.4, 50 mM MOPS, 100 mM NaCl in $D_2O$). 40% (v/v) $D_6$-glycerol was added to the sample as cryoprotectant. The black trace shows CW-EPR spectrum for 100 $\mu$M Cu(II)-NTA with 50 $\mu$M wild-type (WT) hGSTA1-1 CW-EPR spectra. No significant spectral difference between the free Cu(II)-NTA and Cu(II)-NTA with WT hGSTA1-1 is observed. The value of $A_{\parallel}$ (~145 G) is indicated by the dashed lines. This value is significantly different from the dHis-Cu(II)-NTA data obtained on the Lys211His/Glu215His protein mutant shown in blue. (B) ESEEM spectrum (black curve) for Cu(II)-NTA in the presence of WT hGSTA1-1. The peak around 2 MHz appears due to the presence of deuterium in

the solvent. The dHis-Cu(II)-NTA ESEEM spectrum is shown in blue as a comparison. Characteristic peaks shown in the dHis-Cu(II)-NTA sample locate below 2 MHz, indicated by three dotted vertical lines and labeled as NQI (nuclear quadrupole interaction) and ~4 MHz, labeled as DQ (double quantum), are missing for the WT hGSTA1-1 sample. The absence of the NQI and DQ peaks in the WT hGSTA1-1 sample suggest that Cu(II)-NTA does not bind to any native histidine. The inset shows the time-domain ESEEM signal. Both the CW-EPR and the ESEEM results suggest that Cu(II)-NTA does not bind to native histidine residues of hGSTA1-1, but only to the dHis sites.

### 3.3.2 Conventional molecular dynamics simulations

To understand the induced flexibility and conformational change by the addition of GSHex to hGSTA1-1, we performed five independent 1 $\mu s$ conventional molecular dynamics simulations for each of three systems. Beginning with the hGSTA1-1 crystal structure[213] we constructed systems with 1) both GSHex ligands present, 2) one GSHex ligand removed and 3) both GSHex ligands removed. dHis-Cu(II)-NTA labels were introduced to the Lys211His/Glu215His of 9 helices of the model for reporting the Cu(II)-Cu(II) distance distributions.[139]

Based on our calculations of the root-mean-squared-fluctuation (RMSF) for each residue in the ligand-free enzyme (Figure 3-11), the flexibility of both monomers (Chains A and B) is indicated by slightly higher RMSF values than all other residues in the same chain. The RMSF values for the α9 helix around 1.3 to 2.6 Å for both monomers without ligand, shown in Figure 3-11. When a ligand molecule is bound to one of the monomers, the flexibility of the $\alpha$9 helix decreases, indicated by ~1.0 Å decrease in RMSF values. After both ligands are bound to both monomers, the flexibility of $\alpha$9 helix of both monomers is similar and more rigid than the conformation where ligands have been removed. The RMSF plots explain the flexibility reduction at $\alpha$9 helix due to the ligand present, which results in the narrowing of the distance distribution between the dHis-Cu(II)-NTA labeled sites.

Simulated Cu(II)-Cu(II) distance distributions are shown in Figure 3-6C and Figures 3-12 to 3-15. In the models of the dimeric enzyme with both GSHex ligands present, the distance distribution agrees with that from DEER experiments, as shown in Figure 3-6C. However, the most probable Cu(II)-Cu(II) distance in the ligand-free and one-ligand distribution show an opposite trend compared to experiments. In our cMD simulations, the most probable Cu(II)-Cu(II) distance increases in the presence of GSHex (Figure 3-16). However, the most probable distance determined by DEER experiments decreases as a function of ligand concentration, which is in contradiction to the trend observed in the cMD results. This discrepancy is due to the cMD simulations failing to access the unlocked state of the helix given that the ligand-induced conformational change in GSTs is on the seconds timescale.[215,216]

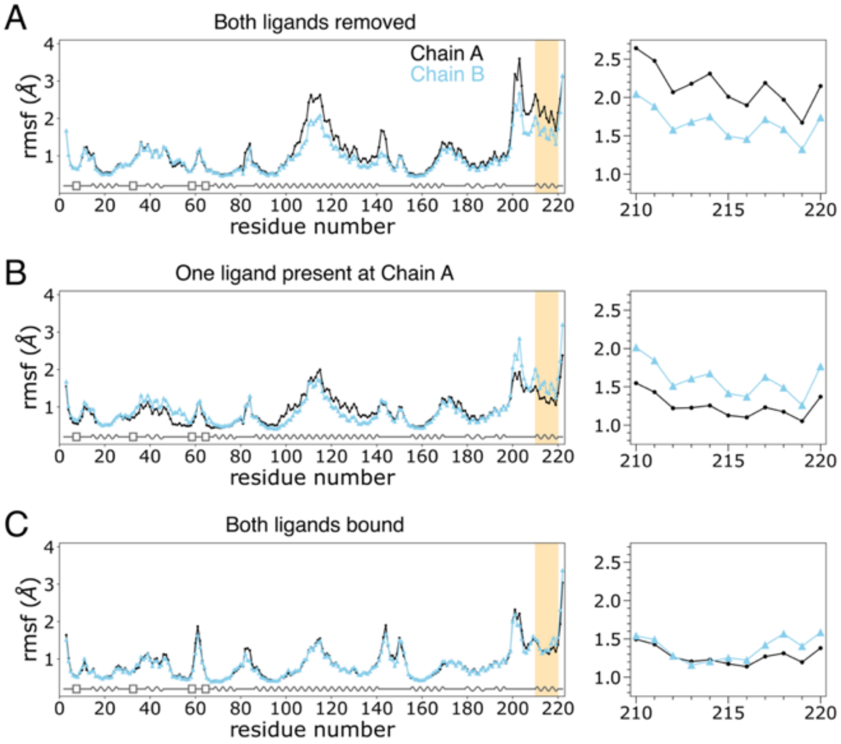

**Figure 3-11.** Root-Mean-Square Fluctuation (RMSF) of each residue in each of the two monomers of the dimeric hGSTA1-1 enzyme. Black curve represents chain A and blue curve represents chain B. (A) RMSF of ligand-free

hGSTA1-1. The $\alpha$9 helix is shaded in yellow and the region is showed with a truncated y-axis immediately to the right. The secondary structure of the protein is shown at the bottom of the plot. Oscillating lines represent $\alpha$-helices, boxes represent $\beta$-sheets, and straight lines represent flexible loops. (B) RMSF of hGSTA1-1 with one ligand added to chain A. (C) RMSF of hGSTA1-1 with both ligands bound. Both chains show similar value and trend in RMSF across all residues in free hGSTA1-1. When one ligand is bound to chain A, the RMSF of $\alpha$9 helix decreases with respect to chain B. With both ligands bound, RMSF is similar between the chains across all residues, with $\alpha$9 helix more rigid compared to the ligand-free form.

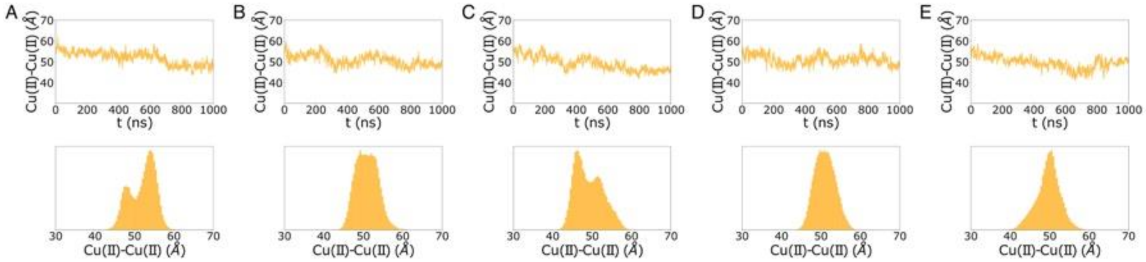

**Figure 3-12.** cMD sampled Cu(II)-Cu(II) distances with both ligands removed. (A-E) Five independent 1 $\mu$s cMD simulations for dHis-Cu(II)-NTA labeled hGSTA1-1 with both ligands removed. Top panel shows Cu(II)-Cu(II) distance, in orange, as a function of simulation time in nanoseconds. Bottom panel shows the histogram of Cu(II)-Cu(II) distances.

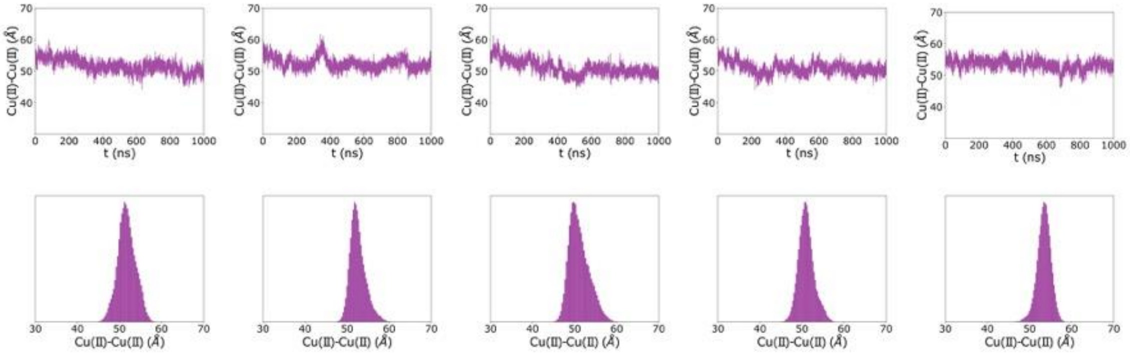

**Figure 3-13.** cMD sampled Cu(II)-Cu(II) distances with one ligand removed. (A-E) Five independent 1 $\mu$s cMD simulations for dHis-Cu(II)-NTA labeled hGSTA1-1 with one ligand removed from monomer A. Top panel shows

Cu(II)-Cu(II) distance, in purple, as a function of simulation time in nanoseconds. Bottom panel shows the histogram of Cu(II)-Cu(II) distances.

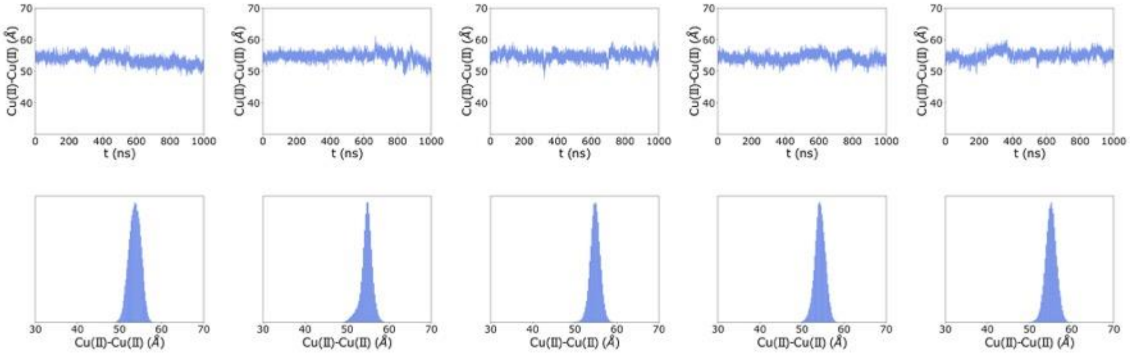

**Figure 3-14.** cMD sampled Cu(II)-Cu(II) distances with both ligand removed. (A-E) Five independent 1 $\mu$s cMD simulations for dHis-Cu(II)-NTA labeled hGSTA1-1 with both ligands present. Top panel shows Cu(II)-Cu(II) distance, in blue, as a function of simulation time in nanoseconds. Bottom panel shows the histogram of Cu(II)-Cu(II) distances.

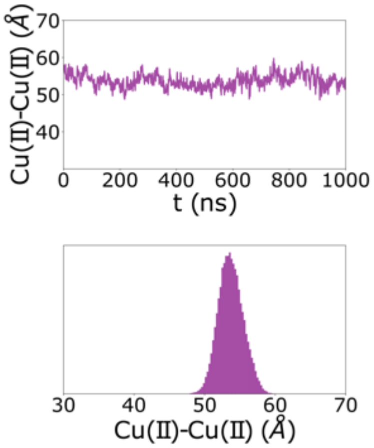

**Figure 3-15.** A single 1 $\mu$s cMD simulation for dHis-Cu(II)-NTA labeled hGSTA1-1 with the ligand from monomer B removed. Top panel shows Cu(II)-Cu(II) distance, in purple, as a function of simulation time in nanoseconds. Bottom panel shows the histogram of Cu(II)-Cu(II) distance. The Cu(II)-Cu(II) distance distribution is similar to that of hGSTA1-1 with the ligand removed from monomer A due to the protein being a homodimer.

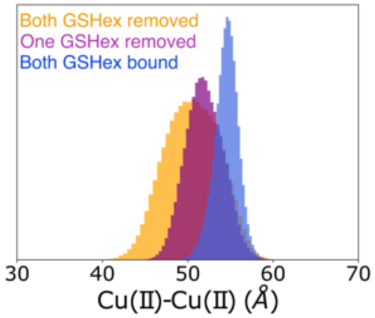

**Figure 3-16.** cMD sampled Cu(II)-Cu(II) distance distributions. The Cu(II)-Cu(II) distances were sampled from five simulations for ligand-free (orange), one GSHex-bound (purple), and both GSHex-bound hGSTA1-1 all starting from both GSHex-bound conformation. The most probable distance sampled by cMD for the ligand-free and one GSHex-bound hGSTA1-1 deviates from the EPR determined distances.

Although the cMD simulations show a similar trend in the flexibility change of $\alpha 9$ helices with the addition of ligands, the most probable Cu(II)-Cu(II) distances from cMD simulations of hGSTA1-1 with either one or both ligands removed do not agree with the EPR determined distances. In addition, the RMSF values reported above in Figure 3-11 for the C-terminal $\alpha 9$ helices with ligand removed are not as high as would be expected for a highly-dynamic termini of an enzyme. This may be due to the fact that the hGSTA1-1 structures used for cMD (where ligand was simply removed from the liganded, closed crystal structure of hGSTA1-1) are not the true ligand-free structures. If the transition from the closed to open state involves a large-scale conformational change on the seconds timescale,[215,216] such as the docking of the C-terminal $\alpha 9$ helices as is suggested in previous literature as part of a two-step mechanism, then our cMD simulations without ligand are likely still only sampling conformations in the closed conformational ensemble.

### 3.3.3 Weighted ensemble MD generates direct views of negative cooperativity in the ligand-free ensemble

We found that the conformational transition from the ligand bound to the ligand-free state is inaccessible to conventional molecular dynamics (cMD) simulations. These results, shown in Figure 3-6C and Figures 3-12 to 3-16, are unsurprising given that this transition is expected to occur on the seconds-timescale.[215,216] Therefore, we performed WE simulations to focus MD simulation time on the transition rather than the stable state. Based on our EPR results, we chose a one-dimensional progress coordinate consisting of the heavy-atom RMSD of both $\alpha 9$ helices after aligning the rest of the dimer in the crystal structure (PDB:1K3L; see Materials and methods). Continuous pathways from the ligand-bound to the ligand-free state were captured from our WE simulations. Figure 3-17A shows a scatter plot with the RMSD of $\alpha 9_A$ (x-axis) versus the RMSD of $\alpha 9_B$ (y-axis) during the course of the WE simulation. The color of each point represents the value of the helicity metric of $\alpha 9_B$ (see Materials and methods for how this metric is calculated).

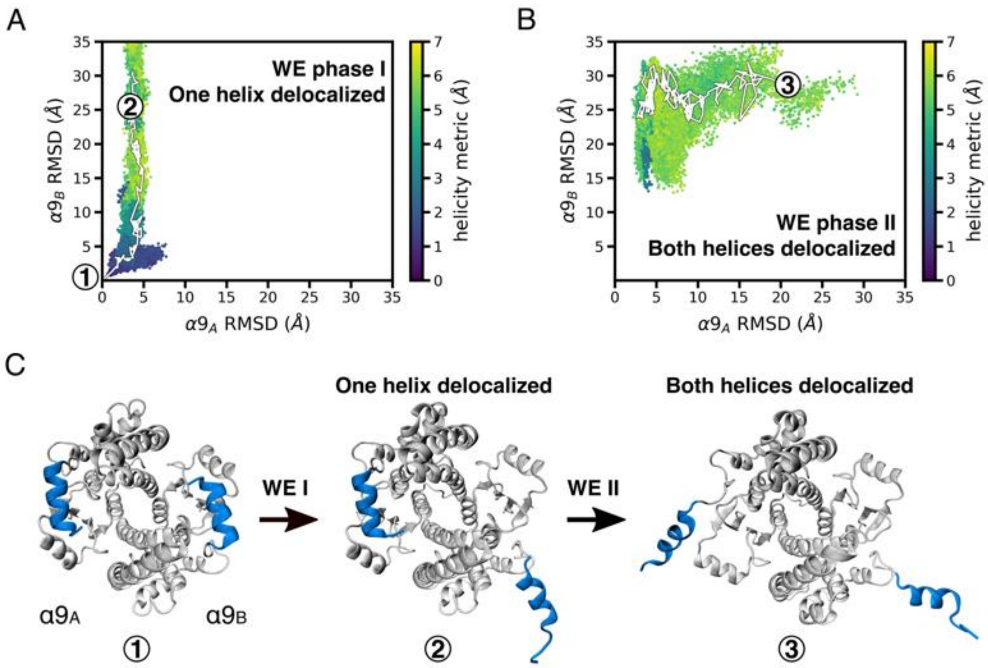

**Figure 3-17.** Combined EPR-weighted ensemble (WE) workflow was able to successfully generate atomically-detailed conformations of hGSTA1-1 in the ligand-free state. (A) A scatter plot of all conformations sampled during this WE simulation as a function of (i) the heavy atom RMSD of $\boldsymbol{\alpha 9_A}$ after aligning on the heavy atoms of the main body of the dimer, and (ii) the heavy atom RMSD of $\boldsymbol{\alpha 9_B}$ after aligning on the heavy atoms of the main body of the dimer. These RMSD metrics quantify the extent of delocalization for each helix. Each point in the scatter plot is colored according to a "helicity metric", i.e. the heavy atom RMSD of $\boldsymbol{\alpha 9_B}$ after aligning $\boldsymbol{\alpha 9_B}$ to the heavy atoms of its initial structure, which indicates the extent to which $\boldsymbol{\alpha 9_B}$ remains folded compared to its corresponding crystal structure conformation. In this first WE simulation, $\boldsymbol{\alpha 9_B}$ was folded and delocalized while $\boldsymbol{\alpha 9_A}$ did not delocalize to the same extent. A continuous pathway starting from the ligand-bound state (1) and ending in the ligand-free state (2) is traced as a white line. (B) Starting from the ligand-free state (2) in panel (A), where $\boldsymbol{\alpha 9_B}$ was delocalized, a second WE simulation was run leading to conformations in which $\boldsymbol{\alpha 9_A}$ also became delocalized. A scatter plot of all conformations generated during the second WE simulation is shown as a function of the same axes as the plot in panel (A) along with a continuous pathway leading to the delocalization of $\boldsymbol{\alpha 9_A}$ (3) traced as a white line. (C) Snapshots of hGSTA1-1 in the ligand-bound state (1), with only $\boldsymbol{\alpha 9_B}$ delocalized (2), and with both $\boldsymbol{\alpha 9_A}$ and $\boldsymbol{\alpha 9_B}$ delocalized (3) from our WE simulations, indicating a large extent of delocalization in the $\boldsymbol{\alpha}$9 helices (blue).

We found that the RMSD of one $\alpha9$ helix ($\alpha9_B$) increases dramatically which indicates that this helix is delocalized to a significant extent. In addition, the helicity metric value of $\alpha9_B$ remains relatively low (around 2 to 3 Å) for most snapshots, which suggests that the helix stays folded and helical as it becomes delocalized. Surprisingly, while $\alpha9_B$ delocalizes, the RMSD of the other helix ($\alpha9_A$) does not increase at all, which suggests that this helix does not delocalize. A representative pathway for the conformational transition is traced in white, shown in Figure 3-17A, ending in the conformation labeled with 2. The shape of the RMSD distribution was even more surprising given that the progress coordinate used during the WE simulation to guide our sampling took the RMSD of *both* helices into account at the same time and given the homodimeric nature of the protein. We expected to observe simultaneous increases in the RMSD value of both helices. Instead, the WE results suggest a mechanism in which the undocking of one helix ($\alpha9_B$) somehow prevents the undocking of the other (in this case, $\alpha9_A$). We also provide a movie of a continuous pathway from the WE simulation in which $\alpha9$ of monomer B ($\alpha9_B$) delocalized. The $\alpha9$ helix of each monomer is highlighted in blue. One of the $\alpha9$ helices ($\alpha9_B$) is undocked from the rest of the protein while the other ($\alpha9_A$) remains docked (Link: https://youtube.com/shorts/V6sBl0zN5kA).

Replicates of this WE simulation show the same behavior, as well as a WE simulation run with a two-dimensional progress coordinate consisting of the RMSD of each helix, providing further support to our claims of negative cooperativity (Figure 3-18).

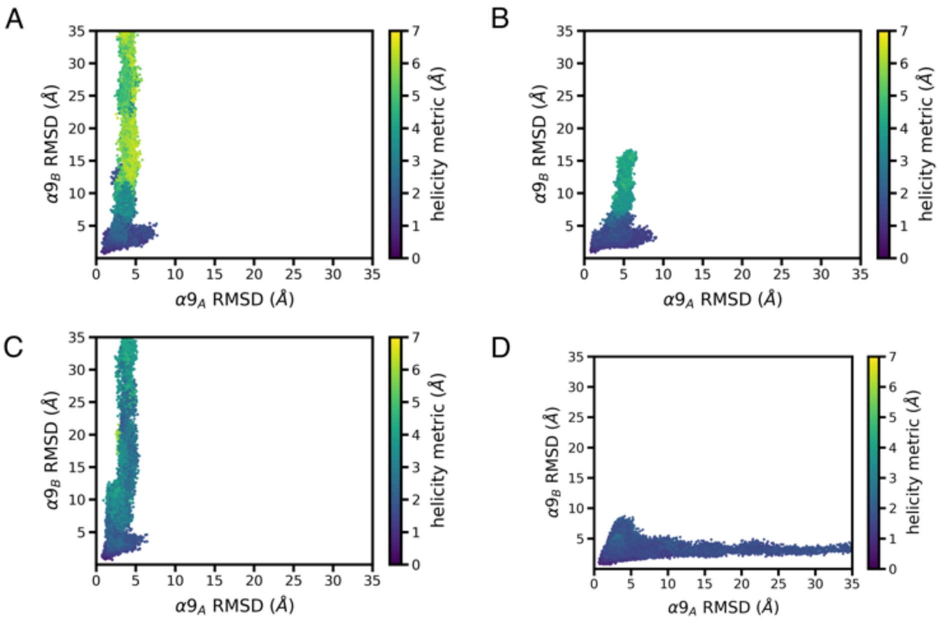

**Figure 3-18.** Replicates of WE simulations. (A-C) Scatter plots of all data from three replicates of WE-MD simulations run with a one-dimensional progress coordinate consisting of the sum of 1) the heavy atom RMSD of $\boldsymbol{\alpha}9_{\mathrm{A}}$ after aligning on the heavy atoms of the main body of the GST dimer and 2) the heavy atom RMSD of $\boldsymbol{\alpha}9_{\mathrm{B}}$ after aligning on the heavy atoms of the main body of the dimer. From these WE simulations, each with 1.5 $\boldsymbol{\mu s}$ of aggregate simulation time, only one helix delocalized while the other remained localized. (D) A scatter plot of all data from a WE-MD simulation run with a two-dimensional progress coordinate consisting of 1) the heavy atom RMSD of $\boldsymbol{\alpha}9_{\mathrm{A}}$ after aligning on the heavy atoms of the main body of the GST dimer and 2) the heavy atom RMSD of $\boldsymbol{\alpha}9_{\mathrm{B}}$ after aligning on the heavy atoms of the main body of the dimer. From this WE simulation with 2 $\boldsymbol{\mu s}$ of aggregate simulation time, only one helix delocalized. Scatter plots are colored according to a helicity metric consisting of the RMSD of $\boldsymbol{\alpha 9_B}$ after aligning $\boldsymbol{\alpha 9_B}$ to its initial structure. Together, the above data provides further support for negative cooperativity in the ligand-free hGSTA1-1 dimer.

To delocalize both $\alpha 9$ helices in the ligand-free hGSTA1-1 enzyme, we initiated a second WE simulation from a conformation in which one helix is delocalized (shown as 2 in Figure 3-17A). For efficiency, we used a one-dimensional progress coordinate in this WE simulation consisting of the heavy-atom RMSD of only the $\alpha 9$ helix that is still localized ($\alpha 9_A$) after aligning the rest of the dimer in the crystal structure. This strategy was able to successfully delocalize the second helix. The RMSD values of each $\alpha9$ helix for all trajectories from the second WE simulation are shown in Figure 3-17B. The coloring of each point here is consistent with Figure 3-17A. The need to apply a two-phase WE strategy suggests that once $\alpha9_B$ has been fully delocalized, only then does the RMSD of $\alpha9_A$ increase, a finding consistent with the first WE simulation. Atomically-detailed snapshot configurations from our WE simulation corresponding to the conformations of 1-3 in Figures 3-17A and 3-17B, are plotted in Figure 3-17C.

Taken together, the WE simulation results indicate that the helices delocalize, one at a time, during the conformational transition to the ligand-free state. In addition, based on the helicity metric, and as easily visualized in Figure 3-17C and the movie shown on YouTube, both α9 helices stay mostly folded (helical) during the delocalization process. This latter finding supports some earlier work[215,295,300,301] and confirms a picture of the ligand-free ensemble in which a fully- or partially-delocalized helix can interact with and potentially recruit ligands. Together, these results also demonstrate the remarkable potential of WE simulations to generate atomically detailed pathways for processes that occur on the seconds timescale. The first WE simulation generated 690 ns of total simulation time in 1.6 days using 16 NVIDIA A100 GPUs in parallel. The second WE simulation generated 309 ns of total simulation time in 16.8 hrs using 16 NVIDIA A100 GPUs in parallel.

Next, we verified that the conformations sampled from our WE simulations were stable states by selecting five conformations in which a <u>single</u> $\alpha9$ helix in monomer B ($\alpha9_B$) was delocalized and initiated a 1 $\mu$s cMD simulation from each conformation. The starting conformations are indicated by a star in Figure 3-19A. The distribution of all cMD-sampled conformations is plotted in Figure 3-19A as a function of the RMSD of each $\alpha9$ helix. Each scatter point is colored according to the internal RMSD (folded-ness) of $\alpha 9_B$. In all cMD simulations, both helices remain folded. Figure 3-19A reveals two populations: one in which a single $\alpha 9$ helix ($\alpha 9_B$) is only partly delocalized from its position in the ligand-bound crystal structure, and the other in which $\alpha 9_B$ is delocalized to a larger extent. This extent of helical delocalization in the ligand-free ensemble challenges previous speculation that both helices are completely delocalized.[215,295] Here, we found that only one of the $\alpha 9$ helices is partly or fully delocalized yet the other $\alpha 9$ is well restricted. The dynamic nature of hGSTA1-1 and other enzymes in general has been previously suggested to potentially enable promiscuity.[339] This statement is further supported by previous comparisons of the dynamics of hGSTA-1 and hGSTA4-4, which shows that the promiscuity is possibly enabled by conformational dynamics.[340] Thus, delocalization of the $\alpha 9$ helices may promote searching for substrates.

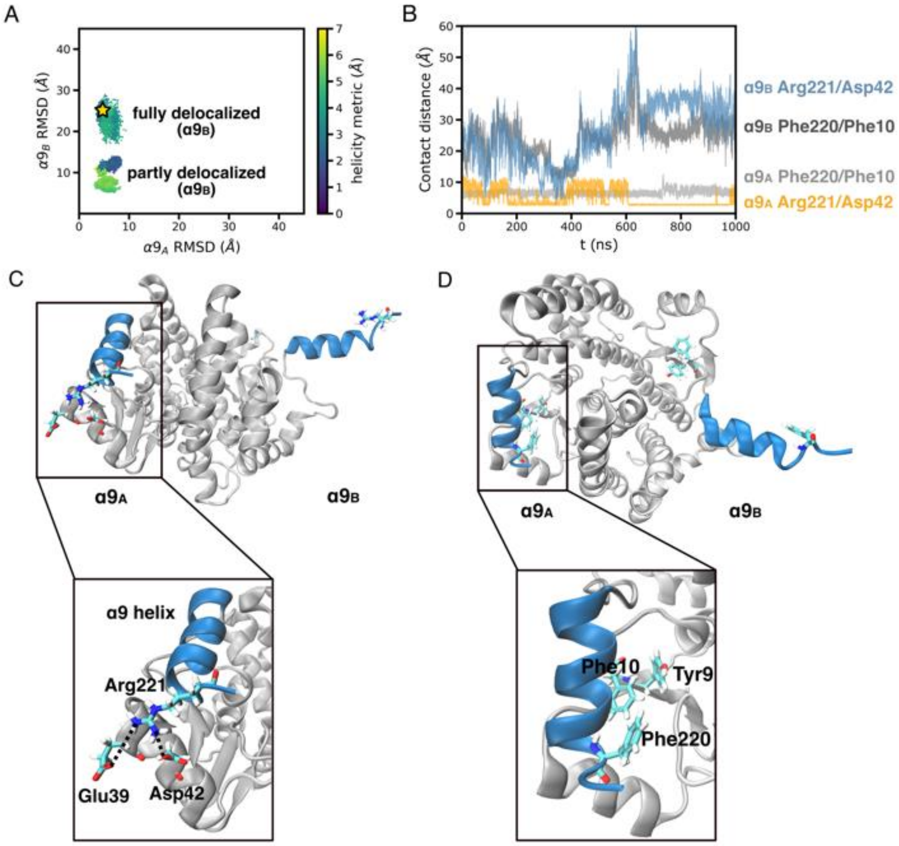

**Figure 3-19.** Conventional MD (cMD) simulations started from hGSTA1-1 conformations extracted from our WE simulations, confirm that we are sampling conformations within the ligand-free state. (A) All conformations sampled during the final 200 ns of 5 independent cMD simulations are plotted as a function of the heavy atom RMSD for each the two $\boldsymbol{\alpha}$9 helices after alignment on the heavy atoms of the main body of the dimer. Each cMD simulation was initiated from a hGSTA1-1 conformation sampled using WE (the gold star). The scatter points are colored according to the heavy atom RMSD (folded-ness) of the $\boldsymbol{\alpha}$9 helix of monomer B ($\boldsymbol{\alpha 9_B}$) after aligning this helix to the heavy atoms in its initial structure. (B) Time-evolution of contacts between key interacting residues at the interface and either $\boldsymbol{\alpha 9_A}$ or $\boldsymbol{\alpha 9_B}$ based on a simulation with only $\boldsymbol{\alpha 9_B}$ fully delocalized while $\boldsymbol{\alpha 9_A}$ localized. These contacts are highlighted in snapshots from the cMD simulations in (C) and (D).

To further investigate key interactions that control the delocalization of each $\alpha$9 helix and any cooperativity due to these interactions, we analyzed a charged residue and hydrophobic interaction at the interface between the $\alpha9$ helix and the rest of the protein. Previous studies have suggested the salt bridge[299] and hydrophobic interactions[295] as being important for the stabilization of $\alpha9$. However, the contribution of these interactions to the cooperativity between the monomers has not been discussed. Mutation of Phe220 to Ala or Thr has been shown to reduce the catalytic activity of hGSTA1-1.[295] In addition, mutation of a nearby residue of the Arg221/Asp42 bridge, Arg45 to Lys, has shown to decrease the catalytic activity of hGSTA1-1 towards CDNB. The authors concluded that the absence of the interaction between Arg45 and Arg42 may lead to the tightened salt bridge between Arg221/Asp42, which in turn may have resulted in the decrease in the catalytic activity against CDNB.[299] The Arg221/Asp42 salt bridge[299] and Phe220/Phe10/Tyr9 hydrophobic interactions[295], which have been reported in the literature, are prominently featured in the cMD simulations initiated from WE sampled conformations. The Arg221/Asp42 and Phe220/Phe10 distances of one such simulation are plotted versus simulation time in Figure 3-19B (and Figure 3-20).

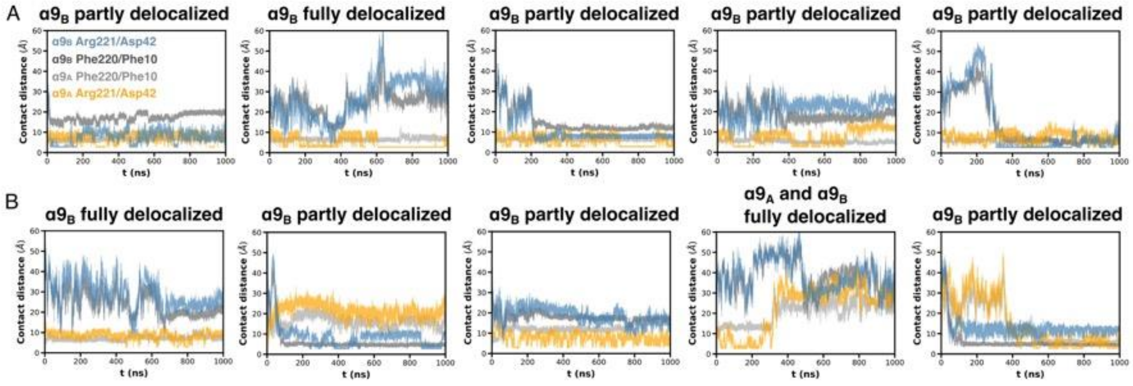

**Figure 3-20.** Salt-bridge interactions between Arg221 of the $\alpha9$ helix and Asp42, and hydrophobic interactions between Phe220 and Phe10. These interactions appear to play key roles in the negative cooperativity of $\alpha9$ motions within each monomer of the hGSTA1-1 homodimer. (A) Time-evolution of the contact distances between the interacting residues, sampled from all five of the cMD simulations starting from a conformation in which only one $\alpha9$ helix is delocalized, as sampled using a WE simulation. (B) The contact distance between the interacting residues,

sampled from all five of the cMD simulations starting from the WE-sampled structures where both $\boldsymbol{\alpha}9$ are fully delocalized, was plotted against simulation time.

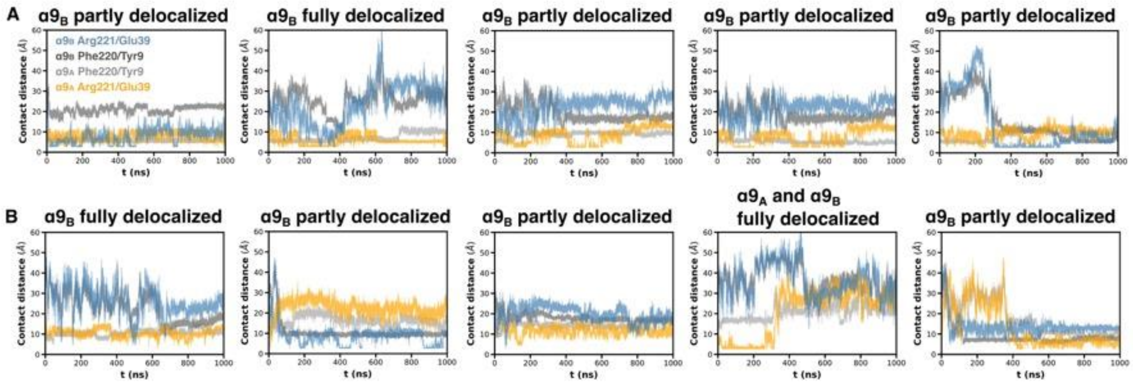

**Figure 3-21.** Salt-bridge interactions between Arg221 of the $\boldsymbol{\alpha}9$ helix and Glu39, and hydrophobic interactions between Phe220 and Tyr9. These interactions appear to play key roles in the negative cooperativity of $\boldsymbol{\alpha}9$ motions within each monomer of the hGSTA1-1 homodimer. (A) Time-evolution of the contact distances between the interacting residues, sampled from all five of the cMD simulations starting from a conformation in which only one $\boldsymbol{\alpha}9$ helix is delocalized, as sampled using a WE simulation. (B) The contact distance between the interacting residues, sampled from all five of the cMD simulations starting from a WE-sampled structures where both $\boldsymbol{\alpha}9$ are fully delocalized, was plotted as a function of simulation time.

While $\alpha 9_B$ is delocalized, the Arg221/Asp42 interaction of $\alpha 9_A$, shown as the orange trace, stabilizes around 2.7 Å. Similarly, shown in light grey and dark grey traces in Figures 3-19B and 3-21, the aromatic-aromatic residue interactions provide another handle to stabilize the $\alpha 9_A$ while $\alpha 9_B$ is being delocalized. The charge-charge and hydrophobic interactions we identified in cMD simulations are represented as snapshots in Figures 3-19C and 3-19D. Interestingly, when taking all five cMD simulations of WE sampled conformations, we do not observe both helical Arg221/Asp42 interactions forming concurrently. These mutually exclusive salt-bridge interactions among the two monomers suggests negative cooperativity between the monomers.

Additionally, we identified an additional, previously unreported salt-bridge interaction between Arg221/Glu39. These distances are shown in Figure 3-21. This additional salt bridge may further stabilize the $\alpha 9$ helix. The presence of these interactions likely leads to a ligand-free ensemble composed of many metastable states that are similar in energy, a known feature of the ligand-free ensemble of hGSTA1-1.[215,216] These findings are consistent with biochemical studies that suggest negative cooperativity in a subset of GSTs,[341,342] including A1-1, towards the toxic nitric oxide adduct, dinitrosyl-diglutathionyl iron (DNDGIC). In the case of some GSTs (GSTPi), the remaining active site remains catalytically functional, allowing the enzyme to both sequester DNDGIC in one site and continue to detoxify in the other active site. However, in the case of A1-1, binding of DNDGIC leads to inactivation of the remaining active site. The cooperativity observed here may explain the behavior of the A1-1 enzyme in response to DNDGIC binding, in that the α9 helix in the empty monomer cannot productively localize over the active site.

To determine the extent to which states with both helices delocalized (undocked) are stable, we returned to the WE simulations and selected five conformations in which *both* $\alpha 9$ helices ($\alpha 9_A$ and $\alpha 9_B$) were delocalized at the same time. The initial states are represented by a star in Figure 3-22A. From each of these five conformations, we initiated 1 $\mu$s cMD simulations (Figure 3-23). Most conformations sampled in these cMD simulations settled into the wells that are similar to the ones shown in Figure 3-19A in which *only* $\alpha 9_B$ (and not $\alpha 9_A$) is partly or fully delocalized. Interestingly, one of these cMD simulations revealed an additional population where both $\alpha 9$ helices remained fully delocalized from the crystal structure of the ligand-bound conformation. Figure 3-22B shows the charged-residue distance between Arg221 and Asp42 from one of the cMD simulations where $\alpha 9_B$ is in the partly delocalized state. The charge-charge interaction has formed on $\alpha 9_B$, but not formed for $\alpha 9_A$, which provides further evidence of some sort of cooperativity within the hGSTA1-1 dimer. Similarly, the hydrophobic interaction between Phe220 and Phe10 keeps $\alpha 9_B$ stable around the binding site.

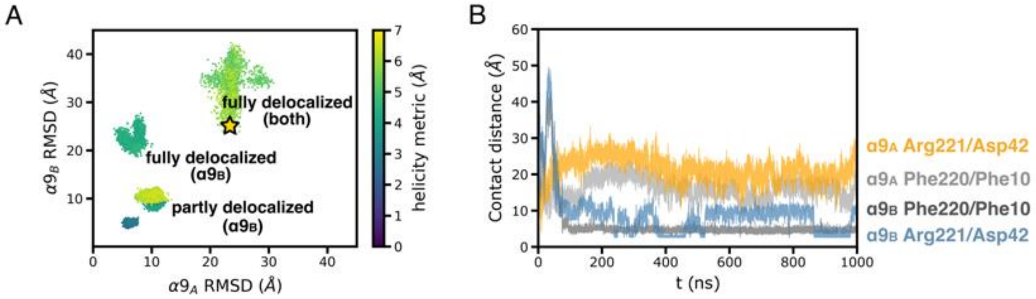

**Figure 3-22.** Additional conventional MD (cMD) simulations, started from hGSTA1-1 conformations extracted from our WE simulations in which both $\boldsymbol{\alpha}$9 helices were delocalized, further reveal the stable states of the ligand-free ensemble. (A) All conformations sampled during the final 200 ns of 5 independent cMD simulations are plotted as a function of the heavy atom RMSD values of each $\boldsymbol{\alpha}$9 helix after alignment on the heavy atoms of the main body of the dimer. The axes for this plot are the same as those in Figure 3-17A. We see much of the same stable conformations being formed during these cMD simulations, with the addition of a stable conformation in which both helices are delocalized to the same extent. The full 1 $\boldsymbol{\mu}$s traces of these simulations, including where each started and ended, are provided in Figure 3-23. (B) The key interactions between the $\boldsymbol{\alpha}$9 helix and protein were plotted versus simulation time. The charge-charge distance of Arg221/Asp42 between $\boldsymbol{\alpha 9_A}$ and protein is shown as an orange trace, and the corresponding interaction in $\boldsymbol{\alpha 9_B}$ is shown as a blue trace. The hydrophobic interactions between Phe220/Phe10 of $\boldsymbol{\alpha 9_A}$ are shown as a light grey trace and the corresponding interaction in $\boldsymbol{\alpha 9_B}$ is shown as a dark grey trace. The Arg221/Asp42 interaction stabilizes $\boldsymbol{\alpha 9_B}$ at a contact distance of around 2.7 Å, plotted as a blue trace. Meanwhile, the Phe220/Phe10 interaction seems to stabilize $\boldsymbol{\alpha 9_B}$, with a contact distance around 5 Å.

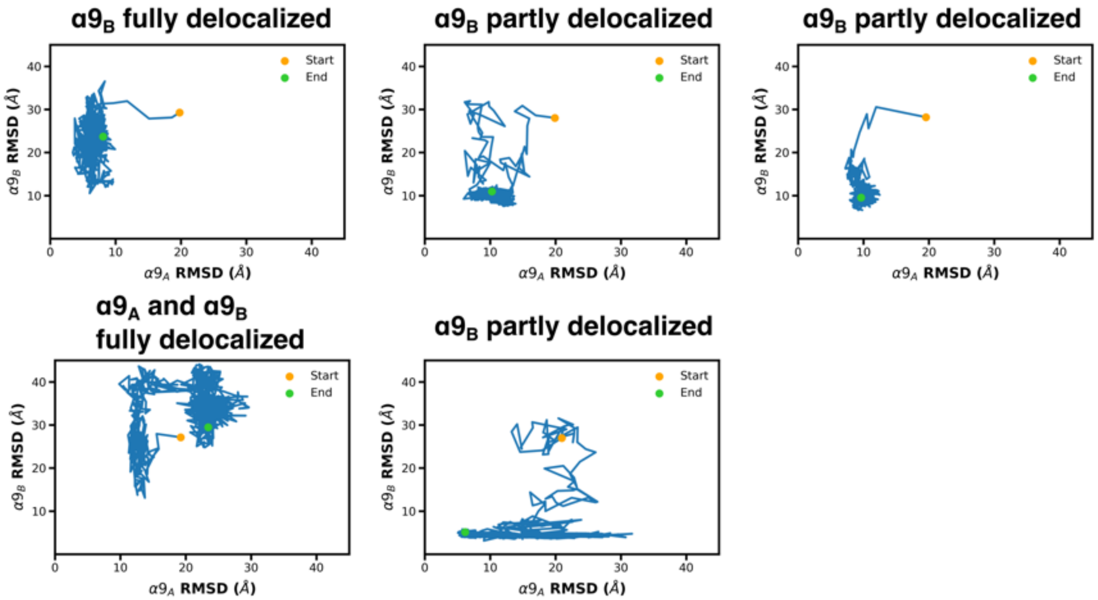

**Figure 3-23.** Traced trajectories for all five parallel cMD simulations starting from structures sampled from WE-MD simulation where both $\boldsymbol{\alpha}9$ helices are delocalized. Traces are projected onto a two dimensional space consisting of 1) the heavy atom RMSD of $\boldsymbol{\alpha}9_A$ after aligning on the heavy atoms of the main body of the GST dimer and 2) the heavy atom RMSD of $\boldsymbol{\alpha}9_B$ after aligning on the heavy atoms of the main body of the dimer.

Combining the observed trend in the EPR distance distributions with the WE-sampled ligand-free conformations, we can conclude that both $\alpha 9$ helices remain at least partially folded when delocalized (as evidenced by the relatively low values of the helicity metric of $\alpha 9_{A/B}$ compared to the corresponding values of the $\alpha 9_{A/B}$ RMSD values), and that only one helix delocalizes at a time. Shown in Figure 3-24, three populations of conformations best describe the ligand-free state: 1) one of the $\alpha 9$ helices remains localized while the other $\alpha 9$ helix is partly delocalized; 2) one of the $\alpha 9$ helices remains localized while the other one is completely delocalized; 3) a minor population with both of the $\alpha 9$ helices fully delocalized. The WE simulations portray a picture of the dominant mode in the ligand-free state consisting of one delocalized and mobile helix and one completely localized and immobile helix. The resulting

$C\beta$—$C\beta$, defined here as the center of mass between the $C\beta$ atoms of Lys211 and Glu215, distance distributions between $\alpha 9_A$ and $\alpha 9_B$ are shown in Figure 3-24C. The distribution in purple was sampled from a cMD simulation where only one $\alpha 9$ helix was fully delocalized, whereas the other distributions (in blue, red, gold and grey) were sampled from the cMD simulations where only one $\alpha 9$ helix was partly delocalized. The overall distribution is shown in cyan. This broad $C\beta$—$C\beta$ distribution corresponds well with the width of the EPR distance distribution, overlaid as a black curve and discussed above. This picture of controlled delocalization also rationalizes prior CW-EPR studies,[28,243] which have consistently shown two-component spectra with different dynamics for the protein. In addition, a previous crystal structure of the ligand-free hGSTA1-1 (PDB: 1PKZ) shows partial electron density at one of the $\alpha 9$ (residues 210 to 219), yet the other $\alpha 9$ helix is mostly unresolved in the diffraction data.[300] Such a scenario is consistent with a partly delocalized $\alpha 9$ helix such that only some residues are resolved in crystallography while the other helix is localized.

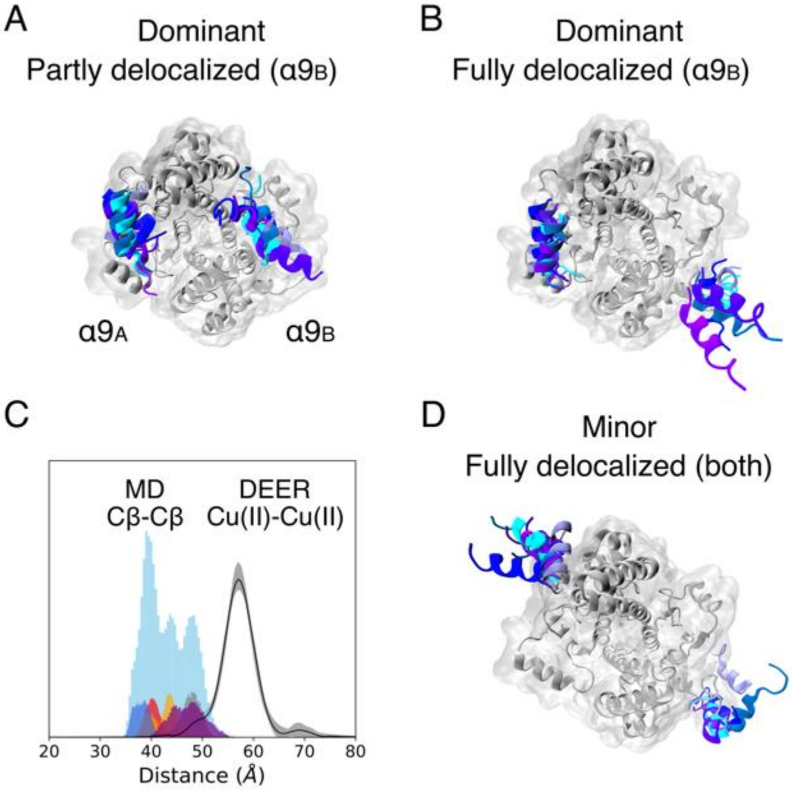

**Figure 3-24.** The WE-MD sampled ligand-free hGSTA1-1 conformations that best describe the EPR distance distribution. The conformations differ mainly at the $\boldsymbol{\alpha}9$ positions, with relative positions highlighted. The rest of the protein is shown in grey color. (A) Representative conformations with one $\boldsymbol{\alpha}9$ helix only partly delocalized from the crystal structure. (B) Representative conformations with one $\boldsymbol{\alpha}9$ helix fully delocalized from the crystal structure. (C) The distance distributions of the C$\boldsymbol{\beta}$ atoms (center of mass between the C$\boldsymbol{\beta}$ of Lys211 and C$\boldsymbol{\beta}$ of Glu215) between the two $\boldsymbol{\alpha}9$ helices within the dimer, compared to the DEER distance distribution in black. The purple distribution was sampled from a cMD simulation with one of the $\boldsymbol{\alpha}9$ fully delocalized conformations, while the other distributions (in blue, red, gold and grey) were sampled from cMD simulations with partly delocalized $\boldsymbol{\alpha}9$ helix. The overall distribution is shown in cyan. (D) One of the cMD simulations sampled the conformations with both $\boldsymbol{\alpha}9$ helices completely delocalized from the crystal structure.

The delocalization of the $\alpha9$ helices appears to be controlled by two charge-charge interactions as well as the hydrophobic interactions in hGSTA1-1 formed between the $\alpha9$ and the hGSTA1-1 dimer. The conserved residues across many alpha class GSTs point to salt bridges and aromatic-aromatic interactions controlling the dynamics of the $\alpha 9$ helices. This controlled delocalization mechanism, in which many metastable states are separated by relatively small energy barriers explains the broad distance distribution of the ligand-free state measured by EPR (cf. Figures 3-6 and 3-9). More importantly, our WE simulations rationalize the trends in the distance distribution with increasing GSHex concentration (cf. Figures 3-6C-D). These data show a change in both the most probable distance and width of the distance distribution as a function of increasing ligand concentration. However, after half of the active sites are occupied with ligand, increasing ligand concentration resulted in smaller changes in the EPR distance distribution. Our WE results suggest a mechanism where only one monomer has a more flexible $\alpha 9$ helix. This monomer with a more flexible, delocalized $\alpha 9$ helix may initially bind to the ligand, locking that helix into place thereby shortening the most probable distance and narrowing the distance distribution. The other monomer with a localized helix may then be able to bind when all the binding sites with flexible, delocalized $\alpha 9$ helix are saturated. As such, the range of motions for this localized $\alpha 9$ helix is not significantly reduced due to ligand binding such that the most probable distance remains mostly the same. Such negative cooperativity between the monomers may be essential to the recruitment of a wide variety of toxins within the cell during the process of toxin conjugation with glutathione. Figure 3-24 shows different conformations sampled in the ligand-free state that illustrate the wide variety of conformations that may constitute the EPR distance distribution.

## 3.4 Conclusion

This work provides a deeper understanding of the ligand-free conformational ensemble of hGSTA1-1 at an atomic level using a combination of EPR experiments and WE simulations. Our EPR data shows that hGSTA1-1, and likely other structurally similar enzymes, exist in many interconvertible, metastable states. Ligand binding triggers a population shift among these metastable states, as indicated by a shift and narrowing of the EPR distance distribution. However, after half of the active sites are occupied with ligand, the EPR distance distribution exhibits much less change with increasing ligand concentration. Our WE simulations reveal three alternate states that are populated by the ligand-free form of hGSTA1-1. In the two dominant alternate states, the $\alpha 9$ helix is localized in one monomer whereas the $\alpha 9$ helix in the other monomer is delocalized. In the third minor alternate state, the $\alpha 9$ helix is delocalized in both monomers. Together, our EPR measurements and simulations provide direct atomistic views of negative cooperativity between the two monomers. Our simulations reveal a mutually exclusive salt bridge between Arg221 of the $\alpha 9$ helix and Asp42 of the $\alpha 2$ helix in each monomer of the hGSTA1-1 homodimer. We hypothesize that the mechanism governing this negative cooperativity involves these salt bridge interactions and does not result from the helices directly interacting with each other, but through some allosteric signal propagated through the main body of the dimer. Given that Arg221 is highly conserved across $\alpha$-class GSTs, this mechanism of negative cooperativity may be general for such enzymes. Finally, our results demonstrate the power of combining EPR with weighted ensemble sampling in providing mechanistic insights of protein function beyond the level of detail that is available using coarse-grained modeling approaches that are widely used in EPR.[170]

## 3.5 Acknowledgement

This research was supported by the National Science Foundation (NSF MCB-2112871). X.B. and A.T.B would like to thank the University of Pittsburgh for the Andrew Mellon Predoctoral Fellowship. Simulations were performed using the shared computing cluster at the University of Pittsburgh's Center for Research Computing (NSF MRI 2117681). This chapter was adapted with permission from reference 90. Copyright 2023 Wiley.

## 4.0 An optimal acquisition scheme for Q-band EPR distance measurements using $Cu^{2+}$-based protein labels

*This work, written in collaboration with Zikri Hasanbasri, Hannah R. Hunter, and Sunil Saxena, was published in Physical Chemistry Chemical Physics. 2022, volume 24, pages 14727-14739. The thesis author and Zikri Hasanbasri contributed equally to this work. The thesis author performed all the EPR experiments, molecular dynamics simulations, and analysed the data. Zikri Hasanbasri wrote the Python program for carrying out the Monte-Carlo simulations and Zikri Hasanbasri and Hannah R. Hunter analysed the theoretical results. The thesis author and Zikri Hasanbasri prepared the manuscript*.

### 4.1 Introduction

Pulsed electron paramagnetic resonance (EPR) distance measurements[38,39,218,219,221–223] have had a major impact in a variety of biophysical contexts, including the measurement of conformational changes,[5,46,302–306,343] determination of relative packing in protein-protein[56–58] and protein-DNA complexes,[70,71] and the elucidation of ligand and metal binding sites in proteins.[62–64] Additionally, these experiments have been introduced both *in vitro* as well as in-cell.[12–15] Such measurements are enabled by site-directed spin labeling methodology that has predominantly used nitroxide spin labels.[1] Recently, several attractive schemes for labeling proteins and nucleic acids with metal ions have been developed to enhance the reach of spin labeling methodology in biophysics.[344,345] In particular, site-directed $Cu^{2+}$ labeling of proteins can provide distance distributions that are up to five-times narrower than similar measurements using nitroxide-based labels.[83] The $Cu^{2+}$ labeling method for protein relies on the strategic placement of two histidines which can bind to the $Cu^{2+}$ ion. The labeling of the double-histidine (dHis) site is achieved by using either a $Cu^{2+}$-iminodiacetic acid[84] or a $Cu^{2+}$-nitrilotriacetic acid (NTA)[85] chelate to prevent non-specific binding of $Cu^{2+}$ elsewhere in the protein. The labeling approach is facile, can be implemented in a wide variety of buffers,[112] and a range of pH.[113] In addition, distance measurements using dHis labeling and Relaxation Induced Dipolar Modulation Enhancement Spectroscopy (RIDME) can be performed at sub-micromolar concentrations.[315] The dHis–$Cu^{2+}$ labeling method provides enhanced resolution to the multi-lateration of native metal binding sites,[64] measurement of relative orientations in proteins,[86] induced conformational changes,[73,243] and the measurement of site-specific dynamics even on β-sheets.[28] For DNA, a nucleotide-independent $Cu^{2+}$ labeling approach that can directly report on backbone distances[124,125] and DNA conformational changes[75] is also available. There is also emerging work on labeling DNA with $Cu^{2+}$ by creating a quadruplex structure.[120–122] On the other hand, due to the large spectral bandwidth of $Cu^{2+}$, compared to nitroxides, the sensitivity of the label is an area for improvement.

The advent of high-field instrumentation, especially at Q-band (ca. 35 GHz) has been particularly impactful by providing more than an order of magnitude enhancement of sensitivity compared to X-band measurements (ca. 9.5 GHz).[346] Overall, the improved sensitivity has been especially valuable for nitroxide based Double Electron–Electron Resonance (DEER) distance measurements. Despite this potential, distance measurements involving $Cu^{2+}$ at Q-band have been limited, due to difficulties in the proper sampling of all orientations of the inter-spin vector in DEER.[86,120] At Q-band the spectral bandwidth of the $Cu^{2+}$-spectrum is ca. 5 GHz due to the large anisotropy of the g-tensor. On the other hand, the pulses that are typically used excite only a bandwidth of ca. 100–300 MHz[347] due to resonator and pulse amplifier limitations. Consequently, DEER measurements at a given magnetic field sample only some orientations of the inter-spin vector. To ameliorate these orientational effects, a DEER experiment at Q-band require the collection of data at different magnetic fields. For example, earlier Q-band DEER work on a dHis–$Cu^{2+}$ labeled protein utilized seventeen different magnetic fields to obtain the same distance distribution observed using X-band DEER measurement at a single magnetic field.[86] This constraint at Q-band can often make X-band measurements more practical, despite their decreased sensitivity. On the other hand, the initial work at Q-band likely suffered from oversampling, and therefore, there is a critical need to establish the minimum number of fields and the associated averaging scheme for practical distance measurements.

In this work, we establish an optimal approach for collecting dHis– $Cu^{2+}$-based distance measurements at Q-band frequency by focusing on the human glutathione S-transferase (hGSTA1-1) enzyme. We first used MD simulations to identify the distance and orientational information of the $Cu^{2+}$-labeled sites. This information was then used as initial values to determine the number of angles excited as a function of magnetic field using a Monte-Carlo scheme. The information on angles was analyzed to establish an excitation scheme that is expected to appropriately sample molecular orientations. We then demonstrate through simulations that the minimal acquisition scheme is applicable for any possible orientation. Thus, the acquisition scheme can be used without the need for prior structural information. Finally, this scheme was validated by experiments on the protein at both Q- and X-bands, and by MD simulations.

## 4.2 Experimental

### 4.2.1 Protein expression, purification, sample preparation, and EPR experiments

All experiments were performed on the S-hexylglutathione (GSHex) bound form of hGSTA1-1. The K211H/E215H mutant was expressed and purified based on the previously published protocol,[28] except the cell growth was done in Luria Broth instead of Terrific Broth media. hGSTA1-1 is a homodimer such that a single dHis mutant provides two $Cu^{2+}$–NTA binding sites. The purified protein was concentrated and aliquoted to ca. 200 μM in buffer (pH = 6.5) with 150 mM NaCl and 50 mM sodium phosphate then stored at −80 °C.

In order to prepare the EPR samples, a 10 mM $Cu^{2+}$–NTA stock was prepared as described previously[31,85,112] and the GSHex ligand was purchased from Sigma Aldrich. All samples in this work were prepared with 3-N-morpholinopropanesulfonic acid (MOPS) buffer to facilitate efficient $Cu^{2+}$–NTA binding to dHis.[112] Each EPR sample was prepared with 800 μM GSHex, 800 μM protein and 800 μM $Cu^{2+}$–NTA (a 1 : 1 : 1 ratio to ensure that the concentration of both protein and ligand are 104 times over KD of GSHex to hGSTA1-1)[317] in 50 mM MOPS buffer in $D_2O$ (pH = 7.4) with 100 mM NaCl. All samples were incubated at 4 °C for 35 min to achieve maximum loading efficiency, and subsequently flash frozen in liquid MAP-Pro Propylene/propane gas with 50% $D_6$-glycerol added as cryoprotectant. A step-by-step protocol for spin labelling and freezing has been published recently.[31]

To determine the coordination of $Cu^{2+}$-NTA to dHis sites, three-pulse electron-spin echo envelope modulation (ESEEM) experiments[318,319] were performed at 20 K with a Bruker ElexSys E680 X-band FT/CW spectrometer with a Bruker EN4118X-MD4 resonator. The pulse sequence was $(\pi/2)-\tau-(\pi/2)-t-(\pi/2)-\tau-$echo. The first pulse delay time, τ, was 140 ns. The second pulse delay time, t, was 288 ns and lengthened by 16 ns for each iteration. The experiments were performed at the magnetic field with the most intense echo based on the echo-detected field sweep. Four-step phase cycling was used to eliminate the undesired echoes. The data were acquired for ca. 20 min. A stretched exponential decay was fitted to and subtracted from the time-domain raw ESEEM signal. Hamming was applied to filter the background noise, followed by zero filling with 2048 points. Fast Fourier Transform was employed and the absolute value was taken to form the ESEEM spectra, which has been shown in Figure 4-1.

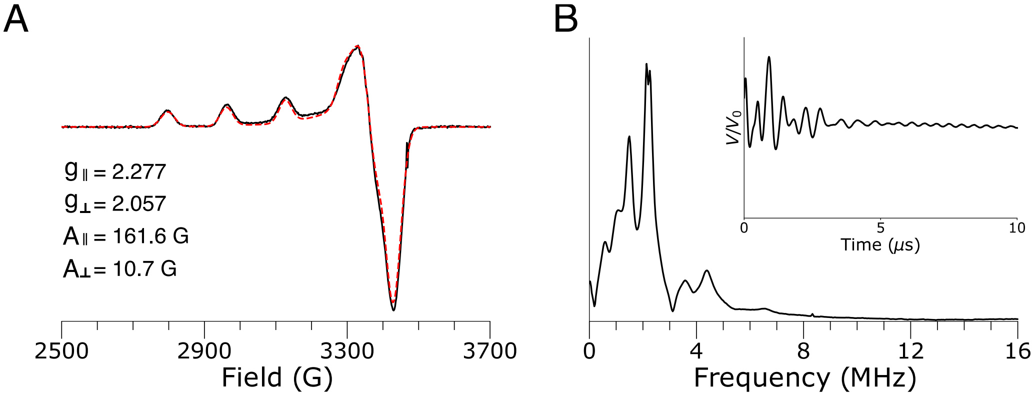

**Figure 4-1.** CW-EPR and ESEEM experiments on dHis-Cu$^{2+}$-NTA labeled hGSTA1-1. (A) CW simulations of dHis-Cu-NTA labeled hGSTA1-1 with GSHex. The simulation was performed using EasySpin.**[320]** The black solid is the experimental data, and the red dashed is the best fit simulation. One-component fit was obtained with $\boldsymbol{g_\parallel = 2.277}$, $\boldsymbol{g_\perp = 2.057}$, $\boldsymbol{A_\parallel = 161.6}$ G and $\boldsymbol{A_\perp = 10.7}$ G. The $\boldsymbol{g_\parallel}$ and $\boldsymbol{A_\parallel}$ values are consistent with multi-nitrogen coordination to Cu$^{2+}$.**[331,335]** (B) ESEEM experiment was performed on the same sample. Characteristic peaks around 0.5, 1, 1.5 MHz, and ca. 4 MHz suggests histidine coordination to Cu$^{2+}$. The double peaks around 2 MHz indicate solvent deuterium. The raw time-domain of the ESEEM is shown as inset.

To determine g and A-tensors and the coordination environment for Cu$^{2+}$–NTA labeled liganded hGSTA1-1, continuous wave (CW) EPR experiment and three-pulse electron-spin echo envelope modulation (ESEEM) experiments[318,319] were performed with a Bruker ElexSys E680 X-band FT/CW spectrometer with a Bruker EN4118X-MD4 resonator. The CW-EPR experiment was performed at 80 K and the ESEEM experiment was performed at 20 K. The CW was collected at microwave frequency ca. 9.70 GHz, with a modulation frequency of 100 kHz, modulation amplitude of 4 G, and a sweep width of 2000 G centered at 3100 G. A total of 1024 data points were collected with an attenuation of 30 dB, conversion time of 20.48 ms, and data was averaged over 50 scans. The X-band sample contains 100 $\mu$L of 400 $\mu$M hGSTA1-1 dimer, 800 $\mu$M GSHex and 800 $\mu$M $Cu^{2+}$–NTA in 50 mM MOPS buffer prepared with $D_2O$ (pH = 7.4) with 100 mM NaCl, 50% $D_6$-glycerol, placed in quartz tube with I.D. = 3 mm and O.D. = 4 mm. The CW spectrum was simulated with EasySpin.[320]

### 4.2.2 MD simulation of dHis-$Cu^{2+}$-NTA labeled protein

The MD simulation was performed starting from the crystal structure of GSHex-bound hGSTA1-1 (PDB: 1K3L).[213] To generate parameters for the ligand GSHex, the PDB of GSHex was extracted from the crystal structure of liganded hGSTA1-1. Using the Antechamber package in Amber18, charges were derived using the AM1-BCC method.[348,349] Force field angles and dihedral terms were assigned with the General Amber Force Field (GAFF).[147] Sites 211 and 215 of each monomer were mutated to histidine for the incorporation of $Cu^{2+}$–NTA. The force fields for $Cu^{2+}$–NTA have been developed in previous work.[139] The hGSTA1-1 was simulated with the ff14SB AMBER force field.[128] Solvent waters were treated with the TIP3P water model.[260] The labeled protein was solvated in a cubic box with the box size of ca. 60 Å$^3$. Sodium and chloride ions were added to neutralize the system. The MD simulation was performed with the pmemd program as part of the AMBER18 software package. The solvated system was first energy minimized with a harmonic force constant applied to the protein and ligand, which was gradually released from 20 to 0 kcal mol$^{-1}$ Å$^{-2}$ over 12 000 steps. The energy minimized system was then equilibrated using a Berendsen barostat at 298 K for 3.2 ns with a decreasing harmonic force constant from 20 to 0 kcal $mol^{-1}$ $Å^{-2}$.[261] The system was then gradually heated from 0 to 298 K. Equilibration was reached after 2 ns. The simulation at the production phase was maintained at 298 K by Langevin thermostat using a 5.0 $ps^{-1}$ collision frequency and collected for 200 ns. A 2 ps time step for motion integration was used for equilibration and production simulations. The system pressure was kept at 1 atm with a pressure relaxation time of 1.0 ps. The SHAKE algorithm was used to restrain the bonding to hydrogens. Periodic boundary condition and particle mesh Ewald were applied to accurately treat the long-range electrostatic interactions.

### 4.2.3 Monte-Carlo simulation

To build an in silico model of our sample, we implemented a home-written Python[350] code, available at the Saxena Lab GitHub (github.com/SaxenaLab/MonteCarloSimulationCopper/). The process starts with the generation of 10 000 vectors, representing $g_{\parallel}$ of $Cu^{2+}$ spins (Spin A). For each Spin A, we generated another spin (Spin B) separated by a vector of length r. The $g_{\parallel}$ tensor of Spin B is rotated by an angle $\gamma$ with respect to the $g_{\parallel}$ tensor of Spin A. Similarly, the $g_{\perp}$ of Spin B is rotated by an angle $\eta$ with respect to the $g_{\perp}$ of Spin A. For each pair, another vector, representing the inter-spin vector, is generated with an orientation of $\chi$ with respect to the $g_{\parallel}$ tensor of Spin A. The angles $\gamma$, $\chi$, and $\eta$, defined pictorially in Figure 4-2, were sampled from three different Gaussian distributions defined by the user. These vectors represent 10 000 spin-pairs of $Cu^{2+}$-labeled hGSTA-1 sample. After generating the vectors, the spin-pairs were then randomly rotated to simulate spin-pairs with random orientations.

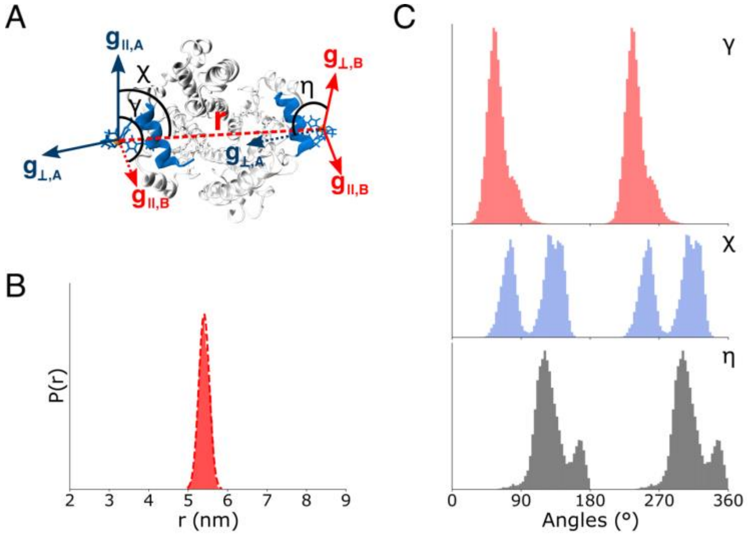

**Figure 4-2.** Distance distribution and relative angles between the two labels sampled from MD. (A) Definition of g-tensors and relative angles within dHis–Cu$^{2+}$–NTA labeled hGSTA1-1. $\boldsymbol{\gamma}$ is the angle between $\boldsymbol{g}_{\parallel,\boldsymbol{A}}$ and $\boldsymbol{g}_{\parallel,\boldsymbol{B}}$; $\boldsymbol{\chi}$ is the angle between $\boldsymbol{g}_{\parallel,\boldsymbol{A}}$ and the interspin vector r; and $\boldsymbol{\eta}$ is the angle between $\boldsymbol{g}_{\perp,\boldsymbol{A}}$ and $\boldsymbol{g}_{\perp,\boldsymbol{B}}$. (B) Cu$^{2+}$–Cu$^{2+}$ distance distribution from a 200 ns MD run. The most probable distance is 5.3 nm, and the standard deviation is ca. 0.2 nm. The distance distribution was reasonably reproduced by a Gaussian shown by the red dashed line. (C) The distribution of each orientational angle.

From each spin, we calculated the effective $g$ and hyperfine interaction term, $A$, as a function of angle, $\phi$, between the applied magnetic field and $g_{\parallel}$ with the following equations: [351]

$$g(\phi) = \sqrt{g_{\perp}^2 \sin^2 \phi + g_{\parallel}^2 \cos^2 \phi} \qquad \textbf{Equation 4-1}$$

$$A(\phi) = \frac{\sqrt{A_{\perp}^2 g_{\perp}^4 \sin^2 \phi + A_{\parallel}^2 g_{\parallel}^4 \cos^2 \phi}}{g_{\perp}^2 \sin^2 \phi + g_{\parallel}^2 \cos^2 \phi} \qquad \textbf{Equation 4-2}$$

Both the $g$ and $A$ tensors were experimentally determined, as shown in Figure 4-1. The effective g and A values of each spin were then used to calculate the resonant field, $B_{res,m_l}$, of the spin using the following equation:

$$B_{res,m_l} = \frac{hv - Am_l}{g\beta_e} \qquad \textbf{Equation 4-3}$$

where h is Planck's constant, v is the microwave frequency, βe is Bohr Magneton, and ml is the nuclear quantum number. For our analysis, we set v as 34.15 GHz to approximate a Q-band frequency. Then, at each resonant field, we built a Lorentzian lineshape with an arbitrary maximum intensity of 1 and a broadening parameter, β. The Lorentzian curve is built based on the following equation:

$$I(B) = \sum_{m_l} \frac{\beta^2}{\left(B - B_{res,m_l}\right)^2 + \beta^2} \qquad \textbf{Equation 4-4}$$

By summing all the Lorentzian functions from each spin, we were able to generate a field-swept spectrum. The broadening parameter $\beta$ was set to be 40 G, which leads to the best fit to the experimental field-swept spectrum (cf. Figure 4-3).

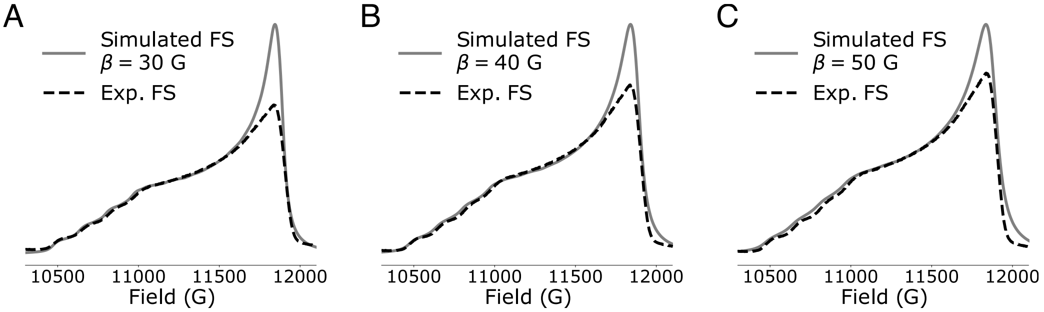

**Figure 4-3.** Fitting of experimental FS-ESE spectrum of dHis-$Cu^{2+}$ labeled hGSTA1-1. The simulated FS-ESE is systematically tested with different Lorentzian broadening parameter, $\boldsymbol{\beta}$, values of (A) 30 G, (B) 40 G, and (C) 50 G. We note that phase memory times vary across the magnetic field, which was not accounted for in our FS-ESE simulations. Hence, there may exist some difference in the intensity of the experimental versus simulated spectrum. Nevertheless, with a $\boldsymbol{\beta}$ of 30 G, the intensity at the $\boldsymbol{g}_{\perp}$ region of ca.11800 G is not properly fitted. However, a $\boldsymbol{\beta}$ of 50

G leads to a loss of features at the $\boldsymbol{g}_{\parallel}$ region of ca.10500 G to ca.11000 G. Therefore, $\boldsymbol{\beta}$ of 40 G is a good compromise between the features at $\boldsymbol{g}_{\parallel}$ and the intensity at $\boldsymbol{g}_{\perp}$.

In addition to the field-swept spectrum, we used $I(B)$ to determine whether a spin with a given $\phi$ can be excited at a given field. Specifically, we consider a spin to be excited only when the intensity of $I(B)$ at a specific field is above a defined threshold parameter, $\alpha$. The $\alpha$ was set to 0.4 in our analysis to ensure a stable counting of the number of spins when $\beta$ was set to 40 G. As the Lorentzian curve $I(B)$ becomes broader (i.e. larger $\beta$ values), $\alpha$ must be adjusted to ensure an optimal sampling of the spins. More details for the choices of $\alpha$ and $\beta$ are provided in Figure 4-4, the results section and at GitHub (github.com/SaxenaLab/MonteCarloSimulationCopper).

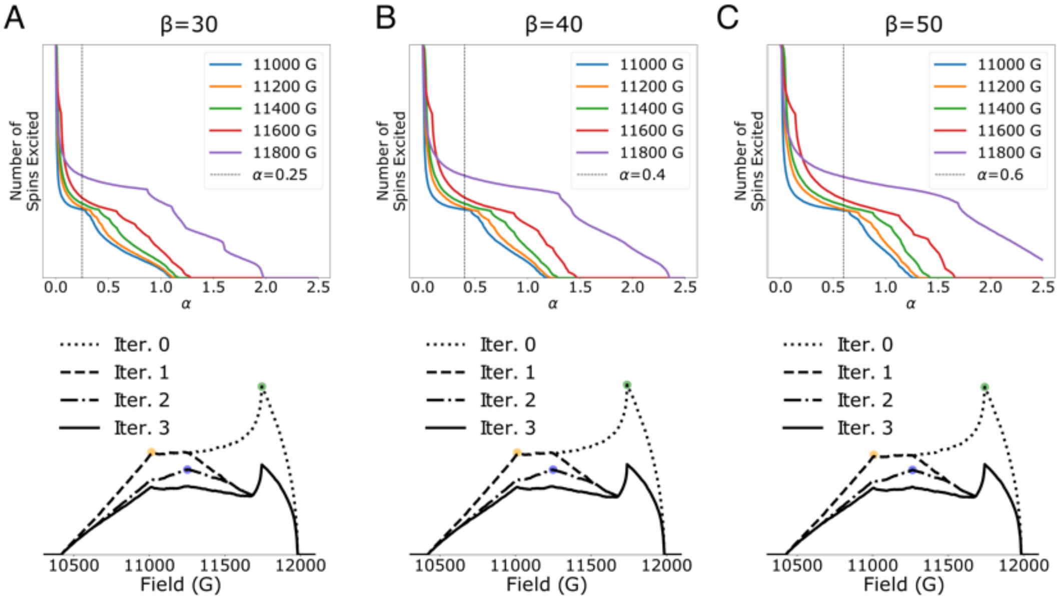

**Figure 4-4.** Determination of the broadening and the threshold parameters. Plots of the number of excited spins as a function of threshold parameter, $\boldsymbol{\alpha}$, at different fields across the simulated FS-ESE spectrum for $\boldsymbol{\beta}$ of (A) 30, (B) 40, and (C) 50. At each field, the plot contains three regions. The first region contains a sharp decay of the number of the excited spins at low $\boldsymbol{\alpha}$ values. This region indicates that low $\boldsymbol{\alpha}$ leads to oversampling of spins. This is a result of the slow decay of I(B) since each Lorentzian goes to 0 only at a magnetic field of infinity. The second region shows a plateau where the change in $\boldsymbol{\alpha}$ does not significantly change the number of excited spins. The third region shows a

further decay of number of spins at high $\boldsymbol{\alpha}$ values. In this region the choice of $\boldsymbol{\alpha}$ leads to a undersampling. The optimal $\boldsymbol{\alpha}$ value for each in $\boldsymbol{\beta}$ was chosen using the criteria that this value provides a stable count (i.e. is in the flat region) for all fields. This $\boldsymbol{\alpha}$ value is shown by dashed line in the top panel. The bottom panel shows the $\boldsymbol{\Phi}$ curve and the three identified fields for each $\boldsymbol{\beta}$ value with the corresponding optimal $\boldsymbol{\alpha}$ value shown in the top panel.

### 4.2.4 Excitation profile of $\boldsymbol{\theta}$

To understand the origin of orientational selectivity, the excitation of $\theta$ angles can be studied. $\theta$ is defined as the angle between the inter-spin vector, r, and the applied magnetic field $B_0$ (Figure 4-1A). To include orientational effects in DEER experiments, DEER signal for a two-$Cu^{2+}$ system can be expressed as: [281]

$$V(t)_{intra} = 1 - \iint \lambda(1 - \cos[\tfrac{k}{r^3}(1 - 3\cos^2\theta)])P(r)\xi(\theta)d\theta dr \qquad \textbf{Equation 4-5}$$

where $\lambda$ is the modulation depth, $k$ is the constant containing the g values of the two spins, $\mathbf{r}$ is the distance between the two spins, $P(r)$ is the distribution function of the distance, and $\xi(\theta)$ is the geometrical factor describing the probability of exciting $\theta$, which is defined as:[352]

$$\begin{aligned}\xi(\theta) = \frac{1}{2}\sum_{m_{I_1},m_{I_2}} \langle k_{xa}^3 k_{xb}^2 \sin\varphi_{1a}(1-\cos\varphi_{2a})(1-\cos\varphi_{3b}) \\ + k_{xb}^3 k_{xa}^2 \sin\varphi_{1b}(1-\cos\varphi_{2b})(1-\cos\varphi_{3a})\,\rangle_{\phi,\delta\omega_1,\delta\omega_2}\end{aligned} \qquad \textbf{Equation 4-6}$$

where $m_{I_i}$ is the nuclear quantum number of the ith spin, $k_{xa}$ and $k_{xb}$ are defined as the ratio of the resonance frequency of the excited spins versus the frequency at observer and pump frequency, respectively, $\varphi_{ia}$ is the flip angle of the first spin by the ith pulse, $\varphi_{ib}$ is the flip angle of the second spin by the ith pulse, and $\delta\omega_i$ is the inhomogeneous broadening of the observer or the pump pulses. If all orientations of the spin-labeled molecules are properly sampled, the geometrical factor $\xi(\theta) = sin(\theta)$.

### 4.2.5 EPR distance measurements

To acquire distance distributions between labels within liganded hGSTA1-1, four-pulse DEER experiments were performed at 18 K at both X-band and Q-band frequencies.[39] For the X-band DEER, the measurement was performed on a Bruker ElexSys E680 X-band FT/CW spectrometer equipped with a Bruker EN4118X-MD4 resonator and a 1 kW amplifier. For the Q-band DEER, the measurements were performed with a Bruker ElexSys E580 X-band FT/CW spectrometer with a Bruker ER5106-QT2 resonator and a 300 W amplifier. The pulse sequence used was $(\pi/2)\upsilon_A$-$\tau$-$(\pi)\,\upsilon_A$-$\tau$+t -$(\pi)\,\upsilon_B$-T-t-$(\pi)\upsilon_A$-T-echo.[353] For X-band DEER, rectangular pulses were used. The lengths of the observer $(\pi/2)\upsilon_A$ and $(\pi)\,\upsilon_A$ were 8 and 16 ns, respectively. The pump pulse had a length of 16 ns. The interval, t, was incremented by a step size of 30 ns over 202 points. For Q-band DEER, the $(\pi/2)\upsilon_A$ and $(\pi)\,\upsilon_A$ pulses were rectangular pulses with lengths of 12 ns and 24 ns, respectively. To increase the modulation depth, an 80 ns chirp pulse was used for the pump pulse. The pump pulse was set with a frequency from −200 MHz to −100 MHz relative to the observer frequency. A 16-step phase cycling was used. The duration, t, was incremented with the same step size as X-band DEER over a total of 237 points. We performed DEER measurements with pump pulses placed 116 G, 566 G, and 746 G, lower than the magnetic field with the highest intensity of the Field Swept Electron Spin Echo (FS-ESE) Spectrum. To further test the sufficiency of the collection scheme, seven additional DEER were collected with pump pulse placed at fields that are ca. 641 G, 516 G, 466 G, 416 G, 334 G, 250 G, and 165 G lower than the magnetic fields with the highest intensity of the FS-ESE spectrum. DEERAnalysis2021[262] was used to analyze the data.

## 4.3 Results and discussion

In this work, we focused on the conformation of the $\alpha9$ helix of hGSTA1-1 in the presence of ligand GSHex. The conformation and dynamics of this helix is intimately related to the function of this protein.[300,301] For this purpose, we generated a K211H/E215H hGSTA1-1 mutant, as described in previous work,[243] which was subsequently labelled with $Cu^{2+}$-NTA. Due to the homodimeric nature of hGSTA1-1, a single dHis mutant provides two labelled sites, one on each subunit, for distance measurements.

### 4.3.1 MD simulation provides initial angle and distance distributions

We first established the anticipated distance distribution and orientational distribution of the g-tensors of the two $Cu^{2+}$ sites using MD simulations. The orientation distribution is characterized by the three angles $\gamma$, $\chi$, and $\eta$, shown in Figure 4-2A. The angle, $\gamma$, is defined as the angle between $g_{\parallel,\mathrm{A}}$ and $g_{\parallel,\mathrm{B}}$; $\chi$ is the angle between $g_{\parallel,\mathrm{A}}$ and inter-spin vector $\mathbf{r}$; and $\eta$ is the angle between $g_{\perp,\mathrm{A}}$ and $g_{\perp,\mathrm{B}}$. For $Cu^{2+}$ distances, orientational selectively is strong for narrower orientational distributions.[86,139,238,281] Therefore, a reference model providing $Cu^{2+}$-$Cu^{2+}$ distances with relative orientations is pertinent to our analysis. We performed a 200 ns MD simulation of GSHex-bound hGSTA1-1 (PDB: 1K3L)[213] with $Cu^{2+}$–NTA labels introduced into $\alpha9$ at site

K211H/E215H. In the MD simulation, we used the force fields parameters for dHis–Cu$^{2+}$–NTA that were recently developed.[139]

From the MD simulation, we obtained the distance, r, between the two Cu$^{2+}$ centers, plotted in Figure 4-2B. The Cu$^{2+}$–Cu$^{2+}$ distance distribution is centered around 5.3 nm, with a standard deviation $\sigma_r$ of ca. 0.2 nm. We then extracted the relative orientations of the Cu$^{2+}$ spin labels from the MD trajectory. The imidazole nitrogen atoms bind to Cu$^{2+}$ equatorially, leading to the $g_{\parallel}$ perpendicular to the equatorial plane. The directions of $g_{\parallel}$ and $g_{\perp}$ in the dHis–Cu$^{2+}$–NTA complex are defined in Figure 4-5. The distributions of $\gamma$, $\chi$, and $\eta$ are shown in Figure 4-2C. For $\gamma$, $\chi$, and $\eta$ the distribution under 180°, there is an identical distribution at $\gamma + 180°$, $\chi + 180°$ and $\eta + 180°$, respectively. This n° and n° + 180° distribution pattern is expected given that $g_{\parallel}$ can be oriented "up" or "down" with respect to the equatorial plane due to the symmetry of the $d_{z^2}$ orbital that the electron spin resides in. On the other hand, $\chi$ shows a bimodal distribution below 180°. A more careful examination of the MD traces, shown in Figure 4-6, suggests that the Cu$^{2+}$ adopts two preferred orientations, likely due to conformations of the $\alpha$9 helix, as has observed previously.[28,243]

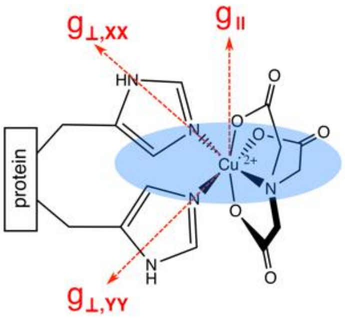

**Figure 4-5.** Directions of $\boldsymbol{g}_{\parallel}$ and $\boldsymbol{g}_{\perp}$ within the dHis-Cu$^{2+}$-NTA complex. dHis-Cu$^{2+}$-NTA is an octahedral complex with Cu$^{2+}$ being a d$^9$ system. Such complexes experience Jahn-Teller effect, leading to the axial elongation. The imidazole nitrogen atoms bind to Cu$^{2+}$ equatorially, leading to the $\boldsymbol{g}_{\parallel}$ perpendicular to the equatorial plane.

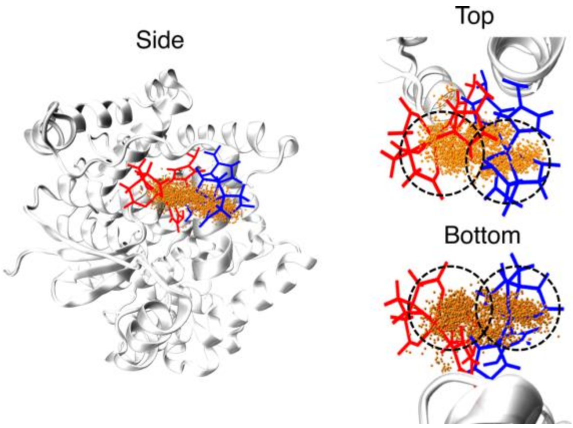

**Figure 4-6.** $Cu^{2+}$ spatial distribution. The helix α9 shows two conformations (indicated by $Cu^{2+}$–NTA conformations in red and blue sticks) in MD that result from a slight turn of the helix around the loop. Thus, the $Cu^{2+}$ atom (yellow dots) shows a bimodal spatial distribution, indicated by the two black dashed circle, leading to a bimodal distribution in $\chi$ below 180°.

Finally, the standard deviation of $\gamma$, $\chi$, and $\eta$ are 14°, 10° and 21°, respectively. This standard deviation for these angles is consistent with earlier estimates on $Cu^{2+}$ coordination to dHis sites in proteins and polynucleic acids that were obtained using a combination of MD and density functional calculations.[127,139,344] In these systems, the $Cu^{2+}$ coordination is elastic leading to a fluctuation in the bond angles and bond lengths of the $Cu^{2+}$ coordinating atoms. Such fluctuations create a distribution in the directions of $g_\parallel$ which generates a distribution in the $\gamma$, $\chi$, and $\eta$ angles. The MD simulation, thus provide reasonable estimates for the standard deviations for the three angles, $\gamma$, $\chi$, and $\eta$. The greater the value of these standard deviations the lower the effects of orientational selectivity.[238,281]

### 4.3.2 The optimal DEER collection scheme

Next, we used the information on expected orientation widths for dHis–$Cu^{2+}$ labelled proteins obtained from MD simulations to devise an optimal collection scheme. First, we used Monte-Carlo methods[354] to generate an *in silico* sample containing 10 000 $Cu^{2+}$-labeled proteins, as shown in Figure 4-7. Details are in the Experimental section. Each blue and green dot in Figure 4-7A represents Spin A and Spin B, respectively, in a doubly $Cu^{2+}$ labeled protein. The g-tensors and the orientation of the inter-spin vector, r, are shown in Figure 4-7B. In the *in silico* sample, each set of Spin A, Spin B, and r is arranged with a given set of $\gamma$, $\chi$, and $\eta$ and r sampled from Gaussian distributions shown in Figure 4-7D. For $\gamma$, $\chi$, and $\eta$, we used the most probable angles of 75°, 60° and 129°, respectively, as the mean angles for their respective Gaussian distributions. Note, that we ignored the bimodality for $\chi$ and the inherent symmetry for each angle (cf. Figure 4-2). We also used a standard deviation of 10° for each angle, which is a conservative estimate for the dHis–$Cu^{2+}$ labeled proteins.[86,139,344] Together, these choices make the in silico sample more prone to orientational selectively. Figure 4-7C shows a count of the number of inter-spin vectors as a function of the angle, $\theta$, between the inter-spin vector and the applied magnetic field. This probability distribution is sinusoidal, as expected for a random distribution.

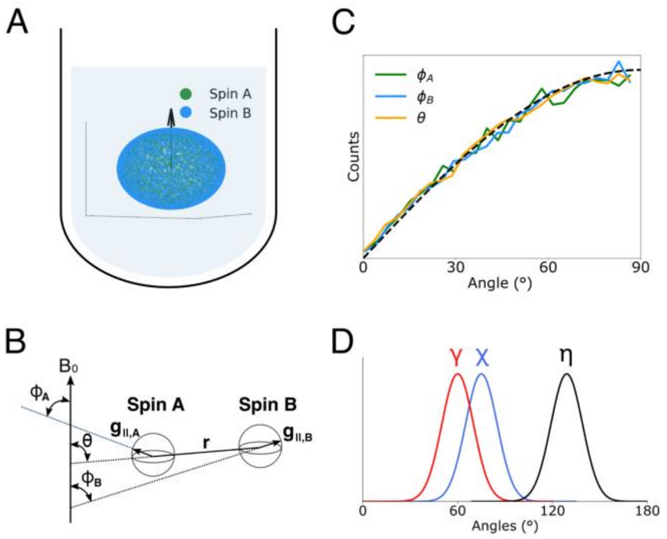

**Figure 4-7.** In silico sample consisting of randomly oriented vectors with two spins. (A) When all doubly labeled molecules are randomly oriented, the orientation of inter-spin vector, r, will also be random, as depicted by the spherical figure. The black arrow represents the applied magnetic field, while blue and green dots on the sphere represent orientations of the $\boldsymbol{g}_{\parallel}$ of Spin A and Spin B generated by the Monte-Carlo simulation. (B) A vector representation of two spins separated by inter-spin vector, *r*. The orientations of each spin can be described with $\boldsymbol{\phi}$ while the orientation of r can be described with $\boldsymbol{\theta}$. (C) Plot of the distribution of $\boldsymbol{\theta}$, $\boldsymbol{\phi_A}$ and $\boldsymbol{\phi_B}$ in the Monte-Carlo simulation. The plot follows a sinusoidal curve depicted by the black dashed line, consistent with a random distribution. (D) Gaussian distributions of $\boldsymbol{\gamma}$, $\boldsymbol{\chi}$ and $\boldsymbol{\eta}$ used for the Monte-Carlo simulations.

To obtain a robust Q-band DEER, the data must be acquired in a manner that samples the $\theta$ distribution shown in Figure 4-7C.[352] On the other hand, the pulses in DEER are finite and can excite only some $\theta$ values at a given magnetic field. The excited θ values are dependent on the $Cu^{2+}$ orientations, $\phi_A$ and $\phi_B$, that are excited by the pump and observer pulses in DEER. Therefore, we first identified fields that can efficiently excite the largest number of $\phi$ angles.

$$\Phi(B) = \int_{0^\circ}^{90^\circ} \left( \begin{cases} 1, & I_\phi(B) \geq \alpha \\ 0, & I_\phi(B) < \alpha \end{cases} \right) sin\phi \, d\phi \qquad \textbf{Equation 4-7}$$

where $\alpha$ is an intensity-threshold parameter. The expression of Φ(B) contains two terms. The bracketed first term represents a counter recognizing whether a $\phi$ value can be excited at a given field. The $\phi$ value is excited only when $I_\phi(B)$ is greater than or equal to $\alpha$. The second term describes the relative probability of spins for a given $\phi$. Overall, Φ(B) quantifies the number of ϕ excitable at a given magnetic field. The curve of Φ(B) is shown in Figure 4-8A. We will refer to this curve as the Φ curve for the rest of this document. The Φ curve depends on the choice of $\alpha$ and breadth of the Lorentzian, $\beta$. The breadth of each Lorentzian was chosen by fitting the experimental FS-ESE spectrum of hGSTA1-1 (cf. Figure 4-3). The optimal value of $\alpha$, was determined by examining the number of excited spins as a function of $\alpha$ for several different fields across the simulated FS-ESE spectrum (cf. Figure 4-4). For a $\beta$ of 40 G, an $\alpha$ of 0.4 leads to a stable count of spins at different fields.

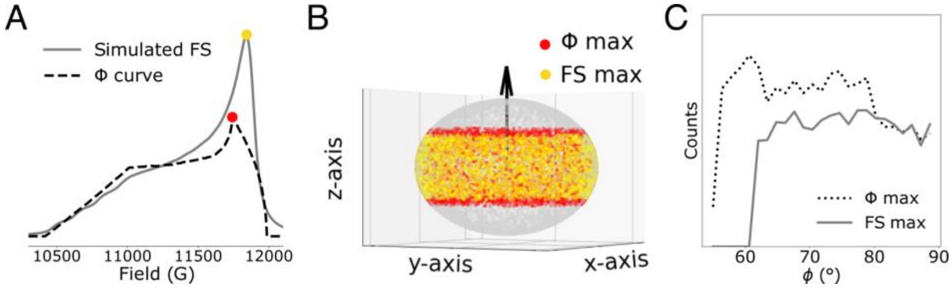

**Figure 4-8.** The Φ curve indicates the field for exciting the most spins. (A) The spectrum in solid grey shows the simulated field-swept spectrum while the dotted line is the **Φ** curve described by Equation 4-7. The **Φ** curve represents the number of $\boldsymbol{\phi}$ excited at a given field. The max of both the field sweep and the **Φ** curve is marked by a yellow circle and a red circle, respectively. (B) Each dot on the sphere represents $\boldsymbol{\phi}$ of a spin in the Monte-Carlo simulation. The yellow dots represent the spin-pairs excited when DEER is performed at the maximum of the field sweep. In contrast, the red dots represent the spin-pairs excited when DEER is performed at the maximum of the **Φ** curve. (C) Number of excited spins in DEER versus angle at the two magnetic fields.

Figure 4-8A shows the $\Phi$ curve generated for the *in silico* sample shown in Figure 4-7A. The value of $\Phi(B)$ (dotted lines) is overlaid on the simulated FS-ESE spectrum. The maximum number $\phi$ angles are excited at a field of 11 738 G (shown by red circle on Figure 4-8A), about 100 G lower than the maximum of the FS-ESE spectrum. To exemplify this point, we determined the spin-pairs excited by DEER at either the max of the $\Phi$ curve, defined as $B_{\phi 0}$, or the max of the FS-ESE spectrum. For simplicity, we assumed a square excitation profile from hyperbolic secant CHIRP pulses.[355] Specifically, we first identified the spins that can be excited by a pump pulse with a bandwidth of 100 MHz, which is set either at the maximum of the $\Phi$ curve or at the maximum of the field sweep. Next, we identified the spins that can be excited by a ca. 38 MHz observer pulse at the field 54 G lower than the pump field. These pulses are chosen to replicate a reasonable DEER on a commercial resonator that has ca. 200 MHz bandwidth. Finally, we identified the spins from the pump excitation that are paired with the spins from the observer excitation. These spin-pairs in our *in silico* sample contribute to the intra-molecular DEER signal at a given field.

The $\phi$ angles excited at $B_{\phi 0}$ (red dot) versus the maximum of FS-ESE spectrum (yellow dot) are shown in Figure 4-8B. At the maximum field sweep intensity, the excited spin-pairs have $\phi$ range of ca. 62° to 90°. In contrast, a more extensive range of $\phi$ from ca. 56° to 90° can be excited at the maximum of the $\Phi$ curve. The increase in the number of $\phi$ is due to the large parallel component of the hyperfine tensor, $A_{\parallel}$. More importantly, this observation indicates that DEER at 100 G lower than the maximum of ESE-FS spectrum is the most optimal for probing the largest number of $\phi$ for $Cu^{2+}$-labeled systems.

Figure 4-9B shows the distribution of $\theta$ that is sampled at $B_{\phi 0}$ (green histogram) by DEER. Data at only this field is clearly insufficient to achieve ideal excitation, which is shown by the dashed line. Therefore, we identified additional fields that can excite the rest of the spin-pairs. Figure 4-9A, shows the recalculated $\Phi$ curve, labeled as Iteration 1, that excludes spins that are excited by the DEER at $B_{\phi 0}$. The maximum of the resultant $\Phi$ curve, $B_{\phi 1}$, is shown by the orange dot on the curve. The field, $B_{\phi 1}$, which is ca. 827 G lower than the maximum of the FS-ESE spectrum, represents a field that can excite the largest number of $\phi$ angles from the unexcited spins. We repeated the identification of the $\theta$ angles that are sampled at the additional field by DEER, shown as the orange histogram in Figure 4-9B. Measurement of DEER at the additional fields improve $\theta$ sampling, especially for angles between 60° to 90°. We reiterated this process and identified a new maximum at a field, $B_{\phi 2}$, which is ca. 580 G lower than the maximum of the FS-ESE spectrum. From these three fields, we see that the overall distribution of sampled $\theta$ is reasonably close to ideal, indicating that the three identified fields are the most promising for $Cu^{2+}$ DEER.

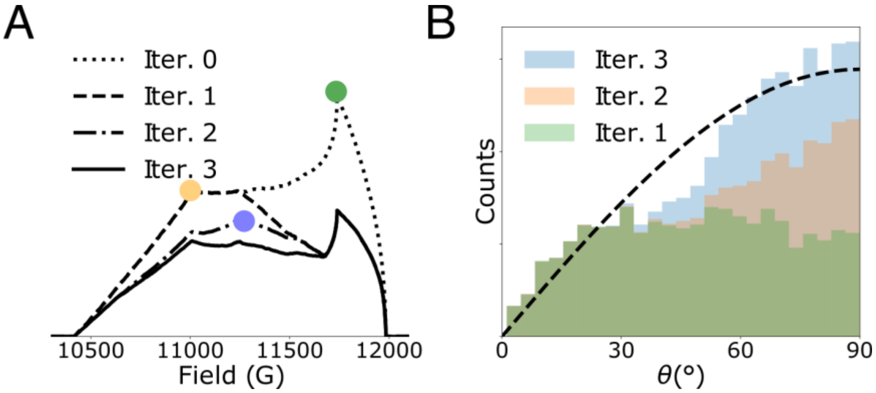

**Figure 4-9.** Identifying the minimum number of fields needed for Q-band DEER experiments. (A) The curve showing the number of excitable $\boldsymbol{\phi}$ angles versus magnetic field. After excitation at one field, the spin-pairs that were excited were removed to generate the curve for subsequent iterations. The maximum $\boldsymbol{\phi}$ angle for each iteration is labeled with a dot. We iterated this process until residual $\boldsymbol{\phi}$ angles cannot be further reduced, and this curve is shown by the black

solid line. (B) Excitation profile of $\boldsymbol{\theta}$ angles. The black dashed sinusoidal curve depicts the ideal excitation of $\boldsymbol{\theta}$, and the histogram shows the cumulative $\boldsymbol{\theta}$ excitation after each DEER at the three identified fields.

The three identified fields are based on the Φ curve. Note, however, that a change in the linewidth parameter, $\beta$, can potentially affect the Φ curve (cf. Equation 4-4). To test the robustness of our approach, we calculated the Φ curve for different values of $\beta$. For each $\beta$, we determined the value of $\alpha$ that ensures optimal sampling of excited spins. The shape of Φ curve and the resulting three identified fields remain consistent with different $\beta$. These results provide further credence to the Φ curve method. However, it is evident from Figure 4-9A that there are still residual $\phi$ angles that are not excited even after four iterations.

To gain further insight, we visualized the orientations of unexcited spin-pairs, Spin A and Spin B, throughout the sample in each iteration, shown in Figure 4-10. Initially both Spin A and Spin B have diverse orientations. After the first iteration, there are no spin-pairs that have both spins at $\phi$ of ca. 56° to 90°. After the second iteration, there are no spin-pairs where both spins are in the region of $\phi$ between 0° to ca. 42°. Finally, after the third iteration, the leftover spin-pairs only consist of A spins with $\phi$ between ca. 56° to 90° that are paired with B spins with $\phi$ between 0° and ca. 56°. In other words, the final unexcited spin-pairs primarily consisted of A spins oriented to the perpendicular region while paired with B spins oriented to the parallel region. Consequently, the resonant fields of most unexcited spin-pairs are too far apart to be excited by conventional DEER with a resonator bandwidth of 200 to 300 MHz.

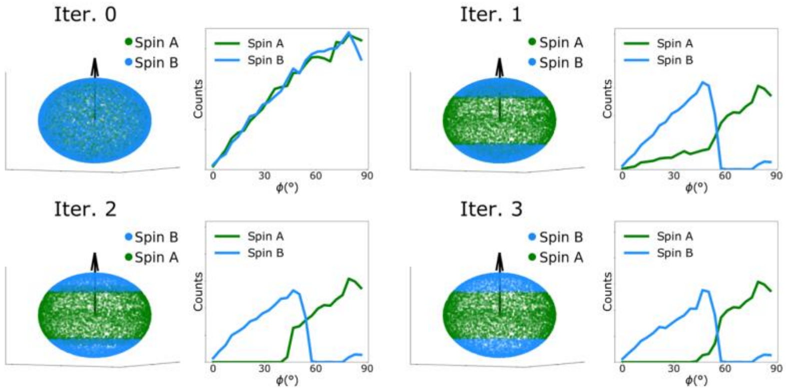

**Figure 4-10.** Spherical resprentations of unexcited spins after each iteration. Each spherical figure shows the $\boldsymbol{\phi}$ angles of unexcited Spin A and Spin B at each iteration. The number of unexcited spins versus angle $\boldsymbol{\phi}$ for Spin A and B is also shown. Initially, the orientations of unexcited Spin A and Spin B follows the same distributions as Figure 4-7C. However, the first DEER at $\boldsymbol{B_{\phi 0}}$ excited spin pairs that have both Spin A and B in the region of $\boldsymbol{\phi}$ between ca. $\boldsymbol{56}$° and $\boldsymbol{90}$°. As a result, the leftover spins in that $\boldsymbol{\phi}$ region only consist of Spin A (cf. Iter. 1) that are paired to Spin B outside of that $\boldsymbol{\phi}$ region. In Iteration 2, the unexcited spins in the region of $\boldsymbol{\phi}$ between $\boldsymbol{0}$° and $\boldsymbol{46}$° only consist of Spin B which are paired to Spin A in a region of $\boldsymbol{\phi}$ above $\boldsymbol{46}$°. After three DEERs in Iteration 3, Spin A and Spin B are largely isolated into two different regions of $\boldsymbol{\phi}$.

Quantitatively, we found that DEER at the three fields cannot excite ca. 4500 spin-pairs out of 10 000 spin-pairs. However, we observed ca. 800 leftover spin-pairs that have $\phi$ around 56° for both Spin A and Spin B. These 800 spin-pairs can be excited by a fourth DEER at a field between $B_{\phi 1}$ and $B_{\phi 3}$ (ca. 338 G lower than the maximum of the FS-ESE spectrum). In this case, the fourth DEER only improves the sampling of $\theta$ slightly.

Next, we simulated the Q-band DEER signal by summing up the contribution from each spin pair that was excited at the three fields. The simulated DEER is shown by the solid blue line in Figure 4-11. Superposed on the curve is the ideal DEER signal (black dashed line) if all possible spin pairs were excited. Comparison of the two traces indicates that DEER experiments performed at the three identified fields are sufficient to obtain the appropriate modulations in the time-domain signal. Furthermore, an additional DEER does not significantly improve the DEER signal (cf. Figure 4-12).

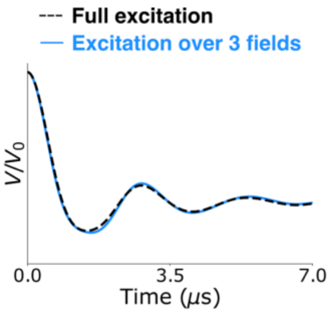

**Figure 4-11.** Simulated DEER time traces based on the MD results. Simulated averaged DEER time trace using the optimal collection method in solid blue line is compared to an ideal DEER time trace with all spins excited (black dashed line). The simulation assumes a Gaussian distance distribution with mean distance = 5.3 nm and $\sigma_r$ = 0.2 nm.

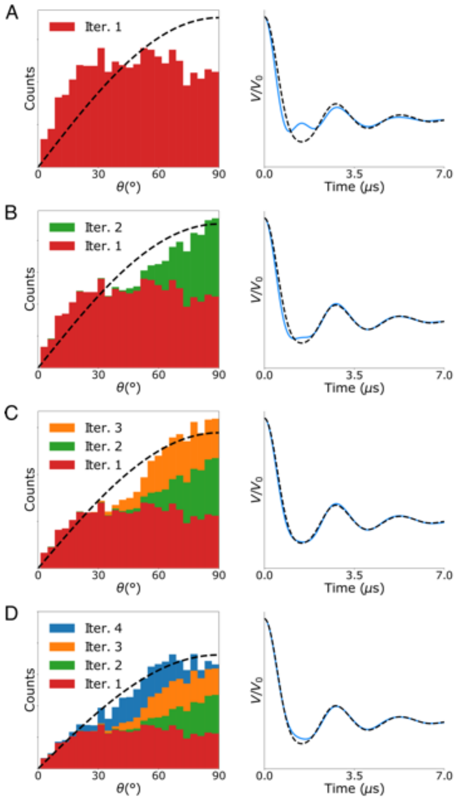

**Figure 4-12.** Simulated DEER at four fields based on the MD results on hGSTA1-1. The left column shows the distribution of probed $\boldsymbol{\theta}$ from DEER simulations with a ca.38 MHz observer pulse and 100 MHz pump pulse after

iteration 1(A), iteration 2 (B), iteration 3 (C), and iteration 4 (D). Iteration 1, 2, 3 and 4 represent DEER simulations at 100 G, ca.827 G, ca.580 G and ca.340 G lower than the maximum of the ESE-FS spectrum. The first three fields are identified in Figure 4-9. The dashed line represents an ideal sinusoidal probability of $\boldsymbol{\theta}$ distribution. Overall, only a slight improvement in the sampling of $\boldsymbol{\theta}$, when compared to Figure 4-9, is observed. The right column of the figure shows the DEER intra-molecular signal from the corresponding probed $\boldsymbol{\theta}$ distribution shown in the left. The solid blue line represents the probed DEER signal. The dashed black line represents an ideal DEER signal, assuming all spin-pairs in the *in silico* model are excited. The fourth DEER does not improve the DEER signal when compared to the DEER from only three fields, shown in Figure 4-11.

Note, the case shown in Figure 4-11 has been calculated for the orientational distribution shown in Figure 4-7D. In order to ensure that the results are general, we calculated DEER traces for 125 combinations of angle $\chi$, $\gamma$ and $\eta$. In each case, the standard deviation of each angle was 10°. Figure 4-13 shows simulated DEER signal with $\eta = 0° \pm 10°$, and for several different values of $\chi$ and $\gamma$ that range from 0° to 90°. Simulations for $\eta > 0°$ are similar to the results shown in Figure 4-13. For all orientations the summed DEER signal averaged over the three identified fields is reasonably identical to the ideal DEER time trace. However, we noticed deviations between the simulated DEER time trace and the expected time trace in a small number of cases (4 out of 125 cases) when $\eta = 0°$, $\chi = 20°$, $\gamma = 40°$ and $60°$; $\eta = 0°$, $\chi = 40°$, $\gamma = 60°$ and $80°$. To evaluate the significance of the discrepancy in distance distributions, we analyzed the DEER time traces with DeerAnalysis21.[262] In the distance analysis, random noise was added to the DEER signals to represent real-life measurements. We show, in Figure 4-14, that the resulting most probable distance as well as the distribution shape generally agree with the expected distance distribution. However, in these cases, a small peak at with an intensity roughly 10% of the main peaks is observed, due to residual orientational effects. This feature originates from the 800 spin-pairs that remain unexcited. In these cases that contain a small feature, an additional DEER with pump pulse placed 338 G lower than the maximum of FS-ESE spectrum is sufficient to suppress the minor peak (cf. Figure 4-14). Overall, DEER measurements at three magnetic fields are valid in most cases, but an additional DEER measurement may be useful to allow confident interpretation of any minor peaks in the distance distribution. The scheme is not dependent on distances of the system (Equation 4-6). Therefore, no prior knowledge of distances or structures are required.

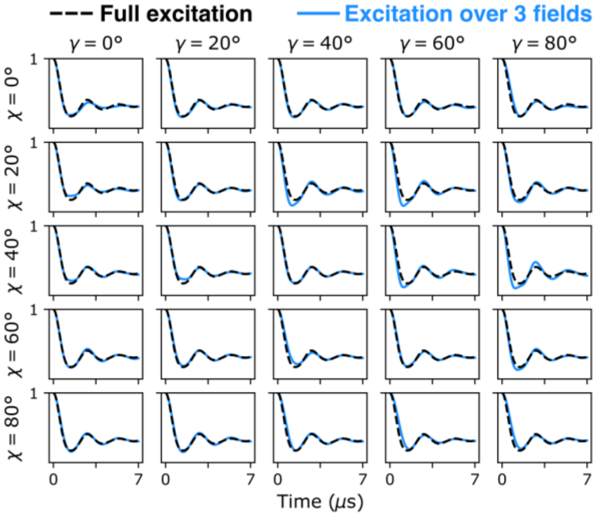

**Figure 4-13.** Simulated DEER time traces considering arbitrary cases. Averaged DEER time traces (blue) simulated for the optimal DEER collection method compared to full excitation (black dashed). The simulation set $\eta = 0°$ and $\sigma_\gamma = \sigma_\chi = \sigma_\eta = 10$, and iterates through $\gamma$ and $\chi$ from 0° to 90°.

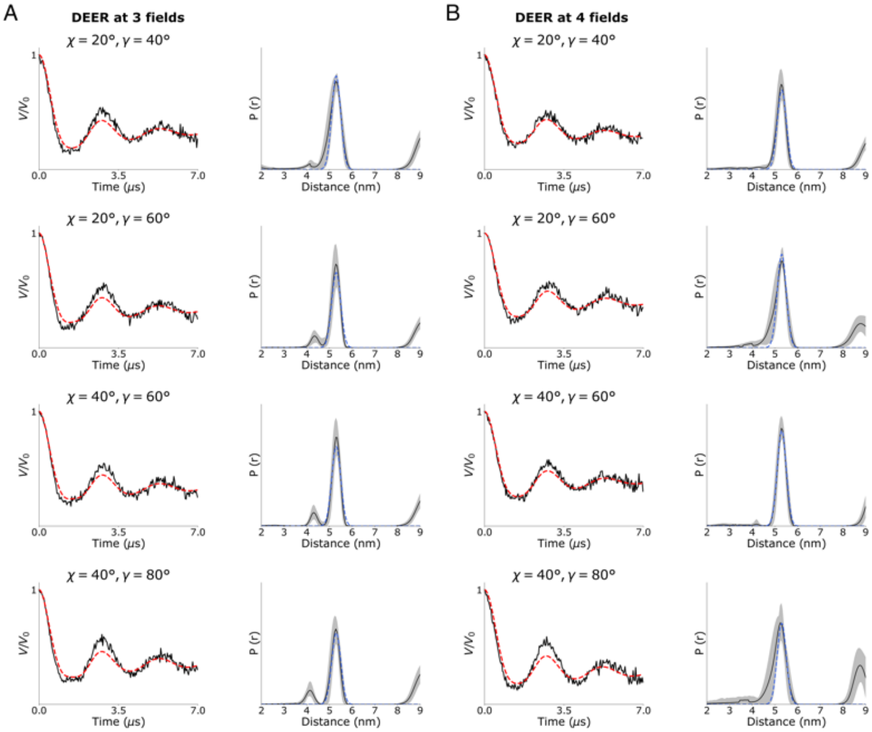

**Figure 4-14.** Simulated DEER at four fields. The left column in (A) and (B) shows the averaged DEER time traces simulated at three and four magnetic fields, respectively. Random noise has been added to the time-domain signals to represent real-life measurements. In addition to the three identified fields, one more field at 338 G lower than the maximum of FS-ESE spectrum make the four-field acquisition scheme. The solid black curves are the simulated DEER time traces, and the red dashed curves are the best fit from DEERAnalysis,[262] for the corresponding angles. The right columns in (A) and (B) show the resulting distance distributions as black solid curves generated by CDA[336,337] for $\boldsymbol{\eta} = \mathbf{0}$°, $\boldsymbol{\chi} = \mathbf{20}$° and $\boldsymbol{\gamma} = \mathbf{40}$°; $\boldsymbol{\eta} = \mathbf{0}$°, $\boldsymbol{\chi} = \mathbf{20}$° and $\boldsymbol{\gamma} = \mathbf{60}$°; $\boldsymbol{\eta} = \mathbf{0}$°, $\boldsymbol{\chi} = \mathbf{40}$° and $\boldsymbol{\gamma} = \mathbf{60}$°; $\boldsymbol{\eta} = \mathbf{0}$°, $\boldsymbol{\chi} = \mathbf{40}$° and $\boldsymbol{\gamma} = \mathbf{80}$° respectively, that have shown some deviation from the expected DEER signal in Figure 4-13. The uncertainty in the distributions is shown in grey shading. The blue dashed curve shows the expected distance distribution.

### 4.3.3 Assumptions and generality of the acquisition scheme

The modeling is encouraging and suggests that three magnetic fields might be sufficient to acquire robust DEER data for $Cu^{2+}$ under the following conditions. First, the parallel component of the hyperfine tensor should be ca. 161 G. Such large values of hyperfine, which are typical for many octahedrally coordinated $Cu^{2+}$ centers,[331,356,357] ensure that many orientations are excited at a given magnetic field. Second, the standard deviation of the orientational distribution is ca. 10° or larger. The value of the standard deviation is consistent with expectations for sites with moderate binding affinity such as dHis.[86,139,241,325] However, for substantially larger orientational distributions, as seen for the $Cu^{2+}$-2,2′-dipicolylamine DNA label,[126,344] a DEER at a single field is sufficient. On the other hand, more fields may be needed for systems that exhibit rigid coordination to $Cu^{2+}$,[281,283,285,290,358] which will lead to lower distribution widths for angles $\chi$, $\gamma$ and $\eta$. Finally, the bandwidth of the pump pulse should be ca. 100 MHz or larger. A value of 100 MHz is conservative and can be readily achieved by pump pulses lengths of around 10 ns or using arbitrary waveform generators and resonators on commercial instrumentation. Furthermore, increasing the pump excitation bandwidth to 300 MHz can potentially reduce the DEER acquisition scheme to only 2 fields (cf. Figure 4-15). The acquisition scheme can be reduced further to one field with the recent development of pent loop-gap resonators[359] and ultra-wideband arbitrary waveform generators (cf. Figure 4-16).[287,360]

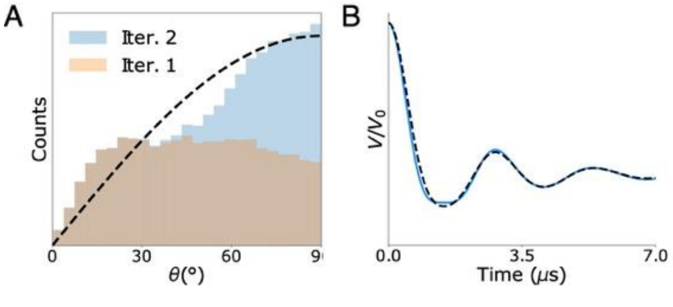

**Figure 4-15.** DEER measurements at two fields are possible. (A) Distribution of probed $\boldsymbol{\theta}$ from two DEER simulations with a ca.38 MHz observer pulse and 300 MHz pump pulse. Iteration 1 and Iteration 2 represents DEER performed at 100 G and ca.740 G lower than the maximum of the ESE-FS spectrum. The dashed line represents an ideal sinusoidal probability of $\boldsymbol{\theta}$ distribution. (B) The DEER intra-molecular signal from the DEER simulation is shown as the solid

blue line. The black dashed line represents an ideal DEER signal assuming all spin-pairs in the in-silico model can be excited.

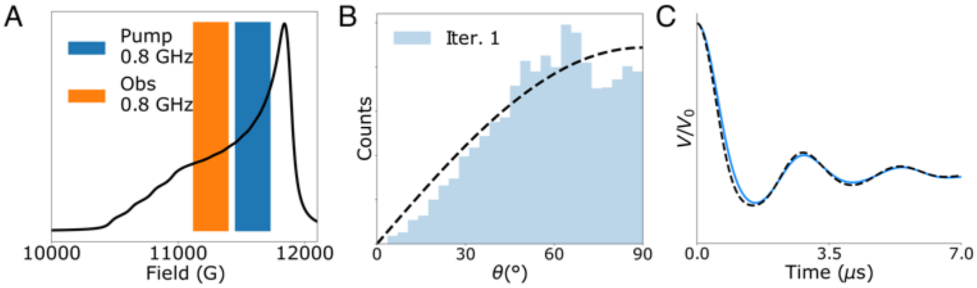

**Figure 4-16.** DEER measurement at one field is possible by using ultra-wide band excitation. (A) Pump and observer pulses exciting regions of the FS-ESE spectrum, depicted by the blue and orange region, respectively. The pump excitation is centered at 11592 G, while the observer excitation is centered at 11259 G. These pulses represent a total excitation bandwidth of 1.6 GHz. (B) Distribution of probed $\boldsymbol{\theta}$ from a single DEER simulation with a 0.8 GHz observer pulse and 0.8 GHz pump pulse at regions depicted by (A). The dashed line represents an ideal sinusoidal probability of $\boldsymbol{\theta}$ distribution. (C) The DEER intra-molecular signal from the DEER simulation is shown as the solid blue line. The dashed black line represents an ideal DEER signal assuming all spin-pairs in the in-silico model can be excited.

### 4.3.4 DEER on liganded hGSTA1-1

We next verified the acquisition scheme experimentally, by collecting DEER data on K211H/E215H hGSTA1-1 mutant which was labelled with $Cu^{2+}$–NTA. Due to the homodimeric nature of hGSTA1-1, a single dHis mutant provides two labelled sites, one on each subunit, for distance measurements. Figure 4-17A shows the FS-ESE spectrum of K211H/E215H hGSTA1-1 and the three pump fields at which DEER was acquired is indicated by solid vertical lines. The values of specific fields are in the Experimental section. We were able to obtain a dipolar evolution time of ca. 7 $\mu$s due to the long phase memory relaxation time achieved (over 9 $\mu s$, cf. Figure 4-

18) by deuteration of the solvent and the glycerol as has been recently reported.[40] Such a dipolar evolution time is important to resolve a ca. 5.0 nm distance, and is a dramatic improvement over previous efforts where short phase memory times limited the dipolar evolution time to ca. 4 $\mu$s.[40,243]

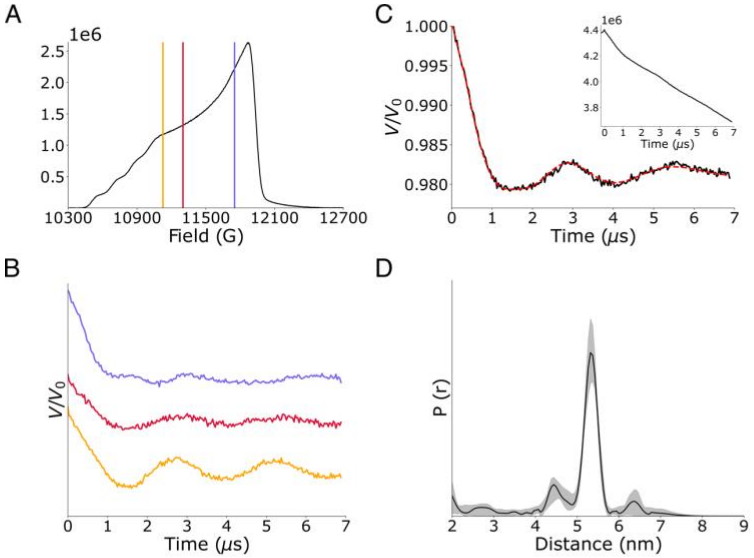

**Figure 4-17.** Experimental validation of the acquisition scheme. (A)Field-swept-electron spin echo spectrum of dHis–$Cu^{2+}$–NTA labeled hGSTA1-1. The magnetic fields for the pump pulses are labeled with color coded vertical lines. (B) The background subtracted DEER time domain at each magnetic field. The data was offset on the *y*-axis for better visualization. (C) The background subtracted average DEER time trace is plotted in black solid line, with Tikhonov fit shown as a red dashed line. The inset is the summed primary DEER time trace. (D) Distance distribution is analyzed by comparative DEER analysis (CDA). The uncertainty in the distribution is shown by grey shading.

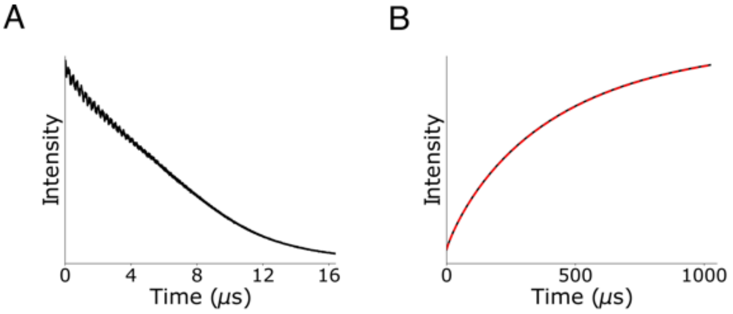

**Figure 4-18.** Determination of relaxation times. (A) Primary Hahn echo decay data. Due to the TWT gate time limit, the full two-pulse decay could not be collected. The best fit using the stretched exponential decay shows a phase

memory time, $T_m$, of over 9 $\boldsymbol{\mu s}$. (B) Primary inversion recovery data and fit of the stretched exponential decay with the form $\boldsymbol{I(t) = c * [1 - 2 * e^{-(\frac{t}{T_1})^y}]}$ for the 800 $\boldsymbol{\mu}$M $Cu^{2+}$-NTA labeled hGSTA1-1 mutant. The best fit, shown as the dashed red line, suggests that $\boldsymbol{T_1 = 418 \pm 84\ \mu s}$.

The background subtracted DEER data using DEERAnalysis[262] at these fields are shown in Figure 4-17B. The time traces are not identical at the three fields, which is a clear indicator of orientational selectivity.

Each time-domain DEER signal was normalized to the intensity of the FS-ESE spectrum (cf. Figure 4-19) and summed to obtain the field average DEER signal (cf. inset of Figure 4-17C). The background subtracted DEER signal and the fit from Tikhonov regularization is shown in Figure 4-17C. Figure 4-17D shows the resulting distance distribution using ComparativeDEERAnalyzer (CDA).[336,337] CDA generates a consensus distance distribution and uncertainty estimate using DEERNet and DEERLab analysis programs. DEERNet utilizes a deep neural network and automatically analyzes the contribution to the baseline from intermolecular dipolar interactions, which reduces potential user bias from the analysis.[337] DEERLab is a single step automated fitting program that utilizes Tikhonov regularization, removing all user bias.[336] The uncertainty of the distributions is plotted in grey shading. The individual results from the different analysis programs are provided in Figure 4-20. A single distance centered around 5.3 nm, labeled by the red dashed vertical line in Figure 4-20, was consistently shown by each analysis tool.

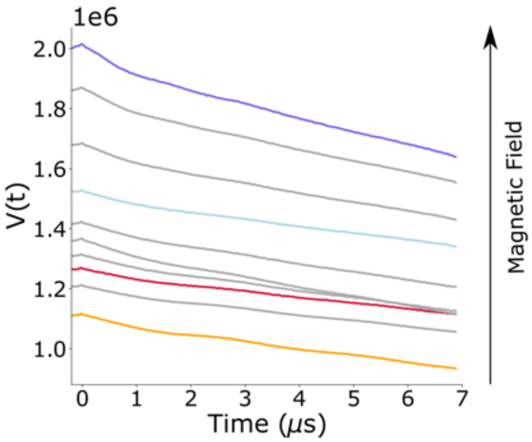

**Figure 4-19.** The primary DEER time domain data. Determination of relaxation times. The primary DEER time domain collected at each magnetic field shown in Figures 4-17A and 4-21A, normalized to the intensity of the field-swept spectrum.

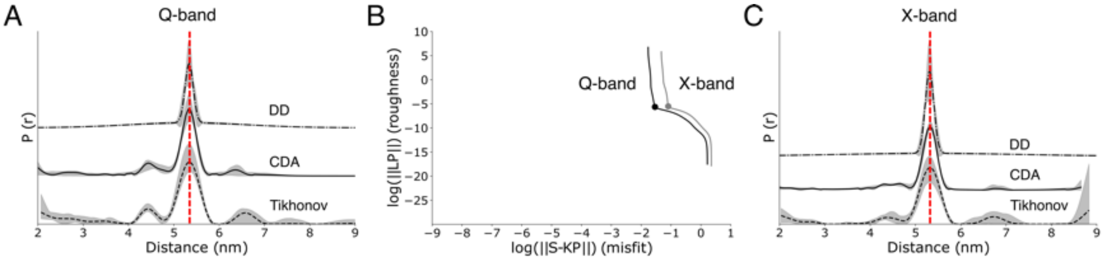

**Figure 4-20.** Comparison of DEER distance distribution using different analysis tools. (A) The Q-band DEER data collected at three magnetic fields was analyzed using Tikhonov regularization in black dashed curve,[262] comparative DEER Analyzer (CDA) in black solid curve,[336,337] as well as DD[191,361,362] in black dash-dot curve. The uncertainty in the distributions is presented in grey shade. Only the 5.3 nm distance, labeled by the vertical red dashed line, is consistently shown by all analysis tools. (B) L-curves by Tikhonov regularization[262] and $\boldsymbol{\alpha}$-values in full circles are for the summed Q-band DEER using the minimal DEER collection method (shown in black) and X-band DEER (shown in grey). (C) The X-band DEER data was analyzed using Tikhonov regularization in black dashed curve,[262] CDA in solid black curve,[336,337] as well as DD[191,361,362] in black dash-dot curve. The uncertainty in the distributions is presented in grey shade. Only the 5.3 nm distance, labeled by the vertical red dashed line, is consistently shown by all analysis tools. The X-band distance distribution agrees with the Q-band DEER results.

To further confirm that three fields are sufficient, we collected 7 more traces at different magnetic fields (cf. details in the Experimental section) marked by a blue and six grey vertical lines in Figure 4-21A. Figure 4-21B shows that collecting one or even seven additional DEER measurements does not change the time trace. The resulting distance distributions, shown in Figure 4-21C, are identical within error. This experimental observation is consistent with our DEER simulations where additional DEER does not significantly improve the sampling of $\theta$ and the DEER signal (cf. Figure 4-12).

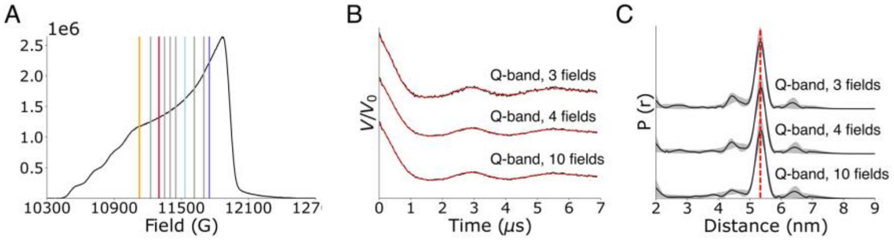

**Figure 4-21.** Comparison of Q-band DEER collected at 3, 4 and 10 magnetic fields. (A) FS-ESE spectrum with DEER time traces collected at one additional magnetic field labeled with blue, and at six more magnetic fields with grey vertical lines. The fields are in addition to the 3 optimal fields that are shown by colored lines in purple, red and yellow. (B) DEER time trace averaged over 3, 4 and 10 magnetic field. The time traces are offset at y-axis for visualization. (C) Distance distribution by CDA. The uncertainty is indicated by the grey shading. The vertical line marks the most probable distance at 5.3 nm. The distance distributions for 3 fields, 4 fields, and 10 fields agree within the uncertainty.

The proposed acquisition scheme is a dramatic improvement of the DEER protocol on commercial instrumentation. Using the optimal scheme, we were able to obtain the expected distance with only three measurements at different magnetic fields. The data collection time at each magnetic fields was between 1 h to 3.5 h, so the total DEER data collection time was ca. 7 h.

In contrast, seventeen magnetic fields were used to measure the distance on a dHis–$Cu^{2+}$ labeled protein at Q-band.[86] The optimal scheme therefore reduces the cryogens cost and data collection time by at least 5 to 6 fold. Note, however, that the acquisition of data at different fields is useful if orientational information is needed.[86]

### 4.3.5 X-band DEER and MD results further proves the validity of the summed Q-band DEER

Next, we acquired DEER data at X-band to further validate the Q-band DEER results. For dHis-$Cu^{2+}$ labeling orientational selectivity is minimal at X-band and acquisition at only one field is needed.[83–86,139] The DEER time trace at both X-band and Q-band are shown in Figure 4-22A. The X-band time trace was collected for ca. 6 $\mu s$ to ensure sufficient signal-to-noise ratio while obtaining enough acquisition time for two modulations of a ca. 60 Å distance. The X-band time trace shows similar modulation frequency seen in the averaged Q-band signal, and the resulting distance distributions from X-band and Q-band are similar, as shown in Figure 4-22B.

Finally, in Figure 4-22C we compare the experimental distance distribution with the distribution obtained from MD simulations. The agreement between the two distributions is remarkable. More importantly, this result adds to previous evidence[139] that MD simulations can accurately predict the EPR distance measurements for $Cu^{2+}$-NTA labeled proteins. The accurate prediction of distances by modeling remains a critical bottleneck for nitroxide labels.[72,82] This body of work therefore foreshadows future work that combine MD simulations with EPR distance constraints to incisively probe protein structure and function.

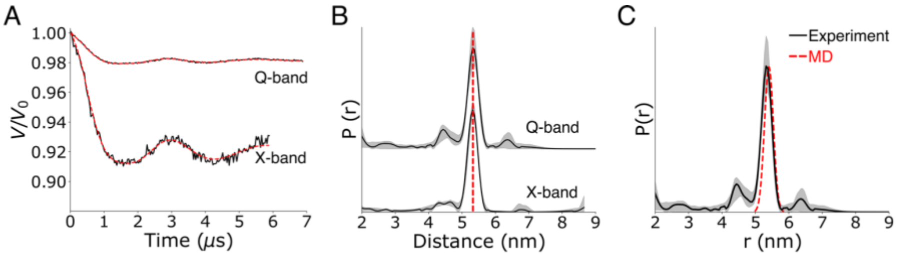

**Figure 4-22**. Summed Q-band DEER signals compared to X-band DEER. (A) The modulation depth for X-band DEER is 7.7%, whereas the Q-band DEER shows a modulation depth of 2.0%. (B) Distance distribution by Consensus DEER analysis of the summed Q-band data compared to the X-band data. The uncertainty is indicated by the grey shading. The most probable distance, shown by the red-dashed line, was the same for X-band and Q-band data. (C) $Cu^{2+}$–$Cu^{2+}$ distance distribution from MD simulation is compared to the EPR distance distribution. The most probable $Cu^{2+}$-$Cu^{2+}$ distance by DEER measurement and MD simulation which agree within the uncertainty level of the experiment.

## 4.4 Conclusions

In this work, we have demonstrated an efficient procedure to perform dHis–$Cu^{2+}$-based Q-band DEER distance measurements. The optimal acquisition scheme can generate a high-resolution distance distribution with five to six times less collection time. Using a novel Monte-Carlo approach, we established that collecting data with the pump pulses at three magnetic fields (ca. 100 G, 580 G and 827 G lower than the maximum of the FS-ESE spectrum) is generally optimal. The summed data from these fields leads to orientational-independent DEER measurements. An additional DEER measurement (at a magnetic field of ca. 338 G lower than the maximum of the FS-ESE spectrum) is suggested to allow confident interpretation of the minor features in the distance distributions. Using these three magnetic fields, we collected a high-quality distance distribution for hGSTA1-1 and verified the obtained distribution with data at X-band and

MD simulation. Importantly, we demonstrated that performing Q-band DEER measurement at seven additional fields did not show further orientational averaging. This protocol will benefit greatly from recently developed ultra-wideband arbitrary waveform generators[287,360] and pent loop-gap resonators.[359]

While this work focuses on the DEER using $Cu^{2+}$-based labels, future application of our Monte-Carlo approach can be applied to ESEEM experiments for $Cu^{2+}$-based systems that also shows orientational selectivity effects.[363,364] We can also apply this approach to $Cu^{2+}$ distance measurements by alternative pulsed-dipolar spectroscopy techniques.[74,365] Additionally, this approach can be adapted for other $Cu^{2+}$ systems with higher binding affinity[281,283,285,290,358] and other paramagnetic spins with large spectral bandwidth such as $Co^{2+}$ and $Fe^{3+}$.[366,367] Further understanding of the orientational selectivity effect will expand the power of pulsed-EPR techniques and make EPR measurements more resource-conscious and widely accessible to the scientific community.

## 4.5 Acknowledgements

This research was supported by the National Science Foundation [NSF BSF MCB-2006154]. X. B. would like to thank the University of Pittsburgh for the Andrew Mellon Predoctoral Fellowship. The molecular dynamics simulation was carried out at the University of Pittsburgh's Center for Research Computing. This chapter was adapted with permission from reference 323. Copyright 2022 Royal Society of Chemistry.

# 5.0 Conclusions and future directions

The work presented in this thesis shows the power of combining EPR with computational modeling to measure conformations and dynamics of biomolecules, especially proteins. I have first described the development of new force field parameters for the dHis-Cu(II)-NTA and the dHis-Cu(II)-IDA spin labels. The MD-sampled distance distributions based on these new force fields showed remarkable agreement with experiments. In addition, these simulations also helped to explain the orientational effects observed in DEER measurements. I have demonstrated how a combination of dHis-Cu(II) EPR and weighted ensemble MD simulations leads to the efficient sampling of conformational changes of a detoxification enzyme. Through this advancement, we have gained atomistic understandings of the entire structural transitions that are responsible for the enzymatic functions. Additionally, I utilized a simulation approach developed by a coworker to determine the optimal way to perform Q-band DEER measurements on dHis-Cu(II)-labeled proteins. The development of this optimal acquisition scheme has reduced data collection time by up to six-fold compared to prior work, and can be adapted to *any* paramagnetic metal ion-labeled systems, and other pulsed-EPR techniques.

My research efforts have led to the following publications:

**X. Bogetti** and S. Saxena, Integrating EPR and computational modeling to measure protein structure and dynamics. **2023**, manuscript submitted to *ChemPlusChem*.

**X. Bogetti**, A. T. Bogetti, J. Casto, L. T. Chong, G. S. Rule and S. Saxena. Direct observation of negative cooperativity in a detoxification enzyme at the atomic level by Electron Paramagnetic Resonance spectroscopy and simulation. *Protein Sci*. **2023**, e4770.

J. Casto, **X. Bogetti**, H. R. Hunter, Z. Hasanbasri and S. Saxena. “Store-Bought is Fine”: Sensitivity Considerations Using Shaped Pulses for DEER Measurements on Cu (II) Labels. *J. Magn. Reson.* **2023**, 349.

M. K. Osei, S. Mirzaei, **X. Bogetti**, E. Castro, M. A. Rahman, S. Saxena and R. Hernández Sánchez. Synthesis of Square Planar $Cu_4$ Clusters. *Angew. Chem*. **2022**, *134*(41), 1-6.

**X. Bogetti**, Z. Hasanbasri, H. R. Hunter and S. Saxena. An optimal acquisition scheme for Q-band EPR distance measurements using $Cu^{2+}$-based protein labels. *Phys. Chem. Chem. Phys.* **2022**, *24*(24), 14727-14739. This paper is highlighted as a journal cover.

A. Gamble Jarvi, **X. Bogetti**, K. Singewald, S. Ghosh and S. Saxena. Going the dHis-tance: Site Directed Cu(II) Labeling of Proteins and Nucleic Acids. *Acc. Chem. Res*. **2021**, *54*(6), 1481-1491. This paper is highlighted as a journal cover.

**X. Bogetti**, S. Ghosh, A. Gamble Jarvi, J. Wang and S. Saxena. Molecular Dynamics Simulations Based on Newly Developed Force Field Parameters for $Cu^{2+}$ Spin Labels Provide Insights into Double-Histidine-Based Double Electron–Electron Resonance. *J. Phys. Chem. B* **2020**, 124(14), 2788-2797. This paper is highlighted as a journal cover.

K. Singewald, **X. Bogetti**, K. Sinha, G. Rule and S. Saxena. Double Histidine Based EPR Measurements at Physiological Temperatures Permit Site-Specific Elucidation of Hidden Dynamics in Enzyme. *Angew. Chem*. **2020**. *132*(51), 23240-23244.

A. Gamble Jarvi, A. Sargun, **X. Bogetti**, J. Wang, C. Achim and S. Saxena. Development of $Cu^{2+}$-Based Distance Methods and Force Field Parameters for the Determination of PNA Conformations and Dynamics by EPR and MD Simulations. *J. Phys. Chem. B* **2020**, *124* (35), 7544–7556. This paper is highlighted as a journal cover.

S. Ghosh, J. Casto, **X. Bogetti**, C. Arora, J. Wang, and S. Saxena. Orientation and Dynamics of $Cu^{2+}$ Based DNA Labels from Force Field Parameterized MD Elucidates the Relationship between EPR Distance Constraints and DNA Backbone Distances. *Phys. Chem. Chem. Phys.* **2020**, *22*(46), 26707-26719. This paper is highlighted as a journal cover.

Looking forward, we anticipate building upon our current efforts to resolve entire protein conformational transition pathways using EPR-obtained distance distributions directly in atomistic MD simulations. The recent development of combining weighted ensemble-MD simulations with minimal insights from EPR (i.e. the increased RMSD values of the $\alpha 9$ helices) has enabled the sampling of the conformational transition leading to the ligand-free ensemble of a detoxification enzyme. However, these simulations do not have the spin labels included, making it unclear how to compare MD-sampled distances with the EPR distance distributions. Without comparing directly to the EPR distribution, direct interpretation of the MD-sampled conformations is ambiguous. In the future, EPR distance distributions should be used directly as a progress coordinate, leading to more efficient sampling of alternate states.

To showcase this method, we will identify benchmark systems that switch between experimentally-resolved functional states, such as the Lysine/Arginine/Ornithine (LAO) binding protein and the maltose binding proteins. These benchmark proteins have two domains, and the angle between these two domains differentiates the two states of proteins. The crystal structures of both the ligand-free (open) and ligand-bound (closed) states of the two proteins have been solved by X-ray crystallography and will be used in our work as initial structures for simulation.

Initial efforts to explore this avenue involved first deciding how to label the benchmark proteins *in silico* with dHis-Cu(II). Next, initial WE simulations using the Cu(II)-Cu(II) distance distributions as a progress coordinate captured conformational transitions from the closed to the open conformation of the LAO binding protein. While this achievement marked significant progress, validations of the open conformation sampled will be needed. In the future, long conventional MD simulations will be performed starting from the open conformations sampled by weighted ensemble to verify if the conformations we sampled are the expected stable conformations.

We have so far only tested the feasibility of the weighted ensemble-EPR approach by using the MD-sampled Cu(II)-Cu(II) distance distributions as a progress coordinate. In the future, one will need to validate our choice of the labeling sites through experimental EPR distance measurements. The EPR distance measurements using dHis-Cu(II) spin labels on both protein systems will require mutagenesis, protein expression and purifications, protein functional tests, and spin labeling for the EPR measurements.

# Bibliography

(1) Hubbell, W. L.; López, C. J.; Altenbach, C.; Yang, Z. Technological Advances in Site-Directed Spin Labeling of Proteins. *Curr. Opin. Struct. Biol.* **2013**, *23* (5), 725–733. https://doi.org/10.1016/j.sbi.2013.06.008.

(2) Hubbell, W. L.; Mchaourab, H. S.; Altenbach, C.; Lietzow, M. A. Watching Proteins Move Using Site-Directed Spin Labeling. *Structure* **1996**, *4* (7), 779–783. https://doi.org/10.1016/S0969-2126(96)00085-8.

(3) Bordignon, E.; Steinhoff, H.-J. Membrane Protein Structure and Dynamics Studied by Site-Directed Spin-Labeling ESR. In *ESR Spectroscopy in Membrane Biophysics*; Biological Magnetic Resonance; Springer US: Boston, MA, 2007; Vol. 27, pp 129–164. https://doi.org/10.1007/978-0-387-49367-1_5.

(4) Klug, C. S.; Feix, J. B. Methods and Applications of Site-Directed Spin Labeling EPR Spectroscopy. In *Methods in Cell Biology*; Elsevier, 2008; Vol. 84, pp 617–658. https://doi.org/10.1016/S0091-679X(07)84020-9.

(5) Dalmas, O.; Sompornpisut, P.; Bezanilla, F.; Perozo, E. Molecular Mechanism of Mg2+-Dependent Gating in CorA. *Nat. Commun.* **2014**, *5* (1), 3590. https://doi.org/10.1038/ncomms4590.

(6) Fanucci, G. E.; Coggshall, K. A.; Cadieux, N.; Kim, M.; Kadner, R. J.; Cafiso, D. S. Substrate-Induced Conformational Changes of the Perplasmic N-Terminus of an Outer-Membrane Transporter by Site-Directed Spin Labeling. *Biochemistry* **2003**, *42* (6), 1391–1400. https://doi.org/10.1021/bi027120z.

(7) Ketter, S.; Gopinath, A.; Rogozhnikova, O.; Trukhin, D.; Tormyshev, V. M.; Bagryanskaya, E. G.; Joseph, B. In Situ Labeling and Distance Measurements of Membrane Proteins in *E. Coli* Using Finland and OX063 Trityl Labels. *Chem. – Eur. J.* **2021**, *27* (7), 2299–2304. https://doi.org/10.1002/chem.202004606.

(8) Sahu, I. D.; McCarrick, R. M.; Troxel, K. R.; Zhang, R.; Smith, H. J.; Dunagan, M. M.; Swartz, M. S.; Rajan, P. V.; Kroncke, B. M.; Sanders, C. R.; Lorigan, G. A. DEER EPR Measurements for Membrane Protein Structures via Bifunctional Spin Labels and Lipodisq Nanoparticles. *Biochemistry* **2013**, *52* (38), 6627–6632. https://doi.org/10.1021/bi4009984.

(9) Kinde, M. N.; Chen, Q.; Lawless, M. J.; Mowrey, D. D.; Xu, J.; Saxena, S.; Xu, Y.; Tang, P. Conformational Changes Underlying Desensitization of the Pentameric Ligand-Gated Ion Channel ELIC. *Structure* **2015**, *23* (6), 995–1004. https://doi.org/10.1016/j.str.2015.03.017.

(10) Pliotas, C.; Ward, R.; Branigan, E.; Rasmussen, A.; Hagelueken, G.; Huang, H.; Black, S. S.; Booth, I. R.; Schiemann, O.; Naismith, J. H. Conformational State of the MscS Mechanosensitive Channel in Solution Revealed by Pulsed Electron–Electron Double Resonance (PELDOR) Spectroscopy. *Proc. Natl. Acad. Sci.* **2012**, *109* (40). https://doi.org/10.1073/pnas.1202286109.

(11) Joseph, B.; Tormyshev, V. M.; Rogozhnikova, O. Yu.; Akhmetzyanov, D.; Bagryanskaya, E. G.; Prisner, T. F. Selective High-Resolution Detection of Membrane Protein-Ligand Interaction in Native Membranes Using Trityl-Nitroxide PELDOR. *Angew. Chem. Int. Ed.* **2016**, *55* (38), 11538–11542. https://doi.org/10.1002/anie.201606335.

(12) Igarashi, R.; Sakai, T.; Hara, H.; Tenno, T.; Tanaka, T.; Tochio, H.; Shirakawa, M. Distance Determination in Proteins inside *Xenopus Laevis* Oocytes by Double Electron−Electron Resonance Experiments. *J. Am. Chem. Soc.* **2010**, *132* (24), 8228–8229. https://doi.org/10.1021/ja906104e.

(13) Roser, P.; Schmidt, M. J.; Drescher, M.; Summerer, D. Site-Directed Spin Labeling of Proteins for Distance Measurements in Vitro and in Cells. *Org. Biomol. Chem.* **2016**, *14* (24), 5468–5476. https://doi.org/10.1039/C6OB00473C.

(14) Martorana, A.; Bellapadrona, G.; Feintuch, A.; Di Gregorio, E.; Aime, S.; Goldfarb, D. Probing Protein Conformation in Cells by EPR Distance Measurements Using Gd $^{3+}$ Spin Labeling. *J. Am. Chem. Soc.* **2014**, *136* (38), 13458–13465. https://doi.org/10.1021/ja5079392.

(15) Teucher, M.; Zhang, H.; Bader, V.; Winklhofer, K. F.; García-Sáez, A. J.; Rajca, A.; Bleicken, S.; Bordignon, E. A New Perspective on Membrane-Embedded Bax Oligomers Using DEER and Bioresistant Orthogonal Spin Labels. *Sci. Rep.* **2019**, *9* (1), 13013. https://doi.org/10.1038/s41598-019-49370-z.

(16) Joseph, B.; Sikora, A.; Bordignon, E.; Jeschke, G.; Cafiso, D. S.; Prisner, T. F. Distance Measurement on an Endogenous Membrane Transporter in *E. Coli* Cells and Native Membranes Using EPR Spectroscopy. *Angew. Chem.* **2015**, *127* (21), 6294–6297. https://doi.org/10.1002/ange.201501086.

(17) Meichsner, S. L.; Kutin, Y.; Kasanmascheff, M. In-Cell Characterization of the Stable Tyrosyl Radical in *E. Coli* Ribonucleotide Reductase Using Advanced EPR Spectroscopy. *Angew. Chem.* **2021**, *133* (35), 19304–19310. https://doi.org/10.1002/ange.202102914.

(18) Kucher, S.; Elsner, C.; Safonova, M.; Maffini, S.; Bordignon, E. In-Cell Double Electron–Electron Resonance at Nanomolar Protein Concentrations. *J. Phys. Chem. Lett.* **2021**, *12* (14), 3679–3684. https://doi.org/10.1021/acs.jpclett.1c00048.

(19) Widder, P.; Schuck, J.; Summerer, D.; Drescher, M. Combining Site-Directed Spin Labeling *in Vivo* and in-Cell EPR Distance Determination. *Phys. Chem. Chem. Phys.* **2020**, *22* (9), 4875–4879. https://doi.org/10.1039/C9CP05584C.

(20) Yang, Y.; Chen, S.-N.; Yang, F.; Li, X.-Y.; Feintuch, A.; Su, X.-C.; Goldfarb, D. In-Cell Destabilization of a Homodimeric Protein Complex Detected by DEER Spectroscopy. *Proc. Natl. Acad. Sci.* **2020**, *117* (34), 20566–20575. https://doi.org/10.1073/pnas.2005779117.

(21) Singewald, K.; Lawless, M. J.; Saxena, S. Increasing Nitroxide Lifetime in Cells to Enable In-Cell Protein Structure and Dynamics Measurements by Electron Spin Resonance Spectroscopy. *J. Magn. Reson.* **2019**, *299*, 21–27. https://doi.org/10.1016/j.jmr.2018.12.005.

(22) Karthikeyan, G.; Bonucci, A.; Casano, G.; Gerbaud, G.; Abel, S.; Thomé, V.; Kodjabachian, L.; Magalon, A.; Guigliarelli, B.; Belle, V.; Ouari, O.; Mileo, E. A Bioresistant Nitroxide Spin Label for In-Cell EPR Spectroscopy: In Vitro and In Oocytes Protein Structural Dynamics Studies. *Angew. Chem. Int. Ed.* **2018**, *57* (5), 1366–1370. https://doi.org/10.1002/anie.201710184.

(23) Jana, S.; Evans, E. G. B.; Jang, H. S.; Zhang, S.; Zhang, H.; Rajca, A.; Gordon, S. E.; Zagotta, W. N.; Stoll, S.; Mehl, R. A. Ultrafast Bioorthogonal Spin-Labeling and Distance Measurements in Mammalian Cells Using Small, Genetically Encoded Tetrazine Amino Acids. *J. Am. Chem. Soc.* **2023**, jacs.3c00967. https://doi.org/10.1021/jacs.3c00967.

(24) Fleck, N.; Heubach, C. A.; Hett, T.; Haege, F. R.; Bawol, P. P.; Baltruschat, H.; Schiemann, O. SLIM: A Short-Linked, Highly Redox-Stable Trityl Label for High-Sensitivity In-Cell

EPR Distance Measurements. *Angew. Chem.* **2020**, *132* (24), 9854–9859. https://doi.org/10.1002/ange.202004452.

(25) Krstić, I.; Hänsel, R.; Romainczyk, O.; Engels, J. W.; Dötsch, V.; Prisner, T. F. Long-Range Distance Measurements on Nucleic Acids in Cells by Pulsed EPR Spectroscopy. *Angew. Chem.* **2011**, *123* (22), 5176–5180. https://doi.org/10.1002/ange.201100886.

(26) Borbat, P. P.; Costa-Filho, A. J.; Earle, K. A.; Moscicki, J. K.; Freed, J. H. Electron Spin Resonance in Studies of Membranes and Proteins. *Science* **2001**, *291* (5502), 266–269. https://doi.org/10.1126/science.291.5502.266.

(27) Van Doorslaer, S.; Jeschke, G. Dynamics by EPR: Picosecond to Microsecond Time Scales. In *Fluxional Organometallic and Coordination Compounds*; Gielen, M., Willem, R., Wrackmeyer, B., Eds.; John Wiley & Sons, Ltd: Chichester, UK, 2005; pp 219–242. https://doi.org/10.1002/0470858451.ch6.

(28) Singewald, K.; Bogetti, X.; Sinha, K.; Rule, G. S.; Saxena, S. Double Histidine Based EPR Measurements at Physiological Temperatures Permit Site-Specific Elucidation of Hidden Dynamics in Enzymes. *Angew. Chem. Int. Ed.* **2020**, *59* (51), 23040–23044. https://doi.org/10.1002/anie.202009982.

(29) Singewald, K.; Hunter, H.; Cunningham, T. F.; Ruthstein, S.; Saxena, S. Measurement of Protein Dynamics from Site Directed Cu(II) Labeling. *Anal. Sens.* **2023**, *3* (1). https://doi.org/10.1002/anse.202200053.

(30) Singewald, K.; Wilkinson, J. A.; Hasanbasri, Z.; Saxena, S. Beyond Structure: Deciphering Site-specific Dynamics in Proteins from Double Histidine-based EPR Measurements. *Protein Sci.* **2022**, *31* (7), e4359. https://doi.org/10.1002/pro.4359.

(31) Singewald, K.; Wilkinson, J.; Saxena, S. Copper Based Site-Directed Spin Labeling of Proteins for Use in Pulsed and Continuous Wave EPR Spectroscopy. *BIO-Protoc.* **2021**, *11* (24). https://doi.org/10.21769/BioProtoc.4258.

(32) Freed, J. H. New Technologies in Electron Spin Resonance. *Annu. Rev. Phys. Chem.* **2000**, *51* (1), 655–689. https://doi.org/10.1146/annurev.physchem.51.1.655.

(33) Patyal, B. R.; Crepeau, R. H.; Gamliel, D.; Freed, J. H. Two-Dimensional Fourier Transform ESR in the Slow-Motional and Rigid Limits: SECSY-ESR. *Chem. Phys. Lett.* **1990**, *175* (5), 445–452. https://doi.org/10.1016/0009-2614(90)85562-Q.

(34) Saxena, S.; Freed, J. H. Two-Dimensional Electron Spin Resonance and Slow Motions. *J. Phys. Chem. A* **1997**, *101* (43), 7998–8008. https://doi.org/10.1021/jp9717047.

(35) Gorcester, J.; Freed, J. H. Two-Dimensional Fourier Transform ESR Correlation Spectroscopy. *J. Chem. Phys.* **1988**, *88* (8), 4678–4693. https://doi.org/10.1063/1.453782.

(36) Franck, J. M.; Chandrasekaran, S.; Dzikovski, B.; Dunnam, C. R.; Freed, J. H. Focus: Two-Dimensional Electron-Electron Double Resonance and Molecular Motions: The Challenge of Higher Frequencies. *J. Chem. Phys.* **2015**, *142* (21), 212302. https://doi.org/10.1063/1.4917322.

(37) Dzikovski, B.; Khramtsov, V. V.; Chandrasekaran, S.; Dunnam, C.; Shah, M.; Freed, J. H. Microsecond Exchange Processes Studied by Two-Dimensional ESR at 95 GHz. *J. Am. Chem. Soc.* **2020**, *142* (51), 21368–21381. https://doi.org/10.1021/jacs.0c09469.

(38) Milov, A. D.; Maryasov, A. G.; Tsvetkov, Y. D. Pulsed Electron Double Resonance (PELDOR) and Its Applications in Free-Radicals Research. *Appl. Magn. Reson.* **1998**, *15* (1), 107–143. https://doi.org/10.1007/BF03161886.

(39) Pannier, M.; Veit, S.; Godt, A.; Jeschke, G.; Spiess, H. W. Dead-Time Free Measurement of Dipole–Dipole Interactions between Electron Spins. *J. Magn. Reson.* **2011**, *213* (2), 316–325. https://doi.org/10.1016/j.jmr.2011.08.035.

(40) Casto, J.; Mandato, A.; Saxena, S. dHis-Troying Barriers: Deuteration Provides a Pathway to Increase Sensitivity and Accessible Distances for Cu $^{2+}$ Labels. *J. Phys. Chem. Lett.* **2021**, *12* (19), 4681–4685. https://doi.org/10.1021/acs.jpclett.1c01002.

(41) Schmidt, T.; Wälti, M. A.; Baber, J. L.; Hustedt, E. J.; Clore, G. M. Long Distance Measurements up to 160 Å in the GroEL Tetradecamer Using Q-Band DEER EPR Spectroscopy. *Angew. Chem. Int. Ed.* **2016**, *55* (51), 15905–15909. https://doi.org/10.1002/anie.201609617.

(42) Schmidt, T.; Jeon, J.; Yau, W.-M.; Schwieters, C. D.; Tycko, R.; Clore, G. M. Time-Resolved DEER EPR and Solid-State NMR Afford Kinetic and Structural Elucidation of Substrate Binding to Ca $^{2+}$ -Ligated Calmodulin. *Proc. Natl. Acad. Sci.* **2022**, *119* (6), e2122308119. https://doi.org/10.1073/pnas.2122308119.

(43) Schmidt, T.; Jeon, J.; Okuno, Y.; Chiliveri, S. C.; Clore, G. M. Submillisecond Freezing Permits Cryoprotectant-Free EPR Double Electron−Electron Resonance Spectroscopy. *ChemPhysChem* **2020**, *21* (12), 1224–1229. https://doi.org/10.1002/cphc.202000312.

(44) Georgieva, E. R.; Roy, A. S.; Grigoryants, V. M.; Borbat, P. P.; Earle, K. A.; Scholes, C. P.; Freed, J. H. Effect of Freezing Conditions on Distances and Their Distributions Derived from Double Electron Electron Resonance (DEER): A Study of Doubly-Spin-Labeled T4 Lysozyme. *J. Magn. Reson.* **2012**, *216*, 69–77. https://doi.org/10.1016/j.jmr.2012.01.004.

(45) Collauto, A.; DeBerg, H. A.; Kaufmann, R.; Zagotta, W. N.; Stoll, S.; Goldfarb, D. Rates and Equilibrium Constants of the Ligand-Induced Conformational Transition of an HCN Ion Channel Protein Domain Determined by DEER Spectroscopy. *Phys. Chem. Chem. Phys.* **2017**, *19* (23), 15324–15334. https://doi.org/10.1039/C7CP01925D.

(46) Hett, T.; Zbik, T.; Mukherjee, S.; Matsuoka, H.; Bönigk, W.; Klose, D.; Rouillon, C.; Brenner, N.; Peuker, S.; Klement, R.; Steinhoff, H.-J.; Grubmüller, H.; Seifert, R.; Schiemann, O.; Kaupp, U. B. Spatiotemporal Resolution of Conformational Changes in Biomolecules by Combining Pulsed Electron–Electron Double Resonance Spectroscopy with Microsecond Freeze-Hyperquenching. *J. Am. Chem. Soc.* **2021**, *143* (18), 6981–6989. https://doi.org/10.1021/jacs.1c01081.

(47) Schmidt, T.; Ghirlando, R.; Baber, J.; Clore, G. M. Quantitative Resolution of Monomer-Dimer Populations by Inversion Modulated DEER EPR Spectroscopy. *ChemPhysChem* **2016**, *17* (19), 2987–2991. https://doi.org/10.1002/cphc.201600726.

(48) Lawless, M. J.; Shimshi, A.; Cunningham, T. F.; Kinde, M. N.; Tang, P.; Saxena, S. Analysis of Nitroxide-Based Distance Measurements in Cell Extracts and in Cells by Pulsed ESR Spectroscopy. *ChemPhysChem* **2017**, *18* (12), 1653–1660. https://doi.org/10.1002/cphc.201700115.

(49) Hubbell, W. L.; Cafiso, D. S.; Altenbach, C. Identifying Conformational Changes with Site-Directed Spin Labeling. *Nat. Struct. Biol.* **2000**, *7* (9), 735–739. https://doi.org/10.1038/78956.

(50) Jeschke, G. Characterization of Protein Conformational Changes with Sparse Spin-Label Distance Constraints. *J. Chem. Theory Comput.* **2012**, *8* (10), 3854–3863. https://doi.org/10.1021/ct300113z.

(51) Assafa, T. E.; Anders, K.; Linne, U.; Essen, L.-O.; Bordignon, E. Light-Driven Domain Mechanics of a Minimal Phytochrome Photosensory Module Studied by EPR. *Structure* **2018**, *26* (11), 1534-1545.e4. https://doi.org/10.1016/j.str.2018.08.003.

(52) Liu, Z.; Casey, T. M.; Blackburn, M. E.; Huang, X.; Pham, L.; De Vera, I. M. S.; Carter, J. D.; Kear-Scott, J. L.; Veloro, A. M.; Galiano, L.; Fanucci, G. E. Pulsed EPR Characterization of HIV-1 Protease Conformational Sampling and Inhibitor-Induced Population Shifts. *Phys. Chem. Chem. Phys.* **2016**, *18* (8), 5819–5831. https://doi.org/10.1039/C5CP04556H.

(53) Hänelt, I.; Wunnicke, D.; Bordignon, E.; Steinhoff, H.-J.; Slotboom, D. J. Conformational Heterogeneity of the Aspartate Transporter GltPh. *Nat. Struct. Mol. Biol.* **2013**, *20* (2), 210–214. https://doi.org/10.1038/nsmb.2471.

(54) Verhalen, B.; Dastvan, R.; Thangapandian, S.; Peskova, Y.; Koteiche, H. A.; Nakamoto, R. K.; Tajkhorshid, E.; Mchaourab, H. S. Energy Transduction and Alternating Access of the Mammalian ABC Transporter P-Glycoprotein. *Nature* **2017**, *543* (7647), 738–741. https://doi.org/10.1038/nature21414.

(55) Joseph, B.; Sikora, A.; Cafiso, D. S. Ligand Induced Conformational Changes of a Membrane Transporter in *E. Coli* Cells Observed with DEER/PELDOR. *J. Am. Chem. Soc.* **2016**, *138* (6), 1844–1847. https://doi.org/10.1021/jacs.5b13382.

(56) Nyenhuis, D. A.; Nilaweera, T. D.; Niblo, J. K.; Nguyen, N. Q.; DuBay, K. H.; Cafiso, D. S. Evidence for the Supramolecular Organization of a Bacterial Outer-Membrane Protein from In Vivo Pulse Electron Paramagnetic Resonance Spectroscopy. *J. Am. Chem. Soc.* **2020**, *142* (24), 10715–10722. https://doi.org/10.1021/jacs.0c01754.

(57) Park, S.-Y.; Borbat, P. P.; Gonzalez-Bonet, G.; Bhatnagar, J.; Pollard, A. M.; Freed, J. H.; Bilwes, A. M.; Crane, B. R. Reconstruction of the Chemotaxis Receptor–Kinase Assembly. *Nat. Struct. Mol. Biol.* **2006**, *13* (5), 400–407. https://doi.org/10.1038/nsmb1085.

(58) Schmidt, T.; Schwieters, C. D.; Clore, G. M. Spatial Domain Organization in the HIV-1 Reverse Transcriptase P66 Homodimer Precursor Probed by Double Electron-Electron Resonance EPR. *Proc. Natl. Acad. Sci.* **2019**, *116* (36), 17809–17816. https://doi.org/10.1073/pnas.1911086116.

(59) Milikisiyants, S.; Wang, S.; Munro, R. A.; Donohue, M.; Ward, M. E.; Bolton, D.; Brown, L. S.; Smirnova, T. I.; Ladizhansky, V.; Smirnov, A. I. Oligomeric Structure of Anabaena Sensory Rhodopsin in a Lipid Bilayer Environment by Combining Solid-State NMR and Long-Range DEER Constraints. *J. Mol. Biol.* **2017**, *429* (12), 1903–1920. https://doi.org/10.1016/j.jmb.2017.05.005.

(60) Valera, S.; Ackermann, K.; Pliotas, C.; Huang, H.; Naismith, J. H.; Bode, B. E. Accurate Extraction of Nanometer Distances in Multimers by Pulse EPR. *Chem. - Eur. J.* **2016**, *22* (14), 4700–4703. https://doi.org/10.1002/chem.201505143.

(61) DeBerg, H. A.; Bankston, J. R.; Rosenbaum, J. C.; Brzovic, P. S.; Zagotta, W. N.; Stoll, S. Structural Mechanism for the Regulation of HCN Ion Channels by the Accessory Protein TRIP8b. *Structure* **2015**, *23* (4), 734–744. https://doi.org/10.1016/j.str.2015.02.007.

(62) Yin, D. M.; Hannam, J. S.; Schmitz, A.; Schiemann, O.; Hagelueken, G.; Famulok, M. Studying the Conformation of a Receptor Tyrosine Kinase in Solution by Inhibitor-Based Spin Labeling. *Angew. Chem. Int. Ed.* **2017**, *56* (29), 8417–8421. https://doi.org/10.1002/anie.201703154.

(63) Abdullin, D.; Florin, N.; Hagelueken, G.; Schiemann, O. EPR-Based Approach for the Localization of Paramagnetic Metal Ions in Biomolecules. *Angew. Chem.* **2015**, *127* (6), 1847–1851. https://doi.org/10.1002/ange.201410396.

(64) Gamble Jarvi, A.; Cunningham, T. F.; Saxena, S. Efficient Localization of a Native Metal Ion within a Protein by Cu $^{2+}$ -Based EPR Distance Measurements. *Phys. Chem. Chem. Phys.* **2019**, *21* (20), 10238–10243. https://doi.org/10.1039/C8CP07143H.

(65) Upadhyay, A. K.; Borbat, P. P.; Wang, J.; Freed, J. H.; Edmondson, D. E. Determination of the Oligomeric States of Human and Rat Monoamine Oxidases in the Outer Mitochondrial Membrane and Octyl β- D -Glucopyranoside Micelles Using Pulsed Dipolar Electron Spin Resonance Spectroscopy. *Biochemistry* **2008**, *47* (6), 1554–1566. https://doi.org/10.1021/bi7021377.

(66) Abdullin, D.; Schiemann, O. Localization of Metal Ions in Biomolecules by Means of Pulsed Dipolar EPR Spectroscopy. *Dalton Trans.* **2021**, *50* (3), 808–815. https://doi.org/10.1039/D0DT03596C.

(67) Gaffney, B. J.; Bradshaw, M. D.; Frausto, S. D.; Wu, F.; Freed, J. H.; Borbat, P. Locating a Lipid at the Portal to the Lipoxygenase Active Site. *Biophys. J.* **2012**, *103* (10), 2134–2144. https://doi.org/10.1016/j.bpj.2012.10.002.

(68) Nguyen, D.; Abdullin, D.; Heubach, C. A.; Pfaffeneder, T.; Nguyen, A.; Heine, A.; Reuter, K.; Diederich, F.; Schiemann, O.; Klebe, G. Unraveling a Ligand-Induced Twist of a Homodimeric Enzyme by Pulsed Electron–Electron Double Resonance. *Angew. Chem. Int. Ed.* **2021**, *60* (43), 23419–23426. https://doi.org/10.1002/anie.202108179.

(69) Yang, Z.; Kurpiewski, M. R.; Ji, M.; Townsend, J. E.; Mehta, P.; Jen-Jacobson, L.; Saxena, S. ESR Spectroscopy Identifies Inhibitory Cu $^{2+}$ Sites in a DNA-Modifying Enzyme to Reveal Determinants of Catalytic Specificity. *Proc. Natl. Acad. Sci.* **2012**, *109* (17). https://doi.org/10.1073/pnas.1200733109.

(70) Stone, K. M.; Townsend, J. E.; Sarver, J.; Sapienza, P. J.; Saxena, S.; Jen-Jacobson, L. Electron Spin Resonance Shows Common Structural Features for Different Classes of *Eco* RI-DNA Complexes. *Angew. Chem.* **2008**, *120* (52), 10346–10348. https://doi.org/10.1002/ange.200803588.

(71) Krumkacheva, O. A.; Shevelev, G. Y.; Lomzov, A. A.; Dyrkheeva, N. S.; Kuzhelev, A. A.; Koval, V. V.; Tormyshev, V. M.; Polienko, Y. F.; Fedin, M. V.; Pyshnyi, D. V.; Lavrik, O. I.; Bagryanskaya, E. G. DNA Complexes with Human Apurinic/Apyrimidinic Endonuclease 1: Structural Insights Revealed by Pulsed Dipolar EPR with Orthogonal Spin Labeling. *Nucleic Acids Res.* **2019**, *47* (15), 7767–7780. https://doi.org/10.1093/nar/gkz620.

(72) Sarver, J. L.; Townsend, J. E.; Rajapakse, G.; Jen-Jacobson, L.; Saxena, S. Simulating the Dynamics and Orientations of Spin-Labeled Side Chains in a Protein–DNA Complex. *J. Phys. Chem. B* **2012**, *116* (13), 4024–4033. https://doi.org/10.1021/jp211094n.

(73) Sameach, H.; Ghosh, S.; Gevorkyan-Airapetov, L.; Saxena, S.; Ruthstein, S. EPR Spectroscopy Detects Various Active State Conformations of the Transcriptional Regulator CueR. *Angew. Chem.* **2019**, *131* (10), 3085–3088. https://doi.org/10.1002/ange.201810656.

(74) Ruthstein, S.; Ji, M.; Mehta, P.; Jen-Jacobson, L.; Saxena, S. Sensitive Cu $^{2+}$ –Cu $^{2+}$ Distance Measurements in a Protein–DNA Complex by Double-Quantum Coherence ESR. *J. Phys. Chem. B* **2013**, *117* (20), 6227–6230. https://doi.org/10.1021/jp4037149.

(75) Casto, J.; Mandato, A.; Hofmann, L.; Yakobov, I.; Ghosh, S.; Ruthstein, S.; Saxena, S. Cu( II )-Based DNA Labeling Identifies the Structural Link between Transcriptional Activation

and Termination in a Metalloregulator. *Chem. Sci.* **2022**, *13* (6), 1693–1697. https://doi.org/10.1039/D1SC06563G.

(76) Schmidt, T.; Tian, L.; Clore, G. M. Probing Conformational States of the Finger and Thumb Subdomains of HIV-1 Reverse Transcriptase Using Double Electron–Electron Resonance Electron Paramagnetic Resonance Spectroscopy. *Biochemistry* **2018**, *57* (5), 489–493. https://doi.org/10.1021/acs.biochem.7b01035.

(77) Butala, M.; Klose, D.; Hodnik, V.; Rems, A.; Podlesek, Z.; Klare, J. P.; Anderluh, G.; Busby, S. J. W.; Steinhoff, H.-J.; Žgur-Bertok, D. Interconversion between Bound and Free Conformations of LexA Orchestrates the Bacterial SOS Response. *Nucleic Acids Res.* **2011**, *39* (15), 6546–6557. https://doi.org/10.1093/nar/gkr265.

(78) Tangprasertchai, N. S.; Di Felice, R.; Zhang, X.; Slaymaker, I. M.; Vazquez Reyes, C.; Jiang, W.; Rohs, R.; Qin, P. Z. CRISPR–Cas9 Mediated DNA Unwinding Detected Using Site-Directed Spin Labeling. *ACS Chem. Biol.* **2017**, *12* (6), 1489–1493. https://doi.org/10.1021/acschembio.6b01137.

(79) Reginsson, G. W.; Shelke, S. A.; Rouillon, C.; White, M. F.; Sigurdsson, S. Th.; Schiemann, O. Protein-Induced Changes in DNA Structure and Dynamics Observed with Noncovalent Site-Directed Spin Labeling and PELDOR. *Nucleic Acids Res.* **2013**, *41* (1), e11–e11. https://doi.org/10.1093/nar/gks817.

(80) Warren, G.; Stein, R.; Mchaourab, H.; Eichman, B. Movement of the RecG Motor Domain upon DNA Binding Is Required for Efficient Fork Reversal. *Int. J. Mol. Sci.* **2018**, *19* (10), 3049. https://doi.org/10.3390/ijms19103049.

(81) Sameach, H.; Ruthstein, S. EPR Distance Measurements as a Tool to Characterize Protein-DNA Interactions. *Isr. J. Chem.* **2019**, *59* (11–12), 980–989. https://doi.org/10.1002/ijch.201900091.

(82) Fajer, M. I.; Li, H.; Yang, W.; Fajer, P. G. Mapping Electron Paramagnetic Resonance Spin Label Conformations by the Simulated Scaling Method. *J. Am. Chem. Soc.* **2007**, *129* (45), 13840–13846. https://doi.org/10.1021/ja071404v.

(83) Cunningham, T. F.; Putterman, M. R.; Desai, A.; Horne, W. S.; Saxena, S. The Double-Histidine Cu $^{2+}$ -Binding Motif: A Highly Rigid, Site-Specific Spin Probe for Electron Spin Resonance Distance Measurements. *Angew. Chem.* **2015**, *127* (21), 6428–6432. https://doi.org/10.1002/ange.201501968.

(84) Lawless, M. J.; Ghosh, S.; Cunningham, T. F.; Shimshi, A.; Saxena, S. On the Use of the Cu $^{2+}$ –Iminodiacetic Acid Complex for Double Histidine Based Distance Measurements by Pulsed ESR. *Phys. Chem. Chem. Phys.* **2017**, *19* (31), 20959–20967. https://doi.org/10.1039/C7CP02564E.

(85) Ghosh, S.; Lawless, M. J.; Rule, G. S.; Saxena, S. The Cu2+-Nitrilotriacetic Acid Complex Improves Loading of α-Helical Double Histidine Site for Precise Distance Measurements by Pulsed ESR. *J. Magn. Reson.* **2018**, *286*, 163–171. https://doi.org/10.1016/j.jmr.2017.12.005.

(86) Gamble Jarvi, A.; Ranguelova, K.; Ghosh, S.; Weber, R. T.; Saxena, S. On the Use of Q-Band Double Electron–Electron Resonance To Resolve the Relative Orientations of Two Double Histidine-Bound Cu $^{2+}$ Ions in a Protein. *J. Phys. Chem. B* **2018**, *122* (47), 10669–10677. https://doi.org/10.1021/acs.jpcb.8b07727.

(87) Fanucci, G.; Cafiso, D. Recent Advances and Applications of Site-Directed Spin Labeling. *Curr. Opin. Struct. Biol.* **2006**, *16* (5), 644–653. https://doi.org/10.1016/j.sbi.2006.08.008.

(88) Hubbell, W. L.; Gross, A.; Langen, R.; Lietzow, M. A. Recent Advances in Site-Directed Spin Labeling of Proteins. *Curr. Opin. Struct. Biol.* **1998**, *8* (5), 649–656. https://doi.org/10.1016/S0959-440X(98)80158-9.

(89) Shelke, S. A.; Sigurdsson, S. Th. Site-Directed Nitroxide Spin Labeling of Biopolymers. In *Structural Information from Spin-Labels and Intrinsic Paramagnetic Centres in the Biosciences*; Timmel, C. R., Harmer, J. R., Eds.; Structure and Bonding; Springer Berlin Heidelberg: Berlin, Heidelberg, 2011; Vol. 152, pp 121–162. https://doi.org/10.1007/430_2011_62.

(90) Bogetti, X.; Bogetti, A.; Casto, J.; Rule, G.; Chong, L.; Saxena, S. Direct Observation of Negative Cooperativity in a Detoxification Enzyme at the Atomic Level by EPR and Simulation. *Protein Sci.* **2023**, e4770. https://doi.org/10.1002/pro.4770.

(91) Shah, A.; Roux, A.; Starck, M.; Mosely, J. A.; Stevens, M.; Norman, D. G.; Hunter, R. I.; El Mkami, H.; Smith, G. M.; Parker, D.; Lovett, J. E. A Gadolinium Spin Label with Both a Narrow Central Transition and Short Tether for Use in Double Electron Electron Resonance Distance Measurements. *Inorg. Chem.* **2019**, *58* (5), 3015–3025. https://doi.org/10.1021/acs.inorgchem.8b02892.

(92) Potapov, A.; Yagi, H.; Huber, T.; Jergic, S.; Dixon, N. E.; Otting, G.; Goldfarb, D. Nanometer-Scale Distance Measurements in Proteins Using Gd $^{3+}$ Spin Labeling. *J. Am. Chem. Soc.* **2010**, *132* (26), 9040–9048. https://doi.org/10.1021/ja1015662.

(93) Cunningham, T. F.; Shannon, M. D.; Putterman, M. R.; Arachchige, R. J.; Sengupta, I.; Gao, M.; Jaroniec, C. P.; Saxena, S. Cysteine-Specific Cu $^{2+}$ Chelating Tags Used as Paramagnetic Probes in Double Electron Electron Resonance. *J. Phys. Chem. B* **2015**, *119* (7), 2839–2843. https://doi.org/10.1021/jp5103143.

(94) Reginsson, G. W.; Kunjir, N. C.; Sigurdsson, S. Th.; Schiemann, O. Trityl Radicals: Spin Labels for Nanometer-Distance Measurements. *Chem. - Eur. J.* **2012**, *18* (43), 13580–13584. https://doi.org/10.1002/chem.201203014.

(95) Shevelev, G. Yu.; Krumkacheva, O. A.; Lomzov, A. A.; Kuzhelev, A. A.; Trukhin, D. V.; Rogozhnikova, O. Yu.; Tormyshev, V. M.; Pyshnyi, D. V.; Fedin, M. V.; Bagryanskaya, E. G. Triarylmethyl Labels: Toward Improving the Accuracy of EPR Nanoscale Distance Measurements in DNAs. *J. Phys. Chem. B* **2015**, *119* (43), 13641–13648. https://doi.org/10.1021/acs.jpcb.5b03026.

(96) Hasanbasri, Z.; Singewald, K.; Gluth, T. D.; Driesschaert, B.; Saxena, S. Cleavage-Resistant Protein Labeling With Hydrophilic Trityl Enables Distance Measurements *In-Cell*. *J. Phys. Chem. B* **2021**, *125* (20), 5265–5274. https://doi.org/10.1021/acs.jpcb.1c02371.

(97) Jeschke, G. Conformational Dynamics and Distribution of Nitroxide Spin Labels. *Prog. Nucl. Magn. Reson. Spectrosc.* **2013**, *72*, 42–60. https://doi.org/10.1016/j.pnmrs.2013.03.001.

(98) Haugland, M. M.; Lovett, J. E.; Anderson, E. A. Advances in the Synthesis of Nitroxide Radicals for Use in Biomolecule Spin Labelling. *Chem. Soc. Rev.* **2018**, *47* (3), 668–680. https://doi.org/anuu.

(99) Jagtap, A. P.; Krstic, I.; Kunjir, N. C.; Hänsel, R.; Prisner, T. F.; Sigurdsson, S. Th. Sterically Shielded Spin Labels for In-Cell EPR Spectroscopy: Analysis of Stability in Reducing Environment. *Free Radic. Res.* **2015**, *49* (1), 78–85. https://doi.org/10.3109/10715762.2014.979409.

(100) Yang, Y.; Yang, F.; Gong, Y.-J.; Bahrenberg, T.; Feintuch, A.; Su, X.-C.; Goldfarb, D. High Sensitivity In-Cell EPR Distance Measurements on Proteins Using an Optimized Gd(III)

Spin Label. *J. Phys. Chem. Lett.* **2018**, *9* (20), 6119–6123. https://doi.org/10.1021/acs.jpclett.8b02663.

(101) Braun, T.; Drescher, M.; Summerer, D. Expanding the Genetic Code for Site-Directed Spin-Labeling. *Int. J. Mol. Sci.* **2019**, *20* (2), 373. https://doi.org/10.3390/ijms20020373.

(102) Mchaourab, H. S.; Kálai, T.; Hideg, K.; Hubbell, W. L. Motion of Spin-Labeled Side Chains in T4 Lysozyme: Effect of Side Chain Structure. *Biochemistry* **1999**, *38* (10), 2947–2955. https://doi.org/10.1021/bi9826310.

(103) Mchaourab, H. S.; Lietzow, M. A.; Hideg, K.; Hubbell, W. L. Motion of Spin-Labeled Side Chains in T4 Lysozyme. Correlation with Protein Structure and Dynamics. *Biochemistry* **1996**, *35* (24), 7692–7704. https://doi.org/10.1021/bi960482k.

(104) Lietzow, M. A.; Hubbell, W. L. Motion of Spin Label Side Chains in Cellular Retinol-Binding Protein: Correlation with Structure and Nearest-Neighbor Interactions in an Antiparallel β-Sheet. *Biochemistry* **2004**, *43* (11), 3137–3151. https://doi.org/10.1021/bi0360962.

(105) Fleissner, M. R.; Bridges, M. D.; Brooks, E. K.; Cascio, D.; Kálai, T.; Hideg, K.; Hubbell, W. L. Structure and Dynamics of a Conformationally Constrained Nitroxide Side Chain and Applications in EPR Spectroscopy. *Proc. Natl. Acad. Sci.* **2011**, *108* (39), 16241–16246. https://doi.org/10.1073/pnas.1111420108.

(106) Stevens, M. A.; McKay, J. E.; Robinson, J. L. S.; El Mkami, H.; Smith, G. M.; Norman, D. G. The Use of the Rx Spin Label in Orientation Measurement on Proteins, by EPR. *Phys. Chem. Chem. Phys.* **2016**, *18* (8), 5799–5806. https://doi.org/10.1039/C5CP04753F.

(107) McCracken, J.; Peisach, J.; Dooley, D. M. Cu(II) Coordination Chemistry of Amine Oxidases. Pulsed EPR Studies of Histidine Imidazole, Water, and Exogenous Ligand Coordination. *J. Am. Chem. Soc.* **1987**, *109* (13), 4064–4072. https://doi.org/10.1021/ja00247a037.

(108) Dooley, D. M.; Scott, R. A.; Knowles, P. F.; Colangelo, C. M.; McGuirl, M. A.; Brown, D. E. Structures of the Cu(I) and Cu(II) Forms of Amine Oxidases from X-Ray Absorption Spectroscopy. *J. Am. Chem. Soc.* **1998**, *120* (11), 2599–2605. https://doi.org/10.1021/ja970312a.

(109) Shepard, E. M.; Dooley, D. M. Inhibition and Oxygen Activation in Copper Amine Oxidases. *Acc. Chem. Res.* **2015**, *48* (5), 1218–1226. https://doi.org/10.1021/ar500460z.

(110) Lai, X.; Wichers, H. J.; Soler-Lopez, M.; Dijkstra, B. W. Structure of Human Tyrosinase Related Protein 1 Reveals a Binuclear Zinc Active Site Important for Melanogenesis. *Angew. Chem. Int. Ed.* **2017**, *56* (33), 9812–9815. https://doi.org/10.1002/anie.201704616.

(111) Noh, H.; Lee, S. J.; Jo, H.-J.; Choi, H. W.; Hong, S.; Kong, K.-H. Histidine Residues at the Copper-Binding Site in Human Tyrosinase Are Essential for Its Catalytic Activities. *J. Enzyme Inhib. Med. Chem.* **2020**, *35* (1), 726–732. https://doi.org/10.1080/14756366.2020.1740691.

(112) Gamble Jarvi, A.; Casto, J.; Saxena, S. Buffer Effects on Site Directed Cu2+-Labeling Using the Double Histidine Motif. *J. Magn. Reson.* **2020**, *320*, 106848. https://doi.org/10.1016/j.jmr.2020.106848.

(113) Wort, J. L.; Arya, S.; Ackermann, K.; Stewart, A. J.; Bode, B. E. Pulse Dipolar EPR Reveals Double-Histidine Motif Cu $^{II}$ –NTA Spin-Labeling Robustness against Competitor Ions. *J. Phys. Chem. Lett.* **2021**, *12* (11), 2815–2819. https://doi.org/10.1021/acs.jpclett.1c00211.

(114) Shelke, S. A.; Sigurdsson, S. Th. Site-Directed Spin Labeling for EPR Studies of Nucleic Acids. In *Modified Nucleic Acids*; Nakatani, K., Tor, Y., Eds.; Nucleic Acids and Molecular

Biology; Springer International Publishing: Cham, 2016; Vol. 31, pp 159–187. https://doi.org/10.1007/978-3-319-27111-8_8.

(115) Reginsson, G. W.; Schiemann, O. Spin Labeling of DNA and RNA. In *Encyclopedia of Biophysics*; Roberts, G. C. K., Ed.; Springer Berlin Heidelberg: Berlin, Heidelberg, 2013; pp 2429–2431. https://doi.org/10.1007/978-3-642-16712-6_586.

(116) Prisner, T. F.; Marko, A.; Sigurdsson, S. Th. Conformational Dynamics of Nucleic Acid Molecules Studied by PELDOR Spectroscopy with Rigid Spin Labels. *J. Magn. Reson.* **2015**, *252*, 187–198. https://doi.org/10.1016/j.jmr.2014.12.008.

(117) Nguyen, P.; Qin, P. Z. RNA Dynamics: Perspectives from Spin Labels: RNA Dynamics by SDSL. *Wiley Interdiscip. Rev. RNA* **2012**, *3* (1), 62–72. https://doi.org/10.1002/wrna.104.

(118) Wojciechowski, F.; Groß, A.; Holder, I. T.; Knörr, L.; Drescher, M.; Hartig, J. S. Pulsed EPR Spectroscopy Distance Measurements of DNA Internally Labelled with Gd $^{3+}$ -DOTA. *Chem. Commun.* **2015**, *51* (72), 13850–13853. https://doi.org/10.1039/C5CC04234H.

(119) Song, Y.; Meade, T. J.; Astashkin, A. V.; Klein, E. L.; Enemark, J. H.; Raitsimring, A. Pulsed Dipolar Spectroscopy Distance Measurements in Biomacromolecules Labeled with Gd(III) Markers. *J. Magn. Reson.* **2011**, *210* (1), 59–68. https://doi.org/10.1016/j.jmr.2011.02.010.

(120) Engelhard, D. M.; Meyer, A.; Berndhäuser, A.; Schiemann, O.; Clever, G. H. Di-Copper( II ) DNA G-Quadruplexes as EPR Distance Rulers. *Chem. Commun.* **2018**, *54* (54), 7455–7458. https://doi.org/10.1039/C8CC04053B.

(121) Stratmann, L. M.; Kutin, Y.; Kasanmascheff, M.; Clever, G. H. Precise Distance Measurements in DNA G-Quadruplex Dimers and Sandwich Complexes by Pulsed Dipolar EPR Spectroscopy. *Angew. Chem. Int. Ed.* **2021**, *60* (9), 4939–4947. https://doi.org/10.1002/anie.202008618.

(122) Donohue, M. P.; Szalai, V. A. Distance Measurements between Paramagnetic Ligands Bound to Parallel Stranded Guanine Quadruplexes. *Phys. Chem. Chem. Phys.* **2016**, *18* (22), 15447–15455. https://doi.org/10.1039/C6CP01121G.

(123) Shevelev, G. Yu.; Krumkacheva, O. A.; Lomzov, A. A.; Kuzhelev, A. A.; Rogozhnikova, O. Yu.; Trukhin, D. V.; Troitskaya, T. I.; Tormyshev, V. M.; Fedin, M. V.; Pyshnyi, D. V.; Bagryanskaya, E. G. Physiological-Temperature Distance Measurement in Nucleic Acid Using Triarylmethyl-Based Spin Labels and Pulsed Dipolar EPR Spectroscopy. *J. Am. Chem. Soc.* **2014**, *136* (28), 9874–9877. https://doi.org/10.1021/ja505122n.

(124) Lawless, M. J.; Sarver, J. L.; Saxena, S. Nucleotide-Independent Copper(II)-Based Distance Measurements in DNA by Pulsed ESR Spectroscopy. *Angew. Chem. Int. Ed.* **2017**, *56* (8), 2115–2117. https://doi.org/10.1002/anie.201611197.

(125) Ghosh, S.; Lawless, M. J.; Brubaker, H. J.; Singewald, K.; Kurpiewski, M. R.; Jen-Jacobson, L.; Saxena, S. Cu2+-Based Distance Measurements by Pulsed EPR Provide Distance Constraints for DNA Backbone Conformations in Solution. *Nucleic Acids Res.* **2020**, *48* (9), e49–e49. https://doi.org/10.1093/nar/gkaa133.

(126) Ghosh, S.; Casto, J.; Bogetti, X.; Arora, C.; Wang, J.; Saxena, S. Orientation and Dynamics of Cu $^{2+}$ Based DNA Labels from Force Field Parameterized MD Elucidates the Relationship between EPR Distance Constraints and DNA Backbone Distances. *Phys. Chem. Chem. Phys.* **2020**, *22* (46), 26707–26719. https://doi.org/10.1039/D0CP05016D.

(127) Gamble Jarvi, A.; Sargun, A.; Bogetti, X.; Wang, J.; Achim, C.; Saxena, S. Development of Cu $^{2+}$ -Based Distance Methods and Force Field Parameters for the Determination of PNA

Conformations and Dynamics by EPR and MD Simulations. *J. Phys. Chem. B* **2020**, *124* (35), 7544–7556. https://doi.org/10.1021/acs.jpcb.0c05509.

(128) Case, D.; Ben-Shalom, I.; Brozell, S.; Cerutti, D.; Cheatham III, T.; Cruzeiro, V.; Darden, T.; Duke, R.; Ghoreishi, D.; Gilson, M.; others. AMBER 2018; 2018. *Univ. Calif. San Franc.* **2018**.

(129) Salomon-Ferrer, R.; Case, D. A.; Walker, R. C. An Overview of the Amber Biomolecular Simulation Package: Amber Biomolecular Simulation Package. *Wiley Interdiscip. Rev. Comput. Mol. Sci.* **2013**, *3* (2), 198–210. https://doi.org/10.1002/wcms.1121.

(130) Brooks, B. R.; Brooks, C. L.; Mackerell, A. D.; Nilsson, L.; Petrella, R. J.; Roux, B.; Won, Y.; Archontis, G.; Bartels, C.; Boresch, S.; Caflisch, A.; Caves, L.; Cui, Q.; Dinner, A. R.; Feig, M.; Fischer, S.; Gao, J.; Hodoscek, M.; Im, W.; Kuczera, K.; Lazaridis, T.; Ma, J.; Ovchinnikov, V.; Paci, E.; Pastor, R. W.; Post, C. B.; Pu, J. Z.; Schaefer, M.; Tidor, B.; Venable, R. M.; Woodcock, H. L.; Wu, X.; Yang, W.; York, D. M.; Karplus, M. CHARMM: The Biomolecular Simulation Program. *J. Comput. Chem.* **2009**, *30* (10), 1545–1614. https://doi.org/10.1002/jcc.21287.

(131) Brooks, B. R.; Bruccoleri, R. E.; Olafson, B. D.; States, D. J.; Swaminathan, S.; Karplus, M. CHARMM: A Program for Macromolecular Energy, Minimization, and Dynamics Calculations. *J. Comput. Chem.* **1983**, *4* (2), 187–217. https://doi.org/10.1002/jcc.540040211.

(132) Oostenbrink, C.; Villa, A.; Mark, A. E.; Van Gunsteren, W. F. A Biomolecular Force Field Based on the Free Enthalpy of Hydration and Solvation: The GROMOS Force-Field Parameter Sets 53A5 and 53A6. *J. Comput. Chem.* **2004**, *25* (13), 1656–1676. https://doi.org/10.1002/jcc.20090.

(133) Scott, W. R. P.; Hünenberger, P. H.; Tironi, I. G.; Mark, A. E.; Billeter, S. R.; Fennen, J.; Torda, A. E.; Huber, T.; Krüger, P.; Van Gunsteren, W. F. The GROMOS Biomolecular Simulation Program Package. *J. Phys. Chem. A* **1999**, *103* (19), 3596–3607. https://doi.org/10.1021/jp984217f.

(134) Sezer, D.; Freed, J. H.; Roux, B. Parametrization, Molecular Dynamics Simulation, and Calculation of Electron Spin Resonance Spectra of a Nitroxide Spin Label on a Polyalanine α-Helix. *J. Phys. Chem. B* **2008**, *112* (18), 5755–5767. https://doi.org/10.1021/jp711375x.

(135) Sale, K.; Song, L.; Liu, Y.-S.; Perozo, E.; Fajer, P. Explicit Treatment of Spin Labels in Modeling of Distance Constraints from Dipolar EPR and DEER. *J. Am. Chem. Soc.* **2005**, *127* (26), 9334–9335. https://doi.org/10.1021/ja051652w.

(136) Cunningham, T. F.; Pornsuwan, S.; Horne, W. S.; Saxena, S. Rotameric Preferences of a Protein Spin Label at Edge-Strand β-Sheet Sites: R1 Rotameric Preferences in β-Sheet Edge Strands. *Protein Sci.* **2016**, *25* (5), 1049–1060. https://doi.org/10.1002/pro.2918.

(137) Islam, S. M.; Stein, R. A.; Mchaourab, H. S.; Roux, B. Structural Refinement from Restrained-Ensemble Simulations Based on EPR/DEER Data: Application to T4 Lysozyme. *J. Phys. Chem. B* **2013**, *117* (17), 4740–4754. https://doi.org/10.1021/jp311723a.

(138) Islam, S. M.; Roux, B. Simulating the Distance Distribution between Spin-Labels Attached to Proteins. *J. Phys. Chem. B* **2015**, *119* (10), 3901–3911. https://doi.org/10.1021/jp510745d.

(139) Bogetti, X.; Ghosh, S.; Gamble Jarvi, A.; Wang, J.; Saxena, S. Molecular Dynamics Simulations Based on Newly Developed Force Field Parameters for Cu $^{2+}$ Spin Labels Provide Insights into Double-Histidine-Based Double Electron–Electron Resonance. *J. Phys. Chem. B* **2020**, *124* (14), 2788–2797. https://doi.org/10.1021/acs.jpcb.0c00739.

(140) Domnick, C.; Eggert, F.; Wuebben, C.; Bornewasser, L.; Hagelueken, G.; Schiemann, O.; Kath-Schorr, S. EPR Distance Measurements on Long Non-coding RNAs Empowered by Genetic Alphabet Expansion Transcription. *Angew. Chem.* **2020**, *132* (20), 7965–7970. https://doi.org/10.1002/ange.201916447.

(141) Heinz, M.; Erlenbach, N.; Stelzl, L. S.; Thierolf, G.; Kamble, N. R.; Sigurdsson, S. T.; Prisner, T. F.; Hummer, G. High-Resolution EPR Distance Measurements on RNA and DNA with the Non-Covalent Ǵ Spin Label. *Nucleic Acids Res.* **2020**, *48* (2), 924–933. https://doi.org/10.1093/nar/gkz1096.

(142) Qin, P. Z.; Haworth, I. S.; Cai, Q.; Kusnetzow, A. K.; Grant, G. P. G.; Price, E. A.; Sowa, G. Z.; Popova, A.; Herreros, B.; He, H. Measuring Nanometer Distances in Nucleic Acids Using a Sequence-Independent Nitroxide Probe. *Nat. Protoc.* **2007**, *2* (10), 2354–2365. https://doi.org/10.1038/nprot.2007.308.

(143) Qin, P. Z.; Butcher, S. E.; Feigon, J.; Hubbell, W. L. Quantitative Analysis of the Isolated GAAA Tetraloop/Receptor Interaction in Solution: A Site-Directed Spin Labeling Study. *Biochemistry* **2001**, *40* (23), 6929–6936. https://doi.org/10.1021/bi010294g.

(144) Tian, C.; Kasavajhala, K.; Belfon, K. A. A.; Raguette, L.; Huang, H.; Migues, A. N.; Bickel, J.; Wang, Y.; Pincay, J.; Wu, Q.; Simmerling, C. ff19SB: Amino-Acid-Specific Protein Backbone Parameters Trained against Quantum Mechanics Energy Surfaces in Solution. *J. Chem. Theory Comput.* **2020**, *16* (1), 528–552. https://doi.org/10.1021/acs.jctc.9b00591.

(145) Spicher, S.; Grimme, S. Robust Atomistic Modeling of Materials, Organometallic, and Biochemical Systems. *Angew. Chem. Int. Ed.* **2020**, *59* (36), 15665–15673. https://doi.org/10.1002/anie.202004239.

(146) Boothroyd, S.; Behara, P. K.; Madin, O. C.; Hahn, D. F.; Jang, H.; Gapsys, V.; Wagner, J. R.; Horton, J. T.; Dotson, D. L.; Thompson, M. W.; Maat, J.; Gokey, T.; Wang, L.-P.; Cole, D. J.; Gilson, M. K.; Chodera, J. D.; Bayly, C. I.; Shirts, M. R.; Mobley, D. L. Development and Benchmarking of Open Force Field 2.0.0: The Sage Small Molecule Force Field. *J. Chem. Theory Comput.* **2023**, *19* (11), 3251–3275. https://doi.org/10.1021/acs.jctc.3c00039.

(147) Wang, J.; Wolf, R. M.; Caldwell, J. W.; Kollman, P. A.; Case, D. A. Development and Testing of a General Amber Force Field. *J. Comput. Chem.* **2004**, *25* (9), 1157–1174. https://doi.org/10.1002/jcc.20035.

(148) Jorgensen, W. L.; Maxwell, D. S.; Tirado-Rives, J. Development and Testing of the OPLS All-Atom Force Field on Conformational Energetics and Properties of Organic Liquids. *J. Am. Chem. Soc.* **1996**, *118* (45), 11225–11236. https://doi.org/10.1021/ja9621760.

(149) Altenbach, C.; López, C. J.; Hideg, K.; Hubbell, W. L. Exploring Structure, Dynamics, and Topology of Nitroxide Spin-Labeled Proteins Using Continuous-Wave Electron Paramagnetic Resonance Spectroscopy. In *Methods in Enzymology*; Elsevier, 2015; Vol. 564, pp 59–100. https://doi.org/10.1016/bs.mie.2015.08.006.

(150) Fleissner, M. R.; Cascio, D.; Hubbell, W. L. Structural Origin of Weakly Ordered Nitroxide Motion in Spin-Labeled Proteins. *Protein Sci.* **2009**, *18* (5), 893–908. https://doi.org/10.1002/pro.96.

(151) Kroncke, B. M.; Horanyi, P. S.; Columbus, L. Structural Origins of Nitroxide Side Chain Dynamics on Membrane Protein α-Helical Sites,. *Biochemistry* **2010**, *49* (47), 10045–10060. https://doi.org/10.1021/bi101148w.

(152) Pliotas, C.; Dahl, A. C. E.; Rasmussen, T.; Mahendran, K. R.; Smith, T. K.; Marius, P.; Gault, J.; Banda, T.; Rasmussen, A.; Miller, S.; Robinson, C. V.; Bayley, H.; Sansom, M.

S. P.; Booth, I. R.; Naismith, J. H. The Role of Lipids in Mechanosensation. *Nat. Struct. Mol. Biol.* **2015**, *22* (12), 991–998. https://doi.org/10.1038/nsmb.3120.

(153) Sezer, D.; Freed, J. H.; Roux, B. Using Markov Models to Simulate Electron Spin Resonance Spectra from Molecular Dynamics Trajectories. *J. Phys. Chem. B* **2008**, *112* (35), 11014–11027. https://doi.org/10.1021/jp801608v.

(154) Sezer, D.; Freed, J. H.; Roux, B. Multifrequency Electron Spin Resonance Spectra of a Spin-Labeled Protein Calculated from Molecular Dynamics Simulations. *J. Am. Chem. Soc.* **2009**, *131* (7), 2597–2605. https://doi.org/10.1021/ja8073819.

(155) Steinhoff, H. J.; Hubbell, W. L. Calculation of Electron Paramagnetic Resonance Spectra from Brownian Dynamics Trajectories: Application to Nitroxide Side Chains in Proteins. *Biophys. J.* **1996**, *71* (4), 2201–2212. https://doi.org/10.1016/S0006-3495(96)79421-3.

(156) Steinhoff, H.-J.; Müller, M.; Beier, C.; Pfeiffer, M. Molecular Dynamics Simulation and EPR Spectroscopy of Nitroxide Side Chains in Bacteriorhodopsin. *J. Mol. Liq.* **2000**, *84* (1), 17–27. https://doi.org/10.1016/S0167-7322(99)00107-5.

(157) Oganesyan, V. S.; Chami, F.; White, G. F.; Thomson, A. J. A Combined EPR and MD Simulation Study of a Nitroxyl Spin Label with Restricted Internal Mobility Sensitive to Protein Dynamics. *J. Magn. Reson.* **2017**, *274*, 24–35. https://doi.org/10.1016/j.jmr.2016.11.001.

(158) Izmailov, S. A.; Rabdano, S. O.; Hasanbasri, Z.; Podkorytov, I. S.; Saxena, S.; Skrynnikov, N. R. Structural and Dynamic Origins of ESR Lineshapes in Spin-Labeled GB1 Domain: The Insights from Spin Dynamics Simulations Based on Long MD Trajectories. *Sci. Rep.* **2020**, *10* (1), 957. https://doi.org/10.1038/s41598-019-56750-y.

(159) Ahammad, T.; Khan, R. H.; Sahu, I. D.; Drew, D. L.; Faul, E.; Li, T.; McCarrick, R. M.; Lorigan, G. A. Pinholin S21 Mutations Induce Structural Topology and Conformational Changes. *Biochim. Biophys. Acta BBA - Biomembr.* **2021**, *1863* (12), 183771. https://doi.org/10.1016/j.bbamem.2021.183771.

(160) Carter, J. D.; Mathias, J. D.; Gomez, E. F.; Ran, Y.; Xu, F.; Galiano, L.; Tran, N. Q.; D'Amore, P. W.; Wright, C. S.; Chakravorty, D. K.; Fanucci, G. E. Characterizing Solution Surface Loop Conformational Flexibility of the GM2 Activator Protein. *J. Phys. Chem. B* **2014**, *118* (36), 10607–10617. https://doi.org/10.1021/jp505938t.

(161) Beier, C.; Steinhoff, H.-J. A Structure-Based Simulation Approach for Electron Paramagnetic Resonance Spectra Using Molecular and Stochastic Dynamics Simulations. *Biophys. J.* **2006**, *91* (7), 2647–2664. https://doi.org/10.1529/biophysj.105.080051.

(162) Budil, D. E.; Sale, K. L.; Khairy, K. A.; Fajer, P. G. Calculating Slow-Motional Electron Paramagnetic Resonance Spectra from Molecular Dynamics Using a Diffusion Operator Approach. *J. Phys. Chem. A* **2006**, *110* (10), 3703–3713. https://doi.org/10.1021/jp054738k.

(163) DeSensi, S. C.; Rangel, D. P.; Beth, A. H.; Lybrand, T. P.; Hustedt, E. J. Simulation of Nitroxide Electron Paramagnetic Resonance Spectra from Brownian Trajectories and Molecular Dynamics Simulations. *Biophys. J.* **2008**, *94* (10), 3798–3809. https://doi.org/10.1529/biophysj.107.125419.

(164) Oganesyan, V. S. A Novel Approach to the Simulation of Nitroxide Spin Label EPR Spectra from a Single Truncated Dynamical Trajectory. *J. Magn. Reson.* **2007**, *188* (2), 196–205. https://doi.org/10.1016/j.jmr.2007.07.001.

(165) Sezer, D.; Freed, J. H.; Roux, B. Simulating Electron Spin Resonance Spectra of Nitroxide Spin Labels from Molecular Dynamics and Stochastic Trajectories. *J. Chem. Phys.* **2008**, *128* (16), 165106. https://doi.org/10.1063/1.2908075.

(166) Martin, P. D.; Svensson, B.; Thomas, D. D.; Stoll, S. Trajectory-Based Simulation of EPR Spectra: Models of Rotational Motion for Spin Labels on Proteins. *J. Phys. Chem. B* **2019**, *123* (48), 10131–10141. https://doi.org/10.1021/acs.jpcb.9b02693.

(167) Rangel, D. P.; Baveye, P. C.; Robinson, B. H. Direct Simulation of Magnetic Resonance Relaxation Rates and Line Shapes from Molecular Trajectories. *J. Phys. Chem. B* **2012**, *116* (22), 6233–6249. https://doi.org/10.1021/jp2062628.

(168) Mchaourab, H. S.; Steed, P. R.; Kazmier, K. Toward the Fourth Dimension of Membrane Protein Structure: Insight into Dynamics from Spin-Labeling EPR Spectroscopy. *Structure* **2011**, *19* (11), 1549–1561. https://doi.org/10.1016/j.str.2011.10.009.

(169) Polyhach, Y.; Bordignon, E.; Jeschke, G. Rotamer Libraries of Spin Labelled Cysteines for Protein Studies. *Phys Chem Chem Phys* **2011**, *13* (6), 2356–2366. https://doi.org/10.1039/C0CP01865A.

(170) Jeschke, G. MMM: A Toolbox for Integrative Structure Modeling: A Toolbox for Integrative Structure Modeling. *Protein Sci.* **2018**, *27* (1), 76–85. https://doi.org/10.1002/pro.3269.

(171) Jeschke, G.; Esteban-Hofer, L. Integrative Ensemble Modeling of Proteins and Their Complexes with Distance Distribution Restraints. In *Methods in Enzymology*; Elsevier, 2022; Vol. 666, pp 145–169. https://doi.org/10.1016/bs.mie.2022.02.010.

(172) Bordignon, E.; Bleicken, S. New Limits of Sensitivity of Site-Directed Spin Labeling Electron Paramagnetic Resonance for Membrane Proteins. *Biochim. Biophys. Acta BBA - Biomembr.* **2018**, *1860* (4), 841–853. https://doi.org/10.1016/j.bbamem.2017.12.009.

(173) Hubbell, W. L.; Altenbach, C. Investigation of Structure and Dynamics in Membrane Proteins Using Site-Directed Spin Labeling. *Curr. Opin. Struct. Biol.* **1994**, *4* (4), 566–573. https://doi.org/10.1016/S0959-440X(94)90219-4.

(174) Columbus, L.; Hubbell, W. L. A New Spin on Protein Dynamics. *Trends Biochem. Sci.* **2002**, *27* (6), 288–295. https://doi.org/10.1016/S0968-0004(02)02095-9.

(175) Torricella, F.; Pierro, A.; Mileo, E.; Belle, V.; Bonucci, A. Nitroxide Spin Labels and EPR Spectroscopy: A Powerful Association for Protein Dynamics Studies. *Biochim. Biophys. Acta BBA - Proteins Proteomics* **2021**, *1869* (7), 140653. https://doi.org/10.1016/j.bbapap.2021.140653.

(176) Oh, K. J.; Altenbach, C.; Collier, R. J.; Hubbell, W. L. Site-Directed Spin Labeling of Proteins: Applications to Diphtheria Toxin. In *Bacterial Toxins*; Humana Press: New Jersey, 2000; Vol. 145, pp 147–169. https://doi.org/10.1385/1-59259-052-7:147.

(177) Tesei, G.; Martins, J. M.; Kunze, M. B. A.; Wang, Y.; Crehuet, R.; Lindorff-Larsen, K. DEER-PREdict: Software for Efficient Calculation of Spin-Labeling EPR and NMR Data from Conformational Ensembles. *PLOS Comput. Biol.* **2021**, *17* (1), e1008551. https://doi.org/10.1371/journal.pcbi.1008551.

(178) Hagelueken, G.; Abdullin, D.; Ward, R.; Schiemann, O. mtsslSuite: *In Silico* Spin Labelling, Trilateration and Distance-Constrained Rigid Body Docking in PyMOL. *Mol. Phys.* **2013**, *111* (18–19), 2757–2766. https://doi.org/10.1080/00268976.2013.809804.

(179) Hagelueken, G.; Ward, R.; Naismith, J. H.; Schiemann, O. MtsslWizard: In Silico Spin-Labeling and Generation of Distance Distributions in PyMOL. *Appl. Magn. Reson.* **2012**, *42* (3), 377–391. https://doi.org/10.1007/s00723-012-0314-0.

(180) Hatmal, M. M.; Li, Y.; Hegde, B. G.; Hegde, P. B.; Jao, C. C.; Langen, R.; Haworth, I. S. Computer Modeling of Nitroxide Spin Labels on Proteins. *Biopolymers* **2012**, *97* (1), 35–44. https://doi.org/10.1002/bip.21699.

(181) Beasley, K. N.; Sutch, B. T.; Hatmal, M. M.; Langen, R.; Qin, P. Z.; Haworth, I. S. Computer Modeling of Spin Labels. In *Methods in Enzymology*; Elsevier, 2015; Vol. 563, pp 569–593. https://doi.org/10.1016/bs.mie.2015.07.021.

(182) Tessmer, M. H.; Stoll, S. chiLife: An Open-Source Python Package for in Silico Spin Labeling and Integrative Protein Modeling. *PLOS Comput. Biol.* **2023**, *19* (3), e1010834. https://doi.org/10.1371/journal.pcbi.1010834.

(183) Spicher, S.; Abdullin, D.; Grimme, S.; Schiemann, O. Modeling of Spin–Spin Distance Distributions for Nitroxide Labeled Biomacromolecules. *Phys. Chem. Chem. Phys.* **2020**, *22* (42), 24282–24290. https://doi.org/10.1039/D0CP04920D.

(184) Ranaldi, S.; Belle, V.; Woudstra, M.; Bourgeas, R.; Guigliarelli, B.; Roche, P.; Vezin, H.; Carrière, F.; Fournel, A. Amplitude of Pancreatic Lipase Lid Opening in Solution and Identification of Spin Label Conformational Subensembles by Combining Continuous Wave and Pulsed EPR Spectroscopy and Molecular Dynamics. *Biochemistry* **2010**, *49* (10), 2140–2149. https://doi.org/10.1021/bi901918f.

(185) Galiano, L.; Bonora, M.; Fanucci, G. E. Interflap Distances in HIV-1 Protease Determined by Pulsed EPR Measurements. *J. Am. Chem. Soc.* **2007**, *129* (36), 11004–11005. https://doi.org/10.1021/ja073684k.

(186) Ding, F.; Layten, M.; Simmerling, C. Solution Structure of HIV-1 Protease Flaps Probed by Comparison of Molecular Dynamics Simulation Ensembles and EPR Experiments. *J. Am. Chem. Soc.* **2008**, *130* (23), 7184–7185. https://doi.org/10.1021/ja800893d.

(187) Schmidt, T.; Wang, D.; Jeon, J.; Schwieters, C. D.; Clore, G. M. Quantitative Agreement between Conformational Substates of Holo Calcium-Loaded Calmodulin Detected by Double Electron–Electron Resonance EPR and Predicted by Molecular Dynamics Simulations. *J. Am. Chem. Soc.* **2022**, *144* (27), 12043–12051. https://doi.org/10.1021/jacs.2c02201.

(188) Marinelli, F.; Faraldo-Gómez, J. D. Ensemble-Biased Metadynamics: A Molecular Simulation Method to Sample Experimental Distributions. *Biophys. J.* **2015**, *108* (12), 2779–2782. https://doi.org/10.1016/j.bpj.2015.05.024.

(189) Roux, B.; Islam, S. M. Restrained-Ensemble Molecular Dynamics Simulations Based on Distance Histograms from Double Electron–Electron Resonance Spectroscopy. *J. Phys. Chem. B* **2013**, *117* (17), 4733–4739. https://doi.org/10.1021/jp3110369.

(190) Qi, Y.; Lee, J.; Cheng, X.; Shen, R.; Islam, S. M.; Roux, B.; Im, W. CHARMM-GUI DEER Facilitator for Spin-pair Distance Distribution Calculations and Preparation of Restrained-ensemble Molecular Dynamics Simulations. *J. Comput. Chem.* **2020**, *41* (5), 415–420. https://doi.org/10.1002/jcc.26032.

(191) Hustedt, E. J.; Marinelli, F.; Stein, R. A.; Faraldo-Gómez, J. D.; Mchaourab, H. S. Confidence Analysis of DEER Data and Its Structural Interpretation with Ensemble-Biased Metadynamics. *Biophys. J.* **2018**, *115* (7), 1200–1216. https://doi.org/10.1016/j.bpj.2018.08.008.

(192) Marinelli, F.; Fiorin, G. Structural Characterization of Biomolecules through Atomistic Simulations Guided by DEER Measurements. *Structure* **2019**, *27* (2), 359-370.e12. https://doi.org/10.1016/j.str.2018.10.013.

(193) Kirkpatrick, S.; Gelatt, C. D.; Vecchi, M. P. Optimization by Simulated Annealing. *Science* **1983**, *220* (4598), 671–680. https://doi.org/10.1126/science.220.4598.671.

(194) Jao, C. C.; Hegde, B. G.; Chen, J.; Haworth, I. S.; Langen, R. Structure of Membrane-Bound α-Synuclein from Site-Directed Spin Labeling and Computational Refinement. *Proc. Natl. Acad. Sci.* **2008**, *105* (50), 19666–19671. https://doi.org/10.1073/pnas.0807826105.

(195) Rohl, C. A.; Strauss, C. E. M.; Misura, K. M. S.; Baker, D. Protein Structure Prediction Using Rosetta. In *Methods in Enzymology*; Elsevier, 2004; Vol. 383, pp 66–93. https://doi.org/10.1016/S0076-6879(04)83004-0.

(196) Hirst, S. J.; Alexander, N.; Mchaourab, H. S.; Meiler, J. RosettaEPR: An Integrated Tool for Protein Structure Determination from Sparse EPR Data. *J. Struct. Biol.* **2011**, *173* (3), 506–514. https://doi.org/10.1016/j.jsb.2010.10.013.

(197) Alexander, N.; Al-Mestarihi, A.; Bortolus, M.; Mchaourab, H.; Meiler, J. De Novo High-Resolution Protein Structure Determination from Sparse Spin-Labeling EPR Data. *Structure* **2008**, *16* (2), 181–195. https://doi.org/10.1016/j.str.2007.11.015.

(198) Del Alamo, D.; Jagessar, K. L.; Meiler, J.; Mchaourab, H. S. Methodology for Rigorous Modeling of Protein Conformational Changes by Rosetta Using DEER Distance Restraints. *PLOS Comput. Biol.* **2021**, *17* (6), e1009107. https://doi.org/10.1371/journal.pcbi.1009107.

(199) Del Alamo, D.; Tessmer, M. H.; Stein, R. A.; Feix, J. B.; Mchaourab, H. S.; Meiler, J. Rapid Simulation of Unprocessed DEER Decay Data for Protein Fold Prediction. *Biophys. J.* **2020**, *118* (2), 366–375. https://doi.org/10.1016/j.bpj.2019.12.011.

(200) Tessmer, M. H.; DeCero, S. A.; Del Alamo, D.; Riegert, M. O.; Meiler, J.; Frank, D. W.; Feix, J. B. Characterization of the ExoU Activation Mechanism Using EPR and Integrative Modeling. *Sci. Rep.* **2020**, *10* (1), 19700. https://doi.org/10.1038/s41598-020-76023-3.

(201) Jumper, J.; Evans, R.; Pritzel, A.; Green, T.; Figurnov, M.; Ronneberger, O.; Tunyasuvunakool, K.; Bates, R.; Žídek, A.; Potapenko, A.; Bridgland, A.; Meyer, C.; Kohl, S. A. A.; Ballard, A. J.; Cowie, A.; Romera-Paredes, B.; Nikolov, S.; Jain, R.; Adler, J.; Back, T.; Petersen, S.; Reiman, D.; Clancy, E.; Zielinski, M.; Steinegger, M.; Pacholska, M.; Berghammer, T.; Bodenstein, S.; Silver, D.; Vinyals, O.; Senior, A. W.; Kavukcuoglu, K.; Kohli, P.; Hassabis, D. Highly Accurate Protein Structure Prediction with AlphaFold. *Nature* **2021**, *596* (7873), 583–589. https://doi.org/10.1038/s41586-021-03819-2.

(202) Tunyasuvunakool, K.; Adler, J.; Wu, Z.; Green, T.; Zielinski, M.; Žídek, A.; Bridgland, A.; Cowie, A.; Meyer, C.; Laydon, A.; Velankar, S.; Kleywegt, G. J.; Bateman, A.; Evans, R.; Pritzel, A.; Figurnov, M.; Ronneberger, O.; Bates, R.; Kohl, S. A. A.; Potapenko, A.; Ballard, A. J.; Romera-Paredes, B.; Nikolov, S.; Jain, R.; Clancy, E.; Reiman, D.; Petersen, S.; Senior, A. W.; Kavukcuoglu, K.; Birney, E.; Kohli, P.; Jumper, J.; Hassabis, D. Highly Accurate Protein Structure Prediction for the Human Proteome. *Nature* **2021**, *596* (7873), 590–596. https://doi.org/10.1038/s41586-021-03828-1.

(203) Del Alamo, D.; Sala, D.; Mchaourab, H. S.; Meiler, J. Sampling Alternative Conformational States of Transporters and Receptors with AlphaFold2. *eLife* **2022**, *11*, e75751. https://doi.org/10.7554/eLife.75751.

(204) Del Alamo, D.; DeSousa, L.; Nair, R. M.; Rahman, S.; Meiler, J.; Mchaourab, H. S. Integrated AlphaFold2 and DEER Investigation of the Conformational Dynamics of a pH-Dependent APC Antiporter. *Proc. Natl. Acad. Sci.* **2022**, *119* (34), e2206129119. https://doi.org/10.1073/pnas.2206129119.

(205) Hammond, C. M.; Owen-Hughes, T.; Norman, D. G. Modelling Multi-Protein Complexes Using PELDOR Distance Measurements for Rigid Body Minimisation Experiments Using XPLOR-NIH. *Methods* **2014**, *70* (2–3), 139–153. https://doi.org/10.1016/j.ymeth.2014.10.028.

(206) MacCallum, J. L.; Perez, A.; Dill, K. A. Determining Protein Structures by Combining Semireliable Data with Atomistic Physical Models by Bayesian Inference. *Proc. Natl. Acad. Sci.* **2015**, *112* (22), 6985–6990. https://doi.org/10.1073/pnas.1506788112.

(207) Schwieters, C. D.; Kuszewski, J. J.; Tjandra, N.; Marius Clore, G. The Xplor-NIH NMR Molecular Structure Determination Package. *J. Magn. Reson.* **2003**, *160* (1), 65–73. https://doi.org/10.1016/S1090-7807(02)00014-9.

(208) Bahar, I.; Rader, A. Coarse-Grained Normal Mode Analysis in Structural Biology. *Curr. Opin. Struct. Biol.* **2005**, *15* (5), 586–592. https://doi.org/10.1016/j.sbi.2005.08.007.

(209) Puljung, M. C.; DeBerg, H. A.; Zagotta, W. N.; Stoll, S. Double Electron–Electron Resonance Reveals cAMP-Induced Conformational Change in HCN Channels. *Proc. Natl. Acad. Sci.* **2014**, *111* (27), 9816–9821. https://doi.org/10.1073/pnas.1405371111.

(210) Jeschke, G. Integration of Nanometer-Range Label-to-Label Distances and Their Distributions into Modelling Approaches. *Biomolecules* **2022**, *12* (10), 1369. https://doi.org/10.3390/biom12101369.

(211) Jeschke, G. MMM : Integrative Ensemble Modeling and Ensemble Analysis. *Protein Sci.* **2021**, *30* (1), 125–135. https://doi.org/10.1002/pro.3965.

(212) Sala, D.; Del Alamo, D.; Mchaourab, H. S.; Meiler, J. Modeling of Protein Conformational Changes with Rosetta Guided by Limited Experimental Data. *Structure* **2022**, *30* (8), 1157-1168.e3. https://doi.org/10.1016/j.str.2022.04.013.

(213) Le Trong, I.; Stenkamp, R. E.; Ibarra, C.; Atkins, W. M.; Adman, E. T. 1.3-Å Resolution Structure of Human Glutathione S-Transferase with S-Hexyl Glutathione Bound Reveals Possible Extended Ligandin Binding Site: hGSTA1-1 With GTX. *Proteins Struct. Funct. Bioinforma.* **2002**, *48* (4), 618–627. https://doi.org/10.1002/prot.10162.

(214) Cameron, A. D.; Sinning, I.; L'Hermite, G.; Olin, B.; Board, P. G.; Mannervik, B.; Jones, T. A. Structural Analysis of Human Alpha-Class Glutathione Transferase A1-1 in the Apo-Form and in Complexes with Ethacrynic Acid and Its Glutathione Conjugate. *Structure* **1995**, *3* (7), 717–727. https://doi.org/10.1016/S0969-2126(01)00206-4.

(215) Pettersson, J. R.; Lanni, F.; Rule, G. S. Dual Lifetimes for Complexes between Glutathione-*S* -Transferase (hGSTA1-1) and Product-like Ligands Detected by Single-Molecule Fluorescence Imaging. *Biochemistry* **2017**, *56* (31), 4073–4083. https://doi.org/10.1021/acs.biochem.7b00030.

(216) Nieslanik, B. S.; Ibarra, C.; Atkins, W. M. The C-Terminus of Glutathione *S* -Transferase A1-1 Is Required for Entropically-Driven Ligand Binding. *Biochemistry* **2001**, *40* (12), 3536–3543. https://doi.org/10.1021/bi001869x.

(217) Saxena, S.; Freed, J. H. Double Quantum Two-Dimensional Fourier Transform Electron Spin Resonance: Distance Measurements. *Chem. Phys. Lett.* **1996**, *251* (1–2), 102–110. https://doi.org/10.1016/0009-2614(96)00075-9.

(218) Borbat, P. P.; Freed, J. H. Multiple-Quantum ESR and Distance Measurements. *Chem. Phys. Lett.* **1999**, *313* (1–2), 145–154. https://doi.org/10.1016/S0009-2614(99)00972-0.

(219) Bonora, M.; Becker, J.; Saxena, S. Suppression of Electron Spin-Echo Envelope Modulation Peaks in Double Quantum Coherence Electron Spin Resonance. *J. Magn. Reson.* **2004**, *170* (2), 278–283. https://doi.org/10.1016/j.jmr.2004.07.006.

(220) Becker, J. S.; Saxena, S. Double Quantum Coherence Electron Spin Resonance on Coupled Cu(II)–Cu(II) Electron Spins. *Chem. Phys. Lett.* **2005**, *414* (1–3), 248–252. https://doi.org/10.1016/j.cplett.2005.08.072.

(221) Kulik, L. V.; Dzuba, S. A.; Grigoryev, I. A.; Tsvetkov, Yu. D. Electron Dipole–Dipole Interaction in ESEEM of Nitroxide Biradicals. *Chem. Phys. Lett.* **2001**, *343* (3–4), 315–324. https://doi.org/10.1016/S0009-2614(01)00721-7.

(222) Milikisyants, S.; Scarpelli, F.; Finiguerra, M. G.; Ubbink, M.; Huber, M. A Pulsed EPR Method to Determine Distances between Paramagnetic Centers with Strong Spectral Anisotropy and Radicals: The Dead-Time Free RIDME Sequence. *J. Magn. Reson.* **2009**, *201* (1), 48–56. https://doi.org/10.1016/j.jmr.2009.08.008.

(223) Jeschke, G.; Pannier, M.; Godt, A.; Spiess, H. W. Dipolar Spectroscopy and Spin Alignment in Electron Paramagnetic Resonance. *Chem. Phys. Lett.* **2000**, *331* (2–4), 243–252. https://doi.org/10.1016/S0009-2614(00)01171-4.

(224) Pannier, M.; Veit, S.; Godt, A.; Jeschke, G.; Spiess, H. W. Dead-Time Free Measurement of Dipole–Dipole Interactions between Electron Spins. *J. Magn. Reson.* **2000**, *142* (2), 331–340. https://doi.org/10.1006/jmre.1999.1944.

(225) Stone, K. M.; Townsend, J. E.; Sarver, J.; Sapienza, P. J.; Saxena, S.; Jen-Jacobson, L. Electron Spin Resonance Shows Common Structural Features for Different Classes of *Eco* RI-DNA Complexes. *Angew. Chem. Int. Ed.* **2008**, *47* (52), 10192–10194. https://doi.org/10.1002/anie.200803588.

(226) Grote, M.; Polyhach, Y.; Jeschke, G.; Steinhoff, H.-J.; Schneider, E.; Bordignon, E. Transmembrane Signaling in the Maltose ABC Transporter MalFGK2-E. *J. Biol. Chem.* **2009**, *284* (26), 17521–17526. https://doi.org/10.1074/jbc.M109.006270.

(227) Hagelueken, G.; Ingledew, W. J.; Huang, H.; Petrovic-Stojanovska, B.; Whitfield, C.; ElMkami, H.; Schiemann, O.; Naismith, J. H. PELDOR Spectroscopy Distance Fingerprinting of the Octameric Outer-Membrane Protein Wza from Escherichia Coli. *Angew. Chem. Int. Ed.* **2009**, *48* (16), 2904–2906. https://doi.org/10.1002/anie.200805758.

(228) Swanson, M. A.; Kathirvelu, V.; Majtan, T.; Frerman, F. E.; Eaton, G. R.; Eaton, S. S. DEER Distance Measurement Between a Spin Label and a Native FAD Semiquinone in Electron Transfer Flavoprotein. *J. Am. Chem. Soc.* **2009**, *131* (44), 15978–15979. https://doi.org/10.1021/ja9059816.

(229) Sen, K. I.; Wu, H.; Backer, J. M.; Gerfen, G. J. The Structure of P85ni in Class IA Phosphoinositide 3-Kinase Exhibits Interdomain Disorder. *Biochemistry* **2010**, *49* (10), 2159–2166. https://doi.org/10.1021/bi902171d.

(230) Drescher, M.; Huber, M.; Subramaniam, V. Hunting the Chameleon: Structural Conformations of the Intrinsically Disordered Protein Alpha-Synuclein. *ChemBioChem* **2012**, *13* (6), 761–768. https://doi.org/10.1002/cbic.201200059.

(231) Pornsuwan, S.; Giller, K.; Riedel, D.; Becker, S.; Griesinger, C.; Bennati, M. Long-Range Distances in Amyloid Fibrils of α-Synuclein from PELDOR Spectroscopy. *Angew. Chem.* **2013**, *125* (39), 10480–10484. https://doi.org/10.1002/ange.201304747.

(232) Joseph, B.; Sikora, A.; Bordignon, E.; Jeschke, G.; Cafiso, D. S.; Prisner, T. F. Distance Measurement on an Endogenous Membrane Transporter in *E. Coli* Cells and Native Membranes Using EPR Spectroscopy. *Angew. Chem. Int. Ed.* **2015**, *54* (21), 6196–6199. https://doi.org/10.1002/anie.201501086.

(233) Li, Q.; Shen, R.; Treger, J. S.; Wanderling, S. S.; Milewski, W.; Siwowska, K.; Bezanilla, F.; Perozo, E. Resting State of the Human Proton Channel Dimer in a Lipid Bilayer. *Proc. Natl. Acad. Sci.* **2015**, *112* (44). https://doi.org/10.1073/pnas.1515043112.

(234) Yardeni, E. H.; Bahrenberg, T.; Stein, R. A.; Mishra, S.; Zomot, E.; Graham, B.; Tuck, K. L.; Huber, T.; Bibi, E.; Mchaourab, H. S.; Goldfarb, D. Probing the Solution Structure of

the E. Coli Multidrug Transporter MdfA Using DEER Distance Measurements with Nitroxide and Gd(III) Spin Labels. *Sci. Rep.* **2019**, *9* (1), 12528. https://doi.org/10.1038/s41598-019-48694-0.

(235) Sahu, I. D.; Dixit, G.; Reynolds, W.; Harding, B.; Jaycox, C.; Mohammed Faleel, F. D.; McCarrick, R. M.; Sanders, C. R.; Lorigan, G. A. Studying Conformation of the Voltage-Sensor Domain (VSD) of the Human KCNQ1 Potassium Ion Channel in Proteoliposomes Using EPR Spectroscopy. *Biophys. J.* **2019**, *116* (3), 26a. https://doi.org/10.1016/j.bpj.2018.11.184.

(236) Fichou, Y.; Eschmann, N.; Han, S. Capturing Conformational Changes of the Tau Protein Upon Aggregation. *Biophys. J.* **2018**, *114* (3), 429a. https://doi.org/10.1016/j.bpj.2017.11.2378.

(237) Rayes, R. F.; Kálai, T.; Hideg, K.; Geeves, M. A.; Fajer, P. G. Dynamics of Tropomyosin in Muscle Fibers as Monitored by Saturation Transfer EPR of Bi-Functional Probe. *PLoS ONE* **2011**, *6* (6), e21277. https://doi.org/10.1371/journal.pone.0021277.

(238) Ji, M.; Ruthstein, S.; Saxena, S. Paramagnetic Metal Ions in Pulsed ESR Distance Distribution Measurements. *Acc. Chem. Res.* **2014**, *47* (2), 688–695. https://doi.org/10.1021/ar400245z.

(239) Goldfarb, D. Pulse EPR in Biological Systems – Beyond the Expert's Courtyard. *J. Magn. Reson.* **2019**, *306*, 102–108. https://doi.org/10.1016/j.jmr.2019.07.038.

(240) Cunningham, T. F.; Putterman, M. R.; Desai, A.; Horne, W. S.; Saxena, S. The Double-Histidine Cu $^{2+}$ -Binding Motif: A Highly Rigid, Site-Specific Spin Probe for Electron Spin Resonance Distance Measurements. *Angew. Chem. Int. Ed.* **2015**, *54* (21), 6330–6334. https://doi.org/10.1002/anie.201501968.

(241) Wort, J. L.; Ackermann, K.; Giannoulis, A.; Stewart, A. J.; Norman, D. G.; Bode, B. E. Sub-Micromolar Pulse Dipolar EPR Spectroscopy Reveals Increasing Cu $^{\mathrm{II}}$ -labelling of Double-Histidine Motifs with Lower Temperature. *Angew. Chem.* **2019**, *131* (34), 11807–11811. https://doi.org/10.1002/ange.201904848.

(242) Sameach, H.; Ghosh, S.; Gevorkyan-Airapetov, L.; Saxena, S.; Ruthstein, S. EPR Spectroscopy Detects Various Active State Conformations of the Transcriptional Regulator CueR. *Angew. Chem. Int. Ed.* **2019**, *58* (10), 3053–3056. https://doi.org/10.1002/anie.201810656.

(243) Lawless, M. J.; Pettersson, J. R.; Rule, G. S.; Lanni, F.; Saxena, S. ESR Resolves the C Terminus Structure of the Ligand-Free Human Glutathione S-Transferase A1-1. *Biophys. J.* **2018**, *114* (3), 592–601. https://doi.org/10.1016/j.bpj.2017.12.016.

(244) Ghosh, S.; Saxena, S.; Jeschke, G. Rotamer Modelling of Cu(II) Spin Labels Based on the Double-Histidine Motif. *Appl. Magn. Reson.* **2018**, *49* (11), 1281–1298. https://doi.org/10.1007/s00723-018-1052-8.

(245) Bhatnagar, J.; Freed, J. H.; Crane, B. R. Rigid Body Refinement of Protein Complexes with Long-Range Distance Restraints from Pulsed Dipolar ESR. In *Methods in Enzymology*; Elsevier, 2007; Vol. 423, pp 117–133. https://doi.org/10.1016/S0076-6879(07)23004-6.

(246) Kazmier, K.; Alexander, N. S.; Meiler, J.; Mchaourab, H. S. Algorithm for Selection of Optimized EPR Distance Restraints for de Novo Protein Structure Determination. *J. Struct. Biol.* **2011**, *173* (3), 549–557. https://doi.org/10.1016/j.jsb.2010.11.003.

(247) Polyhach, Ye.; Godt, A.; Bauer, C.; Jeschke, G. Spin Pair Geometry Revealed by High-Field DEER in the Presence of Conformational Distributions. *J. Magn. Reson.* **2007**, *185* (1), 118–129. https://doi.org/10.1016/j.jmr.2006.11.012.

(248) Boura, E.; Różycki, B.; Herrick, D. Z.; Chung, H. S.; Vecer, J.; Eaton, W. A.; Cafiso, D. S.; Hummer, G.; Hurley, J. H. Solution Structure of the ESCRT-I Complex by Small-Angle X-Ray Scattering, EPR, and FRET Spectroscopy. *Proc. Natl. Acad. Sci.* **2011**, *108* (23), 9437–9442. https://doi.org/10.1073/pnas.1101763108.

(249) Tikhonova, I. G.; Best, R. B.; Engel, S.; Gershengorn, M. C.; Hummer, G.; Costanzi, S. Atomistic Insights into Rhodopsin Activation from a Dynamic Model. *J. Am. Chem. Soc.* **2008**, *130* (31), 10141–10149. https://doi.org/10.1021/ja0765520.

(250) Galiano, L.; Ding, F.; Veloro, A. M.; Blackburn, M. E.; Simmerling, C.; Fanucci, G. E. Drug Pressure Selected Mutations in HIV-1 Protease Alter Flap Conformations. *J. Am. Chem. Soc.* **2009**, *131* (2), 430–431. https://doi.org/10.1021/ja807531v.

(251) Schrödinger, L. PyMOL Molecular Graphics System, Version 1.8; Schrodinger LLC: New York, 2015. *Google Sch. There No Corresp. Rec. This Ref.*

(252) Maier, J. A.; Martinez, C.; Kasavajhala, K.; Wickstrom, L.; Hauser, K. E.; Simmerling, C. ff14SB: Improving the Accuracy of Protein Side Chain and Backbone Parameters from ff99SB. *J. Chem. Theory Comput.* **2015**, *11* (8), 3696–3713. https://doi.org/10.1021/acs.jctc.5b00255.

(253) Moses, V.; Tastan Bishop, Ö.; Lobb, K. A. The Evaluation and Validation of Copper (II) Force Field Parameters of the Auxiliary Activity Family 9 Enzymes. *Chem. Phys. Lett.* **2017**, *678*, 91–97. https://doi.org/10.1016/j.cplett.2017.04.022.

(254) Op't Hol, B. T.; Merz, K. M. Insights into Cu(I) Exchange in HAH1 Using Quantum Mechanical and Molecular Simulations. *Biochemistry* **2007**, *46* (30), 8816–8826. https://doi.org/10.1021/bi7007195.

(255) Zhu, Y.; Su, Y.; Li, X.; Wang, Y.; Chen, G. Evaluation of Amber Force Field Parameters for Copper(II) with Pyridylmethyl-Amine and Benzimidazolylmethyl-Amine Ligands: A Quantum Chemical Study. *Chem. Phys. Lett.* **2008**, *455* (4–6), 354–360. https://doi.org/10.1016/j.cplett.2008.03.004.

(256) Cieplak, P.; Cornell, W. D.; Bayly, C.; Kollman, P. A. Application of the Multimolecule and Multiconformational RESP Methodology to Biopolymers: Charge Derivation for DNA, RNA, and Proteins. *J. Comput. Chem.* **1995**, *16* (11), 1357–1377. https://doi.org/10.1002/jcc.540161106.

(257) Frisch, M.; Trucks, G.; Schlegel, H. B.; Scuseria, G.; Robb, M.; Cheeseman, J.; Scalmani, G.; Barone, V.; Petersson, G.; Nakatsuji, H.; others. Gaussian 16, 2016.

(258) Wang, J.; Wang, W.; Kollman, P. A.; Case, D. A. Automatic Atom Type and Bond Type Perception in Molecular Mechanical Calculations. *J. Mol. Graph. Model.* **2006**, *25* (2), 247–260. https://doi.org/10.1016/j.jmgm.2005.12.005.

(259) Peters, M. B.; Yang, Y.; Wang, B.; Füsti-Molnár, L.; Weaver, M. N.; Merz, K. M. Structural Survey of Zinc-Containing Proteins and Development of the Zinc AMBER Force Field (ZAFF). *J. Chem. Theory Comput.* **2010**, *6* (9), 2935–2947. https://doi.org/10.1021/ct1002626.

(260) Jorgensen, W. L.; Chandrasekhar, J.; Madura, J. D.; Impey, R. W.; Klein, M. L. Comparison of Simple Potential Functions for Simulating Liquid Water. *J. Chem. Phys.* **1983**, *79* (2), 926–935. https://doi.org/10.1063/1.445869.

(261) Berendsen, H. J. C.; Postma, J. P. M.; Van Gunsteren, W. F.; DiNola, A.; Haak, J. R. Molecular Dynamics with Coupling to an External Bath. *J. Chem. Phys.* **1984**, *81* (8), 3684–3690. https://doi.org/10.1063/1.448118.

(262) Jeschke, G.; Chechik, V.; Ionita, P.; Godt, A.; Zimmermann, H.; Banham, J.; Timmel, C. R.; Hilger, D.; Jung, H. DeerAnalysis2006—a Comprehensive Software Package for Analyzing Pulsed ELDOR Data. *Appl. Magn. Reson.* **2006**, *30* (3–4), 473–498. https://doi.org/10.1007/BF03166213.

(263) Brandi-Blanco, M. P.; Benavides-Giménez, M. M. D.; González-Pérez, J. M.; Choquesillo-Lazarte, D. *Cis* -[ *N* -(4-Chlorobenzyl)Iminodiacetato-κ $^3$ *N* , *O* , *O* ′]Bis(1 *H* -Imidazole-κ *N* $^3$ )Copper(II). *Acta Crystallogr. Sect. E Struct. Rep. Online* **2007**, *63* (6), m1678–m1679. https://doi.org/10.1107/S160053680702288X.

(264) Fee, J. A. Copper Proteins Systems Containing the "Blue" Copper Center. In *Biochemistry*; Structure and Bonding; Springer Berlin Heidelberg: Berlin, Heidelberg, 1975; Vol. 23, pp 1–60. https://doi.org/10.1007/BFb0116549.

(265) Burns, C. J.; Field, L. D.; Hambley, T. W.; Lin, T.; Ridley, D. D.; Turner, P.; Wilkinson, M. P. X-Ray Crystal Structural Determination of Copper(II)-Nitrilotriacetic Acid-Bis(N-Methylimidazol-2-Yl)Ketone Ternary Complex. *Arkivoc* **2001**, *2001* (7), 157–165. https://doi.org/10.3998/ark.5550190.0002.713.

(266) Hawkins, G. D.; Cramer, C. J.; Truhlar, D. G. Parametrized Models of Aqueous Free Energies of Solvation Based on Pairwise Descreening of Solute Atomic Charges from a Dielectric Medium. *J. Phys. Chem.* **1996**, *100* (51), 19824–19839. https://doi.org/10.1021/jp961710n.

(267) Gronenborn, A. M.; Filpula, D. R.; Essig, N. Z.; Achari, A.; Whitlow, M.; Wingfield, P. T.; Clore, G. M. A Novel, Highly Stable Fold of the Immunoglobulin Binding Domain of Streptococcal Protein G. *Science* **1991**, *253* (5020), 657–661. https://doi.org/10.1126/science.1871600.

(268) Alexander, P.; Fahnestock, S.; Lee, T.; Orban, J.; Bryan, P. Thermodynamic Analysis of the Folding of the Streptococcal Protein G IgG-Binding Domains B1 and B2: Why Small Proteins Tend to Have High Denaturation Temperatures. *Biochemistry* **1992**, *31* (14), 3597–3603. https://doi.org/10.1021/bi00129a007.

(269) Dockter, C.; Volkov, A.; Bauer, C.; Polyhach, Y.; Joly-Lopez, Z.; Jeschke, G.; Paulsen, H. Refolding of the Integral Membrane Protein Light-Harvesting Complex II Monitored by Pulse EPR. *Proc. Natl. Acad. Sci.* **2009**, *106* (44), 18485–18490. https://doi.org/10.1073/pnas.0906462106.

(270) Walsh, J. D.; Meier, K.; Ishima, R.; Gronenborn, A. M. NMR Studies on Domain Diffusion and Alignment in Modular GB1 Repeats. *Biophys. J.* **2010**, *99* (8), 2636–2646. https://doi.org/10.1016/j.bpj.2010.08.036.

(271) Sengupta, I.; Nadaud, P. S.; Helmus, J. J.; Schwieters, C. D.; Jaroniec, C. P. Protein Fold Determined by Paramagnetic Magic-Angle Spinning Solid-State NMR Spectroscopy. *Nat. Chem.* **2012**, *4* (5), 410–417. https://doi.org/10.1038/nchem.1299.

(272) Nadaud, P. S.; Helmus, J. J.; Kall, S. L.; Jaroniec, C. P. Paramagnetic Ions Enable Tuning of Nuclear Relaxation Rates and Provide Long-Range Structural Restraints in Solid-State NMR of Proteins. *J. Am. Chem. Soc.* **2009**, *131* (23), 8108–8120. https://doi.org/10.1021/ja900224z.

(273) Thoms, S.; Max, K. E. A.; Wunderlich, M.; Jacso, T.; Lilie, H.; Reif, B.; Heinemann, U.; Schmid, F. X. Dimer Formation of a Stabilized Gβ1 Variant: A Structural and Energetic Analysis. *J. Mol. Biol.* **2009**, *391* (5), 918–932. https://doi.org/10.1016/j.jmb.2009.06.031.

(274) Lindman, S.; Xue, W.-F.; Szczepankiewicz, O.; Bauer, M. C.; Nilsson, H.; Linse, S. Salting the Charged Surface: pH and Salt Dependence of Protein G B1 Stability. *Biophys. J.* **2006**, *90* (8), 2911–2921. https://doi.org/10.1529/biophysj.105.071050.

(275) Muñoz, V.; Thompson, P. A.; Hofrichter, J.; Eaton, W. A. Folding Dynamics and Mechanism of β-Hairpin Formation. *Nature* **1997**, *390* (6656), 196–199. https://doi.org/10.1038/36626.

(276) Morrone, A.; Giri, R.; Toofanny, R. D.; Travaglini-Allocatelli, C.; Brunori, M.; Daggett, V.; Gianni, S. GB1 Is Not a Two-State Folder: Identification and Characterization of an On-Pathway Intermediate. *Biophys. J.* **2011**, *101* (8), 2053–2060. https://doi.org/10.1016/j.bpj.2011.09.013.

(277) Bauer, M.; Xue, W.-F.; Linse, S. Protein GB1 Folding and Assembly from Structural Elements. *Int. J. Mol. Sci.* **2009**, *10* (4), 1552–1566. https://doi.org/10.3390/ijms10041552.

(278) Cunningham, T. F.; Putterman, M. R.; Desai, A.; Horne, W. S.; Saxena, S. The Double-Histidine Cu $^{2+}$ -Binding Motif: A Highly Rigid, Site-Specific Spin Probe for Electron Spin Resonance Distance Measurements. *Angew. Chem. Int. Ed.* **2015**, *54* (21), 6330–6334. https://doi.org/10.1002/anie.201501968.

(279) Denysenkov, V. P.; Prisner, T. F.; Stubbe, J.; Bennati, M. High-Field Pulsed Electron–Electron Double Resonance Spectroscopy to Determine the Orientation of the Tyrosyl Radicals in Ribonucleotide Reductase. *Proc. Natl. Acad. Sci.* **2006**, *103* (36), 13386–13390. https://doi.org/10.1073/pnas.0605851103.

(280) Schiemann, O.; Cekan, P.; Margraf, D.; Prisner, T. F.; Sigurdsson, S. Th. Relative Orientation of Rigid Nitroxides by PELDOR: Beyond Distance Measurements in Nucleic Acids. *Angew. Chem. Int. Ed.* **2009**, *48* (18), 3292–3295. https://doi.org/10.1002/anie.200805152.

(281) Yang, Z.; Kise, D.; Saxena, S. An Approach towards the Measurement of Nanometer Range Distances Based on Cu $^{2+}$ Ions and ESR. *J. Phys. Chem. B* **2010**, *114* (18), 6165–6174. https://doi.org/10.1021/jp911637s.

(282) Yang, Z.; Ji, M.; Saxena, S. Practical Aspects of Copper Ion-Based Double Electron Electron Resonance Distance Measurements. *Appl. Magn. Reson.* **2010**, *39* (4), 487–500. https://doi.org/10.1007/s00723-010-0181-5.

(283) Bowen, A. M.; Jones, M. W.; Lovett, J. E.; Gaule, T. G.; McPherson, M. J.; Dilworth, J. R.; Timmel, C. R.; Harmer, J. R. Exploiting Orientation-Selective DEER: Determining Molecular Structure in Systems Containing Cu( II ) Centres. *Phys. Chem. Chem. Phys.* **2016**, *18* (8), 5981–5994. https://doi.org/10.1039/C5CP06096F.

(284) Abé, C.; Klose, D.; Dietrich, F.; Ziegler, W. H.; Polyhach, Y.; Jeschke, G.; Steinhoff, H.-J. Orientation Selective DEER Measurements on Vinculin Tail at X-Band Frequencies Reveal Spin Label Orientations. *J. Magn. Reson.* **2012**, *216*, 53–61. https://doi.org/10.1016/j.jmr.2011.12.024.

(285) Bode, B. E.; Plackmeyer, J.; Prisner, T. F.; Schiemann, O. PELDOR Measurements on a Nitroxide-Labeled Cu(II) Porphyrin: Orientation Selection, Spin-Density Distribution, and Conformational Flexibility. *J. Phys. Chem. A* **2008**, *112* (23), 5064–5073. https://doi.org/10.1021/jp710504k.

(286) Sarver, J.; Silva, K. I.; Saxena, S. Measuring Cu2+-Nitroxide Distances Using Double Electron–Electron Resonance and Saturation Recovery. *Appl. Magn. Reson.* **2013**, *44* (5), 583–594. https://doi.org/10.1007/s00723-012-0422-x.

(287) Breitgoff, F. D.; Keller, K.; Qi, M.; Klose, D.; Yulikov, M.; Godt, A.; Jeschke, G. UWB DEER and RIDME Distance Measurements in Cu(II)–Cu(II) Spin Pairs. *J. Magn. Reson.* **2019**, *308*, 106560. https://doi.org/10.1016/j.jmr.2019.07.047.

(288) Marko, A.; Prisner, T. F. An Algorithm to Analyze PELDOR Data of Rigid Spin Label Pairs. *Phys Chem Chem Phys* **2013**, *15* (2), 619–627. https://doi.org/10.1039/C2CP42942J.

(289) Marko, A.; Margraf, D.; Cekan, P.; Sigurdsson, S. Th.; Schiemann, O.; Prisner, T. F. Analytical Method to Determine the Orientation of Rigid Spin Labels in DNA. *Phys. Rev. E* **2010**, *81* (2), 021911. https://doi.org/10.1103/PhysRevE.81.021911.

(290) Lovett, J. E.; Bowen, A. M.; Timmel, C. R.; Jones, M. W.; Dilworth, J. R.; Caprotti, D.; Bell, S. G.; Wong, L. L.; Harmer, J. Structural Information from Orientationally Selective DEER Spectroscopy. *Phys. Chem. Chem. Phys.* **2009**, *11* (31), 6840. https://doi.org/10.1039/b907010a.

(291) Tkach, I.; Pornsuwan, S.; Höbartner, C.; Wachowius, F.; Sigurdsson, S. Th.; Baranova, T. Y.; Diederichsen, U.; Sicoli, G.; Bennati, M. Orientation Selection in Distance Measurements between Nitroxide Spin Labels at 94 GHz EPR with Variable Dual Frequency Irradiation. *Phys. Chem. Chem. Phys.* **2013**, *15* (10), 3433. https://doi.org/10.1039/c3cp44415e.

(292) Hayes, J. D.; Pulford, D. J. The Glut Athione S-Transferase Supergene Family: Regulation of GST and the Contribution of the Lsoenzymes to Cancer Chemoprotection and Drug Resistance Part I. *Crit. Rev. Biochem. Mol. Biol.* **1995**, *30* (6), 445–520. https://doi.org/10.3109/10409239509083491.

(293) Armstrong, R. N. Structure, Catalytic Mechanism, and Evolution of the Glutathione Transferases. *Chem. Res. Toxicol.* **1997**, *10* (1), 2–18. https://doi.org/10.1021/tx960072x.

(294) Honaker, M. T.; Acchione, M.; Zhang, W.; Mannervik, B.; Atkins, W. M. Enzymatic Detoxication, Conformational Selection, and the Role of Molten Globule Active Sites. *J. Biol. Chem.* **2013**, *288* (25), 18599–18611. https://doi.org/10.1074/jbc.M112.445767.

(295) Nilsson, L. O.; Edalat, M.; Pettersson, P. L.; Mannervik, B. Aromatic Residues in the C-Terminal Region of Glutathione Transferase A1-1 Influence Rate-Determining Steps in the Catalytic Mechanism [Biochimica et Biophysica Acta 1597 (2002) 157-163]. *Biochim. Biophys. Acta BBA - Proteins Proteomics* **2002**, *1598* (1–2), 199–205. https://doi.org/10.1016/S0167-4838(02)00362-X.

(296) Gustafsson, A.; Mannervik, B. Benzoic Acid Derivatives Induce Recovery of Catalytic Activity in the Partially Inactive Met208Lys Mutant of Human Glutathione Transferase A1-1 1 1Edited by A. R. Fersht. *J. Mol. Biol.* **1999**, *288* (4), 787–800. https://doi.org/10.1006/jmbi.1999.2712.

(297) Dirr, H. W.; Wallace, L. A. Role of the C-Terminal Helix 9 in the Stability and Ligandin Function of Class α Glutathione Transferase A1-1. *Biochemistry* **1999**, *38* (47), 15631–15640. https://doi.org/10.1021/bi991179x.

(298) Ibarra, C.; Nieslanik, B. S.; Atkins, W. M. Contribution of Aromatic−Aromatic Interactions to the Anomalous p *K* a of Tyrosine-9 and the C-Terminal Dynamics of Glutathione *S* -Transferase A1-1. *Biochemistry* **2001**, *40* (35), 10614–10624. https://doi.org/10.1021/bi010672h.

(299) Widersten, M.; Björnestedt, R.; Mannervik, B. Involvement of the Carboxyl Groups of Glutathione in the Catalytic Mechanism of Human Glutathione Transferase A1-1. *Biochemistry* **1996**, *35* (24), 7731–7742. https://doi.org/10.1021/bi9601619.

(300) Grahn, E.; Novotny, M.; Jakobsson, E.; Gustafsson, A.; Grehn, L.; Olin, B.; Madsen, D.; Wahlberg, M.; Mannervik, B.; Kleywegt, G. J. New Crystal Structures of Human Glutathione Transferase A1-1 Shed Light on Glutathione Binding and the Conformation of the C-Terminal Helix. *Acta Crystallogr. D Biol. Crystallogr.* **2006**, *62* (2), 197–207. https://doi.org/10.1107/S0907444905039296.

(301) Zhan, Y.; Rule, G. S. Glutathione Induces Helical Formation in the Carboxy Terminus of Human Glutathione Transferase A1-1. *Biochemistry* **2004**, *43* (23), 7244–7254. https://doi.org/10.1021/bi0363329.

(302) Altenbach, C.; Kusnetzow, A. K.; Ernst, O. P.; Hofmann, K. P.; Hubbell, W. L. High-Resolution Distance Mapping in Rhodopsin Reveals the Pattern of Helix Movement Due to Activation. *Proc. Natl. Acad. Sci.* **2008**, *105* (21), 7439–7444. https://doi.org/10.1073/pnas.0802515105.

(303) Dastvan, R.; Mishra, S.; Peskova, Y. B.; Nakamoto, R. K.; Mchaourab, H. S. Mechanism of Allosteric Modulation of P-Glycoprotein by Transport Substrates and Inhibitors. *Science* **2019**, *364* (6441), 689–692. https://doi.org/10.1126/science.aav9406.

(304) Evans, E. G. B.; Morgan, J. L. W.; DiMaio, F.; Zagotta, W. N.; Stoll, S. Allosteric Conformational Change of a Cyclic Nucleotide-Gated Ion Channel Revealed by DEER Spectroscopy. *Proc. Natl. Acad. Sci.* **2020**, *117* (20), 10839–10847. https://doi.org/10.1073/pnas.1916375117.

(305) Evans, E. G. B.; Pushie, M. J.; Markham, K. A.; Lee, H.-W.; Millhauser, G. L. Interaction between Prion Protein’s Copper-Bound Octarepeat Domain and a Charged C-Terminal Pocket Suggests a Mechanism for N-Terminal Regulation. *Structure* **2016**, *24* (7), 1057–1067. https://doi.org/10.1016/j.str.2016.04.017.

(306) Kear, J. L.; Blackburn, M. E.; Veloro, A. M.; Dunn, B. M.; Fanucci, G. E. Subtype Polymorphisms Among HIV-1 Protease Variants Confer Altered Flap Conformations and Flexibility. *J. Am. Chem. Soc.* **2009**, *131* (41), 14650–14651. https://doi.org/10.1021/ja907088a.

(307) Stewart, A. M.; Shanmugam, M.; Kutta, R. J.; Scrutton, N. S.; Lovett, J. E.; Hay, S. Combined Pulsed Electron Double Resonance EPR and Molecular Dynamics Investigations of Calmodulin Suggest Effects of Crowding Agents on Protein Structures. *Biochemistry* **2022**, *61* (17), 1735–1742. https://doi.org/10.1021/acs.biochem.2c00099.

(308) Barth, K.; Hank, S.; Spindler, P. E.; Prisner, T. F.; Tampé, R.; Joseph, B. Conformational Coupling and Trans-Inhibition in the Human Antigen Transporter Ortholog TmrAB Resolved with Dipolar EPR Spectroscopy. *J. Am. Chem. Soc.* **2018**, *140* (13), 4527–4533. https://doi.org/10.1021/jacs.7b12409.

(309) Huber, G. A.; Kim, S. Weighted-Ensemble Brownian Dynamics Simulations for Protein Association Reactions. *Biophys. J.* **1996**, *70* (1), 97–110. https://doi.org/10.1016/S0006-3495(96)79552-8.

(310) Zuckerman, D. M.; Chong, L. T. Weighted Ensemble Simulation: Review of Methodology, Applications, and Software. *Annu. Rev. Biophys.* **2017**, *46* (1), 43–57. https://doi.org/10.1146/annurev-biophys-070816-033834.

(311) Saglam, A. S.; Chong, L. T. Protein–Protein Binding Pathways and Calculations of Rate Constants Using Fully-Continuous, Explicit-Solvent Simulations. *Chem. Sci.* **2019**, *10* (8), 2360–2372. https://doi.org/10.1039/C8SC04811H.

(312) Dommer, A.; Casalino, L.; Kearns, F.; Rosenfeld, M.; Wauer, N.; Ahn, S.-H.; Russo, J.; Oliveira, S.; Morris, C.; Bogetti, A.; Trifan, A.; Brace, A.; Sztain, T.; Clyde, A.; Ma, H.;

Chennubhotla, C.; Lee, H.; Turilli, M.; Khalid, S.; Tamayo-Mendoza, T.; Welborn, M.; Christensen, A.; Smith, D. G.; Qiao, Z.; Sirumalla, S. K.; O'Connor, M.; Manby, F.; Anandkumar, A.; Hardy, D.; Phillips, J.; Stern, A.; Romero, J.; Clark, D.; Dorrell, M.; Maiden, T.; Huang, L.; McCalpin, J.; Woods, C.; Gray, A.; Williams, M.; Barker, B.; Rajapaksha, H.; Pitts, R.; Gibbs, T.; Stone, J.; Zuckerman, D. M.; Mulholland, A. J.; Miller, T.; Jha, S.; Ramanathan, A.; Chong, L.; Amaro, R. E. #COVIDisAirborne: AI-Enabled Multiscale Computational Microscopy of Delta SARS-CoV-2 in a Respiratory Aerosol. *Int. J. High Perform. Comput. Appl.* **2023**, *37* (1), 28–44. https://doi.org/10.1177/10943420221128233.

(313) Ploemen, J. H. T. M.; van Ommen, B.; van Bladeren, P. J. Inhibition of Rat and Human Glutathione S-Transferase Isoenzymes by Ethacrynic Acid and Its Glutathione Conjugate. *Biochem. Pharmacol.* **1990**, *40* (7), 1631–1635. https://doi.org/10.1016/0006-2952(90)90465-W.

(314) Schramm, V. L.; McCluskey, R.; Emig, F. A.; Litwack, G. Kinetic Studies and Active Site-Binding Properties of Glutathione S-Transferase Using Spin-Labeled Glutathione, a Product Analogue. *J. Biol. Chem.* **1984**, *259* (2), 714–722. https://doi.org/10.1016/S0021-9258(17)43516-2.

(315) Ackermann, K.; Wort, J. L.; Bode, B. E. Nanomolar Pulse Dipolar EPR Spectroscopy in Proteins: Cu $^{II}$ –Cu $^{II}$ and Nitroxide–Nitroxide Cases. *J. Phys. Chem. B* **2021**, *125* (20), 5358–5364. https://doi.org/10.1021/acs.jpcb.1c03666.

(316) Oranges, M.; Wort, J. L.; Fukushima, M.; Fusco, E.; Ackermann, K.; Bode, B. E. Pulse Dipolar Electron Paramagnetic Resonance Spectroscopy Reveals Buffer-Modulated Cooperativity of Metal-Templated Protein Dimerization. *J. Phys. Chem. Lett.* **2022**, *13* (33), 7847–7852. https://doi.org/10.1021/acs.jpclett.2c01719.

(317) Kuhnert, D. C.; Sayed, Y.; Mosebi, S.; Sayed, M.; Sewell, T.; Dirr, H. W. Tertiary Interactions Stabilise the C-Terminal Region of Human Glutathione Transferase A1-1: A Crystallographic and Calorimetric Study. *J. Mol. Biol.* **2005**, *349* (4), 825–838. https://doi.org/10.1016/j.jmb.2005.04.025.

(318) Mims, W. B. Envelope Modulation in Spin-Echo Experiments. *Phys. Rev. B* **1972**, *5* (7), 2409–2419. https://doi.org/10.1103/PhysRevB.5.2409.

(319) Mims, W. B. Amplitudes of Superhyperfine Frequencies Displayed in the Electron-Spin-Echo Envelope. *Phys. Rev. B* **1972**, *6* (9), 3543–3545. https://doi.org/10.1103/PhysRevB.6.3543.

(320) Stoll, S.; Schweiger, A. EasySpin, a Comprehensive Software Package for Spectral Simulation and Analysis in EPR. *J. Magn. Reson.* **2006**, *178* (1), 42–55. https://doi.org/10.1016/j.jmr.2005.08.013.

(321) Fauth, J.-M.; Schweiger, A.; Braunschweiler, L.; Forrer, J.; Ernst, R. R. Elimination of Unwanted Echoes and Reduction of Dead Time in Three-Pulse Electron Spin-Echo Spectroscopy. *J. Magn. Reson. 1969* **1986**, *66* (1), 74–85. https://doi.org/10.1016/0022-2364(86)90105-8.

(322) Gemperle, C.; Aebli, G.; Schweiger, A.; Ernst, R. R. Phase Cycling in Pulse EPR. *J. Magn. Reson. 1969* **1990**, *88* (2), 241–256. https://doi.org/10.1016/0022-2364(90)90181-8.

(323) Bogetti, X.; Hasanbasri, Z.; Hunter, H. R.; Saxena, S. An Optimal Acquisition Scheme for Q-Band EPR Distance Measurements Using Cu $^{2+}$ -Based Protein Labels. *Phys. Chem. Chem. Phys.* **2022**, *24* (24), 14727–14739. https://doi.org/10.1039/D2CP01032A.

(324) Schiemann, O.; Heubach, C. A.; Abdullin, D.; Ackermann, K.; Azarkh, M.; Bagryanskaya, E. G.; Drescher, M.; Endeward, B.; Freed, J. H.; Galazzo, L.; Goldfarb, D.; Hett, T.; Esteban Hofer, L.; Fábregas Ibáñez, L.; Hustedt, E. J.; Kucher, S.; Kuprov, I.; Lovett, J. E.; Meyer, A.; Ruthstein, S.; Saxena, S.; Stoll, S.; Timmel, C. R.; Di Valentin, M.; Mchaourab, H. S.; Prisner, T. F.; Bode, B. E.; Bordignon, E.; Bennati, M.; Jeschke, G. Benchmark Test and Guidelines for DEER/PELDOR Experiments on Nitroxide-Labeled Biomolecules. *J. Am. Chem. Soc.* **2021**, *143* (43), 17875–17890. https://doi.org/10.1021/jacs.1c07371.

(325) Wort, J. L.; Ackermann, K.; Norman, D. G.; Bode, B. E. A General Model to Optimise Cu $^{II}$ Labelling Efficiency of Double-Histidine Motifs for Pulse Dipolar EPR Applications. *Phys. Chem. Chem. Phys.* **2021**, *23* (6), 3810–3819. https://doi.org/10.1039/D0CP06196D.

(326) Chen, V. B.; Arendall, W. B.; Headd, J. J.; Keedy, D. A.; Immormino, R. M.; Kapral, G. J.; Murray, L. W.; Richardson, J. S.; Richardson, D. C. *MolProbity* : All-Atom Structure Validation for Macromolecular Crystallography. *Acta Crystallogr. D Biol. Crystallogr.* **2010**, *66* (1), 12–21. https://doi.org/10.1107/S0907444909042073.

(327) Izadi, S.; Anandakrishnan, R.; Onufriev, A. V. Building Water Models: A Different Approach. *J. Phys. Chem. Lett.* **2014**, *5* (21), 3863–3871. https://doi.org/10.1021/jz501780a.

(328) Ryckaert, J.-P.; Ciccotti, G.; Berendsen, H. J. C. Numerical Integration of the Cartesian Equations of Motion of a System with Constraints: Molecular Dynamics of n-Alkanes. *J. Comput. Phys.* **1977**, *23* (3), 327–341. https://doi.org/10.1016/0021-9991(77)90098-5.

(329) Russo, J. D.; Zhang, S.; Leung, J. M. G.; Bogetti, A. T.; Thompson, J. P.; DeGrave, A. J.; Torrillo, P. A.; Pratt, A. J.; Wong, K. F.; Xia, J.; Copperman, J.; Adelman, J. L.; Zwier, M. C.; LeBard, D. N.; Zuckerman, D. M.; Chong, L. T. WESTPA 2.0: High-Performance Upgrades for Weighted Ensemble Simulations and Analysis of Longer-Timescale Applications. *J. Chem. Theory Comput.* **2022**, *18* (2), 638–649. https://doi.org/10.1021/acs.jctc.1c01154.

(330) Torrillo, P. A.; Bogetti, A. T.; Chong, L. T. A Minimal, Adaptive Binning Scheme for Weighted Ensemble Simulations. *J. Phys. Chem. A* **2021**, *125* (7), 1642–1649. https://doi.org/10.1021/acs.jpca.0c10724.

(331) Peisach, J.; Blumberg, W. E. Structural Implications Derived from the Analysis of Electron Paramagnetic Resonance Spectra of Natural and Artificial Copper Proteins. *Arch. Biochem. Biophys.* **1974**, *165* (2), 691–708. https://doi.org/10.1016/0003-9861(74)90298-7.

(332) Shin, B.; Saxena, S. Substantial Contribution of the Two Imidazole Rings of the His13−His14 Dyad to Cu(II) Binding in Amyloid-β(1−16) at Physiological pH and Its Significance. *J. Phys. Chem. A* **2011**, *115* (34), 9590–9602. https://doi.org/10.1021/jp200379m.

(333) Dikanov, S. A.; Tsvetkov, Yu. D.; Bowman, M. K.; Astashkin, A. V. Parameters of Quadrupole Coupling of 14N Nuclei in Chlorophyll a Cations Determined by the Electron Spin Echo Method. *Chem. Phys. Lett.* **1982**, *90* (2), 149–153. https://doi.org/10.1016/0009-2614(82)83630-0.

(334) Burns, C. S.; Aronoff-Spencer, E.; Dunham, C. M.; Lario, P.; Avdievich, N. I.; Antholine, W. E.; Olmstead, M. M.; Vrielink, A.; Gerfen, G. J.; Peisach, J.; Scott, W. G.; Millhauser, G. L. Molecular Features of the Copper Binding Sites in the Octarepeat Domain of the Prion Protein. *Biochemistry* **2002**, *41* (12), 3991–4001. https://doi.org/10.1021/bi011922x.

(335) Silva, K. I.; Michael, B. C.; Geib, S. J.; Saxena, S. ESEEM Analysis of Multi-Histidine Cu(II)-Coordination in Model Complexes, Peptides, and Amyloid-β. *J. Phys. Chem. B* **2014**, *118* (30), 8935–8944. https://doi.org/10.1021/jp500767n.

(336) Fábregas Ibáñez, L.; Jeschke, G.; Stoll, S. DeerLab: A Comprehensive Software Package for Analyzing Dipolar Electron Paramagnetic Resonance Spectroscopy Data. *Magn. Reson.* **2020**, *1* (2), 209–224. https://doi.org/10.5194/mr-1-209-2020.

(337) Worswick, S. G.; Spencer, J. A.; Jeschke, G.; Kuprov, I. Deep Neural Network Processing of DEER Data. *Sci. Adv.* **2018**, *4* (8), eaat5218. https://doi.org/10.1126/sciadv.aat5218.

(338) Wang, J.; Bauman, S.; Colman, R. F. Probing Subunit Interactions in Alpha Class Rat Liver Glutathione S-Transferase with the Photoaffinity Label Glutathionyl S-[4-(Succinimidyl)Benzophenone]. *J. Biol. Chem.* **2000**, *275* (8), 5493–5503. https://doi.org/10.1074/jbc.275.8.5493.

(339) Nobeli, I.; Favia, A. D.; Thornton, J. M. Protein Promiscuity and Its Implications for Biotechnology. *Nat. Biotechnol.* **2009**, *27* (2), 157–167. https://doi.org/10.1038/nbt1519.

(340) Hou, L.; Honaker, M. T.; Shireman, L. M.; Balogh, L. M.; Roberts, A. G.; Ng, K.; Nath, A.; Atkins, W. M. Functional Promiscuity Correlates with Conformational Heterogeneity in A-Class Glutathione S-Transferases. *J. Biol. Chem.* **2007**, *282* (32), 23264–23274. https://doi.org/10.1074/jbc.M700868200.

(341) Bocedi, A.; Fabrini, R.; Lo Bello, M.; Caccuri, A. M.; Federici, G.; Mannervik, B.; Cornish-Bowden, A.; Ricci, G. Evolution of Negative Cooperativity in Glutathione Transferase Enabled Preservation of Enzyme Function. *J. Biol. Chem.* **2016**, *291* (52), 26739–26749. https://doi.org/10.1074/jbc.M116.749507.

(342) Lien, S.; Gustafsson, A.; Andersson, A.-K.; Mannervik, B. Human Glutathione Transferase A1-1 Demonstrates Both Half-of-the-Sites and All-of-the-Sites Reactivity. *J. Biol. Chem.* **2001**, *276* (38), 35599–35605. https://doi.org/10.1074/jbc.M103789200.

(343) Collauto, A.; Bülow, S.; Gophane, D. B.; Saha, S.; Stelzl, L. S.; Hummer, G.; Sigurdsson, S. T.; Prisner, T. F. Compaction of RNA Duplexes in the Cell**. *Angew. Chem. Int. Ed.* **2020**, *59* (51), 23025–23029. https://doi.org/10.1002/anie.202009800.

(344) Gamble Jarvi, A.; Bogetti, X.; Singewald, K.; Ghosh, S.; Saxena, S. Going the dHis-Tance: Site-Directed Cu $^{2+}$ Labeling of Proteins and Nucleic Acids. *Acc. Chem. Res.* **2021**, *54* (6), 1481–1491. https://doi.org/10.1021/acs.accounts.0c00761.

(345) Giannoulis, A.; Ben-Ishay, Y.; Goldfarb, D. Characteristics of Gd(III) Spin Labels for the Study of Protein Conformations. In *Methods in Enzymology*; Elsevier, 2021; Vol. 651, pp 235–290. https://doi.org/10.1016/bs.mie.2021.01.040.

(346) Ghimire, H.; McCarrick, R. M.; Budil, D. E.; Lorigan, G. A. Significantly Improved Sensitivity of Q-Band PELDOR/DEER Experiments Relative to X-Band Is Observed in Measuring the Intercoil Distance of a Leucine Zipper Motif Peptide (GCN4-LZ). *Biochemistry* **2009**, *48* (25), 5782–5784. https://doi.org/10.1021/bi900781u.

(347) Schweiger, A.; Jeschke, G. *Principles of Pulse Electron Paramagnetic Resonance*; Oxford University Press on Demand, 2001.

(348) Bayly, C. I.; Cieplak, P.; Cornell, W.; Kollman, P. A. A Well-Behaved Electrostatic Potential Based Method Using Charge Restraints for Deriving Atomic Charges: The RESP Model. *J. Phys. Chem.* **1993**, *97* (40), 10269–10280.

(349) Jakalian, A.; Bush, B. L.; Jack, D. B.; Bayly, C. I. Fast, Efficient Generation of High-Quality Atomic Charges. AM1-BCC Model: I. Method. *J. Comput. Chem.* **2000**, *21* (2), 132–146. https://doi.org/10.1002/(SICI)1096-987X(20000130)21:2<132::AID-JCC5>3.0.CO;2-P.

(350) Van, R. G.; Drake, F. Python 3 Reference Manual. *Scotts Val. CA Creat.* **2009**, *10*, 1593511.

(351) Hagen, W. R. *Biomolecular EPR Spectroscopy*, 0 ed.; CRC Press, 2008. https://doi.org/10.1201/9781420059588.

(352) Maryasov, A.; Tsvetkov, Y. D.; Raap, J. Weakly Coupled Radical Pairs in Solids: ELDOR in ESE Structure Studies. *Appl. Magn. Reson.* **1998**, *14* (1), 101–113.

(353) Tait, C. E.; Stoll, S. Coherent Pump Pulses in Double Electron Electron Resonance Spectroscopy. *Phys. Chem. Chem. Phys.* **2016**, *18* (27), 18470–18485. https://doi.org/10.1039/C6CP03555H.

(354) Pornsuwan, S.; Schafmeister, C. E.; Saxena, S. Analysis of the Dynamical Flexibility of Bis-Peptide Nanostructures. *J. Phys. Chem. C* **2008**, *112* (5), 1377–1384. https://doi.org/10.1021/jp077523e.

(355) Tannús, A.; Garwood, M. Improved Performance of Frequency-Swept Pulses Using Offset-Independent Adiabaticity. *J. Magn. Reson. A* **1996**, *120* (1), 133–137. https://doi.org/10.1006/jmra.1996.0110.

(356) Savelieff, M. G.; Wilson, T. D.; Elias, Y.; Nilges, M. J.; Garner, D. K.; Lu, Y. Experimental Evidence for a Link among Cupredoxins: Red, Blue, and Purple Copper Transformations in Nitrous Oxide Reductase. *Proc. Natl. Acad. Sci.* **2008**, *105* (23), 7919–7924. https://doi.org/10.1073/pnas.0711316105.

(357) Holm, R. H.; Kennepohl, P.; Solomon, E. I. Structural and Functional Aspects of Metal Sites in Biology. *Chem. Rev.* **1996**, *96* (7), 2239–2314. https://doi.org/10.1021/cr9500390.

(358) Narr, E.; Godt, A.; Jeschke, G. Selective Measurements of a Nitroxide–Nitroxide Separation of 5 Nm and a Nitroxide–Copper Separation of 2.5 Nm in a Terpyridine-Based Copper(II) Complex by Pulse EPR Spectroscopy. *Angew. Chem. Int. Ed.* **2002**, *41* (20), 3907–3910. https://doi.org/10.1002/1521-3773(20021018)41:20<3907::AID-ANIE3907>3.0.CO;2-T.

(359) Tschaggelar, R.; Breitgoff, F. D.; Oberhänsli, O.; Qi, M.; Godt, A.; Jeschke, G. High-Bandwidth Q-Band EPR Resonators. *Appl. Magn. Reson.* **2017**, *48* (11–12), 1273–1300. https://doi.org/10.1007/s00723-017-0956-z.

(360) Doll, A.; Jeschke, G. Fourier-Transform Electron Spin Resonance with Bandwidth-Compensated Chirp Pulses. *J. Magn. Reson.* **2014**, *246*, 18–26. https://doi.org/10.1016/j.jmr.2014.06.016.

(361) Brandon, S.; Beth, A. H.; Hustedt, E. J. The Global Analysis of DEER Data. *J. Magn. Reson.* **2012**, *218*, 93–104. https://doi.org/10.1016/j.jmr.2012.03.006.

(362) Qin, P. Z.; Warncke, K. *Electron Paramagnetic Resonance Investigations of Biological Systems by Using Spin Labels, Spin Probes, and Intrinsic Metal Ions Part B*; Academic Press, 2015.

(363) Flanagan, H. L.; Gerfen, G. J.; Lai, A.; Singel, D. J. Orientation-selective $^{14}$N Electron Spin Echo Envelope Modulation (ESEEM): The Determination of $^{14}$N Quadrupole Coupling Tensor Principal Axis Orientations in Orientationally Disordered Solids. *J. Chem. Phys.* **1988**, *88* (4), 2162–2168. https://doi.org/10.1063/1.454049.

(364) Gunderson, W. A.; Hernández-Guzmán, J.; Karr, J. W.; Sun, L.; Szalai, V. A.; Warncke, K. Local Structure and Global Patterning of Cu $^{2+}$ Binding in Fibrillar Amyloid-β [Aβ(1–40)] Protein. *J. Am. Chem. Soc.* **2012**, *134* (44), 18330–18337. https://doi.org/10.1021/ja306946q.

(365) Meyer, A.; Abdullin, D.; Schnakenburg, G.; Schiemann, O. Single and Double Nitroxide Labeled Bis(Terpyridine)-Copper( II ): Influence of Orientation Selectivity and Multispin

Effects on PELDOR and RIDME. *Phys. Chem. Chem. Phys.* **2016**, *18* (13), 9262–9271. https://doi.org/10.1039/C5CP07621H.

(366) Elsässer, C.; Brecht, M.; Bittl, R. Pulsed Electron−Electron Double Resonance on Multinuclear Metal Clusters: Assignment of Spin Projection Factors Based on the Dipolar Interaction. *J. Am. Chem. Soc.* **2002**, *124* (42), 12606–12611. https://doi.org/10.1021/ja027348+.

(367) Giannoulis, A.; Motion, C. L.; Oranges, M.; Bühl, M.; Smith, G. M.; Bode, B. E. Orientation Selection in High-Field RIDME and PELDOR Experiments Involving Low-Spin Co $^{II}$ Ions. *Phys. Chem. Chem. Phys.* **2018**, *20* (4), 2151–2154. https://doi.org/10.1039/C7CP07248A.